A UNITED STATES DEPARTMENT OF COMMERCE PUBLICATION

NOAA Technical Report ERL 228-AOML 7

U.S. DEPARTMENT OF COMMERCE
National Oceanic and Atmospheric Administration
Environmental Research Laboratories

Sea Surface Topography From Space
Volume 1

JOHN R. APEL, Editor

ENVIRONMENTAL RESEARCH LABORATORIES

The mission of the Environmental Research Laboratories is to study the oceans, inland waters, the lower and upper atmosphere, the space environment, and the earth, in search of the understanding needed to provide more useful services in improving man's prospects for survival as influenced by the physical environment. Laboratories contributing to these studies are:

Earth Sciences Laboratories (ESL): Geomagnetism, seismology, geodesy, and related earth sciences; earthquake processes, internal structure and accurate figure of the Earth, and distribution of the Earth's mass.

Atlantic Oceanographic and Meteorological Laboratories (AOML): Oceanography, with emphasis on the geology and geophysics of ocean basins, oceanic processes, sea-air interactions, hurrican research, and weather modification (Miami, Florida).

Pacific Oceanographic Laboratories (POL): Oceanography; geology and geophysics of the Pacific Basin and margins; oceanic processes and dynamics; tsunami generation, propagation, modification, detection, and monitoring (Seattle, Washington).

Atmospheric Physics and Chemistry Laboratory (APCL): Cloud physics and precipitation; chemical composition and nucleating substances in the lower atmosphere; and laboratory and field experiments toward developing feasible methods of weather modification.

Air Resources Laboratories (ARL): Diffusion, transport, and dissipation of atmospheric contaminants; development of methods for prediction and control of atmospheric pollution (Silver Spring, Maryland).

Geophysical Fluid Dynamics Laboratory (GFDL): Dynamics and physics of geophysical fluid systems; development of a theoretical basis, through mathematical modeling and computer simulation, for the behavior and properties of the atmosphere and the oceans (Princeton, New Jersey).

Research Flight Facility (RFF): Outfits and operates aircraft specially instrumented for research; and meets needs of NOAA and other groups for environmental measurements for aircraft (Miami, Florida).

National Severe Storms Laboratory (NSSL): Tornadoes, squall lines, thunderstorms, and other severe local convective phenomena toward achieving improved methods of forecasting, detecting, and providing advance warnings (Norman, Oklahoma).

Space Environment Laboratory (SEL): Conducts research in solar-terrestrial physics, provides services and technique development in areas of environmental monitoring, forecasting, and data archiving.

Aeronomy Laboratory (AL): Theoretical, laboratory, rocket, and satellite studies of the physical and chemical processes controlling the ionosphere and exosphere of the earth and other planets.

Wave Propagation Laboratory (WPL): Development of new methods for remote sensing of the geophysical environment; special emphasis on propagation of sound waves, and electromagnetic waves at millimeter, infrared, and optical frequencies.

Marine Minerals Technology Center (MMTC): Research into aspects of undersea mining of hard minerals: development of tools and techniques to characterize and monitor the marine mine environment; prediction of the possible effects of marine mining on the environment; development of fundamental mining technology (Tiburon, California).

NATIONAL OCEANIC AND ATMOSPHERIC ADMINISTRATION

BOULDER, COLORADO 80302

U.S. DEPARTMENT OF COMMERCE
Peter G. Peterson, Secretary

NATIONAL OCEANIC AND ATMOSPHERIC ADMINISTRATION
Robert M. White, Administrator

ENVIRONMENTAL RESEARCH LABORATORIES
Wilmot N. Hess, Director

NOAA TECHNICAL REPORT ERL 228-AOML 7

Sea Surface Topography From Space
Volume I

Proceedings of a Conference Sponsored Jointly by
The National Oceanic and Atmospheric Administration,
The National Aeronautics and Space Administration,
and The United States Navy, Key Biscayne, Florida
October 6-8, 1971

Host Organization: Atlantic Oceanic and Meteorological Laboratories, Environmental Research Laboratories, National Oceanic and Atmospheric Administration, U.S. Department of Commerce

JOHN R. APEL, Editor

BOULDER, COLO.
February 1972

For sale by the Superintendent of Documents, U. S. Government Printing Office, Washington, D. C. 20402

$1.25

FOREWORD

Our generation faces two great challenges to our innate curiosity about the place in which we live, the exploration of space and the understanding of our global ocean. These two endeavors are considered by many as completely dissimilar -- even competing -- activities when, in fact, they are in many ways quite similar. Both activities entail the exploration of an environment hostile to man. Both have that magic element of excitement that accompanies most of man's attempts to push back the frontiers. Both call for ingenuity and new technology, and both, unfortunately, are very expensive. It is especially for this last reason that it is gratifying to see attention being paid to utilizing the techniques developed in space exploration for furthering our understanding of the sea.

The great contributions made so far to our understanding of the dynamics of the sea have come primarily from data obtained by oceanographic research ships. The advent of the space era does not remove the need for scientists to go to sea -- hopefully this will never be removed. It does, however, provide us for the first time the ability to "see" great reaches of the ocean at one time and to consider features and processes on an almost global scale. The oceanographer, enamoured as he is with his ships and his work at sea, has been slow, even reluctant at times, to capitalize on the space program to provide information on the sea that could not even be considered a decade ago. But for many oceanographers this earlier reluctance has given way to an eagerness to get instruments up where they can see more and to develop new instrumentation to provide new knowledge of the sea. Earth orbiting satellites can fill this need.

The Joint NOAA-NASA-NAVY Conference held on Key Biscayne, Miami, Florida, October 6-8, 1971, brought together scientists from a broad range of specialities to look specifically at the use of remote sensors on spacecraft for providing new and needed information on the upper surface of the ocean. It was an exciting conference to attend. It should be equally so to read for those who could not be there in person.

The Atlantic Oceanographic and Meteorological Laboratories were pleased to act as host organization and to publish the Proceedings as one of its technical reports.

Harris B. Stewart, Jr.
Director
Atlantic Oceanographic and
Meteorological Laboratories

TABLE OF CONTENTS

VOLUME I

TABLE OF CONTENTS (Cont'd)

TABLE OF CONTENTS (Cont'd)

VOLUME II

PROGRAM COMMITTEE

John R. Apel, Chairman, NOAA/AOML
Jerome D. Rosenberg, NASA/Headquarters
John W. Shermann, III, Navy/SPOC
H. Ray Stanley, NASA/Wallops Station
Martin J. Swetnick, NASA/Headquarters
Friedrich O. Vonbun, NASA/GSFC

CONFERENCE ATTENDEES

Dr. John R. Apel
NOAA/AOML
901 South Miami Avenue
Miami, Florida 33130

Dr. Donald Barrick
Battelle Memorial Institute
505 King Avenue
Columbus, Ohio 43201

Mr. John Berbert
NASA/Goddard Space Flight Center
Greenbelt, Maryland 20771

Mr. Harold Black
The Johns Hopkins University
Applied Physics Laboratory
Silver Spring, Maryland 20910

Mr. Paul Bouchard
DBA Systems
Melbourne, Florida 32901

Dr. Saul Broida
Coast Guard Headquarters
200 Seventh Street, SW
Washington, D.C. 20591

Mr. Ronald L. Brooks
Wolf Research & Development Corp.
Clark & Vine Streets
Pocomoke City, Maryland 21851

Mr. Walter E. Brown, Jr.
Senior Scientist
Jet Propulsion Laboratory
4800 Oak Grove Drive
Pasadena, California 91103

Mr. Bud Burke
Sea-Flight Corporation
940 S.W. 34th Street
Ft. Lauderdale, Florida 33315

Mr. George Bush
Johns Hopkins University, APL
Silver Spring, Maryland 20910

Mr. H. Michael Byrne
Woods Hole Oceanographic Institute
Woods Hole, Mass. 02543

Mr. Bernard Chovitz C111
NOAA/National Ocean Survey
Rockville, Maryland 20852

Dr. Leroy M. Dorman
NOAA/AOML/MG&G Laboratory
901 South Miami Avenue
Miami, Florida 33130

Mr. James K. Estes
USAF Aeronautical Chart & Info. Center
2nd and Arsenal Streets
St. Louis, Missouri 63118

Dr. D. Michael Fubara
Battelle Memorial Institute
505 King Avenue
Columbus, Ohio 43201

Dr. E. M. Gaposchkin
Smithsonian Astrophysical Observatory
60 Garden Street
Cambridge, Mass. 02138

Mr. Thomas W. Godbey
General Electric Company
Utica, New York 13503

Lt. (JG) Lowell Goodman
NOAA/National Ocean Survey, AMC
439 West York Street
Norfolk, Virginia 23510

Mr. Alan Greene
Raytheon Company
Boston Post Road
Wayland, Mass. 01778

Mr. George Hadgigeorge
AFCRL/LWG
L. G. Hanscom Field
Bedford, Mass. 01778

Mr. Robert Harrington
Teledyne/Ryan Aeronautical
8650 Balboa Avenue, P.O. Box 311
San Diego, Calif. 92112

Dr. Klaus Hasselmann
Woods Hole Oceanographic Institution
Woods Hole, Mass. 02543

Dr. George S. Hayne
Research Triangle Institute
P. O. Box 12194

Mr. Craig Hooper
Office of Programs
NOAA/Environmental Res. Laboratories
Boulder, Colorado 80302

Mr. Edward F. Hudson
Raytheon Company
Boston Post Road
Wayland, Mass. 01778

Mr. Albert C. Jones
Space Division
North American Rockwell SL92
12214 Lakewood Boulevard
Downey, Calif. 90241

Dr. W. Linwood Jones
NASA/Langley Research Center
Hampton, Virginia 23365

Mr. Joseph Kaye
Chief of Materiel, U.S. Navy
P.M. 16-22
Washington, D.C. 20360

Mr. Douglas S. Kimball
Westinghouse Defense & Space Center
Mail Stop 337
Baltimore, Maryland 21203

Dr. Kumar Krishen
Lockheed Electronics Co.
16811 El Camino Real
Clearlake City, Texas 77058

Mr. Clifford Leitao
NASA Wallops Station
Wallops Island, Virginia 23337

Dr. Alden Loomis
Jet Propulsion Laboratory
4800 Oak Grove Drive
Pasadena, Calif. 91103

Mr. Thomas J. Lund
Teledyne/Ryan Aeronautical
8650 Balboa Avenue, P.O. Box 311
San Diego, Calif. 92112

Dr. Charles Lundquist
Smithsonian Astrophysical Observatory
60 Garden Street
Cambridge, Mass. 02138

Mr. Paul A. Lux
Teledyne/Ryan
P.O. Box 311
San Diego, Calif. 02138

Dr. Mark M. Macomber
Naval Oceanographic Office
Director, Gravity Div. Code 8300
Washington, D.C. 20390

Dr. Chreston Martin
Wolf Research & Development Corp.
6801 Kenilworth Avenue
Riverdale, Maryland 20840

Mr. George Maul
NOAA/AOML/Physical Oceanographic Lab.
901 South Miami Avenue
Miami, Florida 33130

Mr. Robert W. McCaslin
NOAA/National Weather Service
Silver Spring, Maryland 20910

Dr. William McLeish
NOAA/AOML/Sea-Air Interaction Lab.
461 South Miami Avenue
Miami, Florida 33130

Dr. Lee S. Miller
Research Triangle Institute
P. O. Box 12194
Research Triangle Park, N. C. 27709

Dr. Richard K. Moore
Space Tech. Building
University of Kansas
Irving Hill Road, West Campus
Lawrence, Kansas 66044

Mr. A. George Mourad
Battelle Memorial Institute
505 King Avenue
Columbus, Ohio 43201

Prof. Ivan Mueller
Dept. of Geodetic Science
Ohio State University
164 West 19th Avenue
Columbus, Ohio 43210

Mr. Fred Nathanson
Technology Service Corporation
8555 16th Street
Silver Spring, Maryland 20910

Mr. J. Barry Oakes
Applied Physics Laboratory
8621 Georgia Avenue
Silver Spring, Maryland 20910

Prof. Willard J. Pierson, Jr.
Dept. of Meteorology & Oceanography
New York University
New York, New York 10453

Dr. Henry Plotkin
Code 520
NASA Goddard Space Flight Center
Greenbelt, Maryland 20770

Mr. Robert F. Pontzer
Teledyne/Ryan Aeronautical
1501 Wilson Boulevard, Suite 900
Arlington, Virginia 22209

Prof. Richard H. Rapp
Ohio State University
164 W. 19th Avenue
Columbus, Ohio 43210

Mr. Jerome Rosenberg
OSSA-NASA Headquarters
Washington, D. C. 20546

Mr. Duncan Ross
NOAA/AOML/Sea-Air Interaction Laboratory
461 South Miami Avenue
Miami, Florida 33130

Mr. Laurence Rossi
NASA/Wallops Station
Code 221
Wallops Island, Virginia 23337

Mr. Normand A. Roy
Wolf Research & Development Corp.
Clark & Vine Streets
Pocomoke City, Maryland 21851

Mr. Phillip Schwimmer
Dept. of Defense
DIA MC
The Pentagon
Washington, D.C. 20301

Mr. Alan Shapiro
E.O. Hulburt Center for Space Research
Naval Research Laboratory
Washington, D.C. 20390

Mr. John W. Sherman
Spacecraft Oceanography Project
Naval Research Laboratory
Washington, D. C. 20390

Dr. Miriam Sidran
NOAA/Natl. Marine Fisheries Service
Southeast Fishery Center
75 Virginia Beach Drive
Miami, Florida 33149

Dr. Joseph Siry
NASA/Goddard Space Flight Center
Greenbelt, Maryland 20771

Dr. David E. Smith
Code 553
NASA/Goddard Space Flight Center
Greenbelt, Maryland 20771

Mr. Sam Smith
Naval Weapons Laboratory
Code KAO
Dahlgren, Virginia 22448

Mr. H. Ray Stanley
NASA/Wallops Island Station
Wallops Island, Virginia 23337

Dr. Harris B. Stewart, Jr.
Director, NOAA/AOML
901 So. Miami Avenue
Miami, Florida 33130

Mr. William E. Strange
Computer Science Corp.
6520 Columbia Pike
Falls Church, Virginia 22041

Dr. Alan E. Strong
NOAA/NESS-ESG
3737 Branch Avenue
Washington, D.C. 20031

Dr. Wilton Sturges
Dept. of Oceanography
University of Rhode Island
Kingston, R. I. 02881

Dr. Martin Swetnick
OSSA/NASA Headquarters
Washington, D. C. 20546

Prof. Manik Talwani
Lamong-Doherty Geological Observatory
Palisades, New York 10964

Dr. Byron Tapley
University of Texas at Austin
227 Taylor Hall
Austin, Texas 78712

Capt. Raymond W. Thompson
NASA Headquarters
Code W
Washington, D. C.

Cdr. John Tuttle
Chief of Materiel, U.S. Navy
P.M 16-22
Washington, D. C. 20360

Dr. Fredrich O. Vonbun
Code 550
NASA/Goddard Space Flight Center
Greenbelt, Maryland 20771

Mr. Edward J. Walsh
NASA/Wallops Island Station
Wallops Island, Virginia 23337

Dr. George C. Weiffenbach
Smithsonian Astrophysical Observatory
60 Garden Street
Cambridge, Mass. 02138

Dr. Willard Wells
Tetra Tech., Inc.
360 Halstead
Pasadena, Calif. 91107

Mr. Ralph Willison
The Johns Hopkins University
Applied Physics Laboratory
8621 Georgia Avenue
Silver Spring, Maryland 20910

Mr. Benjamin Yaplee
E.O. Hulburt Center for Space Research
Naval Research Laboratory
Washington, D.C. 20390

Mr. Steven Yionoulis
The Johns Hopkins University
Applied Physics Laboratory
8621 Georgia Avenue
Silver Spring, Maryland 20910

Mr. Bernard D. Zetler
NOAA/AOML/Physical Oceanog. Lab.
901 South Miami Avenue
Miami, Florida 33130

INTRODUCTION

The impetus for the NOAA-NASA-NAVY Conference on Sea Surface Topography from Space was largely due to two forthcoming spacecraft that bear on the problem: SKYLAB and GEOS-C. Each vehicle is to carry an X-band radar altimeter; SKYLAB in addition has a rather comprehensive sensor package designed for observing earth resources in the visible, infrared, and microwave frequency regions.

The Conference was devoted to the subjects of geodesy and oceanography, the two topics being intimately related through the distortions that a dynamic, moving ocean introduces on the geoid as measured with a precision altimeter on an accurately tracked satellite. In a very real sense, the geodescist's noise is the oceanographer's signal. This relationship was recognized and exploited at the conference held at Williams College in August 1969, the report of which recommended the development of a 10-cm precision altimeter for space use, among other things.

As defined for purposes of the present Conference, "sea surface topography" denotes ocean surface features ranging from capillary waves through gravity waves, swell, setups, geostrophic slopes, geoidal undulations, and tides, in order of increasing wavelength. The meeting addressed itself to the problems of measuring these undulations from spacecraft or aircraft using radar or laser instrumentation. As such, it brought together, at Key Biscayne, Florida, specialists in geodesy, oceanography, space science and space technology. The interdisciplinary features of the problem proved especially stimulating to the attendees, not only because of the implications which the subject has for each discipline, but because of the social relevance (to use a current shibboleth) which the research possesses. It appears possible, for instance, to ultimately use radar systems in space to provide all-weather monitoring and prediction of surface winds, sea state, current systems, and perhaps even hurricanes and storm surges. These functions are probably a decade off, but the impact on the welfare of man is obvious.

John R. Apel
Chairman

AN OBSERVATIONAL PHILOSOPHY FOR GEOS-C SATELLITE ALTIMETRY

George C. Weiffenbach
Smithsonian Astrophysical Observatory
Cambridge, Massachusetts 02138

Since the GEOS-C altimetry experiment will be the first of a series of altimeter missions, its objectives should be defined within the context of the long-term objectives of satellite altimetry. One definition of these objectives was stated in the report of the 1969 Williamstown study on Solid Earth and Ocean Physics as the synoptic measurement of the topography of instantaneous mean sea level to an accuracy of 10 cm. In that report, emphasis was placed on determining variations of ocean topography over periods of time ranging from 2 cycles per day to 1 cycle per year with a spatial resolution of 1° (100 km) or better.

The need for establishing the accuracy and reliability of satellite-borne altimeter instruments is self-evident and clearly must be considered a primary GEOS-C objective. However, I would like to suggest that, although these factors are necessary, they are not sufficient for the future design of effective altimetry systems. An altimetry system is not only comprised of satellite instrumentation and data acquisition, but also of all elements of the data analysis functions, including computer software and physical models such as geopotential models, ocean current and density variation models, etc. To fully establish the feasibility of attaining a 10 cm system accuracy, and to provide the inputs needed for the design of efficient altimeter systems in the future, the GEOS-C altimetry experiment must include an extensive investigation of all the above-mentioned factors. This in turn implies that another primary objective of GEOS-C must be to acquire a substantial body of synoptic data to establish the ranges of values of the various oceanographic parameters that will be encountered in practice, to provide the actual experimental data necessary for developing and evaluating software and analytic procedures, and to determine just what ancillary data (e.g., the geopotential) we will need to acquire to reach the 10 cm accuracy level.

Having stated the broad objectives for the GEOS-C experiment, I will now outline what I consider to be the major problem areas in satellite altimetry, and briefly discuss their current status. I will then consider some design and operating questions relevant to the ability of the GEOS-C experiment to contribute to the stated long term altimetry objectives.

To make the subsequent discussion specific enough to provide useful information we must define some characteristics of the altimeter instrumentation. I will first assume that the GEOS-C and subsequent instruments will be pulsed radar altimeters operating in the X- to K-band region. At this time this choice is clearly the best from the standpoint of practical engineering considerations, since suitable components and systems are both available and in an advanced state of development, power requirements and antenna dimensions are consistent with satellite constraints, this region of the electromagnetic spectrum permits all-weather operation, and finally, ionospheric propagation errors are at a tolerable level.

With this type of system, the altimeter "footprint" on the ocean surface will be a circle with a diameter in the range 1 to 10 km. At wavelengths of 1 to 3 cm and for ocean-reflecting areas of square kilometers the radar echo received at the satellite will be the vector sum of the echos from a very large number ($>10^6$) of individual ocean-surface reflecting elements that will be distributed in range (height) over many (r.f.) wavelengths for all but an extraordinarily smooth ocean. The resulting distribution of relative phases among the individual echos will cause the amplitude to vary within each (return) pulse over a very great range. These amplitude variations, which will be distributed according to the Rayleigh probability density function, effectively prevent us from determining satellite-to-ocean altitude from any single pulse. Further, there is a minimum time (or distance travelled by the satellite) that must elapse between successive pulses to ensure the decorrelation of this Rayleigh noise that is necessary before a useful result can be obtained from the average of many pulses. For the case we are considering here, the minimum decorrelation time is of the order of 1 millisecond, and roughly some 1000 pulses must be averaged to obtain a reasonable altitude measurement.

Thus the output of the satellite altimeter will be a measurement roughly once per second of the vertical distance between the satellite and an elongated segment of ocean surface with dimensions of the order of 1 to 10 km perpedicular to the satellite subtrack and perhaps 10 to 20 km along the subtrack. The basic observational information from the altimeter will be a one-dimensional profile (averaged over the elongated footprint) of the ocean surface relative to the satellite orbit as it is traced out in time by the motion of the satellite. In addition, the roughness of the ocean surface will influence the shape and amplitude of the echo pulses, and may provide information on sea state.

Now, what are the problem areas? They are listed in table 1. First, there is the instrument per se, and its calibration. Although these are of primary importance, I will not discuss them further since they will be dealt with in detail by later speakers.

Table 1.

Satellite Altimeter Problem Areas.

INSTRUMENTATION
CALIBRATION
PROPAGATION
SATELLITE TRACKING
GEOID
SEA SURFACE EFFECTS

Since the altimeter measures the time interval for a pulse to travel from satellite to ocean and back, we must know the pulse propagation velocity to compute altitude. If we assume, as most everyone does in practice, that the light second is our primary length standard, we need only be concerned with departures from the vacuum velocity of propagation--viz., the influences of the ionosphere and troposphere on microwave propagation velocities.

For radio frequencies below 20 Ghz, the troposphere produces an apparent altitude change of about 2-1/2 meters. At any one ocean location, the variation of this altitude error with time will have a peak to peak amplitude of about 30 cm, and an RMS value of roughly 10 cm, these variations being the result primarily of variations in atmospheric water vapor content. There is a water vapor resonance line at 23 Ghz ($\lambda = 1.3$ cm) so that should be avoided. There are other molecular absorption lines for radio frequencies above 23 Ghz that will cause both large altitude errors and loss of signal (e.g. the oxygen line at 55 Ghz), so frequencies above 20 Ghz should be avoided. Although the troposphere will not be serious problem for GEOS-C, it is clear that corrections must be devised for a 10-cm system.

At the planned GEOS-C frequency of 13.9 Ghz, the uncorrected ionospheric range error will have a maximum of about 15 cm for daytime observations and about 3 cm at night. At 20 Ghz these errors would be halved. Even a rather crude correction can reduce ionospheric altitude errors to acceptable levels.

The satellite altitude must be known independently before the ocean profile can be gotten from the altimeter measurements. In the particular case of GEOS-C there will be no dearth of accurate tracking observations, since a substantial number of globally distributed ground stations will be available to use the onboard tracking instruments. Indeed, if all of the available systems are employed, GEOS-C will be the most intensively tracked satellite ever. GEOS-C will be tracked by laser ranging (12 or more stations with accuracies of 0.3 to 1 meter), TRANET radio doppler (perhaps 20 stations), C-band radar and the Goddard S-band Range and Range Rate System. As a result the accuracy of the computed GEOS-C orbits will be limited primarily by the accuracy of the gravity field model, and by the accuracy with which solar photon pressure and perhaps drag (depending on the GEOS-C orbital altitude) can be modeled.

The errors that would be introduced into the GEOS-C computed orbits by the best of the currently available gravity field models is in the range 3-10 meters. Improvements in the geopotential model which are in progress should reduce this uncertainty by a factor of 2 by the time GEOS-C is in orbit. (It should be noted that the GEOS-C tracking data should themselves lead to further refinement of the geopotential.)

Taken at face value, these orbital errors would present an unduly pessimistic impression. Actually, the orbit of a satellite at the altitudes now being considered for GEOS-C (perhaps 800 km or so) will be controlled almost entirely by the large scale features of the gravity field, i.e., those corresponding to spherical harmonics of degree and order 20 and lower, and the corresponding orbital perturbations of any significance will have frequencies of 100 per day or less. In other words, there should be no significant orbital perturbations for GEOS-C which have frequencies greater than 100 per day--or wavelengths shorter than about 5000 km. I would estimate that the altitude uncertainty for GEOS-C for wavelengths less than 5000 km will be less than one meter. Furthermore, the amplitudes of orbital perturbations decrease rapidly with decreasing wavelengths.

As a result, no serious problems should be encountered from GEOS-C altitude errors when the altimetry data are used to deduce topographic features with wavelengths less than 5000 km, which is the area of greatest interest.

Although the fine structure in the gravity field has little influence on the satellite orbit, its effect on the geoid is quite another matter. It will, of course, be necessary to separate the influences of the gravity field on ocean topography from those caused by oceanographic and meteorological phenomena. One important means

of effecting this separation will be to examine altimetry records taken at different times. Since time variations in the geoid are either extremely slow or have well defined frequencies (tides), it will be possible to extract from the altimeter data the time varying oceanographic factors. This approach will require substantial data sets obtained over the full operating life of the altimeter. A different method will be needed to identify the more stable oceanographic features. An independent determination of the geoid is obviously one means. Table 2 lists my estimates of the present errors in geoid topography for three somewhat arbitrary wavelength regions of the geoid. The estimates for the short and intermediate regions are quite uncertain because there are too little data. Indeed, GEOS-C will provide the first opportunity for obtaining a systematic survey of these geoid features over the oceans. A survey of this kind will be very useful in designing future altimetry experiments. Thus we have another reason for obtaining a thorough examination of all ocean areas accessible to GEOS-C.

Table 2.

Present uncertainties in the topography of the geoid.

Short wavelength	$\lambda < 200$ km	10 to 20 meters peak.
Intermediate wavelength	$200 < \lambda < 2000$	10 meters
Long wavelength	$\lambda > 2000$	3-5 meters RMS

B

Improvements in the long wavelength region of the geoid will most probably be accomplished through dynamic analyses of satellite orbits. As noted above GEOS-C will be one of the satellites used for this purpose. An independent determination of the geoid in the intermediate region can also be obtained from satellite observations, either by direct integration of doppler observations of a minimum altitude satellite, or through an orbiting gravity gradiometer. The only satellite method appropriate for measuring the short wavelength geoid features is altimetry. An independent measure can only be obtained through surface observations such as shipboard gravimetry. One output of the GEOS-C observations which could be important to the design of future altimeter experiments would be a survey of these short wavelength features. This survey would indicate those regions where acquisition of surface data is most important. This information would be quite valuable, particularly in the light of the long times needed to carry out large scale surface observations.

Sea surface effects will not be discussed in any detail here, as they will be treated at length by subsequent speakers. Briefly there are two effects of interest. First the shape and amplitude of the reflected radar pulses are both expected to be influenced by sea state. This may enable us to obtain synoptic sea state information from satellite altimetry, if unique correlations can be deduced from comparisons of the altimetry data with "ground truth." The second effect is the altitude bias resulting from the difference between the electromagnetic and geometric centroids. This difference should not exceed 10% of the wave height. Since the median wave height for all of the oceans is of the order of 1.5 meters, the altitude bias should be acceptable for GEOS-C on an overall basis. However there will be many occasions, particularly during winter months at higher latitudes, when wave heights may be substantially higher. Thus it will be of considerable importance to monitor echo pulse shape and amplitude to identify sea state. It would then be possible to at least delete data when the altitude bias might be unacceptably large. There is also the possibility of being able to develop suitable corrections for this source of error.

The final point I wish to consider is the question of how much coverage--in terms of both geography and time--the GEOS-C experiment can provide. I consider this point basic to the ability of the GEOS-C experiment to establish the potential capability of satellite altimetry, to quantitatively delineate problem areas and to provide a sound basis for the design of subsequent altimetry missions.

Previous GEOS spacecraft have had three independent power systems: main, optical beacon and transponder. I would like to suggest that the

main and optical beacon supplies be rearranged to provide maximum power for the altimeter experiment. Table 3 lists the steady loads that these two supplies must support. The 0.2 duty cycle for the telemetry system will provide 5 hours per day of telemetry, which is generous. Table 4 shows the power budget for 20 sequences (140 flashes) for 2 lamps flashed simultaneously. Again this should be a generous allowance for this beacon.

Assuming the GEOS-C solar cell array to be the same as for GEOS-2, the total average power available at the battery terminals for the two power systems is 27.7 watts. The power available for the altimeters is thus 27.7 - 12.9 - 2.0 = 12.8 Watts. The total energy per day for the altimeters is 307 Watt-hours.

It is presently planned to have two altimeter modes in GEOS-C: low power synoptic and high accuracy. Estimated power consumption is 40 Watts for the synoptic mode and 80 Watts for the high accuracy mode. If the available energy is divided equally between the two modes, we have the following duty cycle and total operating times for an 18-month operating life.

Mode	Hours/day	Total hours operation (18-month life)
Synoptic	3.84	2100
High Accuracy	1.92	1060

The speed of the satellite over the ground is about 240° per hour. If we assume that the narrow swath traced out by the altimeter footprint is an adequate sample for a path 1° wide, the altimeter sampling rate will be 240 square degrees of ocean per hour. The total coverage in 18 months under these assumptions will then be 506,000 and 253,000 square degrees for the synoptic and high accuracy modes respectively.

For an orbital inclination of 50°, the satellite will fly over some 75% of the total ocean surface, or 22,000 square degrees. For an inclination of 65°, the corresponding numbers will be 85% and 26,000 square degrees. Therefore, on an average, each square degree of ocean

Table 3.

Suggested steady loads for GEOS-C main and altimeter power systems.

Doppler Beacon	5.5 Watts
Command System	1.0 Watts
Attitude Wheel	1.0 Watts
Telemetry System (0.2 Duty Cycle) avg power	1.2 Watts
Altimeter - continuous loads	
Delayed Command System	3.0 Watts
Data storage memory	1.0 Watts
Voltage-sensing cutoff switch	0.2 Watts
Total steady loads	12.9 Watts

Table 4.

Optical beacon power budget for GEOS-C.

Optical beacon	600 Watt-Seconds per lamp-flash from battery
2 lamps	
7 flashes per sequence	
20 sequences per day	
Total energy per day	168,000 Watt-seconds
Average power consumption	2.0 Watts

covered by the satellite will be sampled with the following frequency in the synoptic mode:

Orbit inclination	Average number of samples
50°	23
65°	19

If we assume that the high accuracy mode will be concentrated on more limited "ground truth" areas totaling perhaps 500 square degrees of ocean, then some 500 samples will be obtained in 18 months from this more limited area.

The number of samples per square degree in each mode would seem to provide a quite satisfactory data base for the GEOS-C altimeter experiment.

Refinement of the Geoid from GEOS-C Data

Bernard H. Chovitz
NOAA/National Ocean Survey
Rockville, Md. 20852

I begin with two assumptions: first, the accuracy of the GEOS-C altimeter is known; second, the altimeter measures the distance between the satellite and the geoid, (that is, the geoid is coincident with sea level). In the context of GEOS-C, the first assumption is definitely false. In fact, the primary objective of the GEOS-C altimeter experiment is to verify the accuracy of the altimeter itself. This is as it should be; the altimeter opens up such a fruitful source of data, that it is most important to determine just how good this data is. However, it is hoped that this question can be resolved, so that the data then can be used for geodetic and geophysical application. With respect to the difference between sea level and the geoid, any time-invariant effects (like currents) or long-period effects (like tides) will be an order of magnitude smaller than the fine structure in the geoid separation (of the order of 5 to 10 meters) which cannot be discerned by dynamical satellite analysis but which may be realizable from altimetry.

The basic principle of geoid determination from satellite altimetry over the oceans is as follows (fig. 1). By tracking, the height of the satellite above the ellipsoid, h_e, is obtained. The satellite's height above the geoid (using assumption 2 above), h, is obtained by altimetry. Then the geoid height, $N = h_e - h$.

The question arises: since the height of the geoid above the ellipsoid depends on the determination of a dynamic orbit, and this in turn depends on the knowledge of the gravitational field, which is equivalent to knowing the geoidal height, isn't this a circular approach? The answer is, no, because the variations in N are of much shorter wavelength than their effect on the orbit, and hence the orbit is not appreciably affected by neglect of these short wave variations.

A further step in addition to the determination of the localized ocean geoid is the use of the altimetry data to refine the global gravity field. This will yield a better reference orbit and determination of h_e, and thereby improve the value of N. The altimetry provides data for observation equations which can be added to observation equations obtained from tracking for the improvement of parameters relating to the orbit and the gravitational field.

Figure 1

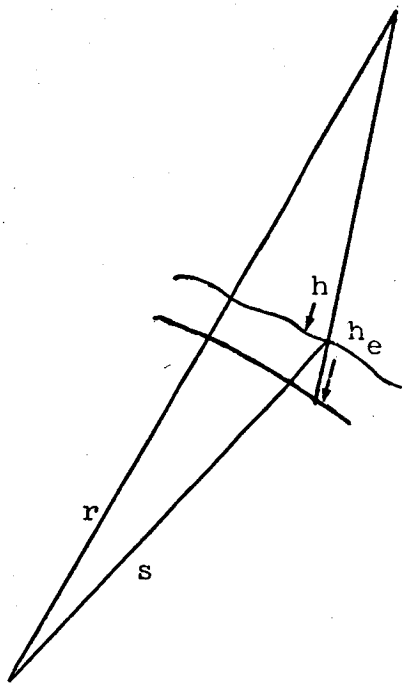

From fig. 1,

$$\vec{h} = \vec{r} - \vec{s}$$

where $\vec{h}$, $\vec{r}$, $\vec{s}$ are vectors, $\vec{r}$ and $\vec{s}$ being the geocentric position of the satellite and sub-satellite ocean surface point, respectively. For the purpose of writing a linearized observation equation, the small angles between these vectors are neglected, and their magnitudes are taken in the relation

$$h = r - s.$$

This approximation can be recovered by iteration.

Then the observation equation for the measured altitude h, is

$$h_{obs} + \delta h = h_{calc} + \frac{\partial h}{\partial p} \Delta p$$

where p is a vector of parameters and δh is due to the imperfection in the observation. Then

$$h_{obs} + \delta h = h_{calc} + \frac{\partial r}{\partial p} \Delta p - \frac{\partial s}{\partial p} \Delta p.$$

Also, $$r = r(E, X)$$

where E is a set of orbital parameters, and X a set of gravitational parameters (non-gravitational effects being neglected or considered as perfectly known).

$$s = A_e (1 + B^T X)$$

represents the radius of a point on the geoid expressed in terms of a scaling factor (which in this case can be taken to be the earth's equatorial radius, A_e) and the set of gravitational parameters X, oriented by the vector B. (For example, if X were the usual spherical harmonic coefficients, B would be a set of spherical harmonics).

$$\text{Then} \quad \frac{\partial r}{\partial p} \Delta p = \frac{\partial r}{\partial E} \Delta E + \frac{\partial r}{\partial X} \Delta X$$

$$\text{and} \quad \frac{\partial s}{\partial p} \Delta p = \Delta A_e (1 + B^T X) + A_e B^T \Delta X$$

$$\approx \Delta A_e + A_e B^T \Delta X$$

finally yielding

$$h_{obs} + \delta h = h_{calc} + \frac{\partial r}{\partial E} E + \left(\frac{\partial r}{\partial X} - A_e B^T\right) \Delta X - \Delta A_e .$$

The form of this observation equation is due to Kaula (unpublished). A similar formulation can be found in Lundquist et. al., [1969].

To state the problem in its most comprehensive form involves two further considerations. First the gravitational parameters, X, have purposely been written in ambiguous form, because many of the detailed solutions to this problem proposed up to now have advocated functions for X which are deliberate alternatives to the conventional spherical harmonic approach. The essential difficulty with spherical harmonic coefficients is that they are integrated averages over the entire surface, and thus the higher degree harmonics can have no meaningful physical correlation with specific portions of the earth's surface. A second consideration is the insertion of all possible data sources for an overall solution. This means taking advantage of gravity data on land, and the tracking data itself.

Let us consider an approach due to Koch [1970]. Since altimetry yields geoid heights, N, as data, the inverse of Stokes' formula can be employed [Molodensky et. al., 1962, p. 50]

$$\Delta g_s = -\gamma\left(\frac{N_s}{R} + \frac{1}{2\pi}\iint_\sigma \frac{N - N_s}{r^3}\, d\sigma\right)$$

where the subscript s denotes the point of measurement, r is the distance between s and the surface elements $d\sigma$ of the sphere σ of radius R, γ is normal gravity, and N is the geoid height at $d\sigma$. To apply this formula the geoid heights N must be known over the entire globe; however, altimetry will not be available over land. But Stokes' formula itself is available:

$$N_s = \frac{1}{4\pi R\gamma}\iint_\sigma \Delta g\, S(\psi)\, d\sigma$$

where ψ is the spherical arc between s and $d\sigma$, $S(\psi)$ is Stokes' function, and Δg is the gravity anomaly on $d\sigma$. This formula depends on knowledge everywhere of Δg which has been obtained mainly on land (and is even sparse in many areas there). But gravity anomalies closest to the fixed point have the greatest influence on the geoid undulations, and approximate values for Δg on the oceans should suffice to give a good initial set of N on the continents. Then successive approximation between these two formulas should yield representative values of Δg_s over the oceans.

This preliminary approach has both mathematical and physical deficiencies. The former lies in the fact that the conditions for convergence of the scheme are not specifically known and proven. However, physical intuition leads us to believe that failure of convergence would be due mainly to a lack of sufficiently well-distributed data. This could be overcome by using statistically obtained, instead of observational, data, although this alternative is not desirable. However, there are also deficiencies due to imperfect physical assumptions. The use of Stokes' formula and its inverse presupposes that the Earth has been "regularized", that is, there are no masses outside the geoid. Thus all topography is neglected. Over broad regions and in the middle of the oceans, this will not mean much, but over special areas of interest--like sea trenches, and the continental shelf regions--this approximation must be accounted for.

This can be accomplished by introducing two sets of integral equations, one of which uses N, the other Δg, as observational

data:

$$\frac{R^2}{\gamma} \iint_{\sigma} \frac{\chi}{r} \, d\sigma = N_s$$

$$2\pi \chi \cos^2 \alpha_s - \frac{3}{2} \frac{1}{R} \iint \frac{\chi}{r} \, d\sigma - \iint \frac{H-H_s}{r^3} \chi \, d\sigma = \Delta g_s$$

The derivation of these equations may be found in Koch [1970] and Molodensky et. al. [1962, Ch. 5]. H is the topographic height and α is the deflection of the vertical. The unknown in these equations is the parameter χ which expresses the anomalous gravitational field as a simple density layer on the reference surface. The practical method for solving these equations is to replace the integration by a summation over a set of surface elements with a single density, χ_i, corresponding to each surface element σ_i. This yields a set of linear equations in χ_i ($i = 1 \ldots, n$) where n is the number of surface elements, which can be treated as observation equations in the usual fashion, taking advantage of redundant data ($s>n$), and employing pertinent weights.

Young [1970] tackles the same problem as Koch in considering worldwide data consisting of a mix of gravity anomalies on land, and geoid heights (from altimetry) at sea. Young sets up a function

$$\zeta = \frac{r}{2} \frac{\partial T}{\partial r}$$

where T is the anomalous potential. By the so-called fundamental theorem of geodesy [Heiskanen and Moritz, 1963, p. 88], there is obtained

$$\zeta = -\frac{r}{2} \Delta g - \gamma N.$$

Young has two purposes; first, to exhibit uniqueness and existence proofs for the determination of T, and second to provide an algorithm for the computation of T. The choice of ζ satisfies these purposes in the following way:

$$T = \frac{1}{4\pi} \iint K\zeta \, d\sigma$$

is the formulation of the Neumann (or second boundary-value) problem, which can be solved on the sphere by representing the kernel K in terms of spherical harmonic functions. Furthermore, to begin the algorithm, one can set the initial ζ equal to

$-\frac{r}{2}\Delta g$ on land, and to $-\gamma N$ at sea. The algorithm then proceeds by solving for T in terms of spherical harmonic corrections δC directly from the integral expression. Practically, this is done by a summation over a set of surface subdivisions, similar to Koch's formulation. However, since spherical harmonics are directly involved in the kernel, each summation term itself is an integral of the form

$$\int_{\phi_1}^{\phi_2} P_n^m (\sin\phi) \cos\phi \, d\phi$$

where $P_n^m (\sin\phi)$ is a spherical harmonic function of the latitude ϕ. Recursion formulas for this are available to expedite the computation. The algorithm proceeds by computing corrections to ζ in terms of the current δC until convergence is reached.

Young provides necessary conditions for the uniqueness and existence of a solution for his method. As long as the zeroth harmonic is given, a solution exists regardless of the relative distribution of the gravimetry and altimetry. The computational procedure, however, does not provide for the use of redundant data, and involves more complicated computations than Koch's method.

The most comprehensive attack on the problem combines altimetry, gravimetry, and tracking data into one simultaneous solution. This has been outlined by Koch [1970] in connection with the density layer method of expressing the geopotential. The integral equation expressing the geoid height, N, as a function of χ is introduced into the observation equation for the altimetry measurement h_{obs}. This is combined with integral equations in Δg and with the conventional tracking data observation equation. Computational complexity is proportional to the size of the surface elements chosen. This particular approach is very flexible since the size can be varied according to the specific use being made. The satellite orbit is not sensitive to high frequency undulations (except in special cases of resonance); hence the residual field can be approximated by a coarse subdivision. On the other hand, to obtain the detailed structure, a finer subdivision will be required. A common solution of all data (altimetry, gravity, and tracking) can employ both the fine and coarse mesh. Final values of N and Δg are computed directly from the corresponding integrals using the final set of χ_i. If desired, spherical harmonic coefficients can also be obtained from the χ_i.

Lundquist et. al. [1969] have concentrated on the problem of best expressing the geopotential. This method employs "sampling" functions which are linear combinations of spherical

harmonics, such that each function peaks strongly in the neighborhood of a particular point. If the formulation is to be equivalent to a spherical harmonic expansion up to degree n, then $(n+1)^2$ such points are chosen. The rationale behind this method lies in the simplification in the computational procedure over the conventional spherical harmonic representation of the gravity field. The coefficients of these functions are those designated by X in the altimetry observation equation exhibited earlier, and their improvement ΔX is obtained by using just this equation. Paraphrasing from Lundquist et. al. [1969], the sampling function coefficients over ground points will maintain their initial values, obtained from the best information available otherwise. However, there appears to be no reason why a further set of observation equations for Δg in terms of sampling function coefficient parameters could not be added, so that the method would be conceptually as complete as the other two. In addition, the approaches of both Young and Lundquist et. al. should be amenable to the addition of tracking data in a simultaneous solution.

It is plausible to assume that all these methods are equally reliable in having the theoretical capability of yielding valid results. The superiority of one over the other will probably be in computing efficiency.

The amount of altimetry data points recoverable from GEOS-C is potentially very large. Assuming one measurement per second for a 20 minute altimeter run each revolution over a two-year lifetime, the number of data points is of the order of 10^7. A more conservative estimate, mentioned by Hudson [1971], is $5.5(10^5)$ data points based on 1500 hours of data. Since there are approximately 36,000 1° squares (subdivisions whose area is the same as a 1° x 1° square at the equator) over water, there will be on the average 15 data points per 1° square. In general, the oceans will be covered by altimetry better than the land by gravity, provided that the coverage is uniform.

Statistical problems will emerge. Since the satellite travels about 7km per second, the points falling within a degree square (100 x 100km) are likely to occur over one or two individual revolutions, and thus present correlation problems. Should aggregation be practiced as in the case of Dopper data of which there is an excess? In fact this is the method employed on land where the Δg are aggregates obtained from individual gravity measurements.

The way to first proceed probably will be to obtain a uniform solution for the global geoid employing large size subdivisions, say 10° x 10°. The altimetry could be aggregated more consistently over a block of this size. Such a solution should be sufficiently accurate to obtain an orbit for the

purpose of securing the geocentric position of the satellite which can serve as a geoidal reference against each altimeter measurement.

References

Heiskanen, W. and H. Moritz, Physical Geodesy, W. H. Freeman & Co., San Francisco, 1967.

Hudson, E. H., A Geodetic and Oceanographic Satellite Altimeter System, AIAA Space Systems Meeting, Denver, Colorado, 1971.

Koch, K. R., Gravity Anomalies for Ocean Areas from Satellite Altimetry, Proceedings of the Second Marine Geodesy Symposium, Marine Technology Society, Washington, D. C., 1970.

Lundquist, C. A., G. E. O. Ciacaglia, K. Hebb, and S. G. Mair, Possible Geopotential Improvement from Satellite Altimetry, Smithsonian Astrophysical Observatory Special Report 294, Cambridge, Mass., 1969.

Molodensky, M. S., V. F. Eremeev, and M. I. Yurkina, Methods for Study of the External Gravitational Field and Figure of the Earth (translated from the Russian, 1960), Israel Program for Scientific Translations, Jerusalem, 1962.

Young, Ronald Ging-wei Eng, Combining Satellite Altimetry and Surface Gravimetry in Geodetic Determinations, Massachusetts Institute of Technology TE-37, Cambridge, Mass., 1970.

GROUND TRUTH DATA REQUIREMENTS FOR ALTIMETER PERFORMANCE VERIFICATION

3

Edward J. Walsh

NASA/Wallops Station

The amount and type of ground truth required for an altimeter experiment is a function of the uncertainty in the satellite orbit, the altimeter error budget and the type of operation being performed. Ground truth requirements will be discussed with reference to three areas of operation: the global mode, the high intensity mode and calibration.

Figure 1 shows the effects of two different orbital uncertainties on the surface mapping capability of an altimeter whose precision is assumed to be half a meter. One curve is for a tracking network which determines the satellite height to five meters. The other curve shows the effects of a modest tracking network which results in a 100 meter height uncertainty. An interesting thing about the figure is that the high frequency asymptote of both curves is the altimeter precision. The ability to map rapidly varying surface features is independent of the orbital uncertainty and is limited only by the precision of the altimeter.

An altimeter must have a well determined orbit in order to map the general (global) shape of the geoid. But over any short arc the

satellite altitude will vary by only a small amount and in a predictable fashion so that the variation of the sea surface can be determined to within the altimeter precision. Even large error in determining the absolute altitude of the satellite is of little consequence when profiling rapid variations in the geoid such as the Puerto Rican Trench.

A typical altimeter error budget for two modes of operation is shown in Table 1. The postulated altimeter has a global mode of operation using a 300 ns pulse width and a high intensity mode using a 25 ns pulse. The only significant noise contributions to the error budget in the global mode are the signal fluctuation and thermal noise residual errors in the instrumentation and the satellite stabilization error. With such a long pulse length the effects of sea state are negligible so that no sea state information is required when operating the altimeter in the global mode. This is the reason for selecting the long pulse length since any intensive ground truth requirement on a global scale would not be possible.

To calibrate the global mode an independent determination of the satellite height above the actual sea surface at some point on the orbit must be made and compared with the altimeter output. Figure 2 shows the quantities of interest at a ground truth site for the calibration of the global mode. The satellite position must be trianglulated and the instantaneous mean sea level (IMSL) of the subsatellite point must be known accurately. The satellite height can be determined to within two meters relative to the tracking stations

C

whose heights are referenced to mean sea level. The geoid and any parameters causing MSL to deviate from the geoid and IMSL from MSL will have to be well known for the calibration site. These include the tides, currents and the effects of any storms.

Ideally the calibration site should be where the satellite ground track crosses itself in one orbit. With this redundant point occurring where the satellite position is well defined, any instrumental drift would become apparent because the ground truth site conditions would change by only a small, predictable amount in the period of one orbit.

The purpose of the global mode is to map the general shape of the geoid to five meter accuracy. Due to the long pulse width, the foot print size and precision, this mode would not be suitable for detailed mapping of the rapidly varying portions of the geoid. The global mode would only fix their location on the geoid and indicate their general shape. The high intensity mode would be used to profile the rapid variations.

In the high intensity mode the propagation dependent errors and the ocean scattering effects become significant. Extensive ground truth data must be gathered in support of this mode to evaluate design parameters for refining future altimeters. Table 2 outlines the Wallops Island Ground Truth Program. There are sufficient ground radars in the area (Wallops Island, Bermuda, Florida) to provide excellent orbital parameters.

The ground truth program is built around the Wallops C-54 aircraft, the NASA Wallops Island ship Range Recoverer, and the Chesapeake Light Tower approximately 15 miles east of Virginia Beach. The goal is to obtain sufficient information to remove the sea-electromagnetic bias error, to test models of the effects of the various sea state and atmospheric parameters on the satellite altimeter and elaborate the fundamental limitations of the altimeter. The instrumentation consists of wave staffs, a laser profilometer, two X-band nanosecond radars, a K-band radiometer and photographic equipment for Stilwell photography. The C-54 is instrumented for recording pitch, roll and vertical motion. The instrumentation will provide profiles of the sea surface as well as rms wave height, ocean surface height and slope directional spectra, surface wind speed and direction, air and water temperature and meteorological conditions.

In addition, Wallops has the capability of measuring atmospherics and rain drop sizes so that these contributions in the error budget could be better defined.

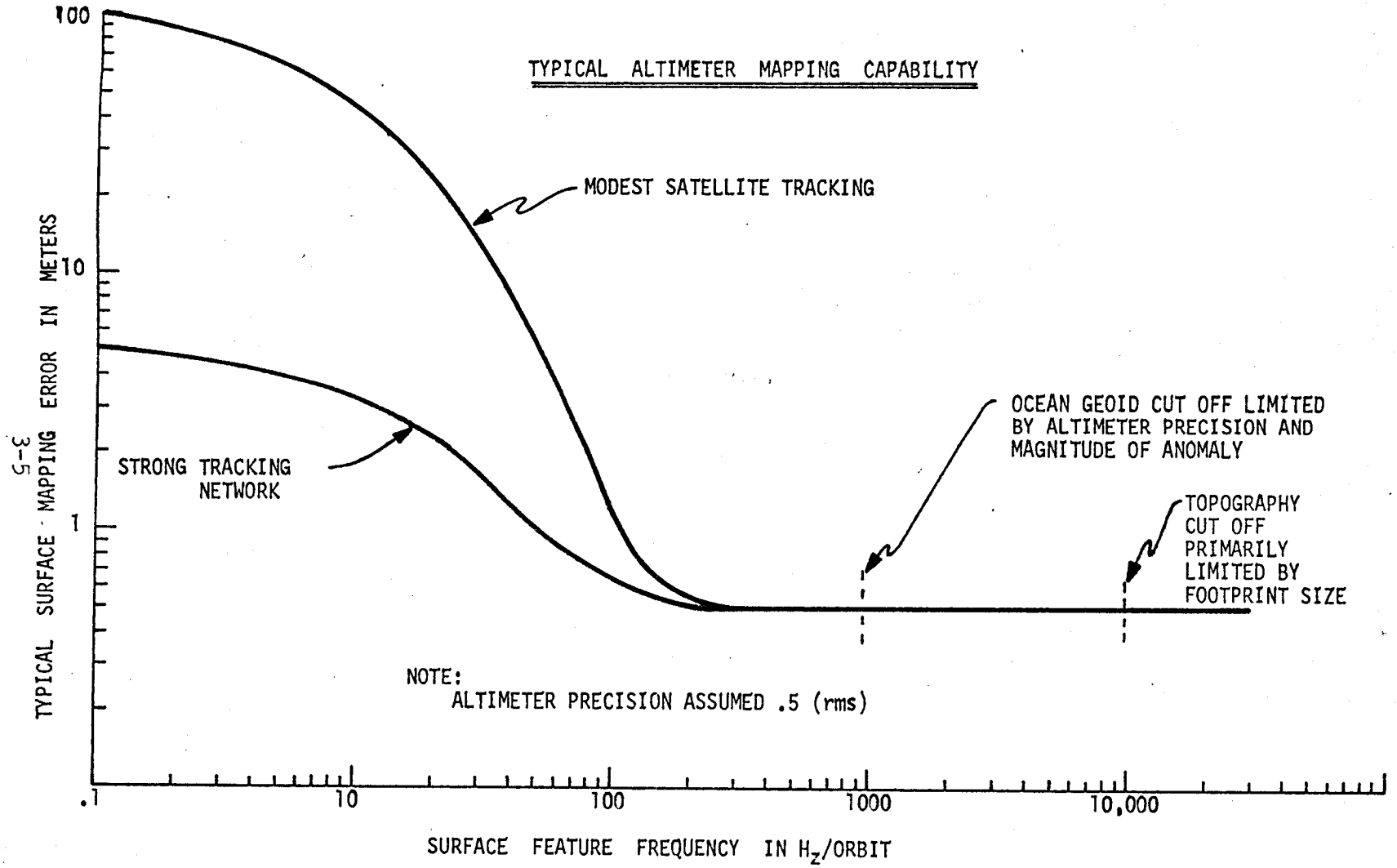
TYPICAL ALTIMETER MAPPING CAPABILITY
100
10
1
TYPICAL SURFACE - MAPPING ERROR IN METERS
MODEST SATELLITE TRACKING
STRONG TRACKING NETWORK
OCEAN GEOID CUT OFF LIMITED BY ALTIMETER PRECISION AND MAGNITUDE OF ANOMALY
TOPOGRAPHY CUT OFF PRIMARILY LIMITED BY FOOTPRINT SIZE
NOTE:
ALTIMETER PRECISION ASSUMED .5 (rms)
.1
10
100
1000
10,000
SURFACE FEATURE FREQUENCY IN H_z/ORBIT

Figure 1

TABLE 1

Typical Altimeter Error Budget

	25 ns	300ns
Instrumentation Errors		
Signal Fluctuation and thermal noise residual errors	.30 meters	2 meters
System time delay uncertainty	.06	.15
Range tracker and/or signal processor errors due to nonlinearity	.12	.12
Tracker granularity and clock uncertainty	.10	.10
Propagation Dependent Errors		
Corrected data	.10	.10
Ocean Scattering Effects		
Residual stabilization errors (assuming $\pm 1^{\circ}$ uncertainty)	$<.1$	1 m
Leading edge linearity assumption ($\sim$60 cm uncorrected)	.06	.06
Electromagnetic msl bias	.15	.05
	0.4	2.25
Total System Errors (rms)		
for: 5 meter orbit uncertainty	5.02	5.5 meters
1 meter orbit uncertainty	1.08	2.5
.2 meter orbit uncertainty	.47	2.25

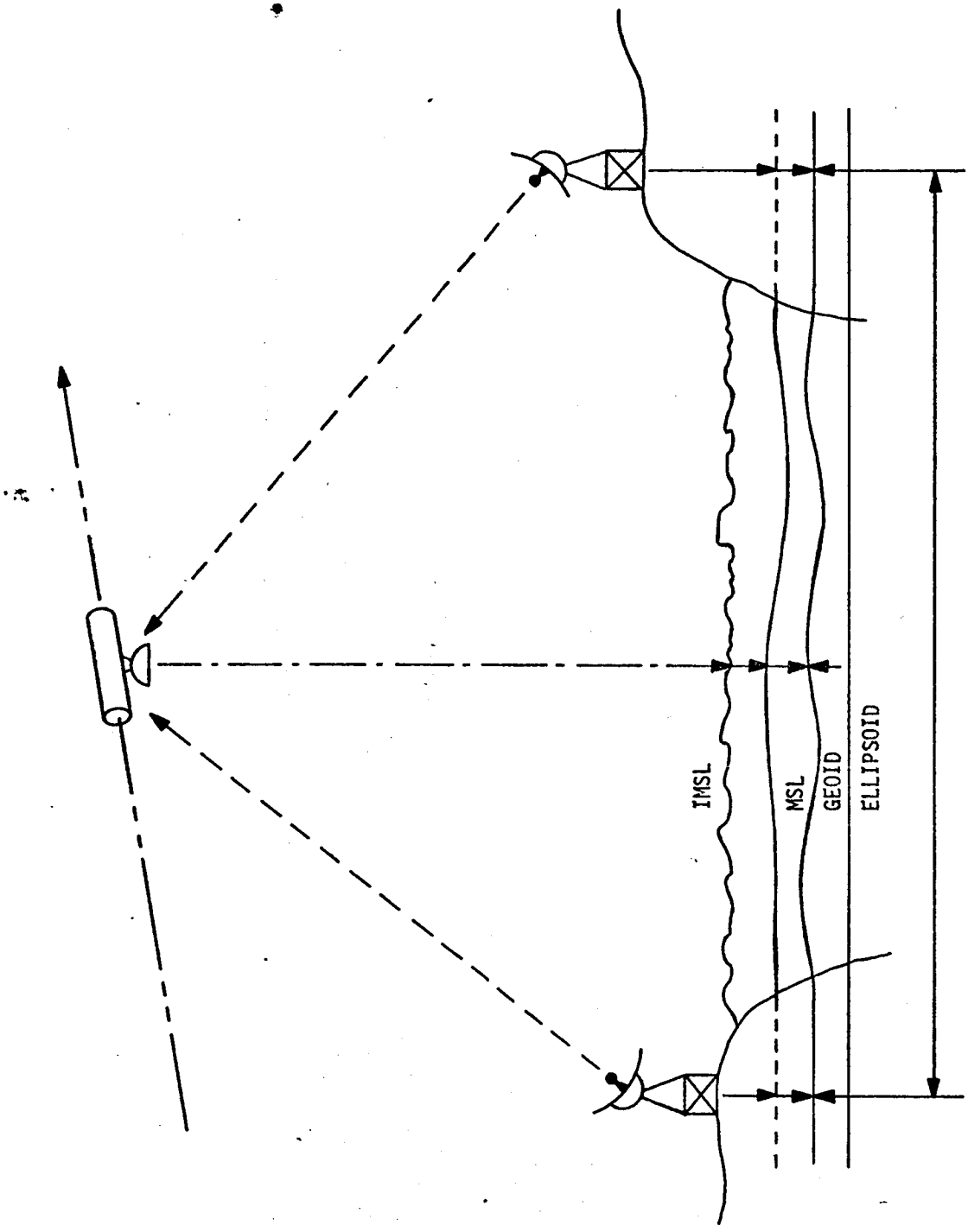

Figure 2

Table 2

Ground Truth System Development Program

1. Instrumented Aircraft and Test Bed

Instrumentation	In-house	External Activity
(a) Stilwell Camera	Lacheman	Katz
(b) Optical Processor	Lacheman	Katz
(c) Nano-second Radar	Selser	Yaplee
(d) Laser Profilometer	Townsend	Peliguin
(e) K-band Radiometer	Novack	Holinger

2. Instrumented Ocean-Tower and Test Bed

Instrumentation	In-house	External Activity
(a) Wavestaff (3 ea.)	Hines	Hammond
(b) Nano-second Radar	Selser	Yaplee
(c) Meteorological Equipment	Spurling	-
(d) Laser Profilometer		

3. Supporting Data Collection System

   (a) ERTS Photographic Data

   (b) Commercial Shipping Reports

   (c) Nembus Photographic Data

Table 2.Continued

(d) Local Meteorological Data

(e) Ground Sites Selection and Evaluation

(f) USNS Range Recoverer for in situ Measurement Data Collection

Ground Truth and Test Bed Activities

1. Ground Truth

(a) Chesapeake Ecological Test Site Support

(b) SKYLAB Support

(c) AAFE Support

2. Test Bed Activities

(a) SKYLAB Support

(b) AAFE Support

(c) Local SR&T Experiments

(d) Prototype Altimeter Testing

(e) Support to Others

USE OF ALTIMETRY DATA IN A SAMPLING-FUNCTION APPROACH TO THE GEOID

C. A. Lundquist*
Smithsonian Astrophysical Observatory, Cambridge, Massachusetts
and
G. E. O. Giacaglia†
University of Texas, Austin, Texas

The planned operation of satellite-to-ocean altimeters will produce measurements that require mastery of particular data-analysis problems for the full utilization of the information in these measurements. Under the premises that the first altimeters will have an accuracy of ~ 1 m and that at this scale the ocean profile can be identified with an equipotential surface, the following problems are among those that must be examined:

1. Convenient mathematical representation of short-wavelength (eventually ~ 1°) features of the geoid or geopotential.

2. Utilization of detailed data from only part of the globe (i.e., the oceans).

3. Application of appropriate formalism to relate the sea-level equipotential below the atmospheric mass to the external potential above the atmosphere.

4. Mathematical applicability of an adopted geopotential representation on the surface of the physical geoid.

These topics are not independent, of course.

---

*This research was supported in part by grant NGR 09-015-002 from the National Aeronautics and Space Administration.

†On leave from the University of São Paulo, São Paulo, Brazil. Partially supported by ONR Contract N00014-67-A-0126-0013.

The concept of using a sampling-function representation of the geoid and geopotential emerged from efforts to prepare for some of these problems, and the evolution of this concept can be followed in other papers (Lundquist and Giacaglia, 1969; 1971a, b; Giacaglia and Lundquist, 1971). The objective here is rather to review the current status of the sampling-function representation as a partial answer to the analysis problems posed by altimetry data.

With respect to the first problem – a convenient representation of short-wavelength features – the coefficients in an expansion in sampling functions are essentially tabular values of the geoid radius or potential at a grid of sampling points on a sphere or similar reference surface. The grid can be scaled as finely as desired. The sampling-function representation through some degree is equivalent to a spherical-harmonic expansion through the same degree, and the transformation from sampling functions to spherical harmonics and its inverse are expressed in analytical form (Lundquist and Giacaglia, 1971b). Therefore, no need arises to invert large matrices numerically, and this aspect of the altimetry problem is resolved.

In an oversimplified scenario for the treatment of altimeter data, each altitude measurement from a determinable position in orbit implies a geocentric radius to the ocean surface. All these measurements of radii in the neighborhood of a sampling point can be accumulated and averaged appropriately to give the radius at the point. This radius value is immediately the coefficient of the corresponding sampling function in the geoid representation. If the equivalent spherical-harmonic expansion is desired, this is obtainable by applying the analytically defined transformation.

Some recent progress toward implementing these calculations has been the preparation at the University of Texas of computer algorithms to evaluate the necessary analytical formulas for fairly high degree. Even though simpler than some other approaches, the calculations involved are extensive, owing to the great detail of the desired representation. In the interest of computer efficiency,

the formulation of the analytical expressions and the computer algorithms have progressed through several steps of refinement.

Degree 36 has been selected for exploratory investigations, although a still higher degree might be more illuminating. In this case, features with wavelengths as short as 5° can be represented. For an expansion through degree 36, there are $(36 + 1)^2 = 1369$ terms in either a sampling-function or a spherical-harmonic expansion. The transformation matrices relating the equivalent forms have nearly two million elements.

As a trial application using the sampling points for degree 36, geocentric radii were calculated to an equipotential surface derived by use of the Smithsonian harmonic coefficients presented at the 1971 IUGG meeting (Gaposchkin, Kozai, Veis, and Weiffenbach, 1971). This calculation at the University of Texas followed the procedure discussed by Lundquist and Giacaglia (1971a). Also, geocentric radii were calculated (Girnius, 1971) for 45 sampling points in the North American Datum, by use of the Army Map Service 1967 Map of Geoid Contours in North America from Astrogeodetic Deflections (Fischer, 1966). Figure 1 shows the 45 sampling points. The geoid heights were transformed to geocentric radii in 1969 Smithsonian Standard Earth (II) coordinates by using the Lambeck (1971) parameters, assuming the Smithsonian and North American Datum axes are parallel.

The radius values from the astrogeodetic geoid could contain somewhat shorter wavelength information than the values from the Standard Earth. To generate a sampling-function representation corresponding to the astrogeodetic geoid in North America, it is only necessary to replace the Smithsonian values with those from the geoid map for the sampling points in North America. This has been done. If one wants the equivalent spherical-harmonic representation, the analytically defined linear transformation can be applied.

Because a very similar operation is envisioned when satellite-to-ocean altitudes are available, a study of the properties of this modified geoid representation

should indicate the utility of this method. Such a study is in progress. Partial answers to both problems 1 and 2 are expected as a result of the trial application to the North American geoid, since this test involves features of both problems.

For problem 1, a crucial aspect is the ability of the sampling-function representation to reproduce short-wavelength features in North America. For problem 2, the crucial question is whether extraneous short-wave detail is introduced with significant amplitude for the geoid outside North America. The desired result should be a geoid in North America resembling the astrogeodetic contours in its 5° and longer wavelength features, with the properties of the satellite-determined field elsewhere. Also, the corresponding geopotential should have essentially the Smithsonian coefficients for the lower degree and order spherical harmonics. An iterative scheme may be necessary to achieve these properties.

The discussion and procedures above have been based on the implicit assumption that the geopotential derived from satellite observations is also applicable at the surface of the earth. While this is an acceptable simplification for exploratory studies, it certainly must be reconsidered for accurate treatment of actual altitude measurements. Problems 3 and 4 recognize the need to proceed with caution.

The mass of the atmosphere is given by Verniani (1966) as 8.594×10^{-7} of the mass of the earth. Clearly this mass contributes differently to the gravitational field at satellite altitudes than it does at sea level. The first step to accommodate this situation would seem to be a decomposition of the external potential into a major portion due to the mass of the solid earth and oceans and a minor portion due to the mass of the atmosphere.

The leading term in the usual spherical-harmonic expansion is proportional to total mass, so that its coefficient can be decomposed into two fractions – respectively, 0.999,999,140,6 and 0.000,000,859,4 of the total. Such an adjustment was made by Veis (1967) in a determination of the equatorial radius and gravity of the earth. This effect was noted also by Rapp (1970) in a discussion of

methods for the computation of geoid undulations from potential coefficients and by others in other contexts (Ecker, 1968; Ecker and Mittermayer, 1969).

Since the atmosphere is constrained to a nearly ellipsoidal lower boundary by the shape of the solid earth and oceans, its mass must make a contribution to the total J_2 of the earth. A first crude estimate of the size of this contribution is obtained by considering the total mass of the atmosphere concentrated in a uniform ellipsoidal shell with the same semimajor axes as the earth. This crude estimate gives J_2 (atmosphere) = 0.002×10^{-6} as compared with the Kozai value $J_2 = (1082.637 \pm 0.001) \times 10^{-6}$ for the total earth system. Thus, the contribution of the solid earth and of the oceans would be J_2 (solid earth and oceans) = 1082.635×10^{-6}. This very small change would not seem to be important until geoid accuracies in the centimeters are obtained.

On the other hand, Kozai reports an annual variation of amplitude $\delta J_2 = 0.0013 \times 10^{-6}$, presumably due to mass displacements somewhere in the earth system (Kozai, 1970). A more accurate calculation of the atmospheric contribution to J_2 would be instructive, to improve the crude estimate above. Kelly (1971) has assembled the atmospheric models and formulas for such a calculation.

In principle, there is a further complication associated with the atmosphere – namely, the gravitational field at sea level due to the nearly elliptical atmospheric shell above. This contribution should be added back into the potential after the external atmospheric contribution has been subtracted from satellite information to isolate the field due to the solid earth and oceans. However, this internal field of the atmosphere is probably even less important than correction of the J_2 value.

The fourth problem, the mathematical applicability of an adopted geopotential representation at sea level, is a perplexing one in potential theory (see, for example, Hotine, 1969; Madden, 1971). It has been argued that the convergence uncertainties expected with a spherical-harmonic expansion could be largely alleviated by the use of ellipsoidal harmonics (see, for example, Madden, 1968; Walter, 1971), presumably because the ellipsoidal functions can better conform to the shape of the earth.

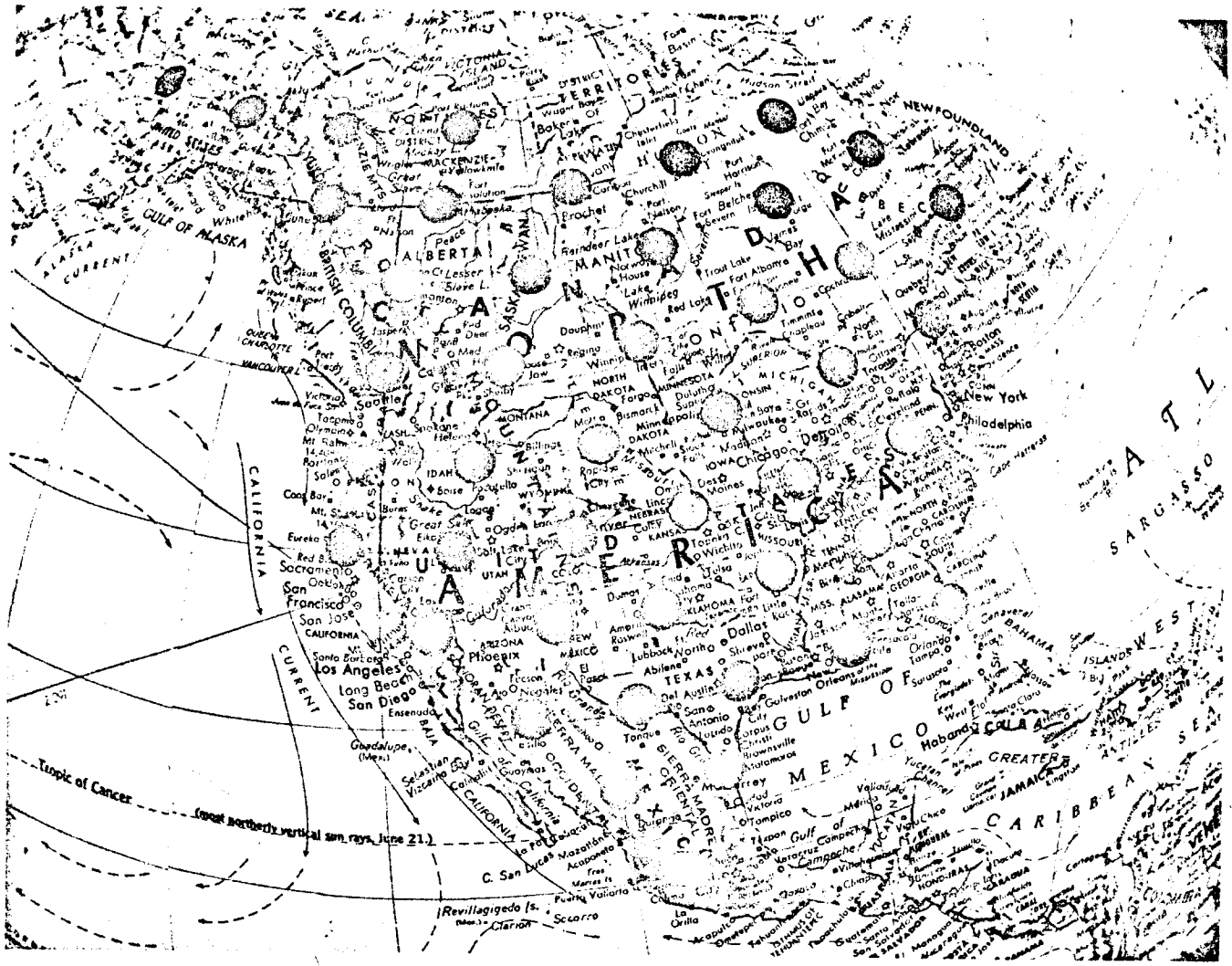

Figure 1. The 45 sampling points in North America used in a trial application of sampling-point representation of the geoid.

The sampling functions can be defined on an ellipse about as easily as on a reference sphere, and if the elliptical formulation is used, it would seem that they should accrue the same benefits as ellipsoidal harmonics. Still further, the sampling functions can also be defined on a surface conforming still more closely to the geoid. It is an open question whether this would still further alleviate the convergence uncertainty.

In summary, although many questions remain to be answered, a sampling-function representation of the geoid still promises to be a useful tool in utilizing satellite-to-ocean altitudes.

REFERENCES

ECKER, E.

1968. The effect of the atmosphere on the theory of the level ellipsoid. Boll. Geofisica Teorica ed Applicata, vol. X, pp. 107-119.

ECKER, E., and MITTERMAYER, E.

1969. Gravity corrections for the influence of the atmosphere. Boll. Geofisica Teorica ed Applicata, vol. XI, pp. 70-80.

FISCHER, I.

1966. A revision of the geoid map of North America. Journ. Geophys. Res., vol. 71, pp. 4905-4908.

GAPOSCHKIN, E. M., KOZAI, Y., VEIS, G., and WEIFFENBACH, G. W.

1971. Geodetic studies at the Smithsonian Astrophysical Observatory. Presented at XVth IUGG General Assembly, Moscow, August.

GIACAGLIA, G. E. O., and LUNDQUIST, C. A.

1971. Sampling functions as an alternative to spherical harmonics. Presented at IAU Symposium No. 48, Rotation of the Earth, Morioka, Japan, May.

GIRNIUS, A.

1971. Geocentric radii calculations were made by Mr. Girnius and provided to the authors in a private communication.

HOTINE, M.

1969. Mathematical Geodesy. ESSA Monograph 2, U.S. Department of Commerce, Washington, D.C., 397 pp.

KELLY, R. E.

1971. The contribution of the atmosphere to the earth's static geopotential. Marshall Space Flight Center, NASA (Communicated privately by Dr. Kelly to the authors, August 13.).

KOZAI, Y.

1970. Temporal variations of the geopotential derived from satellite observations. Presented at COSPAR, Leningrad, May (in press).

LAMBECK, K.

1971. The relation of some geodetic datums to a global geocentric reference system. Bull. Géodésique, no. 99, pp. 37-53.

LUNDQUIST, C. A., and GIACAGLIA, G. E. O.

1969. Possible geopotential improvement from satellite altimetry. In Smithsonian Astrophys. Obs. Spec. Rep. No. 294, pp. 1-44.

1971a. A geopotential representation with sampling functions. Presented at Symposium on the Use of Artificial Satellites for Geodesy, Washington, D.C., April.

1971b. Sampling functions for geophysics. Smithsonian Astrophys. Obs. Spec. Rep. (in preparation).

MADDEN, S. J., Jr.

1968. The geoid in spheroidal coordinates (abstract). In Guidance Theory and Trajectory Analysis Seminar Abstracts, NASA Electronics Research Center, Cambridge, Mass., p. 17.

1971. The transformation of external harmonic series under a translation of origins. M.I.T. Measurement Systems Laboratory RE-68, June.

RAPP, R. H.

1970. Methods for the computation of geoid undulations from potential coefficients. Sci. Rep. No. 5, AFCRL-70-0281, April.

VEIS, G.

1967. The determination of the radius of the earth and other geodetic parameters as derived from optical satellite data. In Geodetic satellite results during 1967, ed. by C. A. Lundquist, Smithsonian Astrophys. Obs. Spec. Rep. 264, pp. 73-99.

VERNIANI, F.

1966. The total mass of the earth's atmosphere. Journ. Geophys. Res., vol. 71, pp. 385-391.

WALTER, H. G.

1971. Ellipsoidal gravity coefficients of the geopotential. Presented at AAS/AIAA, Astrodynamics Specialists Conference, Ft. Lauderdale, Fla., August.

REQUIREMENTS FOR A MARINE GEOID COMPATIBLE WITH GEOID DEDUCIBLE FROM SATELLITE ALTIMETRY

5

D. M. J. Fubara and A. G. Mourad
BATTELLE
Columbus Laboratories
505 King Avenue
Columbus, Ohio 43201

Because bewildering confusion about the geoid exists, the first part of the paper is a systematic review of the concept of the geoid and the various geodetic techniques and associated data employed in the physical determination of the geoid. The deficiencies in theory, data, and practical computational procedures that have made the physical determination of the geoid with true scale, shape, and absolute orientation an elusive target are outlined. The potential of satellite altimetry, in combination with adequate ground support and "sea-truth", to resolve the accurate determination of a global marine geoid (the geoid in the oceans) and other peripheral benefits associated with ocean physics is briefly restated. Attention is drawn to the controversy as to the validity of using a best fitting ellipsoid ($f = 1/298.25$) instead of an equilibrium ellipsoid ($f = 1/299.67$) in all gravimetric work for computing gravity anomalies and the geoid, and for geophysical interpretations from gravity surveys.

Marine gravity measurements alone cannot adequately furnish the required geodetic sea-truth. The paper indicates the "how and "why" a combination of marine astrogravimetry and marine geodetic acoustic techniques is the best approach to meet the requirements for "sea-truth" (segments of the absolute marine geoid in test areas) compatible with the geoid deducible from satellite altimetry. Table 4 at the end of the paper contains a summary of the findings.

1. INTRODUCTION

The geoid is that equipotential surface in the gravity field of the earth which most nearly coincides with the undisturbed mean sea level. In spite of this exactness of definition, the physical determination of the true geoid remains an elusive target to geodesists. Consequently, many concepts and classes of concepts concerning how it should be physically determined have arisen. In scale, shape, and orientation, each class of geoids has little in common with another class. Even within the class, the various geoids differ and depend on many factors such as (1) the parameters of the reference ellipsoid which, for convenience, geodesists always associate with each geoid, (2) the measuring technique, the measurements and their reductions in theory and in practice, (3) the quantity and quality of data, and (4) the datum origin of the geodetic system.

Because the geoid is an irregular surface which does not exactly conform to any known geometric figure, it is geometrically defined by its physical departures from a chosen regular figure which is usually a reference ellipsoid. In some methods, the departures are determined by linear and angular measurements while in others these departures are synthesized from gravity anomalies integrated all over the earth's surface or a combination of both. The latest generation of geoids is deduced from the analysis of the dynamics of satellite orbits or a combination of gravimetry and satellite orbit analysis.

To amplify the dissimilarity between the various geoids, the concepts and data for their determinations and the physical meaning and nature of what is determined will now be reviewed. The objective is to demonstrate why anything that currently goes by the name marine geoid should neither be expected to be compatible in scale,

shape, and orientation with the geoid determinable from satellite altimetry nor be used as a means of geodetic absolute verification or calibration of satellite altimetry. Besides, the immediate direct results of the altimeter data are average sea surface topography and not the required geoid.

Having determined that the best approximation and convenient geometric figure for the geoid is a rotational ellipsoid, geodesists have continued to expend a lot of energy to determine the size and shape of the reference ellipsoid most desirable for geodetic computations. Numerous determinations of reference ellipsoids exist [Mueller, et al, 1966] but will not be discussed to spare the reader further complications. However, one important complication usually ignored but which was emphasized again at the 1967 International Symposium on the Figure of the Earth and Refraction in Vienna is that the best fitting ellipsoids, flattening of about 1/298.25, in geodetic use significantly differ from the hydrostatic or equilibrium ellipsoid, flattening of about 1/299.67. O'Keefe [1967] strongly suggests that all gravimetric work for computing anomalies and the geoid, and for geophysical interpretations from gravity surveys should refer not to the best fitting ellipsoid but to the hydrostatic or equilibrium ellipsoid. Fischer [1967] and Gaposchkin and Lambeck [1970] have the first practical computations for examining this unresolved complication.

Discussions about the quasigeoid [Molodenskii, et al, 1962] as a substitute to bypass certain difficulties concerning the geoid is avoided here because in the oceans, the geoid and quasigeoid coincide [Heiskanen and Moritz, 1967].

Figure 1 is a vertical section depicting a typical relationship between the geoid and an ellipsoid. The general nonparallelity between the geoid and the ellipsoid implies that in the same location, the normals to the two surfaces intersect at an angle, ϵ, called the deflection of the vertical in that plane. The geoidal undulation, N, is the linear vertical separation between the geoid and the ellipsoid.

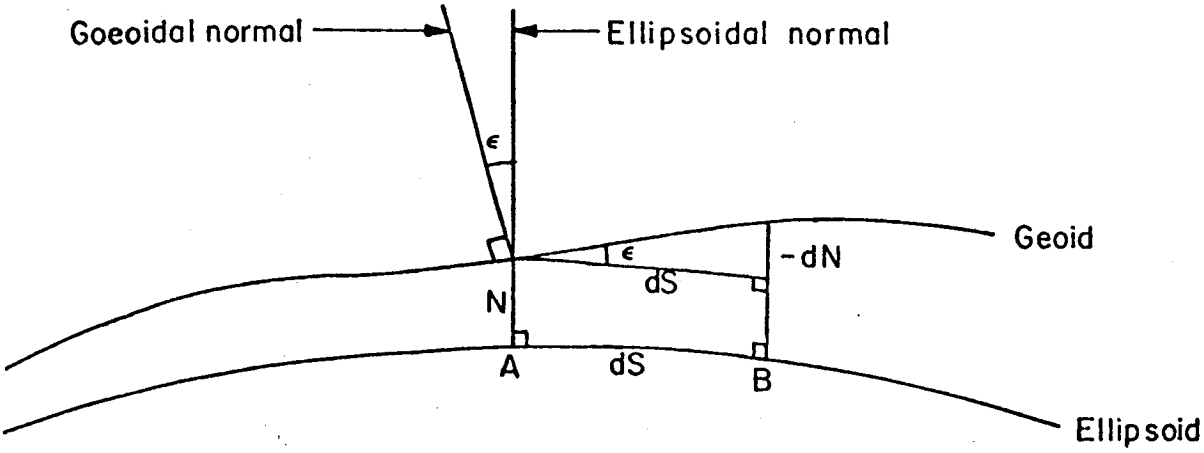

FIGURE 1. SCHEMATIC RELATION BETWEEN GEOID AND ELLIPSOID

With reference to Figure 1, the increment dN in N, over the distance dS is given, according to Helmert as stated in [Heiskanen and Moritz, 1967] by

$$dN = - \epsilon dS \tag{1}$$

which, on integrating, results in

$$N_B = N_A - \int_A^B \epsilon dS \quad , \tag{2}$$

where ϵ is the deflection of the vertical in any arbitrary azimuth, α, measured clockwise from the north, and given by

$$\epsilon = \xi \cos\alpha + \eta \sin\alpha \quad , \tag{3}$$

where ξ and η are the deflection components in the meridian and prime vertical respectively. If the various values of ϵ for different places in an area are determined, then by the use of Equation (2) the geoid of the area can be computed.

Some of the most important categories of the geoid and their characteristics are described below. For each class of geoids, the theory

implied and type of data employed, and the deficiencies in the theory, the quality and quantity of data currently in use, will be outlined. The expectation to map sea surface topography and eventually the marine geoid is widely known. The need for test areas with reliable "ground or sea-truth" including geoidal profiles with accurate scale, shape, and orientation is also widely recognized but the methodology for meeting this need such as by gravity data alone is indicated to be grossly inadequate.

The geodetic processing of reliable satellite altimetry data should determine the true geoid with absolute orientation, correct scale, and detailed features of the true shape. The paper advocates the use of a combination of astrogravimetry [Molodenskii, et al, 1962] and marine geodetic-acoustic techniques [Mourad, et al, 1970b] as the most expedient means for establishing marine geoidal profiles compatible with those deducible from satellite altimetry at sea. Marine geoid is used to denote the geoid in the oceans as distinct from continental geoid computed on land. For the most meaningful and reliable geodetic deductions from satellite altimetry, two calibrations must be distinguished. The first is a hardware calibration to ensure that an altimeter range indicated as xx meters is indeed xx meters to within the instrument's assigned accuracy. The second is a geodetic calibration or control required if a geoid with true scale, true shape, and absolute orientation is to be deduced from satellite altimetry. This paper is addressed to the requirements of the geodetic calibration. This is highly relevant because the altimeter readings are not made to the surface of the actual geoid but to some unknown "electromagnetic mean surface" as discussed in Section 3.

2. CLASSIFICATION OF GEOIDS

Several methods have been developed and/or used in determining the geoid. Examples of these methods which are described here include: (1) astrogeodetic, (2) inertial, (3) gravimetric, (4) satellites, (5) altimetry, and (6) astrogravimetric methods.

2.1 Astrogeodetic Geoids

2.11 The Classical Astrogeodetic Geoid

The coordinates of any point on the surface of the earth can be depicted by its geodetic latitude, φ, geodetic longitude, λ, and geodetic height, h, as determined by classical terrestrial geodesy, where h is the height of the point above the reference ellipsoid. The same point, referenced to the geoid, can be depicted by the astronomic latitude, Φ, astronomic longitude, Λ, and orthometric height, H, above the geoid. The interrelationship between these parameters is generally expressed by

$$\xi = \Phi - \varphi \tag{4}$$

$$\eta = (\Lambda - \lambda) \cos\varphi \tag{5}$$

$$N = h - H \quad . \tag{6}$$

The orthometric height is approximately the geometric height above mean sea level, measured along the geoidal normal [Heiskanen and Moritz, 1967].

The geoid determined by inserting the differences between the astronomic and geodetic coordinates of the same point through the use of Equations (4) and (5) into Equations (3) and (2), is termed astrogeodetic.

The astronomical latitude and longitude are determined directly by observing stars. Within the limits of observational accuracy, the accuracy of star coordinates in space, and the adequate application of all corrections involved in astronomical measurements and reductions, the astronomical latitude and longitude of a place are unique. In sharp contrast, the geodetic coordinates of any point could be made unique but currently most are not "unique" but depend on the geodetic datum. The size and orientation of each datum reference ellipsoid is different and the position of the reference ellipsoid with respect to any unique point such as the center of mass of the earth remained unknown until the advent of dynamic satellite triangulation which has not yet resolved the problem satisfactorily. This will be discussed later using computations from Veis [1965, 1968] and Lambeck [1971]. Theoretical studies by Rapp [1970c] and Fubara [1971] and the work of Mather [1970, 1971] offer resolutions to this problem.

Consequently, the ensuing components of the deflection are not unique

(1) To each datum, there is a different astrogeodetic geoid.

(2) In shape, size, and orientation, astrogeodetic geoids on different datums are incompatible.

(3) Because of several weaknesses in current astrogeodetic practice, falsely exaggerated geoidal undulations and hence false geoidal tilts are progressively perpetrated the further a place is from the datum origin.

As shown by Fischer [1959], at long distances from the datum origin, computed geoidal undulation of 200 to 300 meters exist. Even after the application of the theoretically necessary Molodenskii's correction [Molodenskii, et al, 1962], which amounted to -60 m at a place 80° south of the North American Datum (NAD 1927), the geoidal height was 260 m [Fischer, 1959].

These inherent qualities of the classical astrogeodetic geoid and its rapid deterioration in shape precludes its use as a means of absolute verification of any other type of geoid without translations and transformations which are described later. The parameters for these reconciliations are still not accurately known. Above all, computation of astrogeodetic geoids has usually been limited to the continents because of the difficulties in determining usable geodetic and astronomic coordinates at sea. In this respect, von Arx [1966] made a valuable pioneering effort but also added a caution which is usually not remembered that as he put it: "The accuracy attainable is barely comparable with that achieved by Eratosthenes 2 millennia ago when he estimated the circumference of the earth".

2.12 Astrosatellite Geoid

There are many methods of determining ϵ or ξ and η which, in turn, are used to compute a geoid, using Equation (2). When the geodetic coordinates φ, λ, and h used are obtained from satellite fixes instead of terrestrial triangulation, traverse, etc., the resultant geoid can be termed <u>astro-satellite</u>. Satellite derived coordinates are supposedly known in a

geocentric system to an accuracy between ± 5 to ± 20 meters. Based on absolute geocentric coordinates, an astrosatellite geoid or any other geoid computed by Equation (2) is in absolute position if and only if at the starting point of the integration the absolute geoidal undulation is known.

In principle, the shape and size of such an astrosatellite geoid and the geoid deducible from satellite altimetry should be identical. In practice on land, the precision of each of the geodetic coordinates from satellite fixes is at best about ± 5 meters. At sea, a geodetic position fix, as determined from improved Doppler satellite receivers, could be obtained to perhaps ± 10 to ± 20 m if one used a fixed station defined by a ship positioned over ocean-bottom transponders where many satellite passes are taken and reduced to the same point. Furthermore, long arcs of astrosatellite geoid suffer from the same cumulative deterioration away from the starting point as the classical astrogeodetic geoid.

Also, one meter accuracy in a geoid from the integration of Equation (2) requires that standard errors in the determined astronomic latitude and longitude should be less than 1 arc second and systematic errors be less than 0".2 [Bomford, 1962]. Presently, such accuracies cannot be achieved at sea. The absolute accuracy of Startracker for astrogeodetic applications has not yet been determined. The dependency of the Startracker on the ship's inertial navigation system (SINS) and methods of updating the SINS cause the Startracker outputs not to be truly astronomic. In the background of all this is the problem of kinematic geodesy [Moritz, 1967, 1971b] -- the separation of gravitational and inertial forces.

2.2 Inertial Geoid

Various authors such as Bradley, et al [1966], Schultz, et al [1967], Bradley [1970], Butera, et al [1970] have discussed the use of inertial navigators for determination of the deflection of the vertical at sea. Externally provided geodetic fixes from some other systems such as LORAC or Navigation Satellite are required. The deflections and resultant geoid from this technique are basically similar to the classical

astrogeodetic type. The only difference is that the direction of the gravity vector is determined by SINS instead of by astronomical observations.

First, it should be pointed out that the geodetic datum of these external reference control systems such as LORAC is not in absolute position and unless the necessary accurate transformation prameters are available and the transformations executed the deflections and hence the geoid so determined are relative. Second, the absolute accuracy of these external reference controls, relative to any selected datum, remains unknown. Other disadvantages of this technique for deducing (not measuring) the deflections of the vertical include dependency on inaccurately known systems and measurement dynamics, statistical modeling of error sources, poor choices of a priori statistics, initial condition information, ill-defined determination of when performance is optimal and utilization of an adaptive filter when optimality does not exist, all of which are involved in Kalman filtering and optimal smoothing used in the deductions. Therefore, an "inertial geoid", in addition to its poor accuracy, is not compatible with the geoid deducible from satellite altimetry.

2.3 The Gravimetric Geoid

For a detailed and expert treatment of the gravimetric geoid and its ramifications, the reader is referred to Chapters 2 and 3 of Heiskanen and Moritz [1967], in particular, and to Uotila [1960] for practical computations.

As before, the geoid or undisturbed mean sea level is depicted as a surface by determining its departure, N, from a regular reference ellipsoid. However, in this case, by implication of the mathematical structure and the field measurements involved, the reference ellipsoid and the geoid are in absolute position. In Figure 1, g_p is the gravity vector at point P on the geoid and γ_A is the normal gravity vector at A on the ellipsoid. A vector is characterized by magnitude and direction. The difference in direction between the two vectors is the deflection of

the vertical. In the astrogeodetic methods, the direction of g_p was furnished by the station's astronomical latitude and longitude. For all practical purposes this direction is a constant and a function of position. The direction of γ_A or the ellipsoidal normal defined by the geodetic latitude and longitude of A is arbitrary and completely dependent on the shape, position, and orientation of the reference ellipsoid. The difference in magnitude, Δg

$$\Delta g = g_p - \gamma_A \tag{7}$$

is termed the gravity anomaly. It is related to the geoidal undulation, N (Figure 1), according to the famous Stokes' formula or integral and in principle implies integrating Equation (8).

$$N = \frac{R}{4\pi G} \iint_{\sigma} \Delta g \; S(\psi) \; d\sigma, \tag{8}$$

where

R = the mean earth radius

G = the mean value of gravity over the earth

$S(\psi)$ = Stokes' function

ψ = the spherical distance between the fixed point (say P) and the variable surface element $d\sigma$

σ = surface of the sphere of radius R with center at the center of gravity.

$$S(\psi) = \frac{1}{\sin(\psi/2)} - 6 \sin\frac{\psi}{2} + 1 - 5 \cos\psi - 3 \cos\psi \ln\left(\sin\frac{\psi}{2} + \sin^2\frac{\psi}{2}\right) .$$

The utilization of Equation (8) implies among many other things that:

(1) Δg is known everywhere on the earth

(2) g_p is measured on the geoid or its equivalent is deducible.

Owing to economics and world politics, Δg is not known all over the earth. Predicted values by interpolation or extrapolation are used for areas in which measured values are not available. Figure 2, taken

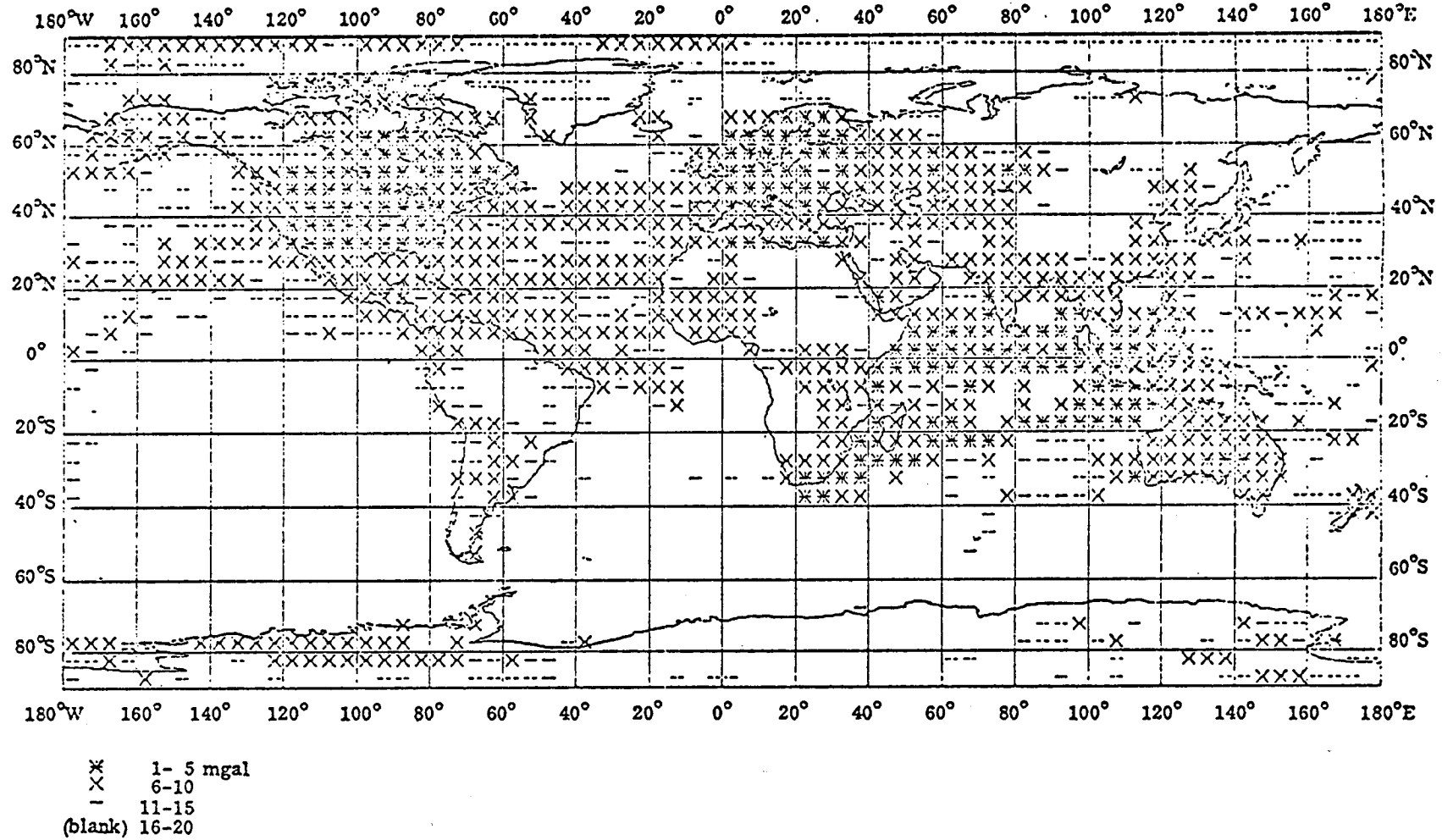

FIGURE 2. DISTRIBUTION AND QUALITY OF UNCLASSIFIED TERRESTRIAL GRAVITY DATA
5° x 5° MEAN ANOMALY COVERAGE (Rapp, 1970b)

from Rapp [1970b] shows the distribution of and quality of unclassifed terrestrial gravity data. In addition, g_p is hardly ever measured at the geoid. Actual measurements are made on the surface of the earth and reduced to their geoidal equivalents by empirical methods. Some of the parameters involved in the reduction, e.g., crustal density, are represented by intelligent guesses. To avoid the hypothetical assumption about the density, Molodenskii, et al [1962], formulated the concept of the quasi-geoid, and Hirvonen [1960], the telluroid. These substitute surfaces for the geoid will not be further considered for reasons given earlier.

There are many types of gravity reduction methods. Each method results in a slightly different type of gravity anomaly. Furthermore, with reference to Equation (8), the function or anomalous potential, T, given by Heiskanen and Moritz [1967], as

$$T = \frac{R}{4\pi} \iint_{\sigma} \Delta g \, S(\psi) \, d\sigma \qquad (9)$$

is assumed to be harmonic outside the geoid. Therefore, the effect of terrestrial masses outside the geoid, or undisturbed mean sea level, must be removed by a suitable gravity reduction method. After the reductions are made, the derived geoid is slightly changed and is termed a "regularized geoid" or "co-geoid". Accordingly, there are as many co-geoids as reduction methods and theories used. The "free-air co-geoid" most nearly coincides with the actual geoid.

In its original form (Equation 8), the Stokes' integral requires also that the reference ellipsoid should (1) have the same potential as the geoid and (2) enclose the same mass as the actual earth. These two requirements are never fulfilled.

The gravimetric geoid as determined by the original Stokes' integral (Equation 8) is not only in absolute position but also has "true" shape, unlike the various categories of astrogeodetic geoids. However, it lacks proper scale. This scale error has been assessed by various experts as ranging from 10 m to 50 m.

2.31 Scaling the Gravimetric Geoid From Stokes' Integral

A detailed exposition of this is given in Heiskanen and Moritz, [1967]. The theoretical step to providing this scale is to generalize Stokes' formula for geoidal undulation, N_a, to hold for any arbitrary reference ellipsoid whose center coincides with the center of the earth. The generalized formula is of the form

$$N_a = \frac{K\delta M}{RG} - \frac{\delta W}{G} + \frac{R}{4\pi G}\iint_{\sigma} \Delta g S(\psi)\, d\sigma \tag{10}$$

or

$$N_a = N_o + \frac{R}{4\pi G}\iint_{\sigma} \Delta g S(\psi)\, d\sigma \quad , \tag{11}$$

where

$$N_o = \frac{K\delta M}{RG} - \frac{\delta W}{G} \tag{11a}$$

δM = exact mass of the earth minus the mass of the ellipsoid in use

δW = potential of the geoid minus that of the ellipsoid

K = Newtonian gravitational constant.

The right side of Equation (11) differs from that of (8) by the term N_o termed the zero-order undulation [Rapp, 1967]. If both δM and δW were known accurately, application of Equation (11) would give the geoid in absolute position and with proper scale. In Heiskanen and Moritz [1967], Rapp [1967], and Fubara [1969], various approaches to the determination of N_o are given, but it is still a formidable problem and the gravimetric geoid is now not generally known accurately to within 10 to 20 meters in the oceans.

Very surprisingly, in most published gravimetric geoids, the issue of proper scale is completely ignored. This scaling can be shown to be equivalent to changing the equatorial radius of the reference

ellipsoid on which the gravity anomalies used in Equation (8) are based [Heiskanen and moritz, 1967]. From gravity data alone, the scale of the geoid can never be determined. Because of incomplete global coverage of observed gravity, predicted $5^\circ \times 5^\circ$ gravity anomalies whose standard errors are estimated at ± 20 mgals to ± 50 mgals and higher are often used. In the face of these, it is surprising that anyone can compute through the use of Stokes' integral an absolute geoid of ± 2 m accuracy.

An alternative to the use of Stokes' integral is to compute, from gravity anomalies all over the earth, the meridian and prime vertical components of the deflection of the vertical ξ and η, respectively, through the use of Vening Meinesz formulas. The abbreviated form of these formulas is

$$\xi = \frac{1}{4\pi G} \iint_{\sigma} \Delta g \frac{ds}{d\psi} \cos \alpha d\sigma \tag{12}$$

$$\eta = \frac{1}{4\pi G} \iint_{\sigma} \Delta g \frac{ds}{d\psi} \sin \alpha d\sigma \tag{13}$$

the theoretical and computational details of which can be found in Heiskanen and Moritz [1967], and Uotila [1960]. The ξ and η so obtained are absolute, i.e., referenced to the earth's center of mass. Thereafter, ϵ can be computed according to Equation (3) and the geoidal undulation computed from Equation (2).

Unlike Stokes' integral, Vening Meinesz formulas are valid for any arbitrary reference ellipsoid. However, they also require the use of gravity anomalies all over the earth, and in particular a dense gravity net around the computation points.

All the deficiencies in theory, data quality and quantity in gravimetric geodesy are extensively discussed in Chapter 7 of Heiskanen and Moritz [1967]. These deficiencies have led to many unanswered questions about the accuracies of gravimetrically computed geoidal undulations and deflections of the vertical. A few of the numerous efforts

addressed to these unresolved issues include Kaula [1957, 1959, 1966], Groten and Moritz [1964], Heiskanen and Moritz [1964], Moritz [1962, 1966, 1969, 1971, 1971a], Shaw, et al [1969], Henrikson, et al [1970], Rapp [1970a, 1970b]. The most important source of disagreement is on statistical modeling and estimation recognized by all to be indispensable in efficient gravity data analysis.

Consequently there is general disagreement on all or some of these:

(1) Estimation of interpolation and extrapolation errors of the gravity anomaly, Δg

(2) Estimation of the effects of these errors on the derived N, ξ, and η

(3) Determination of the best prediction method

(4) Estimation of the effect of neglected distant zones

in the works of Molodenskii, Kaula, Moritz, Henrikson, and Rapp. Figure 3, taken from Groten and Moritz [1964] depicts the standard errors M_N due to neglect of distant zones beyond a radius of ψ_o from the computation points of gravimetrically computed geoidal undulation using the improperly scaled Stokes' integral. The computation is for latitude 45° and global gravity anomaly distribution of one point per blocks of $n^\circ \times n^\circ$, n being the numbers shown on the graphs. A comparable computation in Molodenskii, et al [1962], gives values about 70 percent larger.

Perhaps the biggest source of systematic scale error in gravimetric geoidal profiles through the use of Vening Meinesz formulas is that an initial point (N_A in Equation (2)) at which the correct absolute value of the geoidal undulation is known must be specified. Such a value is hardly known accurately anywhere. Any geoid based on gravity data alone is therefore not suitable for the geodetic absolute calibration or verification of the geoid deducible from satellite altimetry.

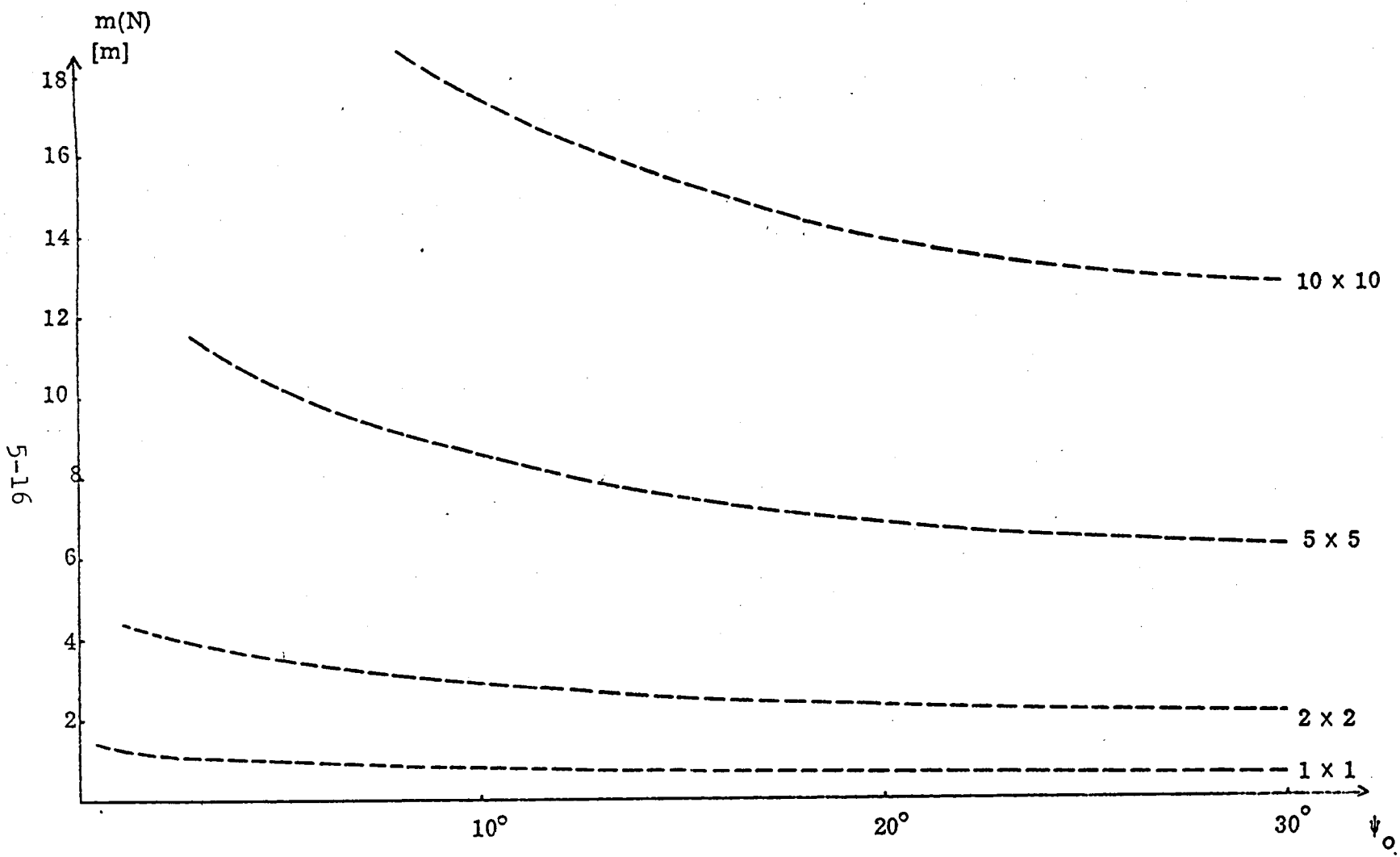

FIGURE 3. m(N) FROM POINT MEASUREMENTS AS A FUNCTION OF ψ_o

2.4 Satellite Geoids

The dynamics of artificial satellite motions around the earth can be used for (a) a geopotential or (b) a dynamic geometric computation of the geoid.

2.41 Geopotential Satellite Geoid

Satellite orbits are influenced by the irregularities of the earth's gravity field, which are usually expressed in terms of a development in spherical harmonics [Moritz, 1964]. The spherical harmonic coefficients can be determined from the analysis of known satellite orbits or from gravity measurements all over the earth's surface. The undulations of the geoid can be computed from those spherical harmonic potential coefficients [Bursa, 1968, 1969], [Bacon, 1970], [Moritz, 1964], [Rapp, 1970a].

At satellite heights, this technique cannot detect small-scale features of the geoid but only the general outline. All the satellite geoid so far computed by this technique differ in details by about 10 to 80 meters. The technique has a fundamental drawback. On the one hand, the gravity field, i.e., the potential coefficients, must be known for precise prediction of satellite orbits. On the other hand, and ironically, the computation of the coefficients depend on analysis of preknown satellite orbits.

The summary of the various modes of this technique in Rapp [1970a] also contains implicit drawbacks of the technique. The recommendation to use Method 1 of that reference by setting the zero order undulation N_o to zero unfortunately gives, as in the original Stokes' integral, a scaleless geoid because the undulations so obtained will refer to some ellipsoid of unknown size but which has the same mass as the earth and whose surface has the same potential as the geoid, whatever the unknown mass of the earth and the unknown potential of the geoid may be. In view of this, the equality of the results in Table 3 of

Rapp [1970a] raises an important question. This equality is questionable because it implies that his Equation (6) or our Equation (11a) must be truly zero which means that his assigned constants for the geocentric gravitational constant, angular rotational velocity of the earth, the flattening and equatorial radius of the reference ellipsoid, the potential of the geoid must be the true values.

Besides the theoretical problem about the convergence of the series in spherical harmonic expansion [Heiskanen and Moritz, 1967], [Moritz, 1971a], the poor quality of these coefficients are often overlooked in spite of values such as $C_{6,2} = 0.0283$ with standard error of $\pm$ 0.0396 [Rapp, 1969]. It is often argued that the quality of each individual coefficient does not critically affect the quality of the set of coefficients as a whole. How can coefficients be unreliable individually and yet be accurate collectively unless they have equal cancelling errors?

2.42 Geometric Satellite Geoid

The geoidal undulation, N, the orthometric height, H, and the ellipsoidal height, h, are related according to Equation (6). The absolute space rectangular coordinates, x, y, z of a station can be deduced from "dynamic satellite resection". From iterative procedures as in Heiskanen and Moritz [1967],

$$h = (x^2 + y^2)^{1/2} \operatorname{Sec}\varphi - \nu \quad , \tag{14}$$

where

φ = geodetic latitude of resected point

ν = prime vertical radius of curvature of the reference ellipsoid in use for the resected point

$h = H + N$ (as in Equation (6)).

On land, H is deduced from spirit leveling and gravity measurements. On the geoid or mean sea level H is zero. Thus the deduction of h at sea gives the geoidal undulation, N, to within the accuracy of the separation of the sea surface topography and the actual geoid.

The use of this technique at sea is under investigation [Mourad and Fubara, 1971a], [Martin, et al, 1971], [Stanley, et al, 1971]. From ships positioned over ocean bottom acoustic transponders, this technique can be effectively implemented. If geostationary and orbiting satellites of accurately known geocentric coordinates are available, ranging systems such as laser or C-band radar can be used in a geometric solution.

2.5 Combination Geoids

Two types of combination geoids exist. One is from a combination of satellite and terrestrial data such as gravity, triangulation, and astronomic observations. Some works along this line are Kaula [1961, 1966], Mather [1970, 1971]; Rapp [1970c], Heiskanen and Moritz [1967], Yeremeev, et al [1971], and Fubara [1971]. The fundamental problem is establishing practical and efficient mathematical and statistical models that give stable solutions in generalized least squares adjustments of these hybrid data. There is no doubt that this combination has to be effected in order to resolve the problems of scale, shape, and orientation on a global basis for the geoid and interrelation of various geodetic datums. The method is usable both on land and also at sea in the light of results in Mourad, et al [1970a, 1970b, 1971a,b] and Fubara, et al [1971]. However, it is more complex, less economical, more time consuming, more suited to broad features of global geoid mapping, and much less accurate or suitable for detailed local mapping of the geoid as required for altimetry sea-truth than astrogravimetry.

The second method is termed astrogravimetry [Molodenskii, et al, 1962], [Heiskanen and Moritz, 1967]. It is basically a combination of all the desirable features of the astrogeodetic and gravimetric computations of the geoid. At the same time, it is not affected by any

of the disadvantages of either method and particularly it does not require complete global coverage of gravity data as the influence of distant zones is not important. The technique is applicable at sea but the accuracy achievable at sea will depend on the reliability of the systems for astronomic and geodetic coordinates measurements.

The astrogravimetric geoid acquires correct shape and absolute orientation from the gravity data employed. It obtains correct scale from the astrogeodetic parameters. It is highly suitable and accurate for mapping local details of the geoid. It is speedy and economical because it requires only a dense local gravity-net in the test area alone.

3.0 SATELLITE ALTIMETRY "GEOID"

Figure 4 is a representation of a cross section containing a satellite altimeter orbit and some surfaces associated with satellite altimetry. Satellite altimetry is faced with several problems including the effective "hardware" calibration of the range TM and the physical definition of the surface, M, which is some mean surface defined by the altimeter ranges but whose exact position relative to either the geoid, G, or some mean sea surface, S, at any instant of time is currently unknown.

The interreslationships between the surfaces E, G, and S can be handled in test areas. There are analytical procedures in combination with "sea-truth" data by which a geoid can eventually be computed from satellite altimetry data. The solutions for these problems are not the subject of this paper. Subject to the accuracies of computed satellite positions and the altimeter calibration, the geoid so deduced should be in absolute position (i.e., centered at the earth's center of mass) and should have proper scale, shape, and orientation. The benefits of the success of this mission have been widely publicized in such as Greenwood, et al [1969], Koch [1970], Lundquist [1967], NASA [1970], Young [1970], Stanley, et al [1971], and Kaula [1970].

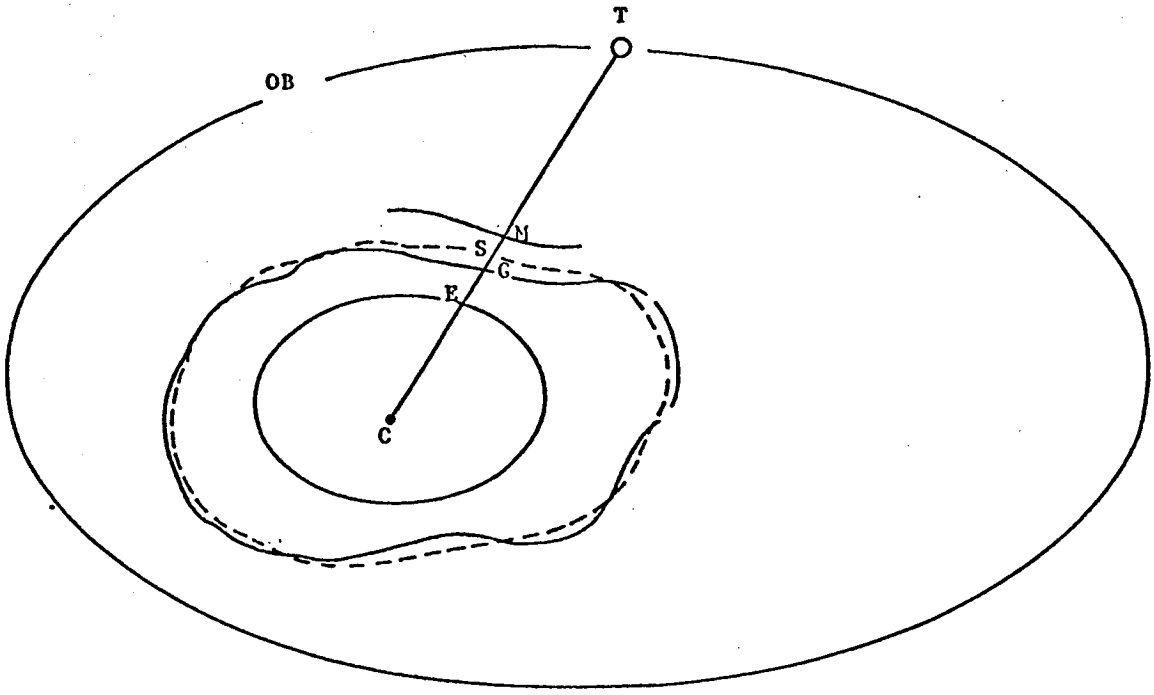

FIGURE 4. REPRESENTATION OF SURFACES ASSOCIATED WITH SATELLITE ALTIMETRY

C = Earth's Center of Gravity

E = Surface of a Geocentric Reference Ellipsoid

G = Geoid (the undisturbed Mean Sea Level)

S = Mean Instantaneous Sea Surface (MISS)

OB = Mean Satellite Orbit

T = Satellite Altimeter at an Instant

M = An Arbitrary Surface Defined by a "Hardware" Calibrated Altimeter

Based on all the foregone discussions, it is proposed to outline the conditions and the practical way for computing, in test sites,

geoidal profiles that are compatible in scale, shape, and orientation with the geoid deducible from satellite altimetry, so that geodetic processing of satellite altimetry data for computing the true geoid can be accurately effected.

4.0 COMPATIBILITY REQUIREMENTS

The determination in several test areas of "sea-truth" [Weiffenbach, 1970], [Raytheon, 1970], or segments of the absolute marine geoid will serve two main purposes from the geodetic point of view: (1) calibration and evaluation of the satellite altimeter; (2) as controls required for the geodetic analytical processing of satellite altimetry to determine the absolute marine geoid. To achieve these two goals, the sea-truth must have true scale, true shape, and true absolute orientation.

In geodesy, these conditions mean that (a) the center of the reference ellipsoid (equitorial radius, a, and flattening, f) employed in geoidal computations must coincide with the earth's center of mass and (b) the minor axis of the reference ellipsoid must coincide with the mean rotation axis of the earth so that the geoidal undulation, N, the meridian and prime vertical components of the deflection of the vertical, ξ and η, are absolute. These five parameters, a_o, f_o, N_o, ξ_o, η_o, as used in all local geodetic datums do not satisfy these conditions. Therefore, geoids based on different local datums are incompatible until they have been reduced to the same geocentric system based on a single "general terrestrial ellipsoid". Unfortunately, the parameters required in such reductions are currently too inaccurately known for use in geodetic calibrations or controls. The necessary correction parameters such as (1) datum shifts, (2) datum tilts of some major geodetic (local) datums have been computed, for example, by Veis [1965, 1968], Lambeck [1971]. The uncertainties in these geodetic parameters can be up to 70 meters or more as shown in Tables 1 and 2.

TABLE 1. DATUM SHIFTS FOR MAJOR GEODETIC DATUMS IN CARTESIAN COORDINATES (IN METERS)

	Veis [1965]*				Veis [1968]**			Lambeck [1971]***		
Datum	ΔX	ΔY	ΔZ	σ ±	ΔX	ΔY	ΔZ	ΔX	ΔY	ΔZ
NAD	- 2	+ 119	+ 229	10	- 26	+ 155	+ 155	- 31.8 ± 8.0	178.0 ± 12.2	177.6 ± 11.9
HAW	+ 12	- 145	- 19	24	+ 59	- 263	- 203	--	--	--
EUR	- 70	- 93	- 115	14	- 93	- 132	- 143	- 64.5 ± 19.0	-154.8 ± 11.0	- 46.2 ± 17.5
CEN	+ 45	- 74	+ 41	9	--	--	--	--	--	--
JAP	- 9	+ 626	+ 727	18	- 140	+ 510	+ 683	--	--	--
ARG	- 117	- 155	+ 30	27	- 167	+ 128	+ 25	-320.2 ± 12.1	203.8 ± 24.1m	391.7 ± 7.5
IND	+ 227	- 769	+ 216	33	+ 293	+ 697	+ 228	--	--	--

	a	1/f
* Veis [1965]	6,378,169 m. ± 8 m.	298.25
** Veis [1968]	6,378,142 m. ± 6 m.	298.255 ± 0.005
*** Lambeck [1971]	6,378,155 m.	298.25

TABLE 2. CORRECTIONS TO THE ADOPTED DEFLECTION OF THE VERTICAL AND GEOIDAL UNDULATION AT DATUM ORIGIN

	Veis [1965]				Veis [1968]			Lambeck [1971]		
Datum	$\delta\xi_o$	$\delta\eta_o$	δN_o	σ	$\delta\xi_o$	$\delta\eta_o$	δN_o	$\delta\xi_o$	$\delta\eta$	δN_o
NAD	- 0.60"	+ 0.62"	- 4.2m	± 10m	- 0.23"	+ 1.61"	- 28 meters	-0.02" ± 0.10"	- 1.60" ± 0.11"	- 42.2m ± 3.3
HAW	+ 6.28"	- 4.51"	+ 43.5	± 24	+11.85"	- 8.55"	0	--	--	--
EUR	+ 2.84"	+ 2.41"	+ 16.2	± 14	+ 2.61"	+ 3.45"	+ 3	- 3.16"	- 5.79"	0.5m
CEN	- 1.30"	+ 2.75"	- 12.3m	± 9m	--	--	--	--	--	--
JAP	-13.44"	+15.30"	+ 9.7m	± 8m	-11.85"	+ 9.63"	+ 31	--	--	--
ARG	- 0.05"	+ 1.00"	+ 15.0m	± 27m	+ 0.15"	+ 2.85"	+ 44	- 13.3	- 6.4	- 70m
IND	- 0.11"	+ 3.44"	- 33.8m	± 33m	- 1.35"	+ 4.40"	- 64			

where

NAD = North American Datum (1927)

HAW = Hawaiian Datum

EUR = European Datum

CEN = Australian Datum (1963)

JAP = Japanese Datum

ARG = Argentinian Datum

IND = Indian Datum

and

X-axis = Longitude 0°

Y-axis = Longitude 90° E

Z-axis = Earth mean rotation axis (mean pole of 1900-1905)

The corrections

$\delta\xi_o$ for meridian component of deflection of vertical

$\delta\eta_o$ for prime vertical component of deflection of the vertical

δN_o for height of geoid above the ellipsoid

are due to purely translatory corrections to the geocenter to satisfy condition (a) above. The corresponding datum tilts to fulfill the parallelity requirements $\Delta\xi$, $\Delta\eta$, ΔN are shown in Table 3.

TABLE 3. DATUM TILTS

	Veis [1968]			Lambeck [1971]	
Datum	$\Delta\xi$	$\Delta\eta$	ΔN	$\Delta\xi$	$\Delta\eta$
NAD	1".5	0".2	-2	-0".62 ± 0".50	-0".53 ± 0".5
EUR	1".6	-1".2	+10	2".2 ± 0".7	1".4 ± 0.6

It needs to be emphasized that the shifts are for the specified local datum origins. Quantitatively, any other arbitrary point is affected slightly differently. A thorough exposition on this subject can be found in Heiskanen and Moritz [1967]. However, the derivations in that reference are for the ideal case when the absolute orientation parameters

$$\Delta\xi = \Delta\eta = \Delta N = 0 \tag{15}$$

i.e., that the tilts at the datum origin are zero, implying that the minor axis and the major axis of the reference ellipsoid of each datum are strictly parallel to the mean rotation axis and the mean equator of the earth respectively. Under these conditions, a geoid can be transformed from one datum to another by a change of δa, δf, $\delta\xi_o$, $\delta\eta_o$, and δN_o in the initial parameters of the datum origin of the geoid. The corresponding corrections of $\delta\xi$, $\delta\eta$, and δN to the values of the deflection components and the geoidal undulation at any arbitrary point are given by

$$\begin{aligned}\delta\xi = {} & (\cos\varphi_o\cos\varphi + \sin\varphi_o\sin\varphi\cos\Delta\lambda)\delta\xi_o - \sin\varphi\sin\Delta\lambda\,\delta\eta_o \\ & - (\sin\varphi_o\cos\varphi - \cos\varphi_o\sin\varphi\cos\Delta\lambda)\left(\frac{\delta N_o}{a_o} + \frac{\delta a}{a_o} + \sin^2\varphi_o\,\delta f\right) \\ & - 2\cos\varphi(\sin\varphi - \sin\varphi_o)\,\delta f \quad .\end{aligned} \tag{16}$$

$$\begin{aligned}\delta\eta = {} & \sin\varphi_o\sin\Delta\lambda\,\delta\xi_o + \cos\Delta\lambda\,\delta\eta_o + \cos\varphi_o\sin\Delta\lambda\left(\frac{\delta N_o}{a_o} + \frac{\delta a}{a_o} + \right. \\ & \left. + \sin^2\varphi_o\,\delta f\right).\end{aligned} \tag{17}$$

$$\begin{aligned}\delta N = {} & a_o\left\{(\sin\varphi_o\cos\varphi\cos\Delta\lambda - \cos\varphi_o\sin\varphi)\,\delta\xi_o + \cos\varphi\sin\Delta\lambda\,\delta\eta_o\right\} \\ & + (\sin\varphi_o\sin\varphi + \cos\varphi_o\cos\varphi\cos\Delta\lambda)(\delta N_o + \delta a + a_o\sin^2\varphi_o\,\delta f) \\ & - \delta a + a_o(\sin^2\varphi - 2\sin\varphi_o\sin\varphi)\,\delta f\end{aligned} \tag{18}$$

F

Where

φ_o and λ_o = geodetic latitude and longitude of the datum origin, respectively

φ and λ = geodetic latitude and longitude, respectively of any arbitrary point in that geodetic system

$\Delta\lambda = \lambda_o - \lambda$

$\delta a = a_o - a$ } Parameters of the old reference

$\delta f = f_o - f$ } ellipsoid minus those of the new one.

The absolute orientation vectors can be determined by either analytical reconciliation of gravimetric deflections (or undulations) and astrogeodetic deflections (or undulations) of corresponding stations [Mather, 1970] or by satellite geodesy techniques in combination with terrestrial data. They should be corrected for implicitly as in Lambeck [1971] or as explicit rotation corrections before computing at the datum origin the shift dependent $\delta\xi_o$, $\delta\eta_o$, and δN_o involved in Equations 16, 17, and 18. However, the accuracies with which these tilts can be determined on a global scale is still questionable due to measurement errors, inaccuracies in orbital dynamics computations, and quantity and global distribution of available data.

The various problems and inaccuracies involved in trying to reconcile various geoids on different datums on a global basis are discussed by Fischer, et al [1968]. The title of that paper, "New Pieces in the Picture Puzzle of an Astrogeodetic Geoid Map of the World" truly tells it as it is. One of the conclusions of that paper, "If one expects a geodetic accuracy of a few meters, the variety of numbers is bewildering", is still valid today. Figures 5a, b, and c taken from from Gaposchkin and Lambeck [1969] amplify the magnitudes of the incompatibility between astrogeodetic geoids (Section 2.1) and combination geoids (Section 2.5) even after all necessary translations and rotations

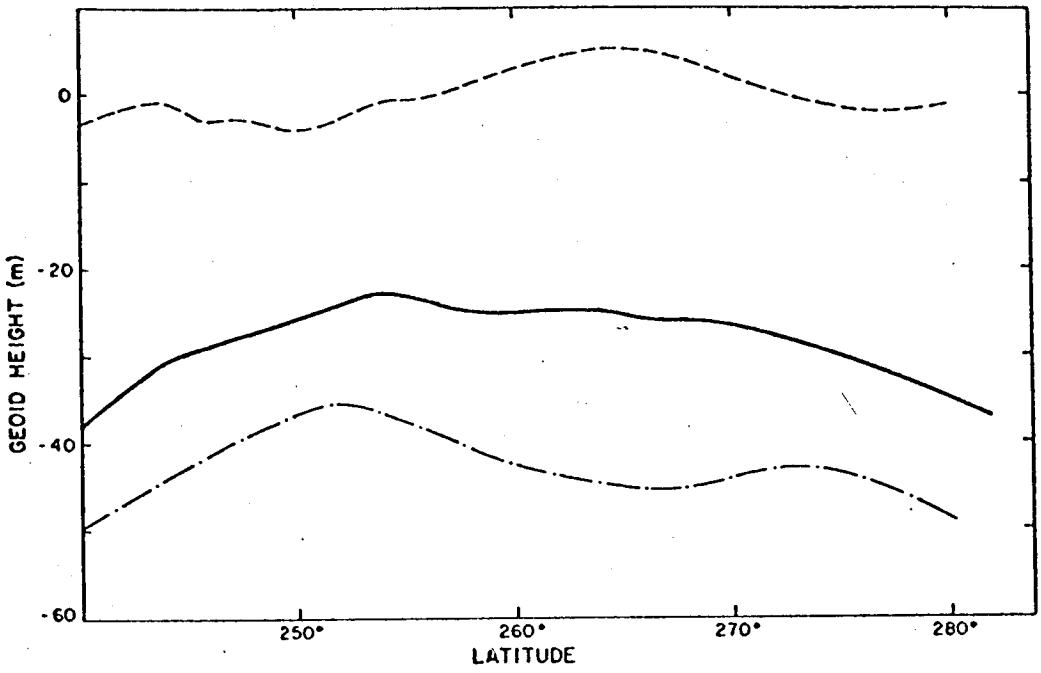

$\phi = 35°$

a

FIGURE 5 a, b, c. COMPARISONS BETWEEN GEOID PROFILES OBTAINED FROM THE COMBINATION SOLUTION (SOLID LINES) WITH PROFILES OBTAINED FROM ASTROGEODETIC MEASUREMENTS TRANSFORMED INTO THE GLOBAL REFERENCE SYSTEM (DASHED LINES). THE DIFFERENCE BETWEEN THE TWO PROFILES, AFTER THE SYSTEMATIC PART HAS BEEN SUBTRACTED, IS INDICATED BY THE DOTTED LINE.

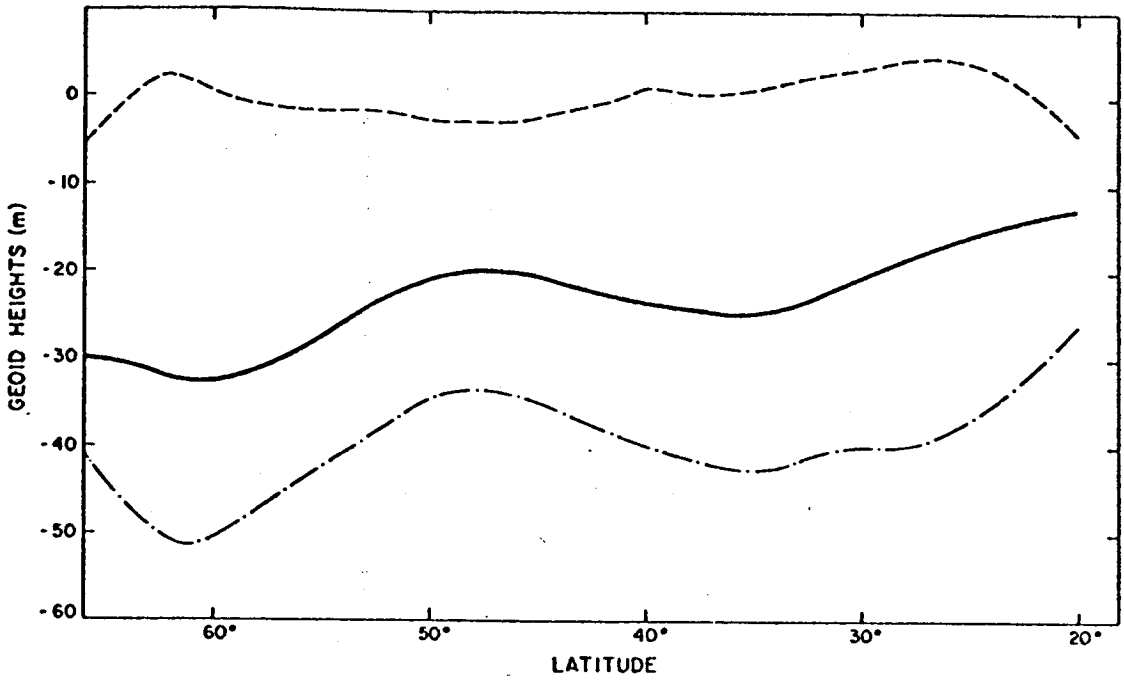

$\lambda = 260°$

North American Datum

5b

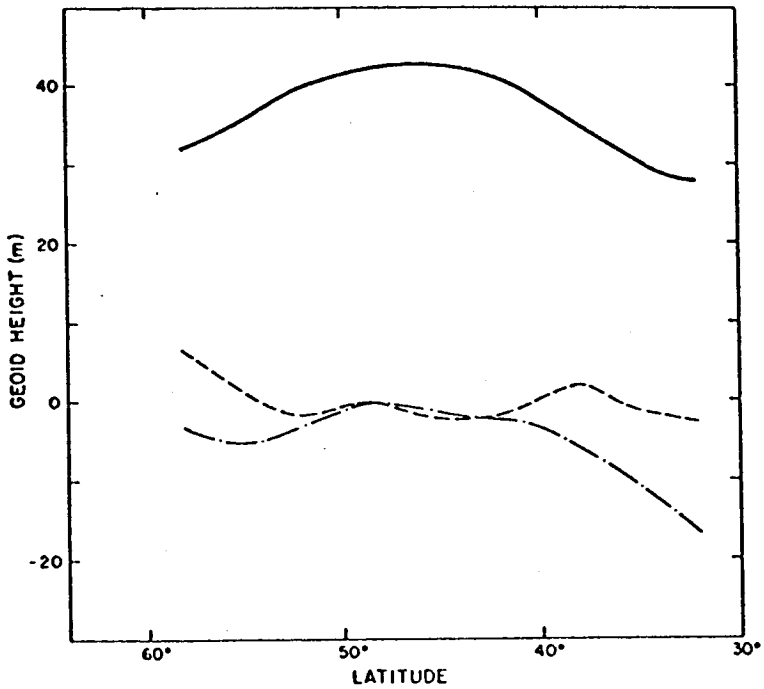

$\lambda = 16°$

European Datum

5c

have been performed to make them compatible. These figures refer to North American and European datums which supposedly have the best accurate geodetic data and computations.

The requirements of scale, shape, and orientation and expediency in practical determinations in test sites for geodetic sea-truth required by satellite altimetry rule out the applicability of any of the categories of geoid described except the astrogravimetry.

5. MARINE GEOID BY ASTROGRAVIMETRY

It has been shown how and why a marine geoid by astrogravimetry meets accurately the compatibility requirements in scale, shape, and absolute orientation required for satellite altimetry processing. A brief outline of the marine operations needed is as follows.

At any chosen test site marine geodetic controls using geodetic-acoustic techniques are established [Mourad, et al, 1970 a, b, c, d], [Fubara, et al, 1971] at say about 100 to 150 km intervals. Over these control points several repeated measurements of astronomic latitudes and longitudes are made to about 1 to 2 arc seconds accuracy. The corresponding geodetic latitude, longitude, and height are accurately and repeatedly measured over the same control points. At each geodetic control point, both the astronomic and geodetic measurements are reduced to a single point using techniques as in Mourad, et al [1970b], which continuously determine accurately the ship's position, speed, and heading relative to the geodetic ocean bottom markers.

In the test site and its surroundings, a dense gravity net of profile runs at about 10 to 20 km intervals should be conducted. The geodetic control points already established at the site should be linked up with gravity profile runs. At the same time, these control points will serve as base stations for the gravity profile runs and also furnish highly accurate ground ship speed and heading needed in the

gravity data reduction [Kaula, 1970]. The astronomic, geodetic coordinates, and gravity data are then processed together to give accurate details of the marine geoid at the test site.

6. CONCLUSION

The need for ocean surface mapping and the eventual determination of the absolute geoid at sea and the peripheral benefits to geodesy, oceanography, space research, marine environmental control, prediction, and resources exploitation is widely recognized. Satellite altimetry is expected to meet this need. The success of satellite altimetry depends on factors including adequate sea-truth. It has been shown that geodetic determination of certain features of the sea-truth is indispensable, and that gravity measurements alone cannot meet the requirements. Astrogravimetry is suggested as the most speedy, economical, and reliable answer. The implementation of astrogravimetry at sea is well within the current state of the art.

Furthermore, it is necessary to determine from satellite altimetry an absolute geoid and not a relative geoid because there are more than enough relative geoids already computed. These relative geoids cannot satisfy many of the needs of geodesy, oceanography, and earth-gravity modeling. Without the use of absolute geoid profiles as controls in the geodetic processing of satellite altimetry data, a relative geoid will be the result. In view of the foregone discussions, should more funds and efforts be spent to determine yet another relative geoid without proper scale, shape, and absolute orientation? Table 4 contains a summary of the findings of the paper.

TABLE 4. COMPARISON OF CONVENTIONAL MARINE GEOIDS AND SATELLITE ALTIMETRY "GEOID" FOR COMPATIBILITY

Type of Geoid	Compatibility Criteria: Absolute Orientation	Compatibility Criteria: Correct Scale	Compatibility Criteria: True Shape	Quality of Geoid and Sources of Deficiencies
(1) Astrogeodetic (classical)	No	Yes	False tilt	Detailed local geoid highly dependent on density and accuracy of deflection stations. Rapid error accumulation. Bad local datum influence. Currently not expedient at sea. Not compatible.
(2) Astrosatellite	Yes/No	Yes	Possible	Currently poor accuracy at sea as geoid details need highly accurate and dense data distribution. Suitable for evaluation but not absolute calibration of Sat. Alt. "Geoid".
(3) Inertial	No	Not reliable	Not reliable	Very poor accuracy, deficiencies in theory for data deduction. Accurate external geodetic reference required in navigation mode. Not compatible with Sat. Alt. "Geoid".
(4) Gravimetric (a) Stokes'	Yes	No	Possible	Not for ABSOLUTE CALIBRATION but good for shape evaluation. Needs adequate global coverage of data; theory problems in data prediction and reduction. Compatible in shape and orientation only but not in scale.
(b) Vening Meinesz	Yes	Possible dependent on initial point	Possible	More dependent on dense local gravity net and less influenced by distant zone data which are still needed. Problems in prediction and reduction theories. Compatible in shape and orientation but correctness of scale dependent on assumed initial point.
(5) Satellite (a) Geopotential coefficients	Yes	Dependent on method used	General outline	Poor coefficient accuracy, inadequate for geoid details. Not suitable for calibration of Sat. Alt. "Geoid".
(b) Geometric/dynamic	Possible	Yes	Possible	Highly dependent on orbit accuracy and geometry. Could provide in the future compatible detailed geoid profiles.
(6) Combined Satellite/Terrestrial, Astronomic, Geodetic, Gravity	Yes?	Yes?	Yes?	Development of techniques in progress. Theoretically, could provide global geoid using world-wide data coverage. Not suitable for local geoid details as required for satellite altimetry test areas.
(7) Astrogravimetry	Yes	Yes	Yes	Requires ONLY LOCAL GRAVITY data, speedy and economical. BEST suitable for geoid details in Test Areas. COMPATIBLE with expected Sat. Alt. "Geoid" in scale, shape, and orientation.
(8) Satellite Altimetry	Yes	Yes	Yes	Development in progress. If successful, provides the best hope currently for speedy, economical determination of global marine geoid with sufficient accuracy and details to meet oceanographic, geodetic, space programs, environmental control and prediction needs.

REFERENCES

Bacon, D. et al. "Geoid Representation From Satellite--Determined Coefficients," TR-70-3, IBM, Gaithersbury, Maryland, 1970.

Bomford, G., Geodesy, Second Edition, Oxford University Press, 1962.

Biro, P., "On the Accuracy of the Deviations of the Vertical Interpolated by Gravimetric Methods", Proc. of the International Symposium Figure of the Earth and Refraction, Edited by K. Ledersteger, p. 86, Vienna, 1967.

Bradley, C. L., "Identification of Vertical Deflections Utilizing an Inertial Navigator and Optimum Data Processing", Advances in Dynamic Gravimetry, Edited by W. T. Kattner, p. 95, Instrument Society of America, Pittsburgh, Penn., 1970.

Bradley, C. L., Sandberg, H. J., DeMatteo, J., "Identification of Deflection of the Vertical Using an Inertial System", Proc. of the First Marine Geodesy Symposium, Battelle Memorial Institute, Columbus, Ohio, 1966.

Bursa, M., "Earth's Flattening and Harmonic Coefficients of Geopotential", Studia Geoph. et Geod. 12, p. 237, 1968.

Bursa, M., "Potential of the Geoid Surface, the Scale Factor for Lengths and Earth's Figure Parameters from Satellite Observations", Studia Geoph. et Geod. 13, p. 337, 1969.

Butera, A. W., DeMatteo, J. J., and Goclowski, J. C., "Direct Measurement of Deflection of the Vertical Using a Ship's Inertial Navigation System (SINS)", Proceeding of Second Symposium on Marine Geodesy, Marine Technology Society, Washington, 1970.

Fischer, I., "The Hough Ellipsoid or The Figure of the Earth from Geoidal Heights". Presented at I.U.G.G. General Assembly, Toronto, 1957. (See also J. of Geophysical Res., Vol 64, p. 73, 1959).

Fischer, I., "Comments on Comparison and Combination of Satellite with other Results", The Use of Artificial Satellite for Geodesy, Edited by G. Veis, p. 378, North-Holland Pub. Co., Amsterdam, 1963.

Fischer, I., "Deviations of the Geoid from an Equilibrium Figure", Proc. of the International Symposium Figure of the Earth and Refraction, Edited by K. Ledersteger, p. 53, Vienna, 1967.

Fischer, I., et al. "New Pieces in the Picture Puzzle of an Astrogeodetic Geoid Map of the World", Bulletin Geod. No. 88, p. 199, 1968.

Fubara, D. M. J., Three-Dimensional Geodesy Applied to Terrestrial Networks, Ph.D. Thesis, University of New Brunswick, Fredericton, 1969.

Fubara, D. M. J. and Mourad, A. G., "Nonclassical Determination of Spatial Coordinates of Ocean-Bottom Acoustic Transponders", Presented at the 52nd Annual Meeting of the American Geophysical Union, Washington, D. C., 1971.

Fubara, D. M. J., "Unification of Intrinsic Space and Terrestrial Parameters and Data in Three-Dimensional Geodesy" (in prep) 1971.

Gaposchkin, E. M. and Lambeck, K., "1969 Smithsonian Standard Earth (II)", Smithsonian Astrophysical Observatory, Spec. Report No. 315, May 18, 1970.

Greenwood, J. A., Nathan, A., Neumann, G., Pierson, W. J., Jackson, F. C., and Pease, T. E., "Radar Altimetry from a Spacecraft and Its Potential Applications to Geodesy", Remote Sensing of Environment 1, p. 59, 1969.

Groten, E., and H. Moritz, On the Accuracy of Geoid Heights and Deflections of the Vertical. Report No. 38, Inst. of Geod., Phot. and Cartography, Ohio State University, 1964.

Heiskanen, W. A., "Potentialities of Satellite Geodesy and Physical Geodesy", The Use of Artificial Satellites for Geodesy, Edited by G. Vies, p. 346, North-Holland Pub. Co., Amsterdam, 1963.

Heiskanen, W. A., and Moritz, H., Methods of Physical Geodesy, Report No. 32, Inst. of Geod., Photo. and Cartography, Ohio State University, Columbus, Ohio, 1964.

Heiskanen, W. A., and Moritz, H., Physical Geodesy, W. H. Freeman and Company, San Francisco, 1967.

Henrikson, P. and Nash, R. A., Jr., "A Statistical Analysis of Errors in Gravimetrically Computed Vertical Deflections", J. of Geophs. Res., Vol. 75, p. 4017, 1970.

Hirvonen, R. A., New Theory of The Gravimetric Geodesy, Isostatic Institute of The International Association of Geodesy, No. 32, Helsinki, 1960.

Hotine, M., Mathematical Geodesy, U. S. Government Printing Office, Washington, D. C., 1969.

Kaula, W. M., "Accuracy of Gravimetrically Computed Deflections of the Vertical", Trans. Am. Geophs. Union, Vol. 38, p. 297, 1957.

Kaula, W. M., "Reconciliation of Stokes' Function and Astrogeodetic Geoid Determination", J. of Geophys. Research, Vol. 64, p. 61, 1959a.

Kaula, W. M., "Statistical and Harmonic Analysis of Gravity", J. of Geophs. Res., Vol. 64, p. 2401, 1959b.

Kaula, W. M., "A Geoid and World Geodetic System Based on a Combination of Gravimetric, Astrogeodetic, and Satellite Data", J. of Geophs. Res., Vol. 66, p. 1799, 1961.

Kaula, W. M., "Comparison and Combination of Satellite with other Results for Geodetic Parameters", The Use of Artificial Satellites for Geodesy, Edited by G. Veis, p. 335, North-Holland Pub. Co., Amsterdam, 1963.

Kaula, W. M., "Global Harmonic and Statistical Analysis of Gravimetry", Proc. of the Symposium-Extension of Gravity Anomalies to Unsurveyed Areas, Geophys. Monograph 9, Edited by H. Orlin, p. 58, 1966.

Kaula, W. M., "Application of Space and Astronomic Techniques to Solid Earth and Ocean Physics", Advances in Dynamic Gravimetry, Edited by W. T. Kattner, p. 130, Instrument Society of America, Pittsburgh, Penn., 1970.

Koch, K. R., "Gravity Anomalies for Ocean Areas from Satellite Altimetry", Proceedings of Second Symposium on Marine Geodesy, Marine Technology Society, Washington, D. C., 1970.

Lambeck, K., "The Relation of Some Geodetic Datums to a Global Geocentric Reference System", Bull. Geod. No. 99, p. 37, 1971.

Lundquist, C. A., Satellite Altimetry and Orbit Determination, Smithsonian Astrophysical Observatory, Spec. Report No. 248, 1967.

Martin, C. F., Roy, N. A., and Stanley, H. R., "Puerto Rican Trench Surface Profile Measurement Using Satellite Tracking Data", Paper presented at the Symposium on Marine Geodesy, Sponsored by IAG and IAPSO of IUGG, Moscow, August 9, 1971.

Mather, R. S., "The Geocentric Orientation Vector for the Australian Geodetic Datum", Geophs. J. R. Astr. Soc., 22, p. 55, 1970.

Mather, R. S., "Practical Techniques for the Establishment of a World Geodetic System from Gravity Data" Presented at IUGG XV General Assembly, Moscow. 1971.

Molodenskii, M. S., Eremeev, V. F., and Yurkina, M. I., Methods for Study of The External Gravitational Field and Figure of the Earth, Israel Program for Scientific Translations, Jerusalem, 1962a.

Molodensky, M. S., Yeremeyev, V. F., and Yourkina, M. I., "An Evaluation of Accuracy of Stokes' Series and of some Attempts to Improve His Theory", Bull. Geod., No. 63, p. 19, 1962.

Moritz, H., Interpolation and Prediction of Gravity and Their Accuracy, Report No. 24, Inst. of Geod., Phot. and Cart., Ohio State Univ., 1962.

Moritz, H., On the Accuracy of Spherical Harmonics and Orbital Predictions, Report No. 36, Inst. of Geod., Phot. and Cart., Ohio State Univ., 1964.

Moritz, H., "Accuracy of Mean Gravity Anomalies Obtained from Point and Profile Measurements", Bull. Geod., No. 80, p. 157, 1966.

Moritz, H., "Kinematical Geodesy", presented at IUGG XIV General Assembly, Switzerland, 1967.

Moritz, H., A General Theory of Gravity Processing, Report No. 122, Dept. of Geod. Sci., Ohio State Univ., 1969.

Moritz, H., Mathematical Techniques in Physical Geodesy, Report of Special Study Group No. 5:31 of the IAG, Presented at IUGG XV General Assembly, Moscow, 1971a.

Moritz, H., "Possible Applications of Kinematical Geodesy", Presented at Symposium on Marine Geodesy, XV General Assembly of IUGG, Moscow, 1971b.

Mourad, A. G., Holdahl, J. H., and Frazier, N. A., "Preliminary Results of the Establishment of a Marine Geodetic Control Point in The Pacific Ocean", Bulletin Geodesique, No., 96, pp. 107-124, June 1970a.

Mourad, A. G., Hopper, A. T., Fubara, D. M., and Ruck, G. T., Acoustic Techniques and Results from C-Band Radar Marine Geodesy Experiment Using USNS Vanguard, Battelle Memorial Institute, Columbus, Ohio, 1970b.

Mourad, A. G., and Fubara, D. M. J., "Analysis of a Marine Geodetic Control Establishment Technique and Potential Applications", Presented at the AGU National Fall Meeting, San Francisco, California, December, 1970c.

Mourad, A. G., "New Techniques for Geodetic Measurements at Sea", Trans. American Geophys. Union, E@S, 1970d.

Mourad, A. G., and Fubara, D. M. J., "Planning and Conducting an Ocean Surface Mapping Experiment Using Apollo Ship Instrumentation", Final Report prepared by Battelle to NASA/Wallops Station, 1971a.

Mourad, A. G., "Marine Geodesy 1967-1971", Report of Special Study Group (SSG1-25) to IAG, Moscow, 1971b.

Mueller, I. I., and Rockie, J. D., Gravimetric and Celestial Geodesy, Frederick Ungar Publishing Company, New York, 1966.

NASA, The Terrestrial Environment, Solid-Earth and Ocean Physics, Report of a Study at Williamstown, Mass., 1970.

O'Keefe, J. A., "Equilibrium Figure of the Earth and the Scientific Reference Surface", Proc. of the Int. Symposium Figure of the Earth and Refraction, Vienna, Edited by K. Ledersteger, p. 18, 1967.

Rapp, R. H., "The Equatorial Radius of the Earth and the Zero-Order Undulation of the Geoid", J. of Geophysical Research, Vol. 72, No. 2, p. 589, 1967.

Rapp, R. H., "Analytical and Numerical Differences Between Two Methods for the Combination of Gravimetric and Satellite Data", Boll. Di Geofisica, Vol. XI, No. 41-42, 1969.

Rapp, R. H., Methods for the Computation of Geoid Undulations from Potential Coefficients, Report No. 132, Dept. of Geodetic Sc., Ohio State Univ., 1970a.

Rapp, R. H., The Role of Gravity Data in Determination of The Gravitational Potential of the Earth, Report No. 134, Dept. of Geodetic Sc., Ohio State Univ., 1970b.

Rapp, R. H., A General Combination of Satellite and Gravity Data for Position and Gravity Field Determinations, Report No. 133, Dept. of Geodetic Sc., Ohio State Univ., 1970c.

Raytheon Company Equipment Division, Space Geodesy Altimetry Verification Experiment Design Study, Report SR70-4108, Sudbury, Massachusetts, 1970.

Schultz, O. T., and Winokur, J. A., "Shipboard or Aircraft Gravity Vector Determination by Means of a Three-Channel Inertial Navigator", Presented at the meeting of the American Geophysical Union in Washington, D. C., April 17-20, 1967.

Shaw, L., Paul, I., and Henrikson, P., "Statistical Models for the Vertical Deflection from Gravity-Anomaly Models", J. of Geophs. Res., Vol. 74, p. 4259, 1969.

Stanley, H. R., and McGoogan, J. T., "Satellite Altimetry and Its Applications to Marine Geodesy--The GEOS C and Skylab Programs", presented at the IAG/IAPSO Symposium on Marine Geodesy, Moscow, 1971.

Stanley, H. R., Martin, C. F., Roy, N. A., and Vetter, J. R., "An Error Analysis of the Recovery Capability of the Relative Sea-Surface Profile Over the Puerto Rican Trench From Multi-Station and Ship Tracking of GEOS-II", NASA Wallops Station,Report X-300-71-1, Wallops Island, Virginia, May 1971.

Uotila, U. A., Investigations on the Gravity Field and Shape of the Earth, Inst. of the International Association of Geodesy, No. 33, Helsinki, 1960.

Veis, G., "The Deflection of the Vertical of Major Geodetic Datums and the Semimajor Axis of the Earth's Ellipsoid as Obtained from Satellite Observations", Bull. Geod., No. 75, p 13, 1965.

Veis, G., "The Determination of the Radius of the Earth and Other Geodetic Parameters as Derived from Optical Satellite Data", Bull. Geod., No. 89, p. 253, 1968.

von Arx, W. S., "Relationship of Marine Physical Geodesy to Physical Oceanographic Measurements", Proceedings of First Marine Geodesy Symposium, Battelle Memorial Institute, Columbus, Ohio, 1966.

Weiffenbach, G. C., "The GEOS C Radar Altimeter" in Marine Geodesy, A Practical View, p. 291, Proceedings of The Second Marine Geodesy Symposium, Marine Technology Society, Washington, D. C., 1970.

Yeremeev, V. F., and Yurkina, M. I., The Grade Measurements Equations by the Simultaneous Utilization of Terrestrial and Satellite Data, Presented at XV General Assembly of IUGG, Moscow, 1971.

Young, R. G. E., "Combining Satellite Altimetry and Surface Gravimetry in Geodetic Determinations", Mass. Inst. Tech., TE-37, 1970.

SATELLITE HEIGHT DETERMINATION USING SATELLITE-TO-SATELLITE TRACKING AND GROUND LASER SYSTEMS

6

F. O. Vonbun

NASA/Goddard Space Flight Center
Trajectory Analysis and Geodynamics Division
Mission and Data Operations Directorate

The height of the GEOS-C spacecraft is one of the more important parameters for earth and ocean dynamics and geodesy. It is the intent to utilize this parameter, as measured by the onboard radar altimeter, for an improved determination of the earth's gravitational field and for the determination of the variation of the physical surface of the oceans.

Two tracking system approaches to accurately determine the spacecraft height (orbit) are described and their results stated. These are satellite-to-satellite tracking (SST) and ground-laser tracking (GLT). Height variations can be observed in the dm - regions using SST and in the m-region using present GLT.

1. INTRODUCTION

The GEOS-C spacecraft will be the first one to make a connection between the National Geodetic Satellite Program and hopefully a new program, namely the Earth and Ocean Dynamics Satellite Applications Program.

The major difference between GEOS-C and the two previous spacecraft, GEOS-A and -B, is that this one carries a radar altimeter and a satellite-to-satellite tracking system.[1] Both are major experiments needed for future applications programs in the area of earth and ocean dynamics.[2]

Altimeter data with errors of, say, ±3 to ±5 m will be used for a more rigorous analysis, as done in the past, of the earth gravity field and the variations of the physical surface of the sea (gravity anomalies, geostrophic equilibrium of the sea, wind loading, storm surges, etc.). One of the main advantages of height information for orbit and thus gravity field analysis is the large number of data points

obtainable (2 per second), their high accuracy and extremely good along track distribution. For the determination of the ocean height and its variations, the altimeter is at present the only capable instrument.

As is the case for all measurements made, a zero adjustment or an initial calibration will have to be performed by each of the pertinent experimenters. The SST and GLT for altimeter calibration and along track evaluation will be briefly discussed.

II. ATS-F AND GEOS-C SATELLITE TO SATELLITE TRACKING

The ATS-F spacecraft will track, as shown in figure 1, the GEOS-C using a ~2000 MHz SST which measures range and range rate sums.[1] With such a system, the orbits of ATS-F and GEOS-C can be determined simultaneously with a high degree of accuracy. In addition, after an initial independent determination of the GEOS-C height (using, say, a radar, or a laser ground or shipborne station), the SST will be able to "follow" the GEOS-C spacecraft in a phase-locked fashion over half the earth. Thus a constant "watch" can be kept on the altimeter independent of any ground support. This is important if the height is to be used to check the variation of the physical surface of the ocean, say from the U.S. to Europe. The SST, as presently configured, should be able to "detect" satellite height variations in the submeter level, figure 2. Please note that only systems errors are included which are of primary importance at this time. It is clear that these system errors have to be smaller by a factor of 5 to 10 as compared to those expected from the eventual experiments.

Figure 3 shows the height differences of GEOS-C orbit due to different gravity fields as used in present day accurate orbit determination. The fields used are the NWL and the SAO fields.[3] [4] Variations in the order of tens of meters

G

do occur. Improvements made in the meantime may reduce these values by a factor of 3 to 5. Nevertheless this indicates that for the GEOS-C, at least at the beginning of the flight evaluation period, only relative height variations in the submeter level will be detectable.[5] In other words, one can only determine these variations consistent with one particular gravity field used in the orbit determination process.

These considerations do not hold for the variation of the physical sea surface. A trench (5 to 10 m over 100 to 200 km) can and will be fairly easy to detect. This holds true for other variations in the height of the ocean surface (tides, storm surges). Figure 4 shows a mathematically simplified trench profile (Puerto Rico trench) and the expected height variations (Δh = 15 m, $\Delta \dot{h}$ = 1.6 m/s).[1] Since the satellite orbit will certainly not follow this kind of a profile and the altimeter can be "watched" from the ATS for any eventual drifts, such profiles should be fairly easy detectable with the GEOS-C altimeter system as configured.

The contribution of the SST to the analysis of the gravity field, and in particular to the determination of anomalies, is out of the content of this paper and is discussed in references 5, 6, and 7.

III. GEOS-C LASER GROUND TRACKING

In addition to the SST approach, precision GLT systems will be used as an additional method of determining the "real" height of the GEOS-C spacecraft independent of the dynamics of the orbit.

As shown in figure 5, three precision ground laser stations are planned to be used in the Caribbean area. The stations will be near the sea (for ease of level determination) at Key West, Canal Zone, and Antigua to form a good three-dimensional triangle (station distances commensurate with satellite height) of near optimum conditions. It is assumed that the uncertainty of the sea surface over this area is

approximately two meters. Using these three stations, the height of the spacecraft can be determined completely independent of the orbital dynamics earth gravity field and its rather large uncertainties, as shown in figure 3. Figure 6 depicts the height errors of the spacecraft as a function of the ground track.[8] Please see also for comparison figure 5 showing the ground track and the position of the spacecraft (time ticks) relative to the three ground stations. It can be seen (fig. 6) that over a rather large subsatellite track (500 to 1000 km), the spacecraft height can be determined with these laser systems to within two to three meters. Please note that this assumes that the relative errors are ±5 to 10 m in longitude and latitude, and ±2 m in height for Key West and Antigua and zero (arbitrary reference) for the Canal Zone.

The present (10 cm in the future) tracking system's capabilities of 30 cm (noise, bias) of the laser systems are far below the errors considered, so they do not constitute a limit. On the contrary, they enable one to determine relative intersite distances from 30 to 50 cm. This result was obtained during the recent Goddard Polar Motion Experiment as reported in reference 9. Thus, the errors of five meters, as shown in figure 6, for the error of the intersite distances can be reduced considerably by the method used for the Polar Motion Experiment which in turn will reduce the depicted height errors. This, of course, assumes that the problems associated with the reflection from the sea surface have been solved to a compatible accuracy.

In conclusion it can be stated: Both methods, the SST as well as the GLT can be used, under the conditions stated, to determine the height of the GEOS-C spacecraft with errors commensurate of the radar altimeter. It should be noted that both methods are rather independent of the final choice of the orbit.

approximately two meters. Using these three stations, the height of the spacecraft can be determined completely independent of the orbital dynamics earth gravity field and its rather large uncertainties, as shown in figure 3. Figure 6 depicts the height errors of the spacecraft as a function of the ground track.[8] Please see also for comparison figure 5 showing the ground track and the position of the spacecraft (time ticks) relative to the three ground stations. It can be seen (fig. 6) that over a rather large subsatellite track (500 to 1000 km), the spacecraft height can be determined with these laser systems to within two to three meters. Please note that this assumes that the relative errors are ±5 to 10 m in longitude and latitude, and ±2 m in height for Key West and Antigua and zero (arbitrary reference) for the Canal Zone.

The present (10 cm in the future) tracking system's capabilities of 30 cm (noise, bias) of the laser systems are far below the errors considered, so they do not constitute a limit. On the contrary, they enable one to determine relative intersite distances from 30 to 50 cm. This result was obtained during the recent Goddard Polar Motion Experiment as reported in reference 9. Thus, the errors of five meters, as shown in figure 6, for the error of the intersite distances can be reduced considerably by the method used for the Polar Motion Experiment which in turn will reduce the depicted height errors. This, of course, assumes that the problems associated with the reflection from the sea surface have been solved to a compatible accuracy.

In conclusion it can be stated: Both methods, the SST as well as the GIT can be used, under the conditions stated, to determine the height of the GEOS-C spacecraft with errors commensurate of the radar altimeter. It should be noted that both methods are rather independent of the final choice of the orbit.

REFERENCES

DeWitt, R. N. (1962), Derivations of expressions describing the gravitational field of the earth, Technical Memorandum #K-35/62, U.S. Naval Weapons Laboratory, Dahlgren, Virginia.

Gaposchkin, E. M., and K. Lambeck (1970), 1969 Smithsonian standard earth, SAO, Special Report #315, May.

Mueller, P. M., and H. L. Sjorgeu (1968), MASCONS: Lunar mass concentrations, Science, 161, 680-684.

NASA (1970), Earth and ocean dynamics satellite applications program, April 1 (Washington, D. C.) (Preliminary Issue).

Schwartz, C. R. (1970), Gravity field refinement by satellite-to-satellite Doppler tracking, Contract Number NGL 36-008-093, OSURF Project Number 2514, December, Ohio State University, Report Number 147.

Vonbun, F. O. (1971), The ATS-F/NIMBUS-E tracking experiment Presented at the 48th IAU Symposium, May 9-15, Morioka, Japan.

Vonbun, F. O. (1971), Geodetic satellite mission and GEOS-C spacecraft, Space Res. XI, Academy Verlag, Berlin, 457-467.

TRACKING GEOMETRY FOR ATS–F AND GEOS-C

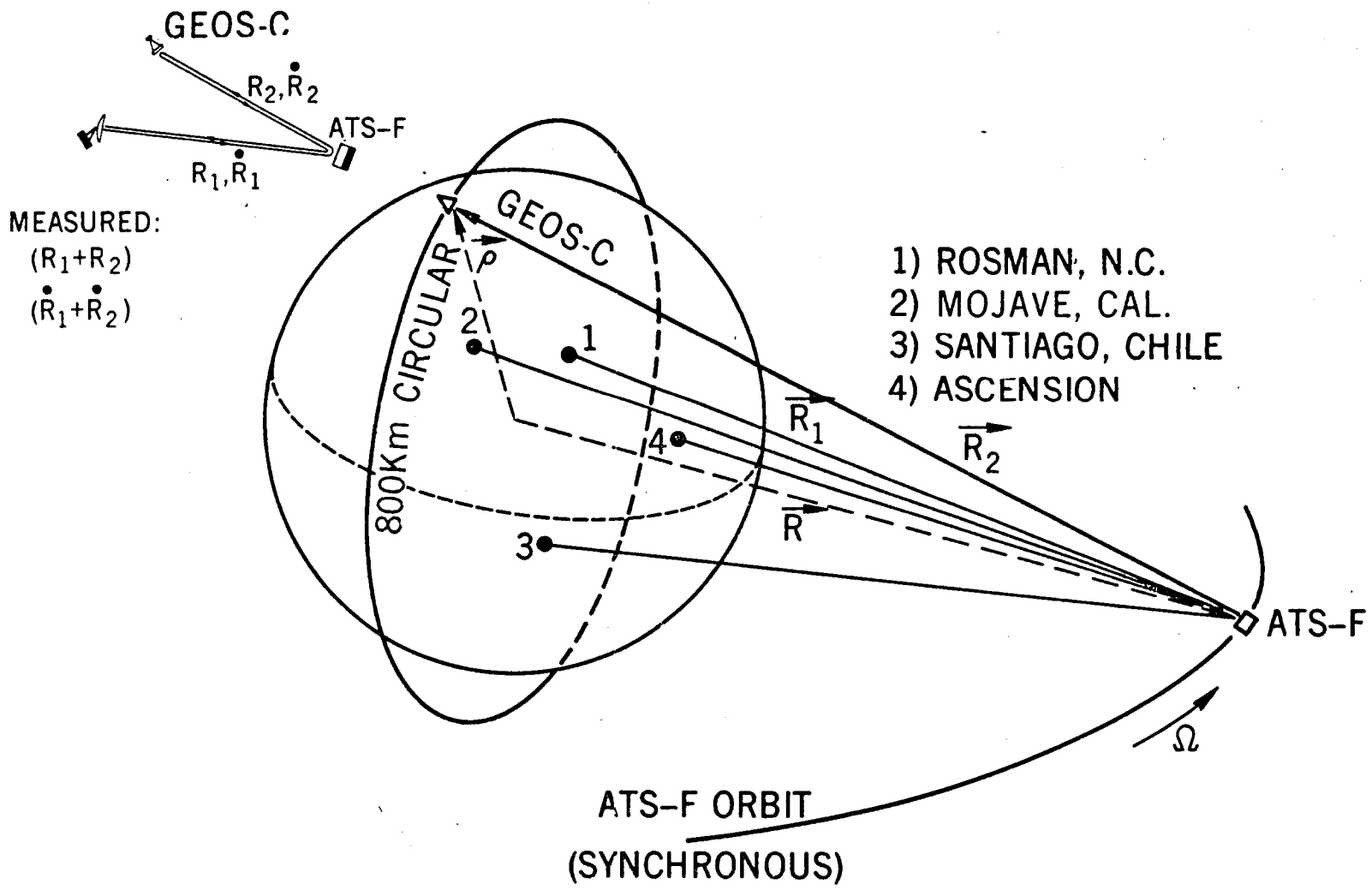

Figure 1

ATS–F AND GEOS-C SYSTEM HEIGHT ERRORS vs. ROSMAN STATION ERRORS

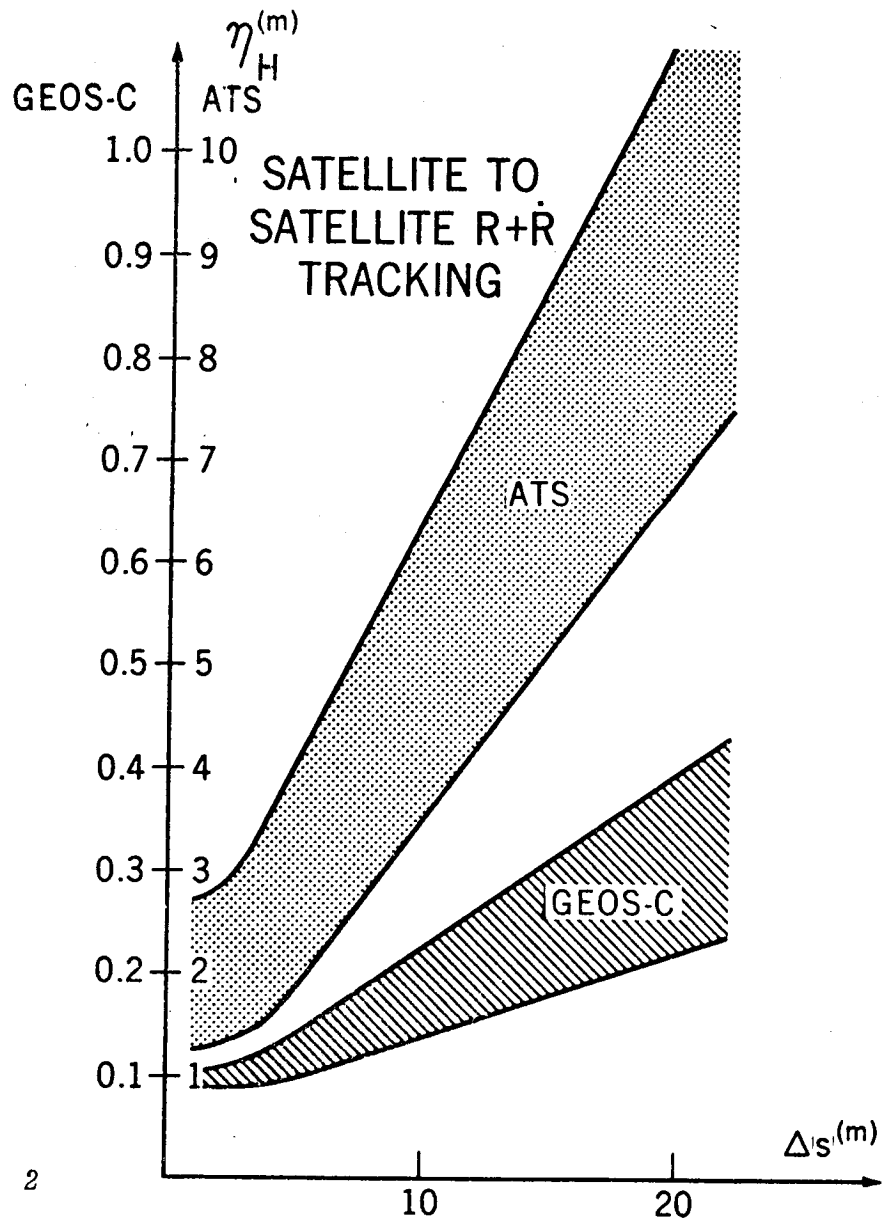

Figure 2

GEOS-C HEIGHT DIFFERENCES DUE TO SAO AND NWL FIELDS

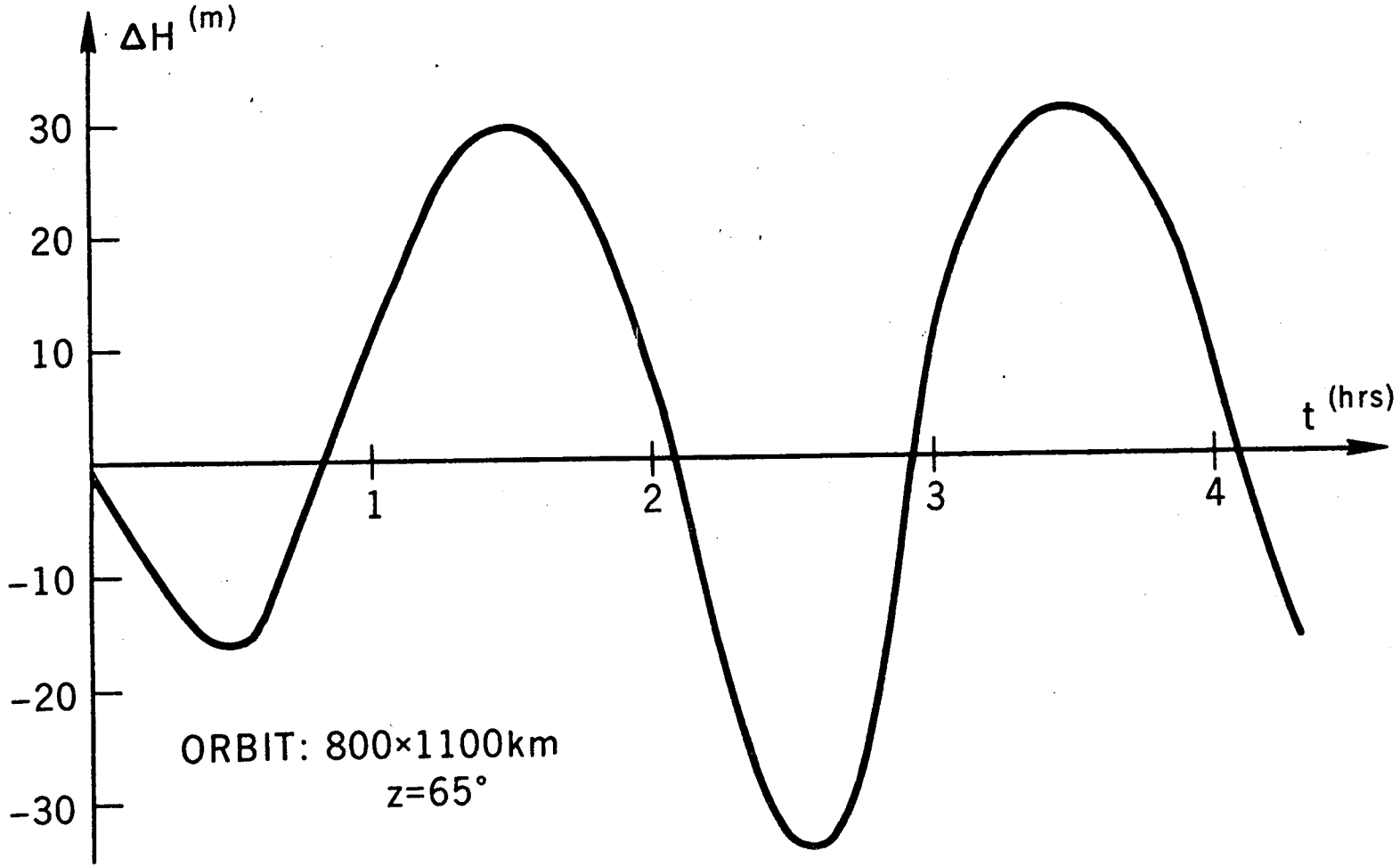

Figure 3

RADAR HEIGHT CHANGES OVER A TRENCH

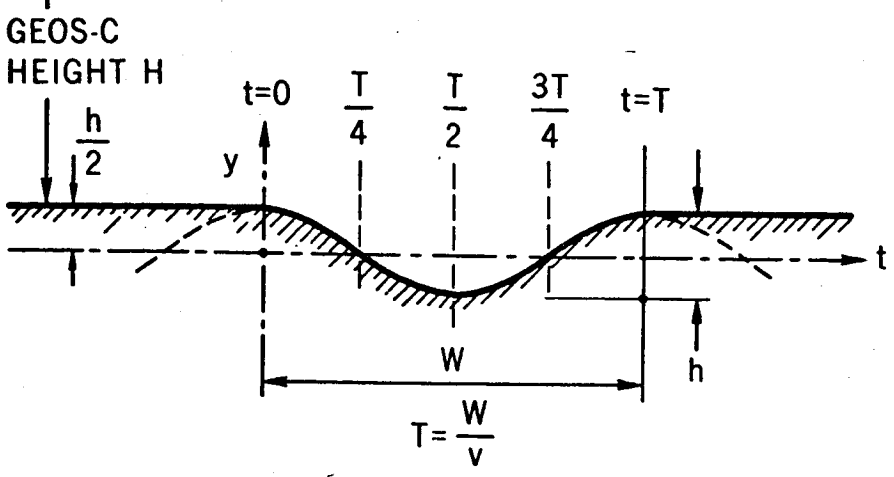

$\dot{H} \doteq v\, e \sin \eta$ GEOS-C HEIGHT VELOCITY $e \ll 1$

$$y = \frac{h}{2} \sin\left(\frac{2\pi}{T} t + \frac{\pi}{2}\right)$$ TRENCH PROFILE (Approx.)

$$\dot{y} = \frac{h}{2}\left(\frac{2\pi}{T}\right) \cos\left(\frac{2\pi}{T} t + \frac{\pi}{2}\right)$$ TRENCH HEIGHT VELOCITY

$$\ddot{y} = -\left(\frac{2\pi}{T}\right)^2 \frac{h}{2} \sin\left(\frac{2\pi}{T} t + \frac{\pi}{2}\right)$$ TRENCH HEIGHT ACCELERATION

FOR GEOS-C:

WITH h=15m, w=210km, T=30 sec, $v \doteq 7$ km/s $e=0.0322$

$\dot{H}_{MAX} \doteq 230$ m/s, $\dot{y}_{MAX} \doteq 1.6$ m/s, $\ddot{y}_{MAX} \doteq 0.34$ m/s^2

$= 3.4 \cdot 10^{-2} g$

Figure 4

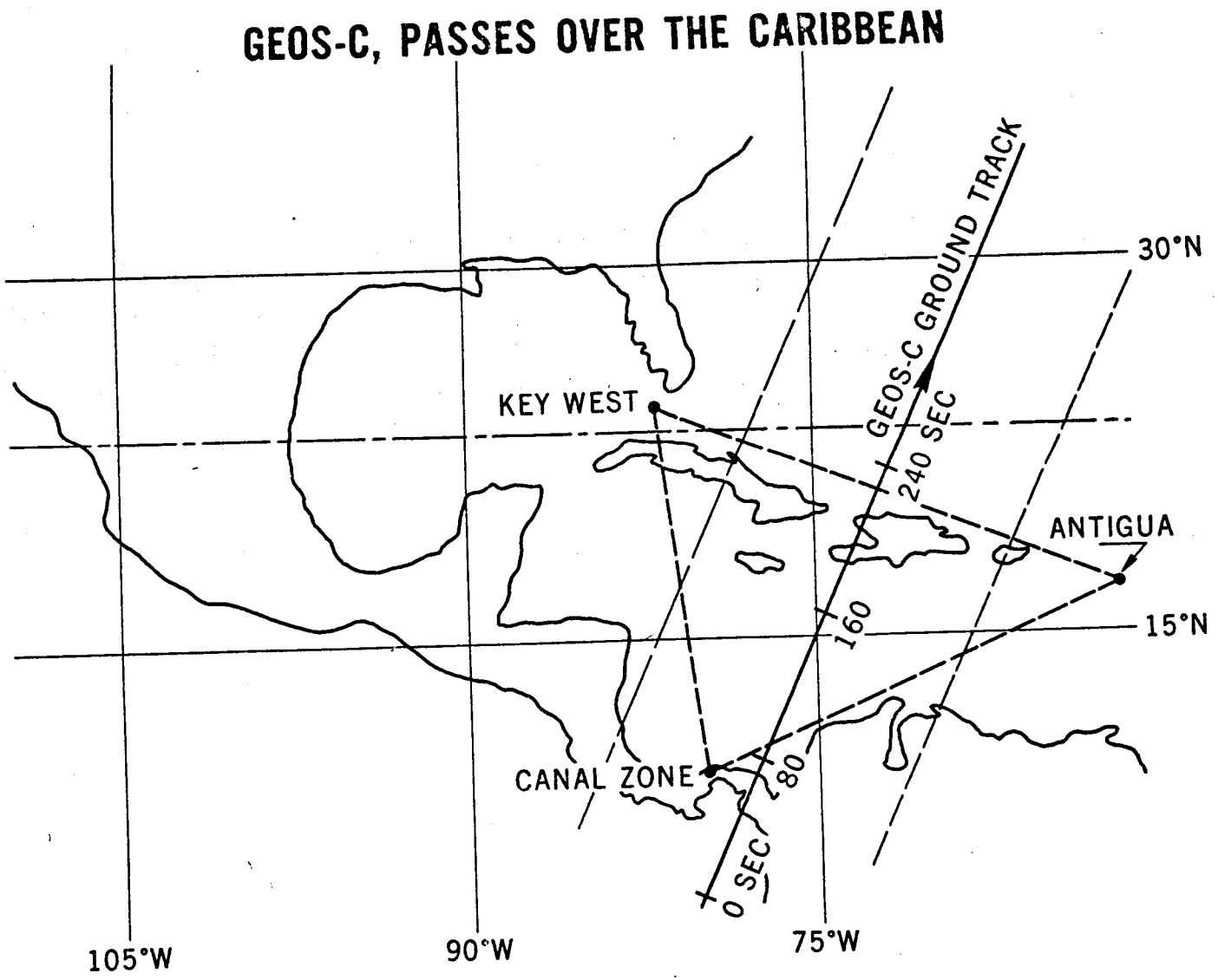
GEOS-C, PASSES OVER THE CARIBBEAN
30°N
15°N
105°W
90°W
75°W
KEY WEST
CANAL ZONE
ANTIGUA
GEOS-C GROUND TRACK
240 SEC
160
80
0 SEC

Figure 5

GEOS-C HEIGHT ERRORS USING LASER TRACKING

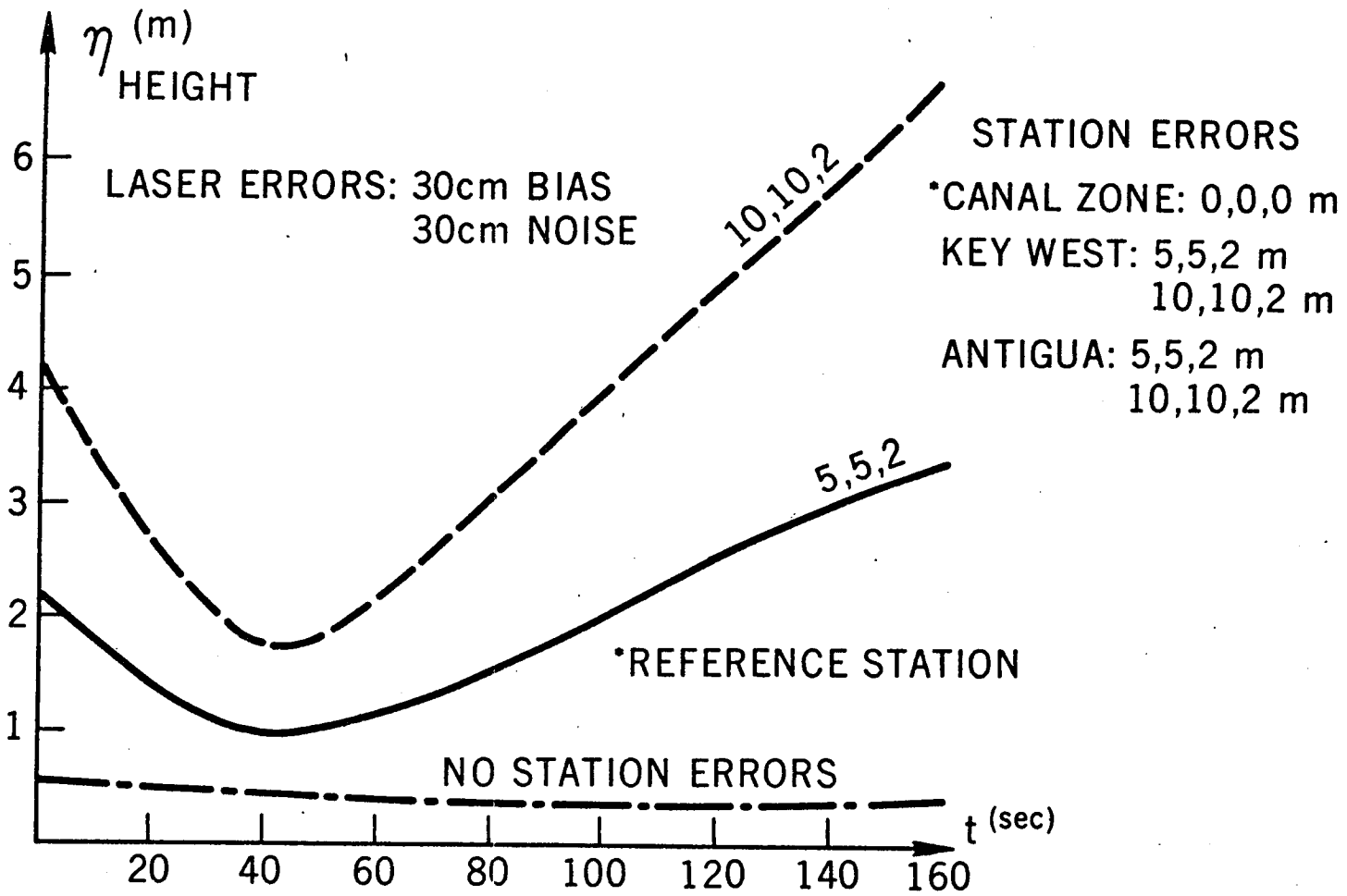

Figure 6

GEOS-C ALTIMETER HEIGHT CALIBRATION

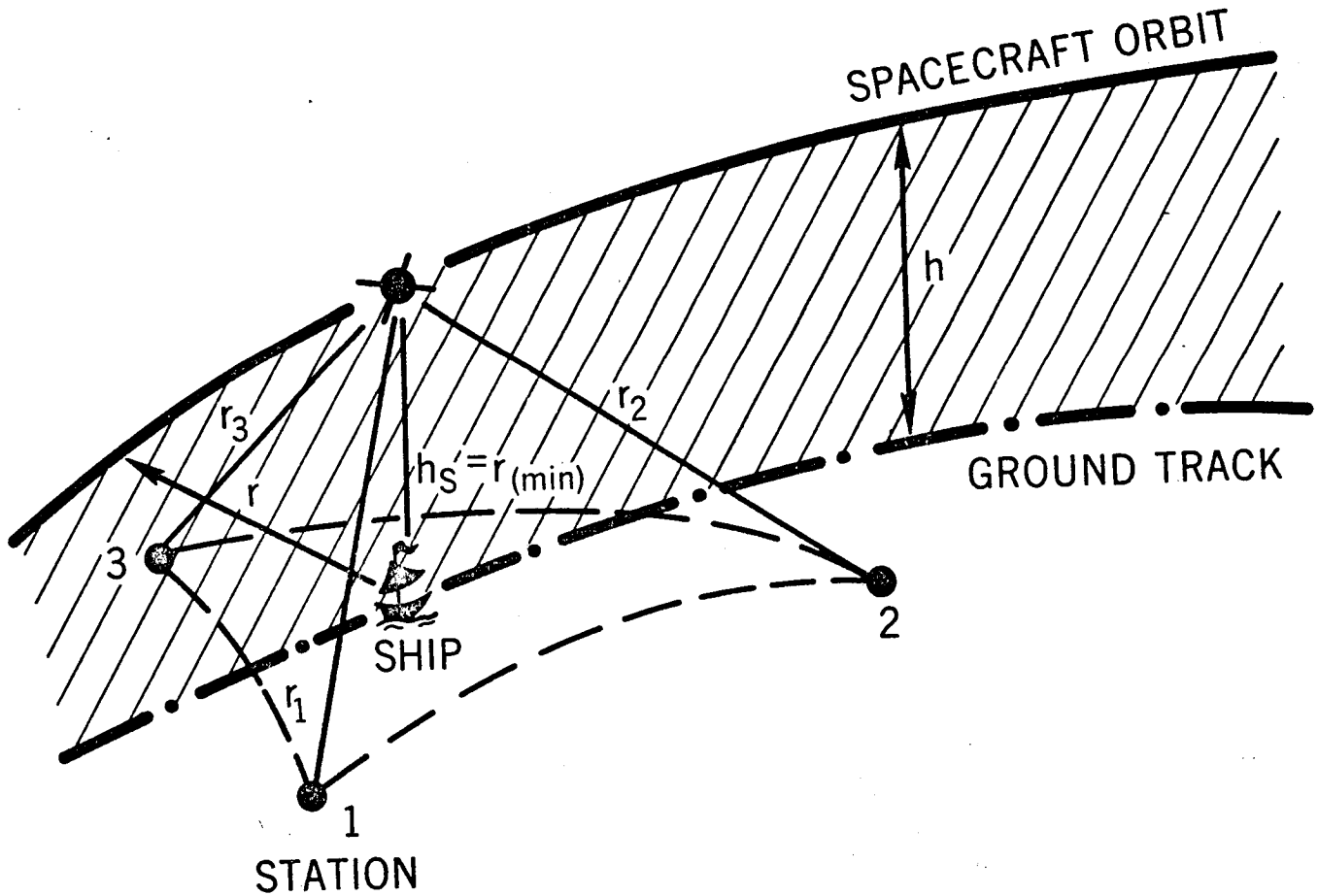

Figure 7

HEIGHT ERROR vs PERPENDICULAR SHIP LOCATION ERROR

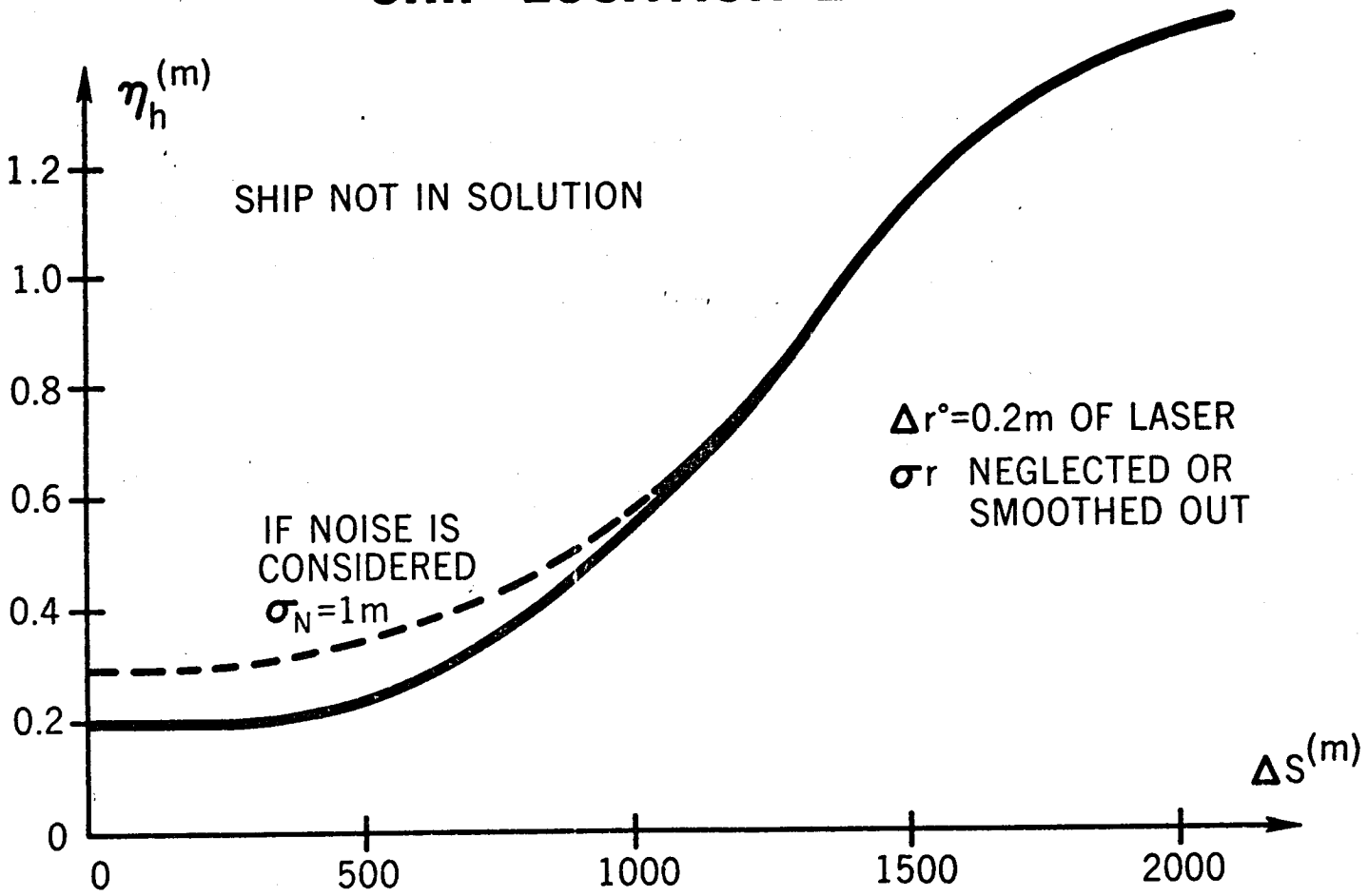

Figure 8

SATELLITE ALTITUDE DETERMINATION UNCERTAINTIES

7

Joseph W. Siry
NASA, GODDARD SPACE FLIGHT CENTER
TRAJECTORY ANALYSIS AND GEODYNAMICS DIVISION
MISSION AND DATA OPERATIONS DIRECTORATE

Presented at the Sea Surface Topography Conference,
Key Biscayne, Florida, October 6-8, 1971

I. INTRODUCTION

The subject of Satellite altitude determination uncertainties will be discussed from the standpoint of the GEOS-C satellite, which is representative of the state of the art of the first half of the decade of the seventies, and also from the longer range viewpoint afforded by the Geopause concept which gives us a glimpse of the possibilities for the latter half of this decade. GEOS-C will be tracked by a number of the conventional satellite tracking systems which have been used with GEOS-I and GEOS-II, which were tracked by range and range rate systems, laser systems having accuracies of the order of a meter, C-band radar systems and the Tranet Doppler system. GEOS-C will also be tracked by two advanced systems; namely, a satellite-to-satellite tracking system and lasers capable of decimeter accuracies which are being developed in connection with the Goddard Earth and Ocean Dynamics Satellite Applications Program (1 - 4). Aspects of satellite-to-satellite tracking and laser tracking are also being discussed in other papers presented at this conference. (11, 17)

The present discussion will focus on methods for short-arc tracking which are essentially geometric in nature. One uses combinations of lasers and collocated cameras. The other method relies only on lasers, using three or more to obtain the position fix. Two typical locales are looked at, the Caribbean area, and a region associated with tracking sites at Goddard, Bermuda and Canada which encompasses a portion of the Gulf Stream in which meanders develop. This latter region, which is of interest for oceanographic, earth dynamics, and practical reasons, will be referred to here simply as the Gulf Stream Meander region.

The discussion is organized in terms of a specific type of GEOS-C orbit which would satisfy a number of scientific objectives including the study of the gravitational field by means of both the altimeter and the satellite-to-satellite tracking system, studies of tides and of the Gulf Stream meanders. This serves to indicate an experimental configuration which is compatible with these several objectives of a program such as that of GEOS-C.

The long-arc tracking of GEOS-C can be considered in terms of satellite-to-satellite tracking and in terms of tracking by means of other systems such as precision laser systems, for example.

For the purposes of the first part of the discussion, two GEOS cases will be considered. The first deals with results of a study conducted by Berbert and Loveless to indicate capabilities in the Caribbean area using a short-arc approach (5). Here the orbital inclination was taken to be 22°, a value which was originally planned for GEOS-C. The results of this study are not, however, affected significantly by this choice since geometrical arrangements similar to those considered here would occur for other inclinations now under consideration. The second case deals with an inclination of 65° which is one of the higher values now being considered for GEOS-C. The final choice will probably lie somewhere between these two values. For this case too, there is interest in a short-arc calibration and validation capability. It is of interest to select a region which will serve as many of the scientific objectives as possible and yet be reasonably practicable to implement too. In order to indicate the kinds of scientific objectives which might be served, a particular typical selection for the orbit of GEOS-C will be discussed.

II. SHORT-ARC TRACKING OF GEOS-C IN THE CARIBBEAN AREA

The consideration of short-arc and long-arc tracking error budgets can begin with a look at the overall error problem. A typical error breakdown for the GEOS-C altimeter is indicated in Table I (6). Quantities associated with factors other than the orbit errors have an rms value of approximately 3 meters. This leaves 4 meters or so which can be assigned to the calibration process if the 5 meter rms overall accuracy goal is to be met. Allowing 1 or 2 meters for uncertainties associated with the geoid means that the uncertainties associated with the orbit determination process should contribute no more than about 3.5 meters.

A detailed analysis of short-arc tracking using lasers and cameras in the Caribbean area has been conducted by Berbert and Loveless (5). A GEOS-C ground track for the 22° inclination case in the neighborhood of several possible tracking locations in the Caribbean is seen in Figure 1. Elevation angles as functions of time for 4 of these sites for an orbit at a mean height of about 800 nautical miles are seen in Figure 2. The durations of the corresponding tracks above an angle of about 48° are indicated in Figure 3.

Results of an analysis of orbital altitude uncertainties determined by means of geometric error propagation using range and angle data from Antigua are seen in Figure 4. A reasonably conservative value of 2 meters is assumed for the laser range uncertainty and results for various values assumed for the angle uncertainties are indicated by the several curves. Accuracies of a second of arc should be achievable with cameras of the MOTS type, for example.

An analysis of a number of cases involving various combinations of lasers and cameras is summarized in Figure 5. Assumptions underlying these analyses are listed in Table II. The other angle measure accuracies of 100" listed there were those assumed for the laser angles used in the

analyses indicated by the open circles in Figure 5. In all cases, in addition to the altimeter bias uncertainty, uncertainties in orbital, survey, and range measure parameters were also estimated. The triangle corresponds to a similar analysis of a three-laser-only case made for a much larger triangle based on stations at Antigua, Key West, and Panama. It resulted in a value of 4.1 meters, only slightly higher than that for the smaller triangle. As can be seen, a number of cases meet both the basic 4 meter requirement and the 3.5 meter figure obtained by allowing a couple of meters for uncertainties associated with the geoid.

Berbert and Loveless concluded that the 2 laser 2 camera combination was probably the most cost effective in terms of the probabilities of obtaining reasonable amounts of data.

III. THE SELECTION OF A TYPICAL GEOS-C ORBIT

The GEOS-C altimeter is expected to be of value in connection with studies of the earth's gravitational field and, if sufficient accuracy can be obtained, also in connection with studies of tides and circulation phenomena such as those associated with the Gulf Stream, for example.

A. Gravitational Field Studies

Studies of the gravitational field will also be conducted by means of the satellite-to-satellite tracking system. If one begins with the assumption of the value of 65° for the inclination of GEOS-C, and a value of 0.005 or less for the eccentricity to simplify the altimeter design, one is at liberty to adjust the mean altitude or the period within certain limits in the attempt to achieve as many of the scientific goals as possible. Altitudes within one or two hundred kilometers of, say, 900 kilometers are not unreasonable to consider here on the basis of current thinking about GEOS-C choices.

1. Satellite-to-Satellite Tracking Studies of the Gravitational Field

The gravity field experiment conducted with the satellite-to-satellite tracking system can resolve gravitational features only down to a certain size which is a function of the satellite altitude. This function has been studied by Schwartz who presents the relationship shown in Figure 6(7). On this basis, a satellite at an altitude between 900 and 1000 kilometers could resolve gravitational features about six degrees in size if it is tracked from another satellite. There is interest then in achieving a ground track spacing of approximately 6° at the equator for the purposes of the satellite-to-satellite gravitational field experiment. Such a study of the gravitational field will be of great interest intrinsically, and will provide the material for a most valuable comparison with altimeter studies of the gravitational field.

C2

2. Altimeter Studies of the Gravitational Field

The altimeter, on the other hand, is capable of finer resolution. Ultimately, a one degree survey is desirable, for example. A mean altitude of about 980 kilometers and a nodal period of about a 105 minutes permits the achieving of both of these objectives. It is characterized by equator crossing spaced about 26° apart between each revolution and separated by about 6-1/4° each day, as is indicated in Figure 7. Thus, at the end of four days, the equator crossing has moved some 25° and the tracing of the one degree pattern then begins. This takes some 25 days to complete. Since the altimeter cannot operate continuously, due to power limitations, an actual survey of this type would take much longer, on the order of a year, in fact.

Clearly other strategies are possible, e.g., by selecting patterns which would give spacings of 6°, 3°, 1.5°, etc. The example sketched here will suffice for the purposes of the present discussions, however. Resonances may be associated with some of these choices. A preliminary look at this point indicates that these will not be unduly severe, however.

With these specific choices in mind, then, one is in a position to consider the problem of short-arc tracking concretely.

B. Oceanographic Studies

The Atlantic region off the coast of the Northeastern United States is of particular interest from the standpoint of the Gulf Stream meanders as is indicated in Figure 8 which is given by Hansen (8). These features have amplitudes on the order of a meter and hence might be within the capability of an altimeter of the kind to be flown on GEOS-C, or possibly on a spacecraft of the SATS type. Tidal variations in this same region, while not quite as large as those found elsewhere, are nevertheless of considerable size, i.e., of the order of a meter also. This is indicated in Figures 9 through 11, where the certain tidal components are seen (9, 10). This region is also a reasonably attractive one from the standpoint of some of the practicalities of short-arc tracking. Good advantage could be taken of lasers usually available at Goddard, and possibly also at SAO.

An unusually useful system could be obtained by adding lasers at Bermuda and at a Canadian site chosen to be on the same meridian as Bermuda and as far north of Goddard as Goddard is north of Bermuda. This configuration is ideal for precision, short-arc tracking of GEOS-C in the region we are focusing upon. This can be seen readily from an inspection of Figures 12 & 13. Lasers having 10 centimeter accuracy capabilities will, when located at these sites, make it possible to determine the altitude of GEOS-C with relative accuracies of the order of a meter or better over a considerable portion of the region defined by these tracking sites at Goddard, Bermuda, and in Canada. A fourth laser at SAO would provide the important checks on the instrumental biases by providing the redundant information. It would also be most valuable in connection with reducing the impact of the cloud cover problem.

1. Gulf Stream Meander Studies

The altimeter tracking patterns are also good for observing the Gulf Stream meanders. Shown in Figure 13 are surface tracks of a 65° orbit with 6-1/4° daily spacing which was obtained in the earlier discussion. It is seen that the northward and southward going tracks cross the two principal branches of a typical Gulf Stream meander orthogonally, providing almost ideal geometry for studying the behavior of these interesting features. Each ground track seen in Figure 13 will be followed four days later by one removed just one degree from it, hence it will be possible to observe each feature once every four days. This frequency is well matched to the observational needs of a Gulf Stream meander experiment, as can be seen from inspection of Figures 13 and 14(8). The mean wave length of a meander is often of the order of 300 kilometers, as Figures 13 and 14 show. A typical meander moves a distance equal to its own wave length in about a couple of months. This interval might be thought of as a characteristic time constant which can be associated with the Gulf Stream meanders in this sense. Observations every four days are well suited for such an experiment. In fact observations every ten days or so would be most welcome, as Hansen has already pointed out (8). This also allows a margin for gaps in the observing program which might be due to such things as weather conditions or operational factors.

Similar studies of the Kuroshio current could be conducted by means of lasers similarly placed in Japan and nearby islands such as Iwo Jima.

2. Tidal Studies

Tidal studies can also be conducted in this region by means of short-arc tracking. Once each day the GEOS-C altimeter satellite ground track passes through or very close to the Goddard-Bermuda-Canada triangle as is indicated in Figures 13 and 15. At least one of the tracks of the type seen in Figure 15, for example, would occur each day. These tracks are nearly orthogonal to the co-range lines of the semi-diurnal tide as can also be seen from Figure 15. The orbit selected for GEOS-C in the above discussion has the property of moving about 10.5 degrees each day relative to the moon. A complete cycle of the semi-diurnal lunar tide is thus observed by GEOS-C about once every 17 days. The daily observations of GEOS-C in the Goddard-Bermuda-Canada triangle thus occur about 10.5° apart in this cycle, and hence provide ideal data for sampling this important tidal component.

C. Earth Dynamics Studies

The Goddard-Bermuda-Canada triangle also has other uses in connection with the Earth Dynamics side of the Earth and Ocean Dynamic Satellite Applications program (1).

1. Polar Motion and UT 1

The Bermuda-Canada leg is suitable for observing polar motion in the manner of the experiment conducted by Smith (11). The Goddard-Bermuda and Goddard-Canada links taken together are also useful for a companion experiment to observe the variations of the earth's rotational rate.

2. Gravitational Field Fine Structure

Fine structure in the gravity field should also be deducible from the observations made in this general area, but perhaps somewhat away from the immediate neighborhood of the Gulf Stream meanders.

IV. LONG-ARC TRACKING

The surveys of the gravitational field over longer arcs will be greatly facilitated by the long-arc satellite-to-satellite tracking of GEOS-C which can be conducted through ATS-F. The accuracy capability of this tracking approach is indicated in Figure 16. In the case looked at here, accuracies of some four meters or better persisted for almost three hours beyond the time interval shown in the Figure before the results deteriorated. It is seen that altitude accuracies in the 3 to 4 meter range can be achieved in this way. This is reasonably comparable to the current estimates of the accuracy of the world-wide geoid obtained from satellite orbit analyses (12). The latter have spatial resolution of the order of 12°, however. Hence, altimeter and satellite-to-satellite tracking surveys even at the 6° resolution level will definitely provide new information. They will of course also provide the extremely valuable independent views which are so important. Satellite-to-satellite tracking may also be useful when combined with precision laser tracking in the Goddard-Bermuda-Canada triangle in making observations in the neighborhood of the amphidromic point in the North Atlantic seen in Figures 9 and 10. Such a region could be a good one in which to make the cross-over point checks which have been proposed by Stanley (13).

V. THE GEOPAUSE SATELLITE SYSTEM CONCEPT

From the long range point of view the aim is to study sea surface topography at the decimeter level (1, 16). Difficulties in the current state of the art associated with lack of sufficient knowledge of the gravity field prevent this at the present time. The Geopause satellite concept offers the promise of being able to contribute here in connection with the main problem of satellite oceanography, i.e., that of observing the height of the ocean surface relative to the geoid at sub-meter accuracy levels (4). The Geopause spacecraft is conceived of as being in a polar, nearly circular orbit at a distance of about 4.6 earth radii and having a period of about 14 hours in an orbit plane which is both polar and normal to the ecliptic. (Cf. Figure 17.) At this height uncertainties in only a few gravitational harmonic terms correspond to orbit perturbation amplitudes above the decimeter level. The tracking data coverage afforded by the Geopause orbit is ideal for doing the three things necessary for dealing with the orbit determination problem at the decimeter level, i.e., solving

for those remaining environmental parameters which are effective and observable at this level, solving for tracking station locations, and monitoring tracking system biases on a continuing basis. (Cf. Figure 18.) Estimates indicate that the Geopause, tracked by two-centimeter ranging systems from ten selected NASA-affiliated sites for a week, could yield locations of these stations and of the Geopause satellite altitude with decimeter accuracy.

1. Earth Dynamics Experiments

This furnishes the basis for high-resolution polar motion and UT 1 studies and advanced fault motion experiments.

2. Oceanographic Experiments

Tracking from two Geopause satellites separated by a quarter of a revolution to an altimeter spacecraft in a coplanar low-altitude orbit should furnish the basic data for finding two components of the altimeter's position in the Geopause orbit plane with accuracies approaching a decimeter. From these two components one can determine any other two components including, in particular, the radial distance component. (Cf. Figure 19.) This is obtained relative to the coordinate system defined by the Geopause system, and hence relative to the earth's center. Decimeter altimeter data of the type which is anticipated will then give the position of the ocean surface relative to the altimeter spacecraft at this accuracy level. The position of the geoid is determined independently through information gotten from the tracking between Geopause and a coplanar, low-altitude gravity field satellite by means of a range rate system having 0.03 millimeters per second accuracy. (Cf. Figure 20.) A survey of the gravitational field can be completed by this approach in about a couple of months using a drag-free satellite orbiting at an altitude of about 250 km. This will furnish the basic information for determining the position of the geoid at decimeter accuracy with 2.5° spatial resolution. Thus one has, independently, the positions of the geoid and of the ocean surface to submeter accuracies, from which the heights of the ocean surface above the geoid follow directly. A whole new range of oceanographic experiments will thus be opened up. For example, the surface heights just mentioned will provide the basic boundary condition data for use in unlocking problems associated with the general circulation of the oceans. Detailed studies of currents, tides, storm surges, and tsunamis will also then become feasible.

VI. REFERENCES

1. "Earth and Ocean Dynamics Satellite Applications Program," NASA, Washington, D. C., April 1, 1971 (Preliminary Issue).

2. Siry, Joseph W., "Proposed Earth Physics and Geodesy Programs Including an ATS-GEOS Tracking and Orbit Determination Experiment" letter to NASA Headquarters, J. Naugle and J. Rosenberg with enclosure, August 27, 1969.

3. Felsentreger, T. L., Grenchik, T. J., and Schmid, P. E., "Geodetic Earth Orbiting Satellite (GEOS-C)-Applications Technology Satellite (ATS-F) Tracking Experiment," GSFC X-552-70-96, March 1970.

4. Siry, Joseph W., "A Geopause Satellite System Concept," Presented at the Symposium on the Use of Artificial Satellites for Geodesy of the American Geophysical Union Annual Meeting, Washington, D. C., April 15-17, 1971.

5. Berbert, John H., and Loveless, Fred M., "A Satellite Altimeter Bias Recovery Simulation," GSFC X-550-71-224, May, 1971.

6. Stanley, H. Ray, Private Communication.

7. Schwarz, Charles R., "Gravity Field Refinement by Satellite to Satellite Doppler Tracking," Department of Geodetic Science Report No. 147, Ohio State University Research Foundation, December, 1970.

8. Hansen, Donald V., "Gulf Stream Meanders Between Cape Hatteras and the Grand Banks" Deep-Sea Research and Oceanographic Abstracts, 17, 495-511, 1970.

9. Hendershott, Myrl, and Munk, Walter, "Tides," Annual Review of Fluid Mechanics, 2, 205-224, 1970.

10. Defant, Albert, "Physical Oceanography" Volume II, Macmillan, New York, 1961.

11. Smith, D. E. , these proceedings.

VI. REFERENCES (continued)

12. Gaposchkin, E. M., and Lambeck, K., 1969 Smithsonian Standard Earth (II), SAO Special Report 315, May 18, 1970.

13. Stanley, H. Ray, Private Communication.

14. Vonbun, F. O., "The ATS-F/Nimbus-E Tracking Experiment," Presented at the 48th IAU Symposium, May 9-15, 1971, Morioka, Japan

15. Vonbun, F. O., "Geodetic Satellite Mission and GEOS-C Spacecraft" Space Research XI, Academy Verlag, Berlin 1971, 457-467.

16. NASA, "The Terrestrial Environment: Solid Earth and Ocean Physics" Prepared by MIT for NASA, ERC, April, 1970.

17. Vonbun, F. O., these proceedings.

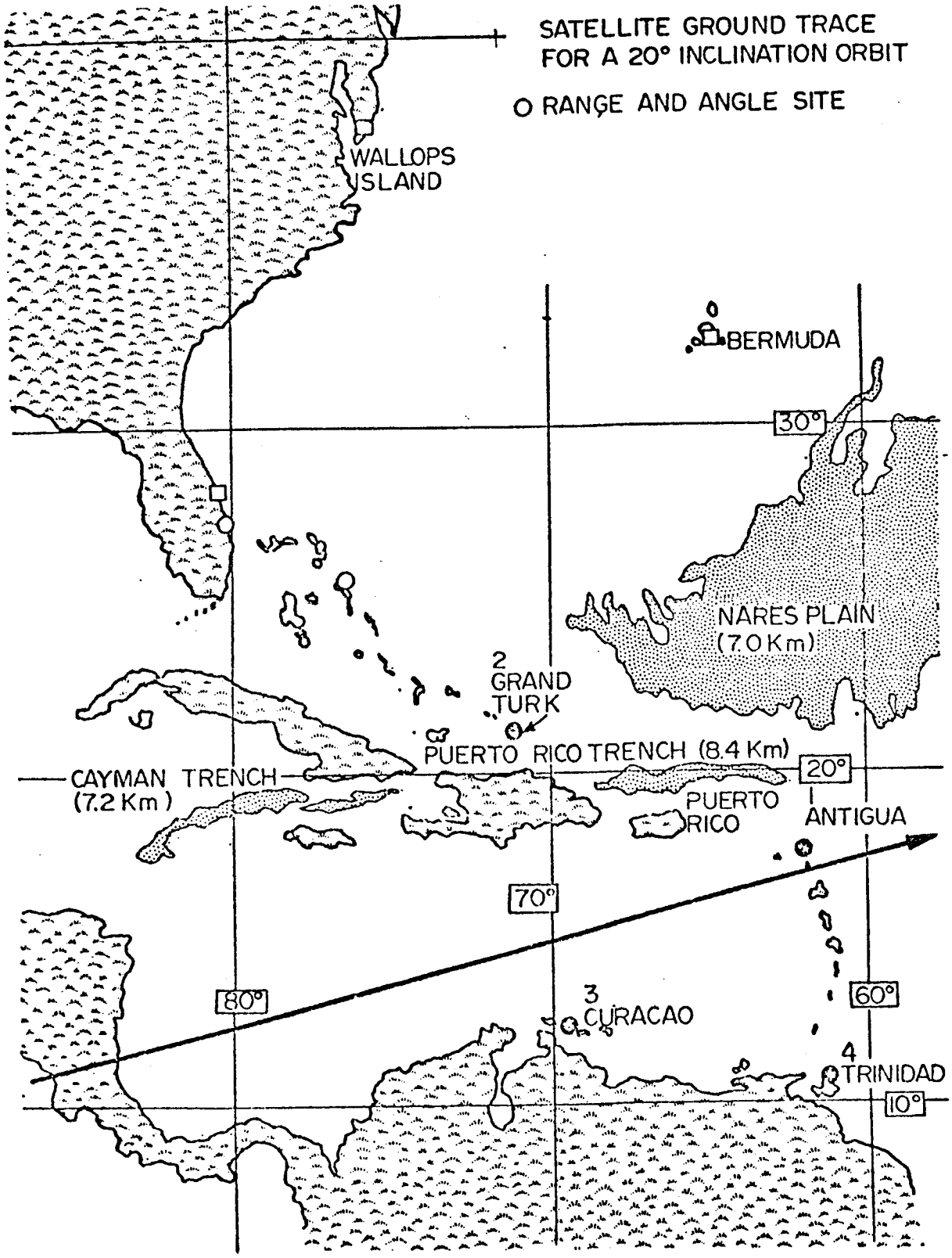
SATELLITE GROUND TRACE
FOR A 20° INCLINATION ORBIT
O RANGE AND ANGLE SITE
WALLOPS
ISLAND
BERMUDA
30°
NARES PLAIN
(7.0 Km)
2
GRAND
TURK
PUERTO RICO TRENCH (8.4 Km)
CAYMAN TRENCH
(7.2 Km)
20°
PUERTO
RICO
ANTIGUA
70°
80°
3
CURACAO
60°
4
TRINIDAD
10°

Figure 1

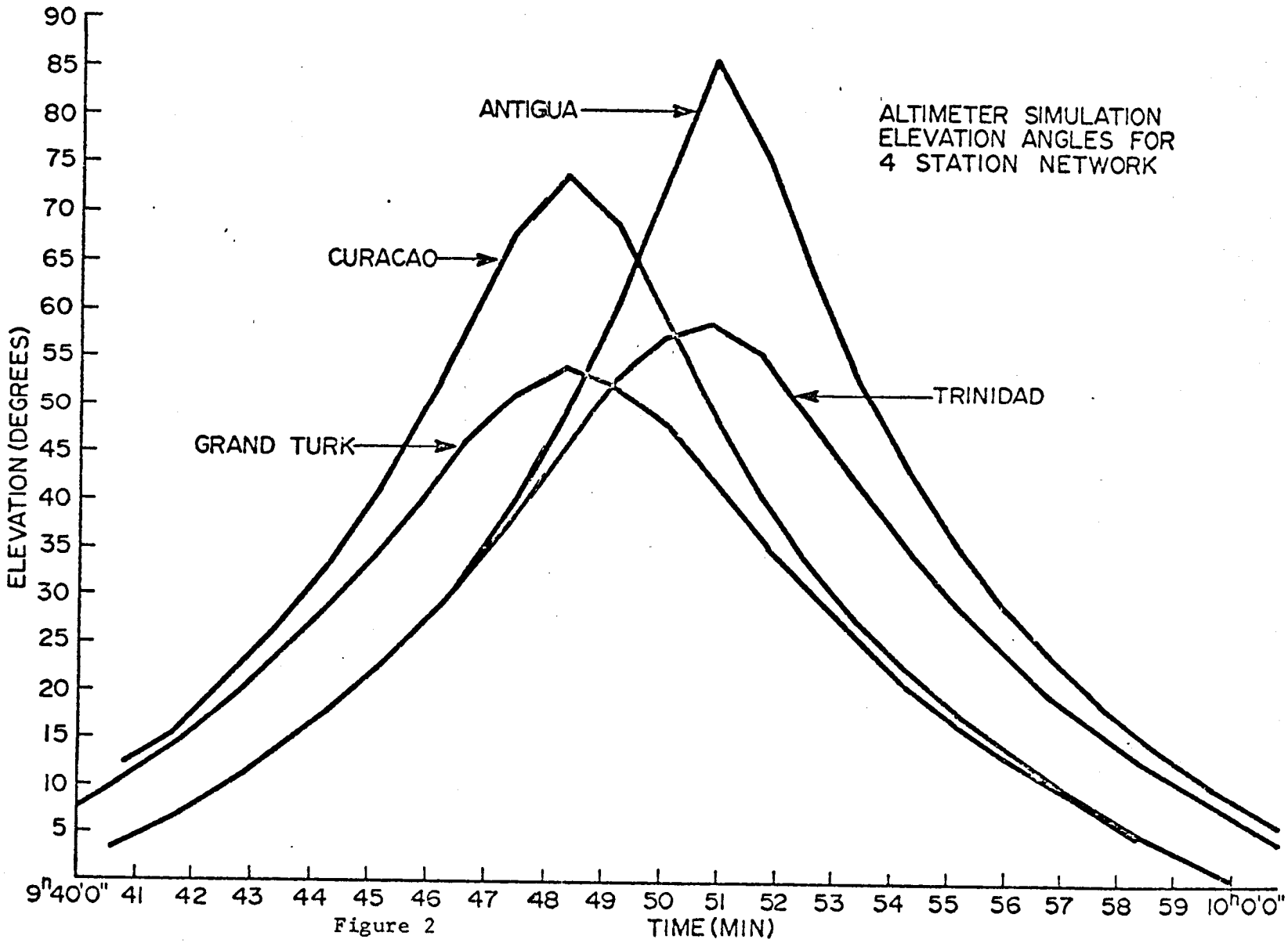
ALTIMETER SIMULATION
ELEVATION ANGLES FOR
4 STATION NETWORK
ANTIGUA
CURACAO
GRAND TURK
TRINIDAD
ELEVATION (DEGREES)
90
85
80
75
70
65
60
55
50
45
40
35
30
25
20
15
10
5
9h40'0"
41
42
43
44
45
46
47
48
49
50
51
52
53
54
55
56
57
58
59
10h0'0"
TIME (MIN)

Figure 2

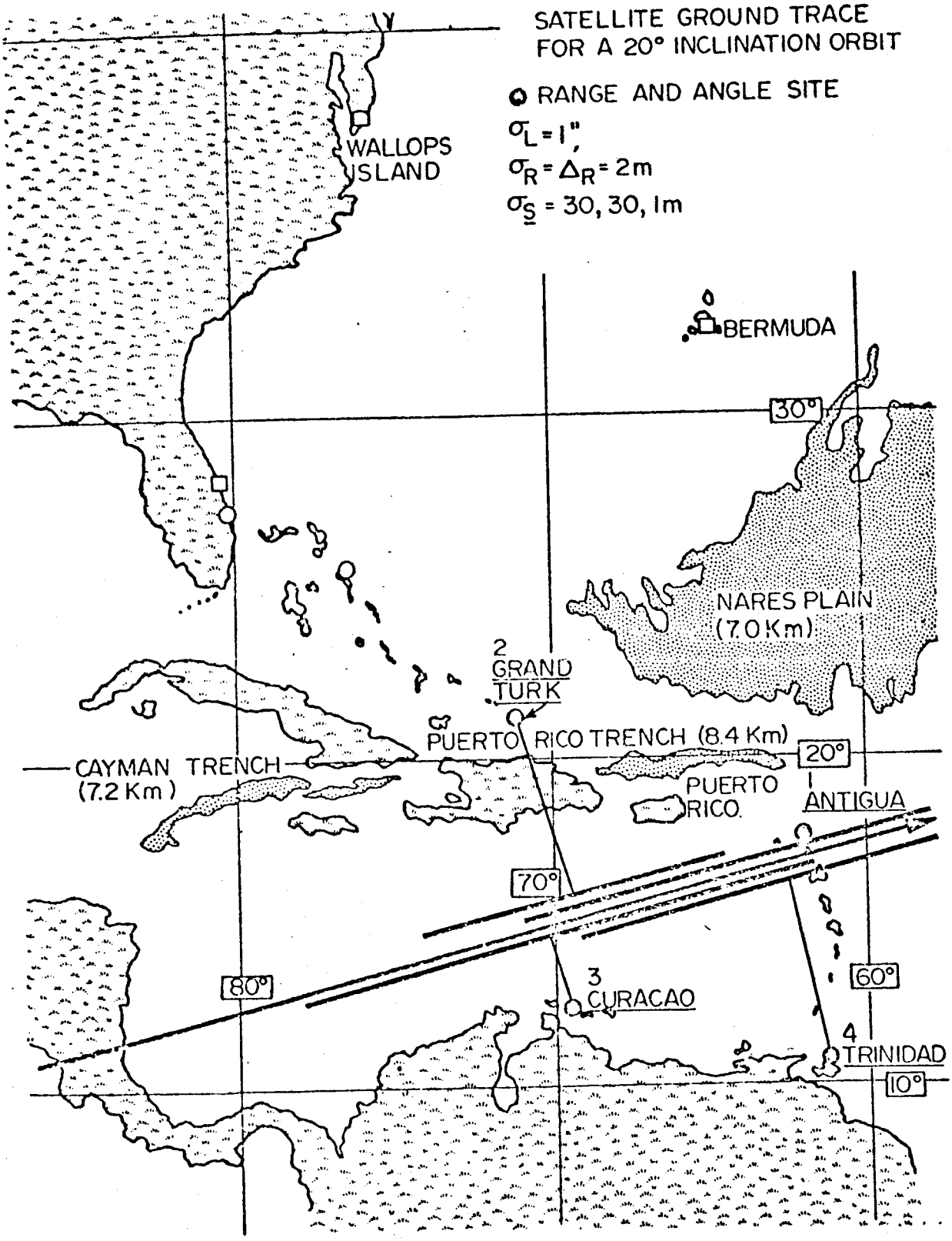
SATELLITE GROUND TRACE
FOR A 20° INCLINATION ORBIT
RANGE AND ANGLE SITE
$\sigma_L = 1''$,
$\sigma_R = \Delta_R = 2m$
$\sigma_{\underline{S}} = 30, 30, 1m$
WALLOPS ISLAND
BERMUDA
30°
NARES PLAIN (7.0 Km)
2 GRAND TURK
PUERTO RICO TRENCH (8.4 Km)
CAYMAN TRENCH (7.2 Km)
20°
PUERTO RICO
ANTIGUA
70°
80°
3 CURACAO
60°
4 TRINIDAD
10°

Figure 3

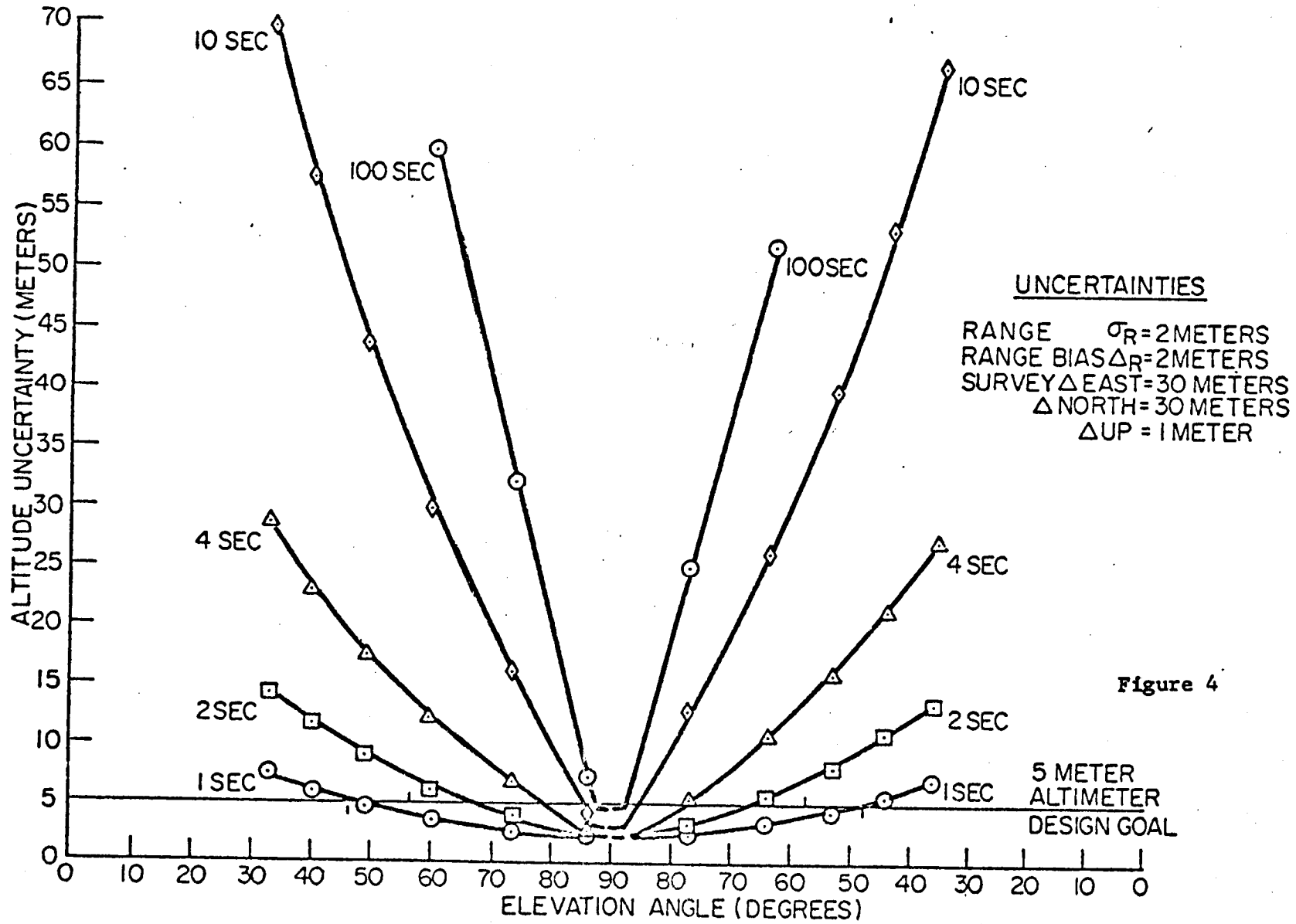
ALTITUDE UNCERTAINTY (METERS)
70
65
60
55
50
45
40
35
30
25
20
15
10
5
0
10 SEC
100 SEC
100SEC
10 SEC
4 SEC
4 SEC
2SEC
2 SEC
1 SEC
1SEC
5 METER
ALTIMETER
DESIGN GOAL
UNCERTAINTIES
RANGE σ_R = 2METERS
RANGE BIAS Δ_R = 2METERS
SURVEY Δ EAST = 30 METERS
Δ NORTH = 30 METERS
Δ UP = 1 METER
0 10 20 30 40 50 60 70 80 90 80 70 60 50 40 30 20 10 0
ELEVATION ANGLE (DEGREES)

Figure 4

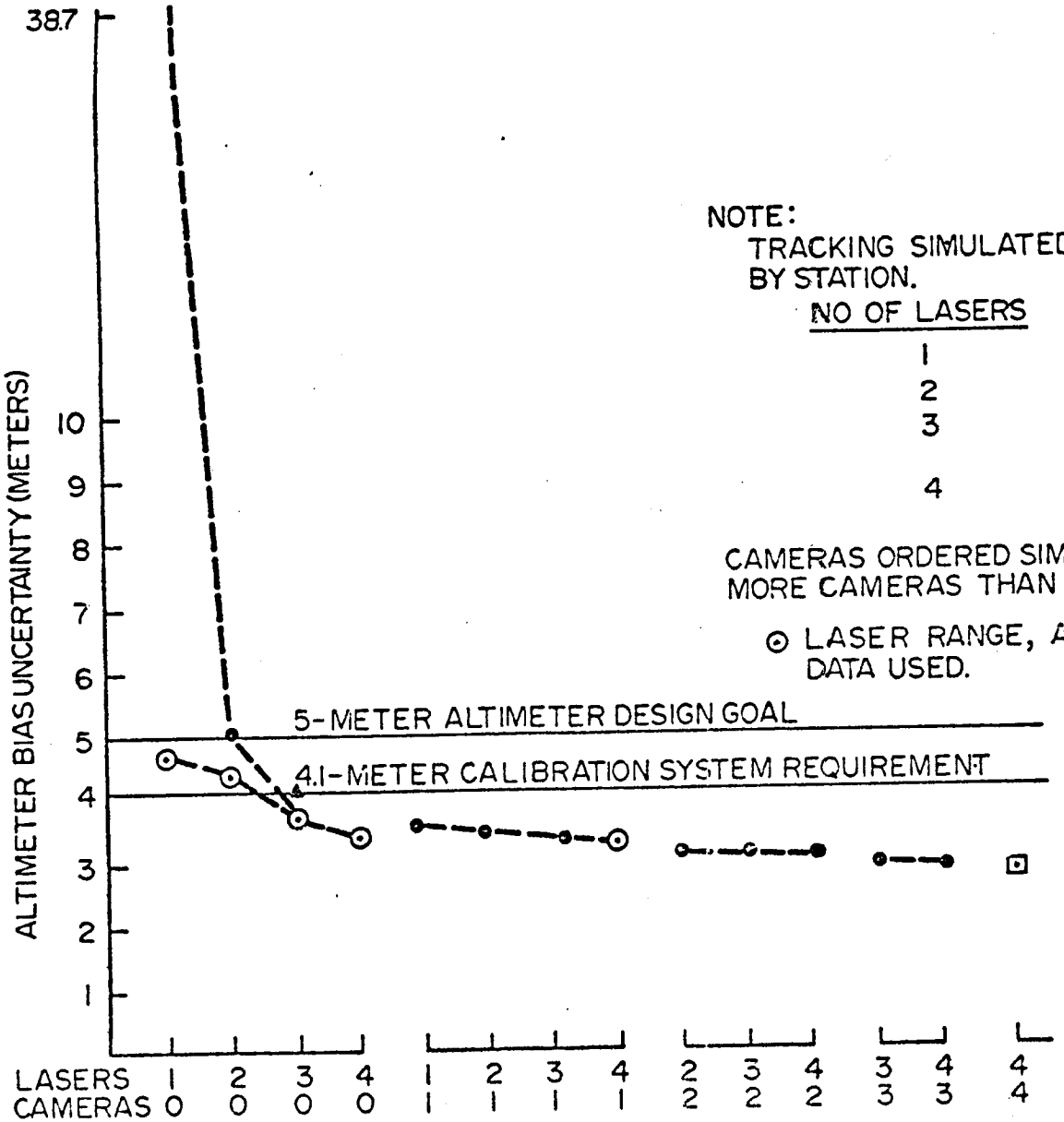

NOTE:
TRACKING SIMULATED FOR LASERS WAS ORDERED BY STATION.

NO OF LASERS	STATIONS
1	ANTIGUA
2	ANTIGUA, GRAND TURK
3	ANTIGUA, GRAND TURK, CURACAO
4	ANTIGUA, GRAND TURK, CURACAO, TRINIDAD

CAMERAS ORDERED SIMILARLY. THERE WERE NEVER MORE CAMERAS THAN LASERS.

⊙ LASER RANGE, AZIMUTH & ELEVATION ANGLE DATA USED.

▲ ANTIGUA, KEY WEST, PANAMA

Figure 5

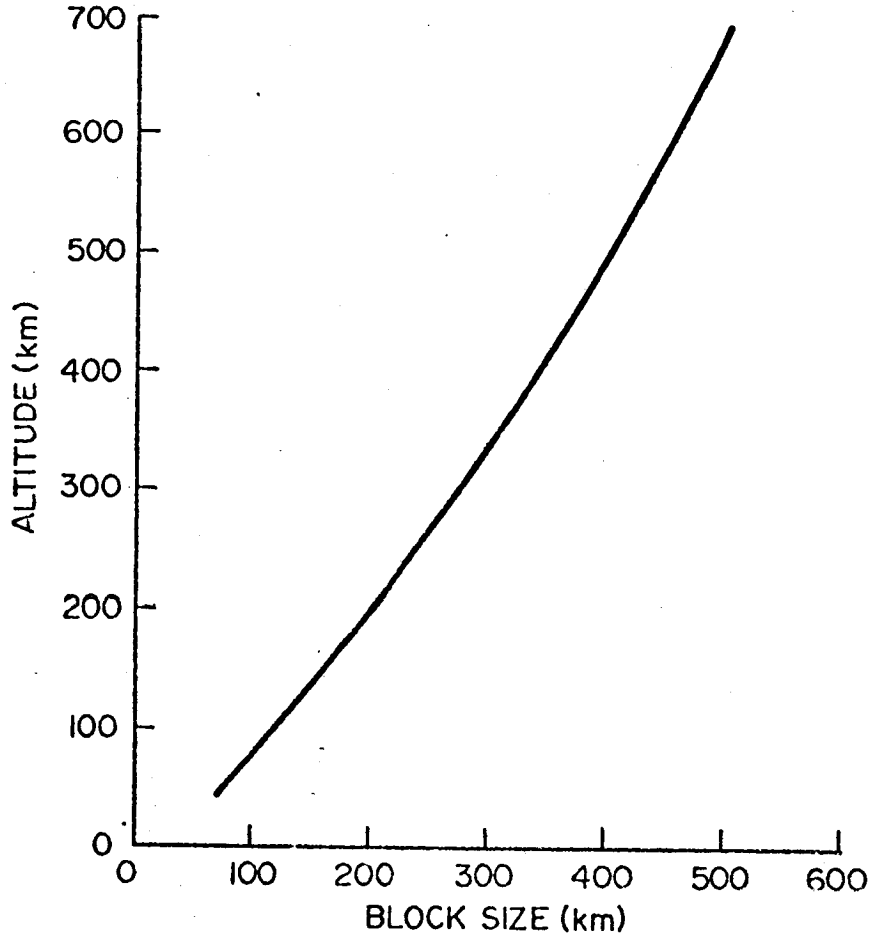
700
600
500
400
300
200
100
0
ALTITUDE (km)
0
100
200
300
400
500
600
BLOCK SIZE (km)

Figure 6

EQUATOR CROSSING PATTERN
FOR A TYPICAL GEOS-C ORBIT
h_m = 980 km. P = 105 min.
i = 65° e = 0.005

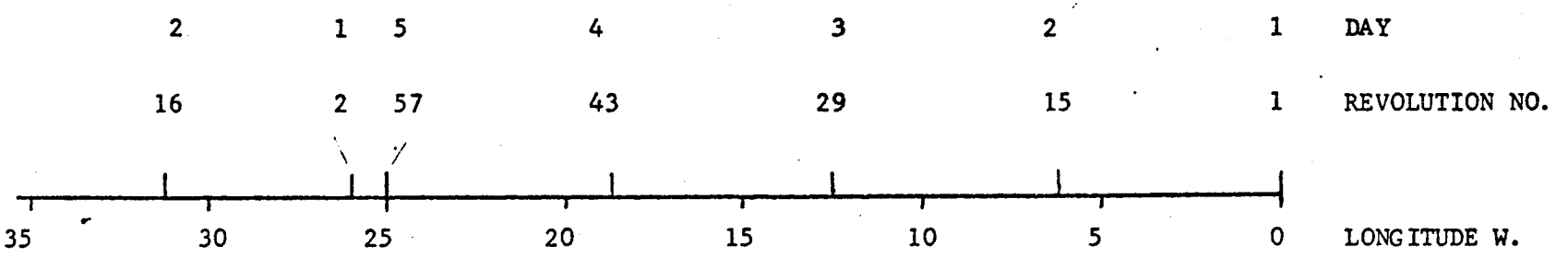

Figure 7

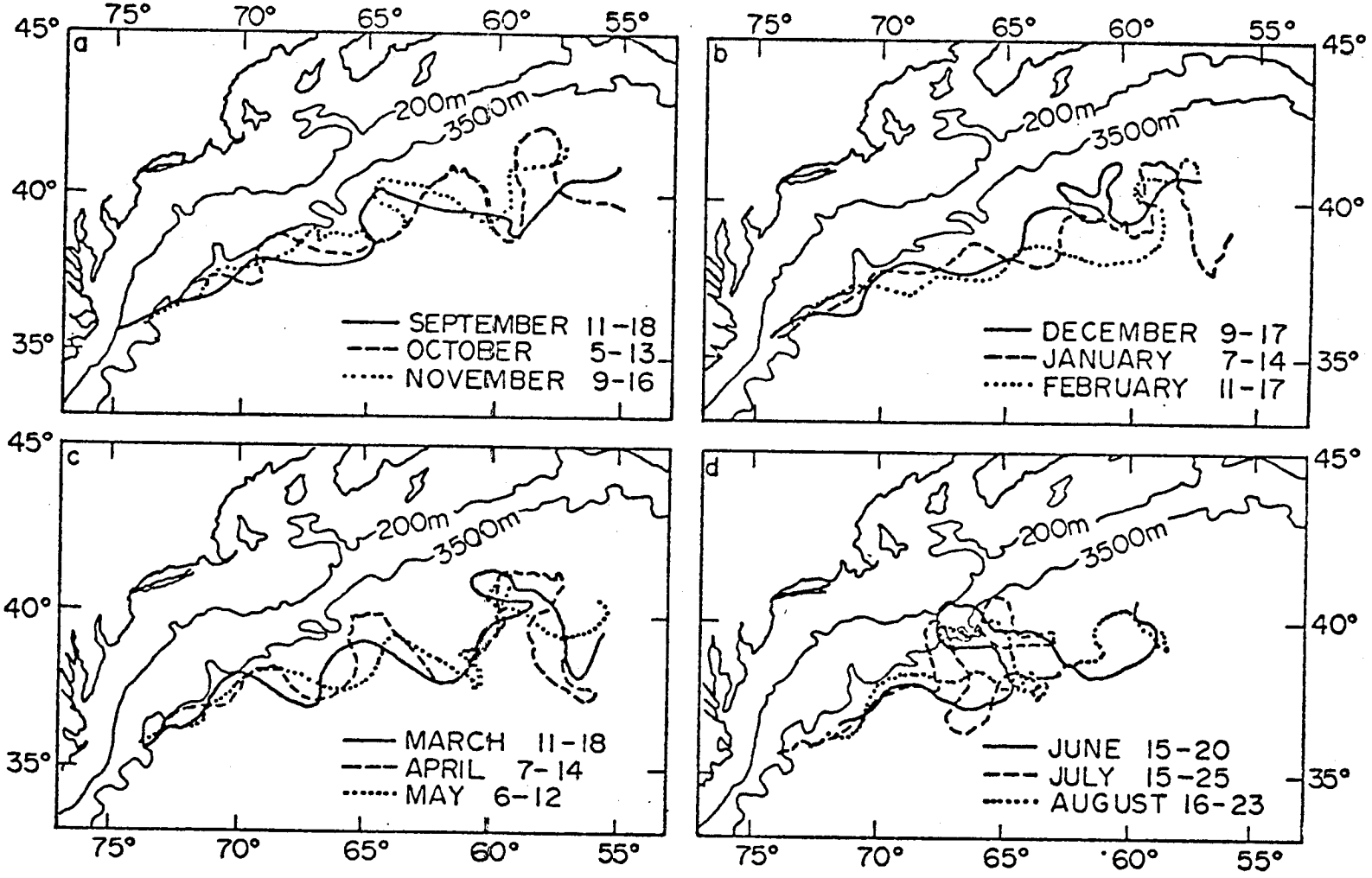
a
75°
70°
65°
60°
55°
45°
40°
35°
200m
3500m
SEPTEMBER 11-18
OCTOBER 5-13
NOVEMBER 9-16
b
DECEMBER 9-17
JANUARY 7-14
FEBRUARY 11-17
c
MARCH 11-18
APRIL 7-14
MAY 6-12
d
JUNE 15-20
JULY 15-25
AUGUST 16-23

Figure 8

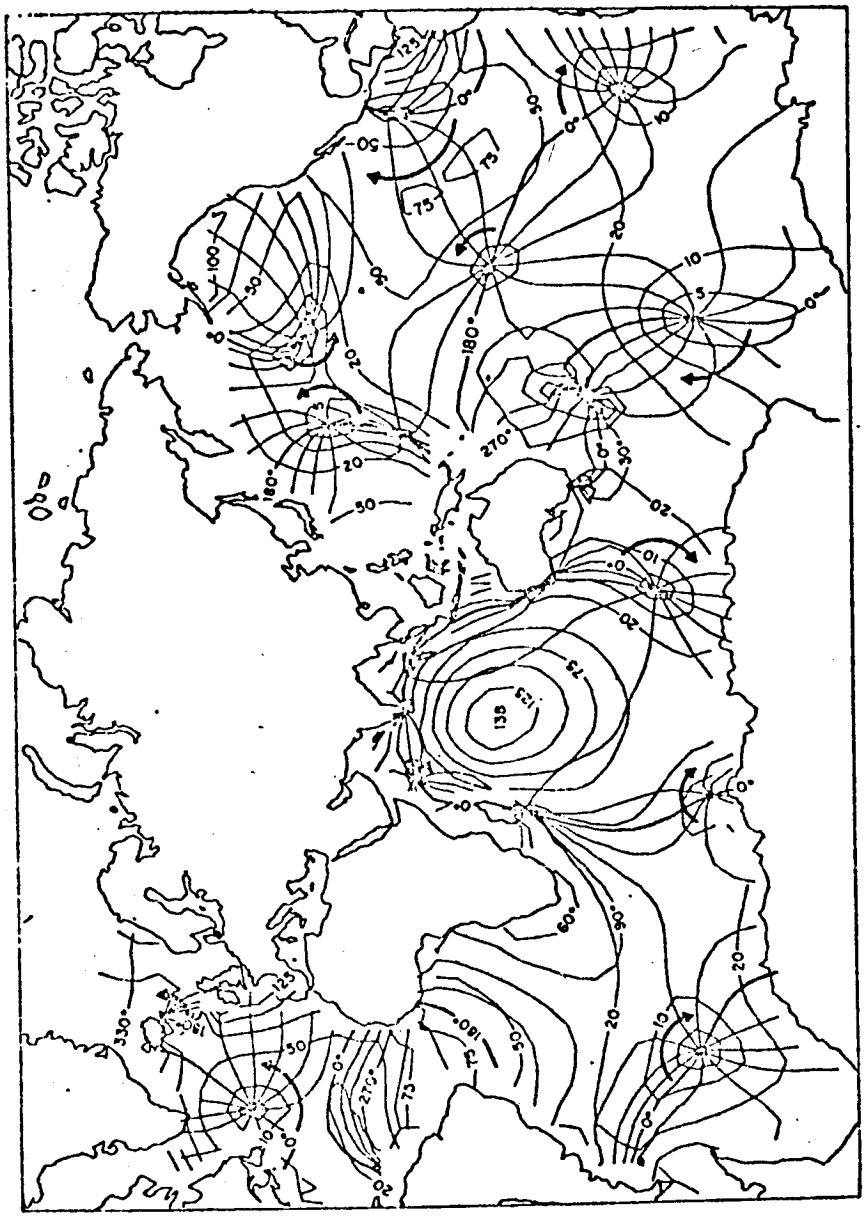

Figure 9

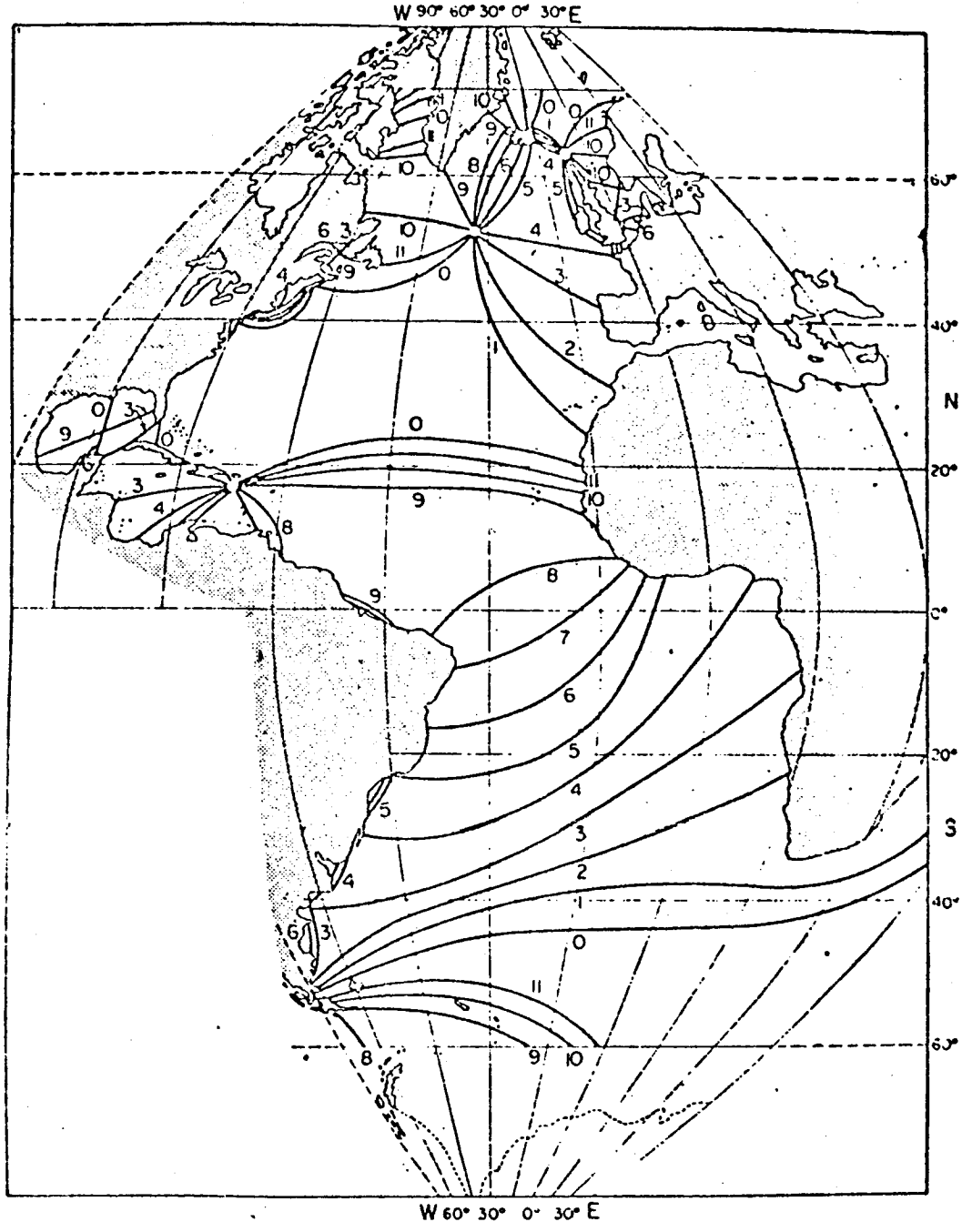

Figure 10
7-19

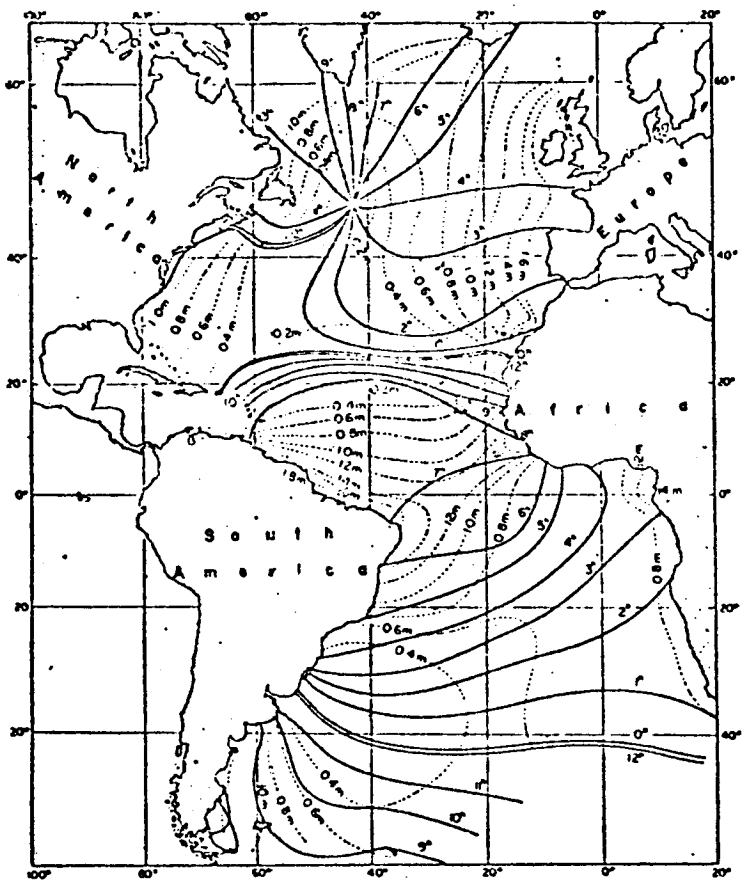

Theoretical tides of Atlantic Ocean. Full lines: co-tidal lines referred to moon-transition through meridian of Grw., dashed lines: co-range lines of the semi-diurnal tide M_2 in m (according to Hansen).

Figure 11

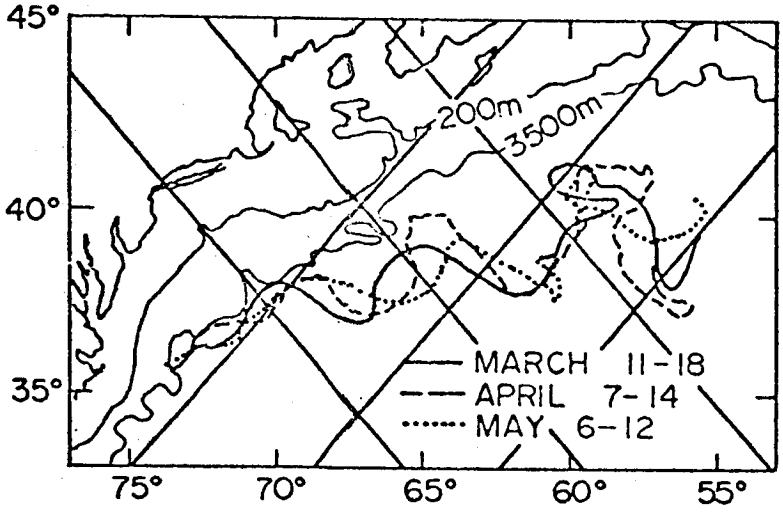

Figure 12

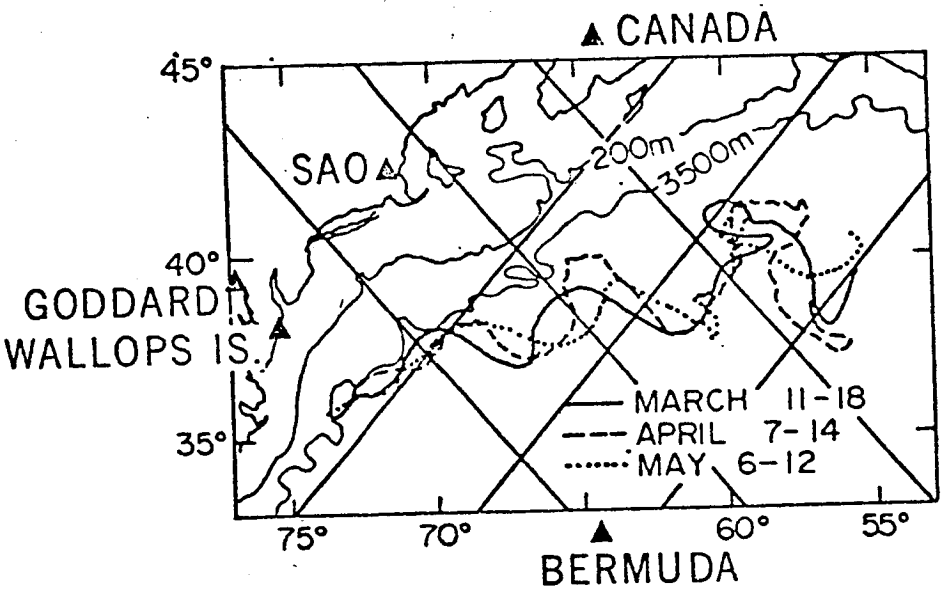
CANADA
45°
SAO
200m
3500m
40°
GODDARD
WALLOPS IS.
35°
MARCH 11-18
APRIL 7-14
MAY 6-12
75°
70°
60°
55°
BERMUDA

Figure 13

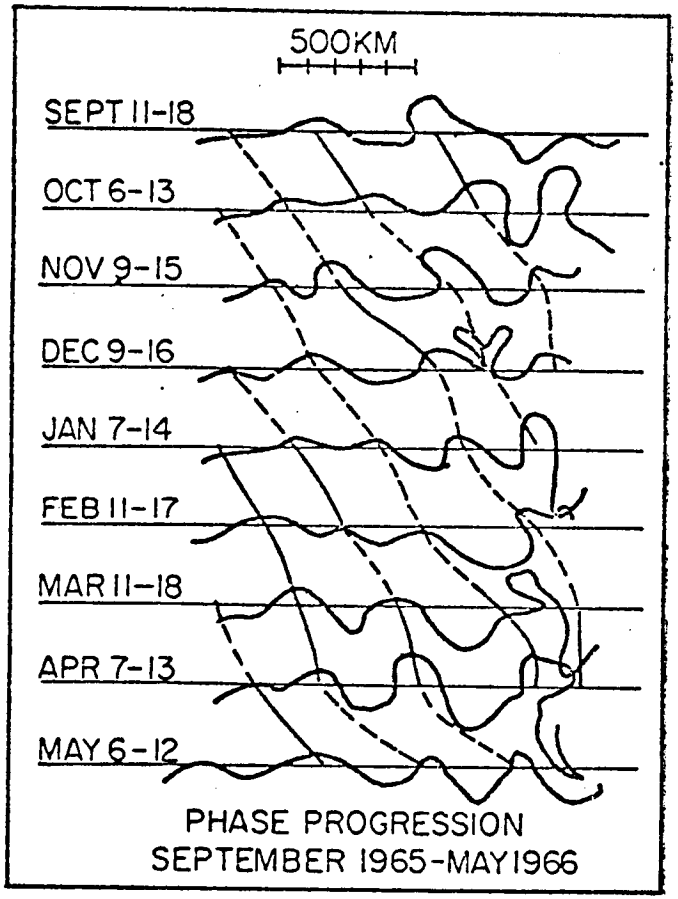
500KM
SEPT 11-18
OCT 6-13
NOV 9-15
DEC 9-16
JAN 7-14
FEB 11-17
MAR 11-18
APR 7-13
MAY 6-12
PHASE PROGRESSION
SEPTEMBER 1965-MAY 1966

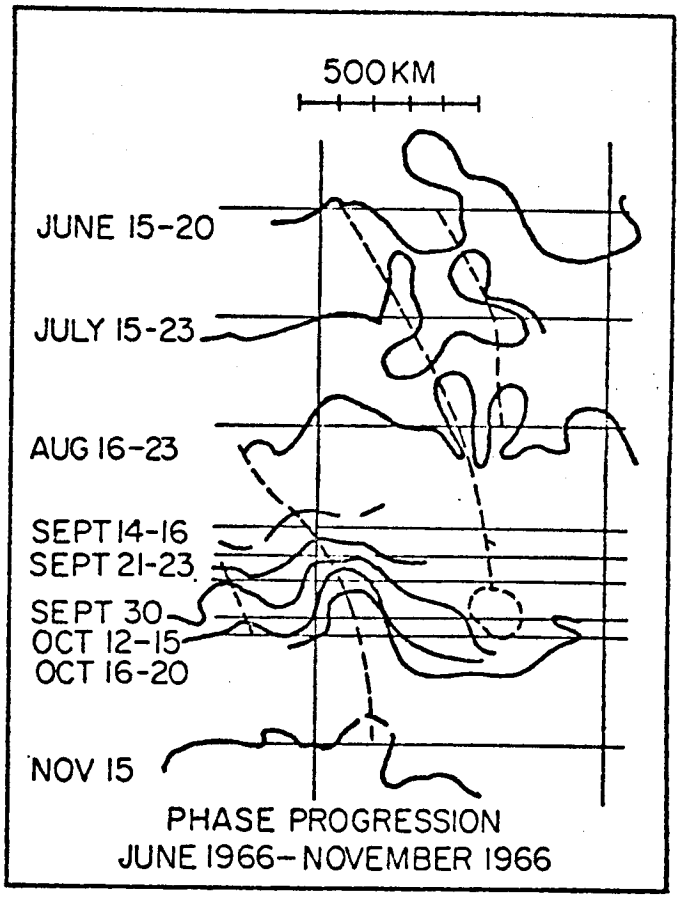
500KM
JUNE 15-20
JULY 15-23
AUG 16-23
SEPT 14-16
SEPT 21-23
SEPT 30
OCT 12-15
OCT 16-20
NOV 15
PHASE PROGRESSION
JUNE 1966-NOVEMBER 1966

Figure 14

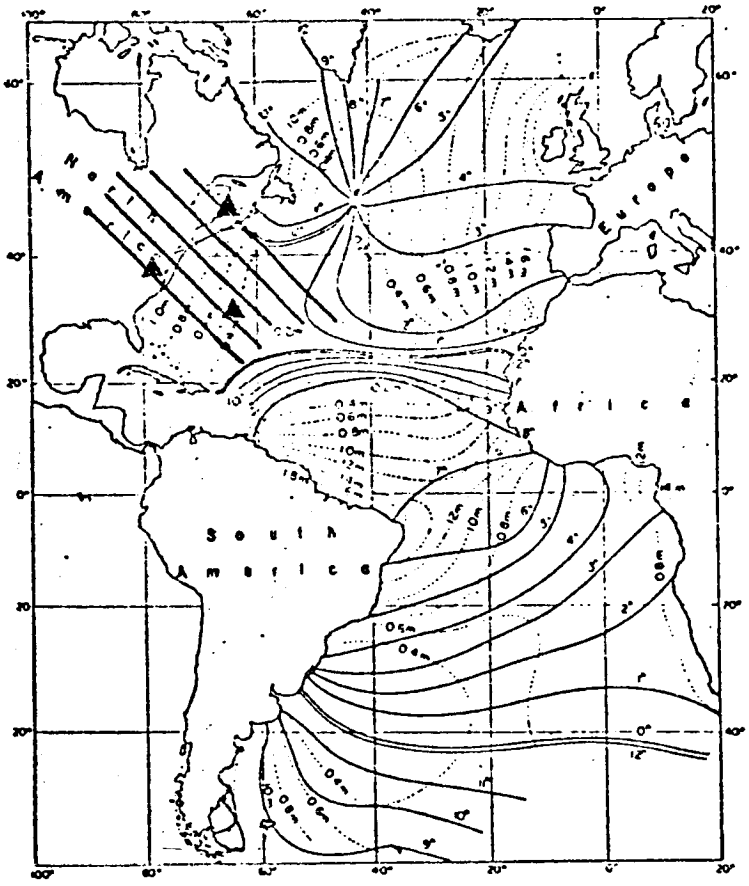

Theoretical tides of Atlantic Ocean. Full lines: co-tidal lines referred to moon-transition through meridian of Grw., dashed lines: co-range lines of the semi-diurnal tide M_2 in m (according to Hansen).

Figure 15

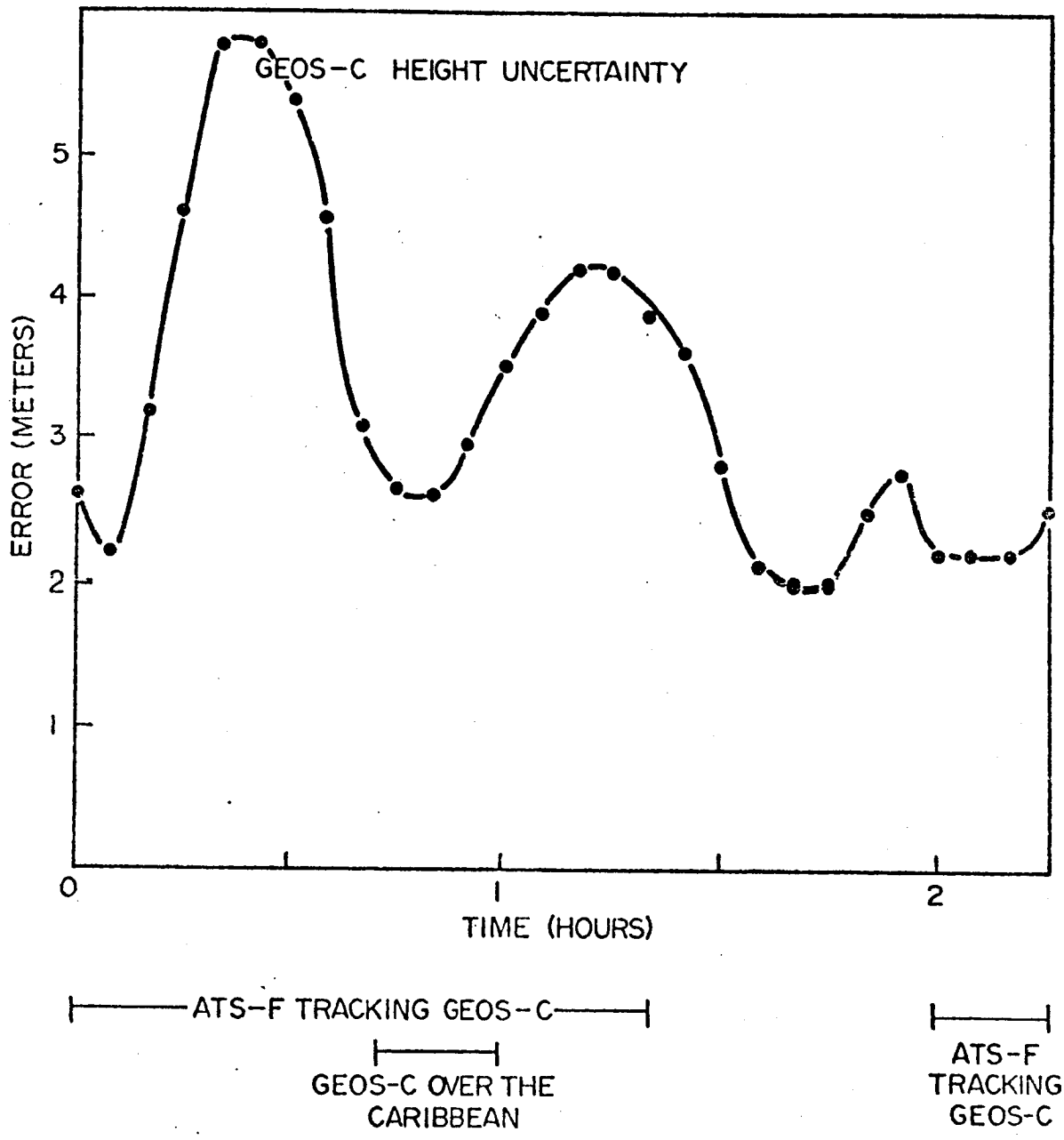
GEOS-C HEIGHT UNCERTAINTY
ERROR (METERS)
5
4
3
2
1
0
1
2
TIME (HOURS)
ATS-F TRACKING GEOS-C
GEOS-C OVER THE CARIBBEAN
ATS-F TRACKING GEOS-C

Figure 16

A GEOPAUSE SATELLITE SYSTEM CONCEPT
THE GEOPAUSE SATELLITE ORBIT

- PERIOD ~ 14 HOURS, A ~ 4.6 EARTH RADII
- POLAR, NORMAL TO ECLIPTIC
- NEARLY CIRCULAR
- FEW GRAVITY TERM UNCERTAINTIES CORRESPOND TO PERTURBATIONS OVER A DECIMETER
- IN THIS SENSE, THE ORBIT IS NEAR THE GEOPOTENTIAL BOUNDARY, i.e., THE GEOPAUSE

Figure 17

GEOPAUSE SUBSATELLITE TRACKS DURING ONE WEEK

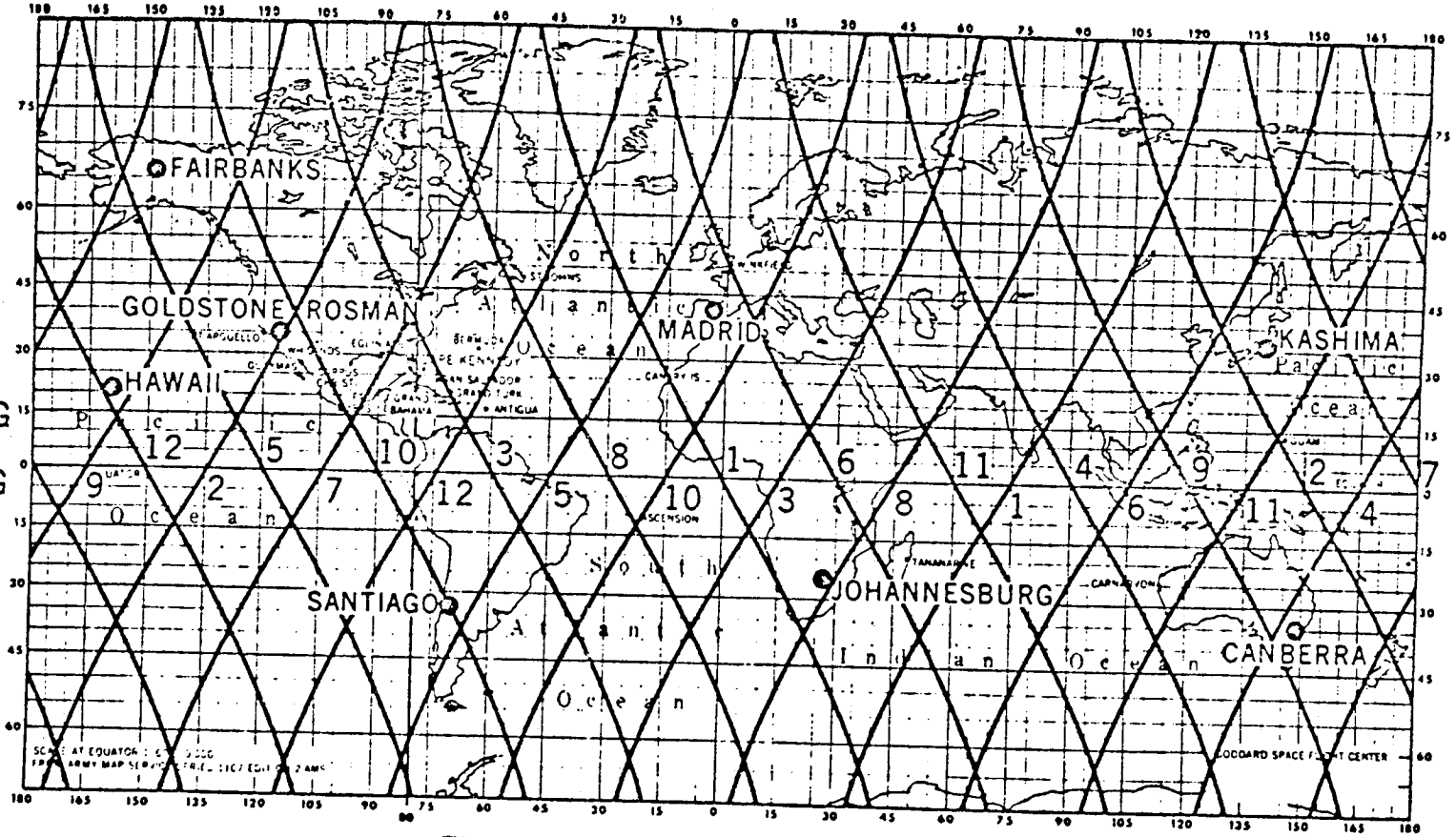

Figure 18

GEOPAUSE
DRAG FREE & ALTIMETER SPACECRAFT
SATELLITE-TO-SATELLITE TRACKING

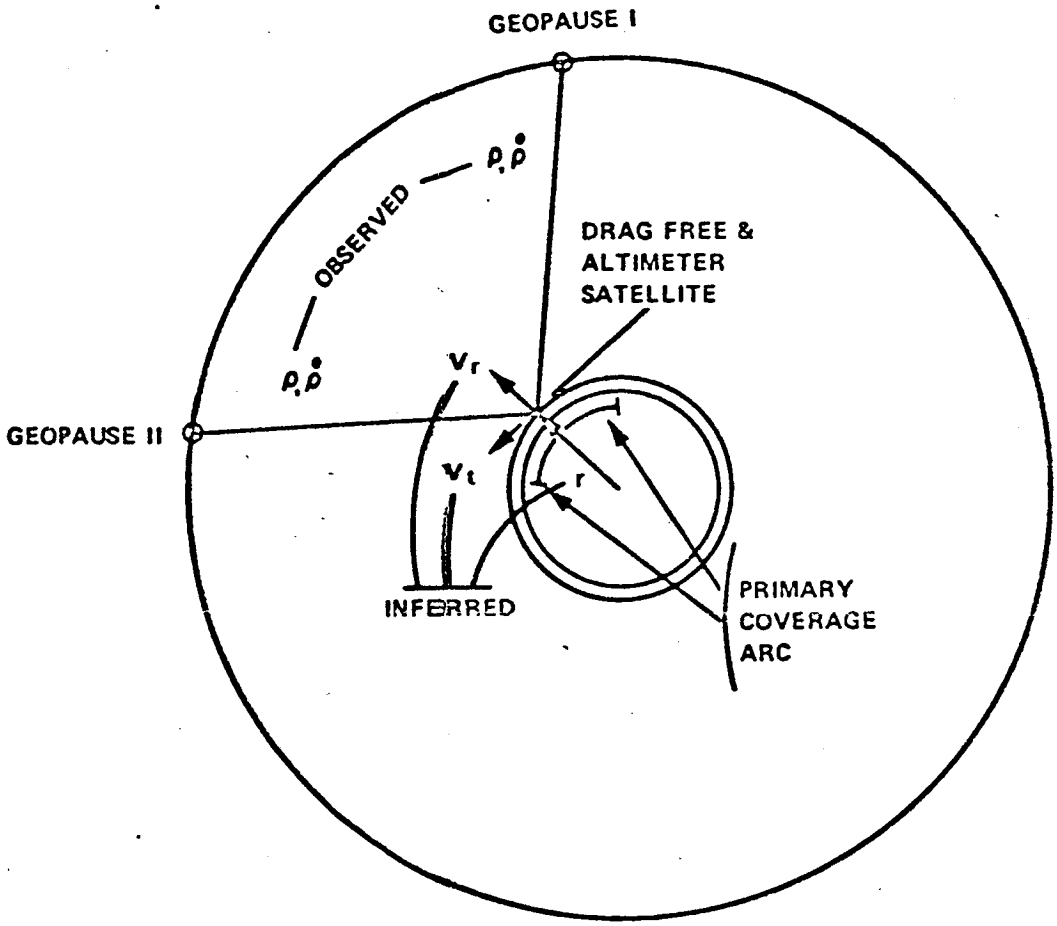

PRIMARY COVERAGE ARC MOVES ABOUT 24° LONGITUDE
AND 40° IN LATITUDE EACH REVOLUTION

Figure 19

A GEOPAUSE SATELLITE SYSTEM CONCEPT

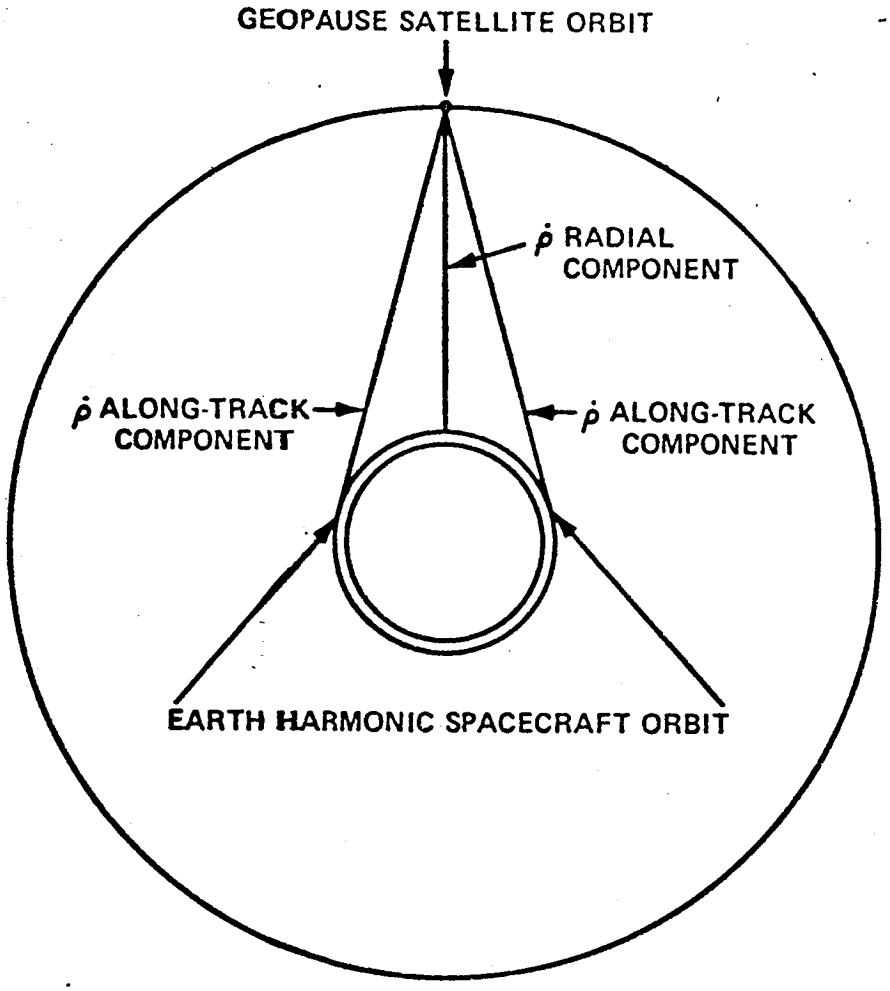

SATELLITE-TO-SATELLITE RANGE RATE TRACKING GEOMETRY FOR VARIOUS RELATIVE POSITIONS OF THE GEOPAUSE AND COPLANAR EARTH HARMONIC SPACECRAFT

Figure 20

Table I

GEOS-C Mission Altimeter Evaluation

Satellite Altimeter System Measurement Error Source	Error (m)
Altimeter Instrumentation	2
Refraction	0.2
Reflection from Waves	0.5
Spacecraft Attitude	2
Root Sum Square	2.9
Calibration Error Allocation	4.1
Altimeter System Evaluation Goal	5

Table II

GEOS-C Mission Altimeter Evaluation Analysis

Assumptions	A Priori Uncertainties	Noise rms
Recovered Quantities		
Range Measures	2 m	2 m
Altimeter Height Measures	100 m	10 m
Orbit – R&V Components	1 km, 1 km/sec	
Station Positions – E, N, V Components	30, 30, 1 m	
Other Quantities		
Camera Angle Measures		1"
Other Angle Measures		100"

DESIGN CONSIDERATIONS FOR A SPACE-BORNE OCEAN SURFACE LASER ALTIMETER

8

Henry H. Plotkin
NASA Goddard Space Flight Center

Introduction

The desirable features of pulsed lasers as components of a satellite tracking system were recognized very soon after their initial development (Fig. 1). After design of some tentative systems, NASA launched the Beacon-Explorer B in 1964, containing fuzed silica retroreflectors especially for laser tracking. Several stations were soon ranging successfully, with precision generally about 2 meters. Other satellites were soon launched, so that there are now seven earth-orbiting arrays of laser retroreflectors (Fig. 2). The four arrays on the lunar surface are also used for the same purpose.

Precision and accuracy of present laser ranging systems are in the neighborhood of 25 cm. The systems now being built with state-of-the-art components are expected to achieve 10 cm or even better. Such techniques, applied to earth satellites have great value in geodesy and earth physics studies. Our task here is to examine how we might turn the system around: with the ranging system in the spacecraft, to reflect pulses vertically from the ocean surface, and so measure spacecraft altitude with great precision. For each such measurement, we assume the spacecraft position is known well enough so that the result will be a precise map of the shape of the ocean surface. This could be studied under varying tidal, seasonal, ocean current, and wind conditions.

Many of the features of a laser satellite ranging system are similar to those of an ocean surface altimeter. On the other hand, the altimeter also presents new problems. Some preliminary designs have already been suggested (see Ref. 1, 2, 3). A laser altimeter with considerably less sensitivity and resolution than we require was successfully flown on Apollo 15 to provide metric information for lunar photographs (Ref. 4) (Fig. 3) (Appendix A).

DESIRABLE FEATURES OF PULSED LASERS FOR SATELLITE TRACKING

- VERY SHORT PULSES
- HIGH POWER
- GOOD COLLIMATION WITH SMALL ANTENNAS
- S/C REFLECTORS ARE INEXPENSIVE, PASSIVE, LONG-LIVED
- SENSITIVE RECEIVERS, INTERNAL GAIN
- WIDEBAND RECEIVING SYSTEM
- STABLE CALIBRATION IN RANGE AND ANGLE
- POSSIBLE PHOTOGRAPHIC RECORD VS. STARS

FIGURE 1

RETROREFLECTORS IN SPACE

EARTH SATELLITES

Oct 1964	BE-B	GSFC
Apr 1965	BE-C	GSFC
Nov 1965	GEOS-I	GSFC
Feb 1967	DI-C	French
Feb 1967	DI-D	French
Jan 1968	GEOS-II	GSFC
Dec 1970	PEOLE	French

LUNAR REFLECTORS

Apollo 11	USA
Apollo 14	USA
Lunachod	USSR
Apollo 15	USA

FIGURE 2

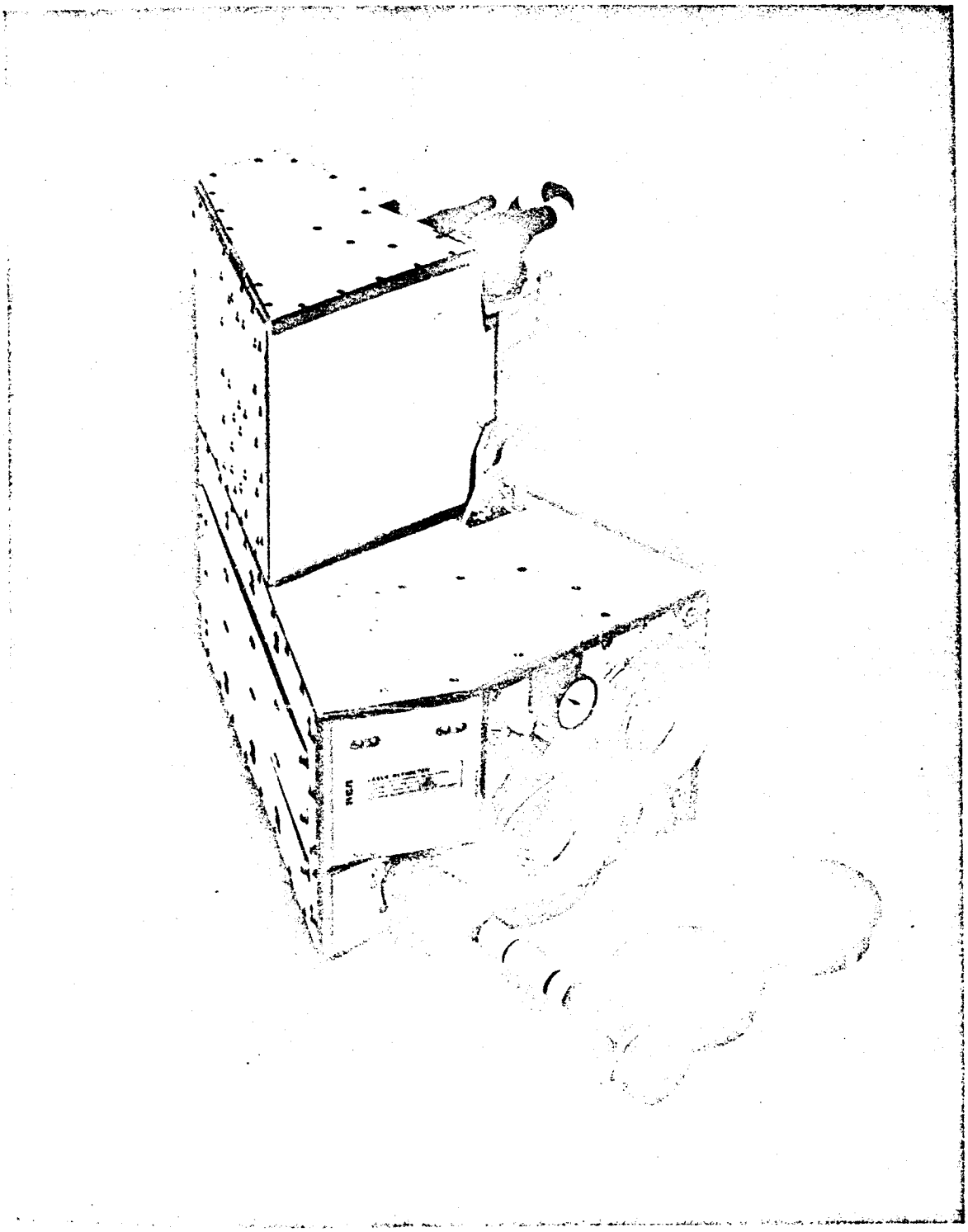

FIGURE 3

We shall review the principles and performance experience of the laser satellite ranging systems developed and operated at GSFC and then extrapolate them to possible space-borne altimetry systems. We shall not describe a definitive design, but merely present a representative list of parameters which may serve as a basis for discussing alternative approaches.

Laser Satellite Ranging Systems

The retroreflector array on BE-B and BE-C is shown in Figure 4. Each reflector is made of fuzed silica in the shape of a cube corner with a silvered coating on the three perpendicular reflecting faces. The property of the cube corner reflector (see, e.g. Ref. 5, 6) is that a ray entering the front face makes three reflections and returns in the same direction from which it was incident. This property is independent of the orientation of the cube corner except that the effective area of the entrance aperture will decrease rapidly as the angle between the incident ray and the symmetry axis increases. The Beacon-Explorer Satellites were oriented along the earth's magnetic field, and could spin about that direction. In order to insure that a sufficient number of reflectors would have a favorable aspect with respect to a ground station (in the northern hemisphere), the reflectors were arrayed over a truncated pyramid on the north-seeking end of the satellite. A similar arrangement was necessary on the French Diamont Satellites, which were also magnetically oriented. On the other hand, the GEOS Satellites are oriented by the earth's gravity-gradient, and so one face always points down. On these, the laser reflectors are arranged in a plane on the face directed to the earth.

The arrangement of the reflectors is significant here, because not only does it determine how the reflected signal intensity will vary over a satellite pass, but it also determines, indirectly, the precision with which we will be able to measure range. A sharp pulse incident on the satellite will be reflected as a pulse spread over the various distances to each of the individual reflectors. Since BE-B and BE-C are .5 meters in diameter and GEOS-I and II are 1 meter in diameter, typical signal pulse widths due to reflector array geometry correspond to range uncertainties between 20 and 50 cm.

Figure 5 is a picture of the experimental laser satellite tracking station at the Goddard Space Flight Center. It uses an altitude-azimuth mount adapted from a surplus Nike-Ajax radar. Five optical telescopes are seen on the central elevation ring, but only two are actually used for the laser ranging function. The small telescope

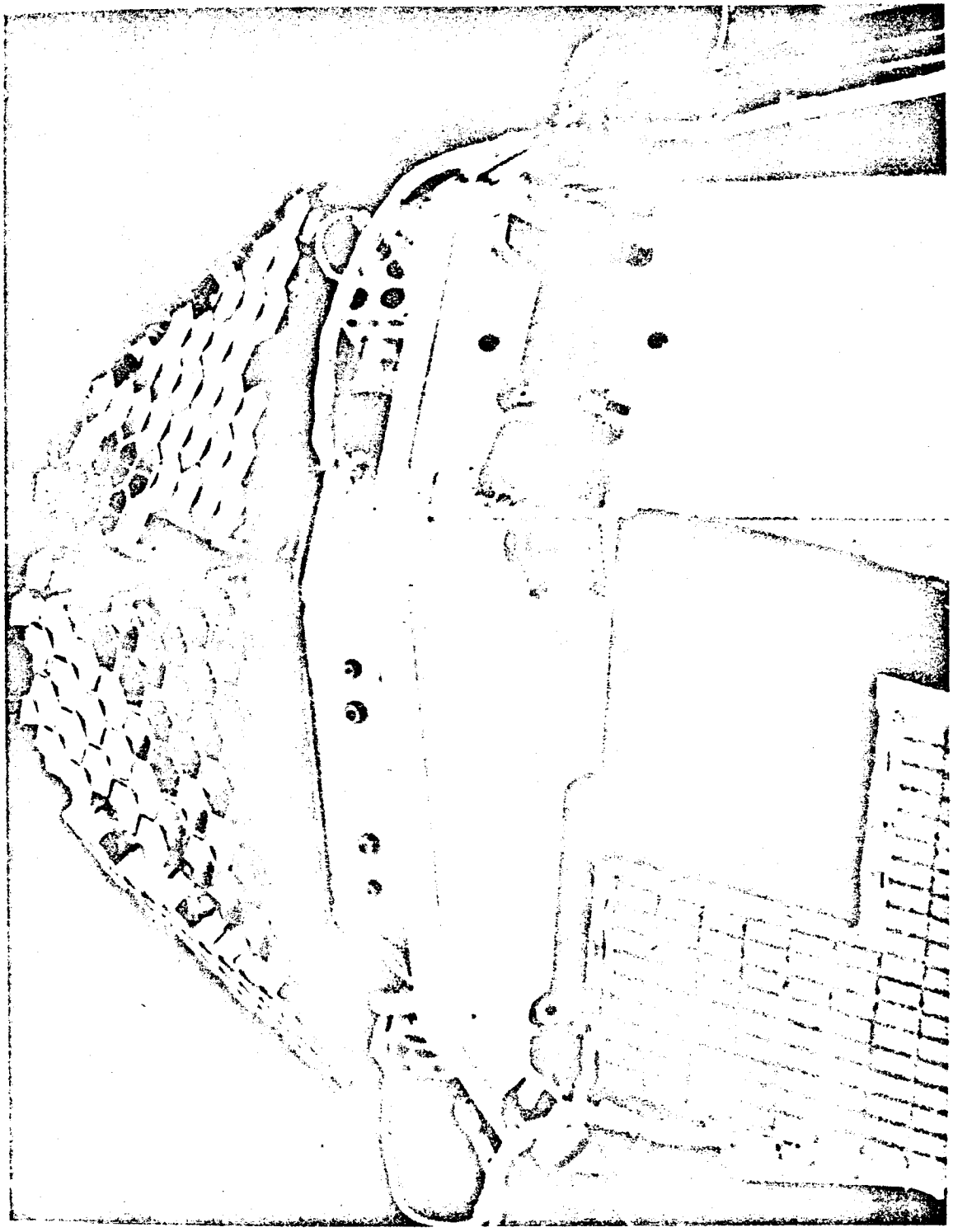

FIGURE 4

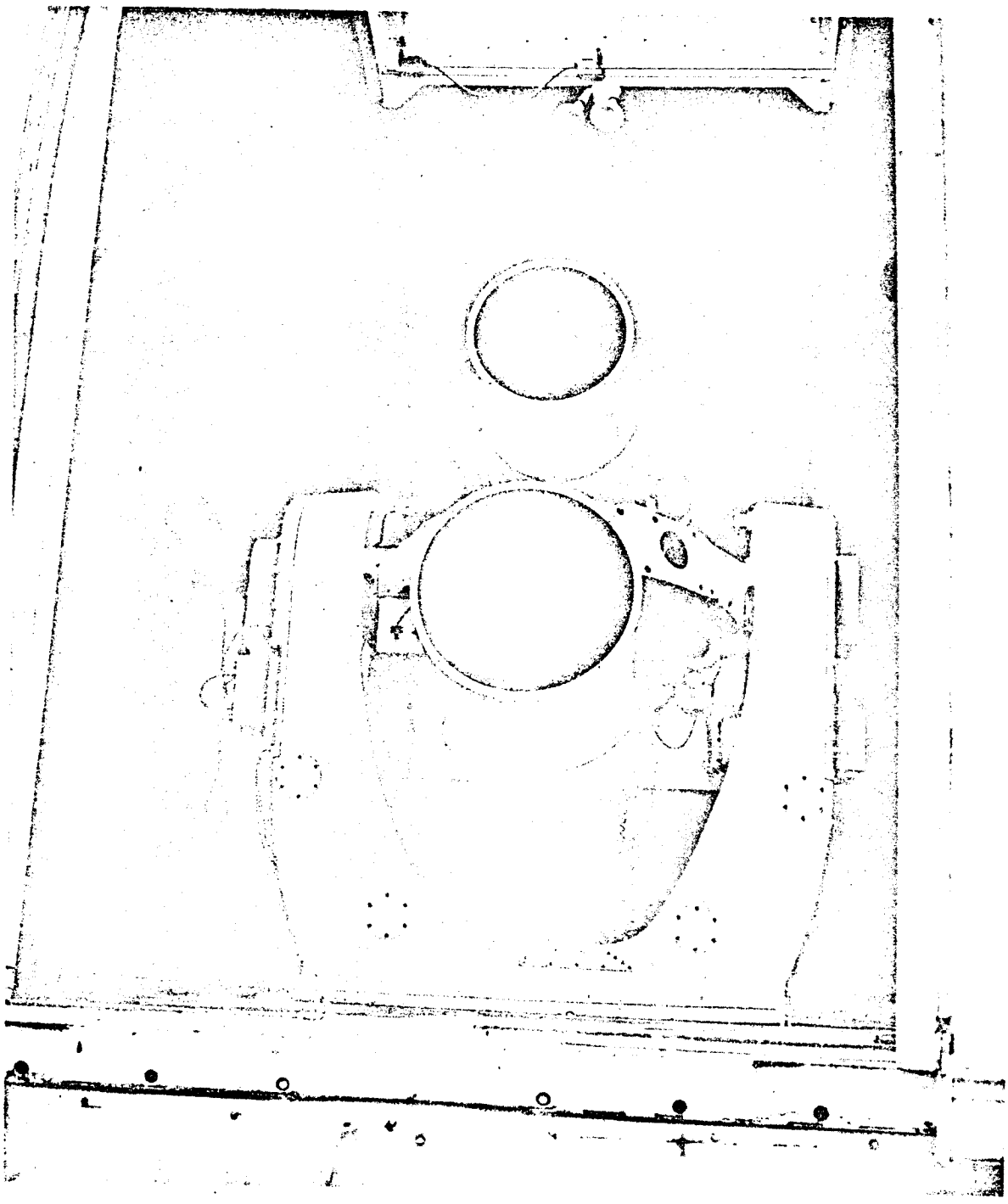

NASA G-71- 965

FIGURE 5

at the left end of the elevation axis is a low power telescope used for rough setting during boresighting. Above the ring, on the left is the laser collimating telescope (5" aperture); top center is the reflecting telescope (16" aperture) normally used as receiver in the ranging system; top right is a high power telescope used occasionally by an operator to provide manual correction to the pointing of the system if the satellite target is visible; bottom center is a reflecting telescope (20" aperture) used experimentally during NASA's program to improve the techniques of laser tracking; bottom right is a star tracker used sometimes to lock the system onto a bright object for alignment.

A mobile laser tracking system developed and operated by GSFC is shown in Figure 6. It differs from the fixed station described above in that the laser itself is not mounted on the moving telescope platform, but is placed below the platform. The laser beam is reflected from five plane mirrors and moves through the moving axis before finally passing through the collimating telescope shown on the left side of the elevation platform. This has the advantage that cooling fluid hoses and power cables need not be made flexible to move during a satellite pass, and the laser can operate in a fixed position. The disadvantage is that we suffer losses during the additional reflections. The central telescope (16" aperture) is the receiving antenna, and the telescope at the right is used by an operator, as shown, to help aim the system when the target is visible. The electronics and control system is housed in an instrumentation van and the opto-mechanical system is carried on a trailer bed when being moved.

Operation of the system is controlled by a central computer, Figure 7. From the elements of the expected orbit, the computer generates the angle coordinates which are used to operate the mount servo control system. The laser is fired once per second, the beam passing through the collimating optics, which supplies the required antenna gain. The transmitter power is sampled and recorded, and used to start the "range time interval unit". When the echo pulse is received its intensity is also recorded and it is used to stop the range counter, which has a resolution of 0.1 nanosecond. The receiving detector is gated "on" only for a short interval at a time predicted by the central computer, so as to minimize the possibility that the range counter would be stopped by a noise pulse. The block diagram also shows an ability to generate angle tracking corrections, which is now being installed. Finally, for each pulse, we record time of the measurement, time of flight, energy of the transmitted and received pulses, and the aximuth and elevation angles.

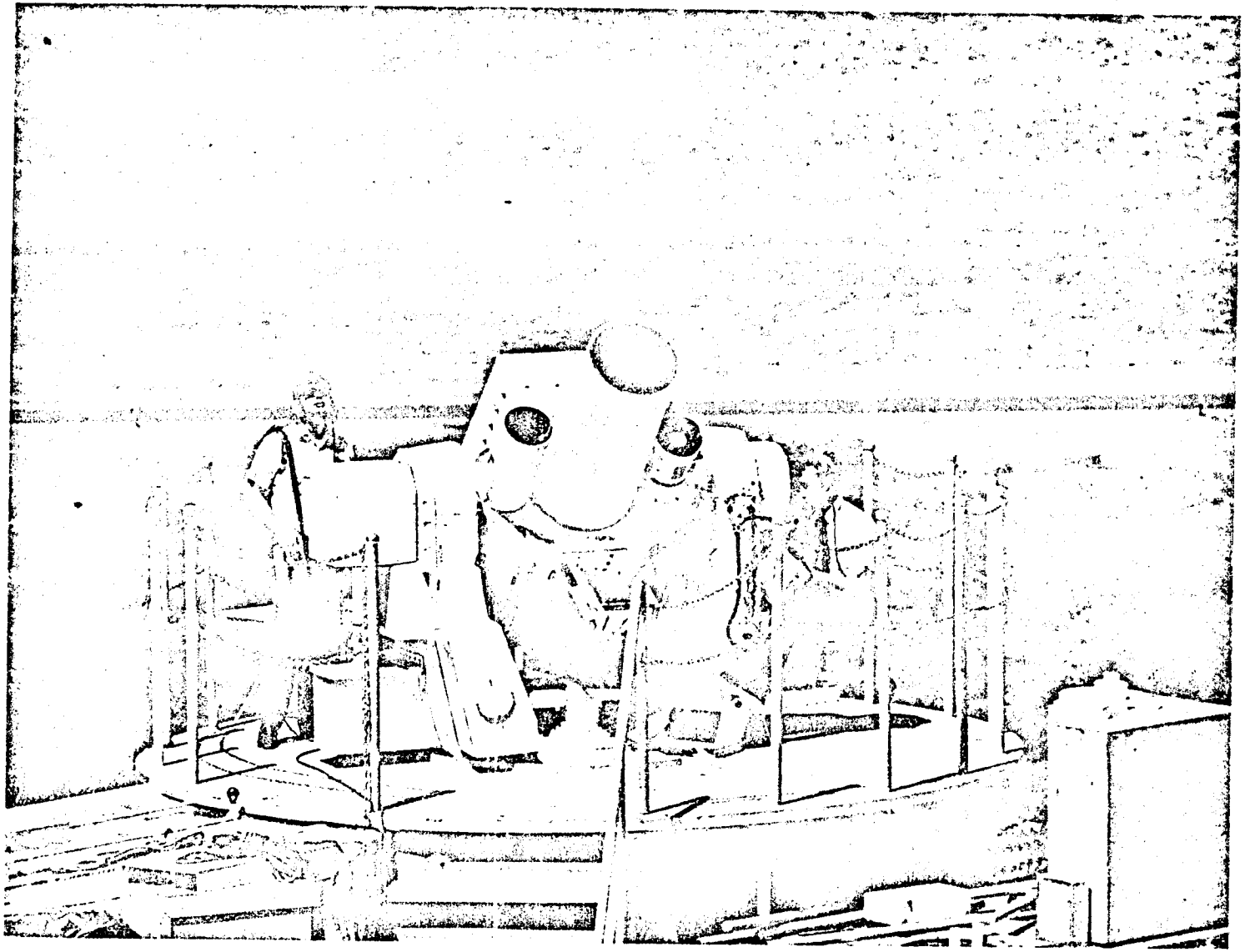

FIGURE 6

LASER SATELLITE RANGING SYSTEM

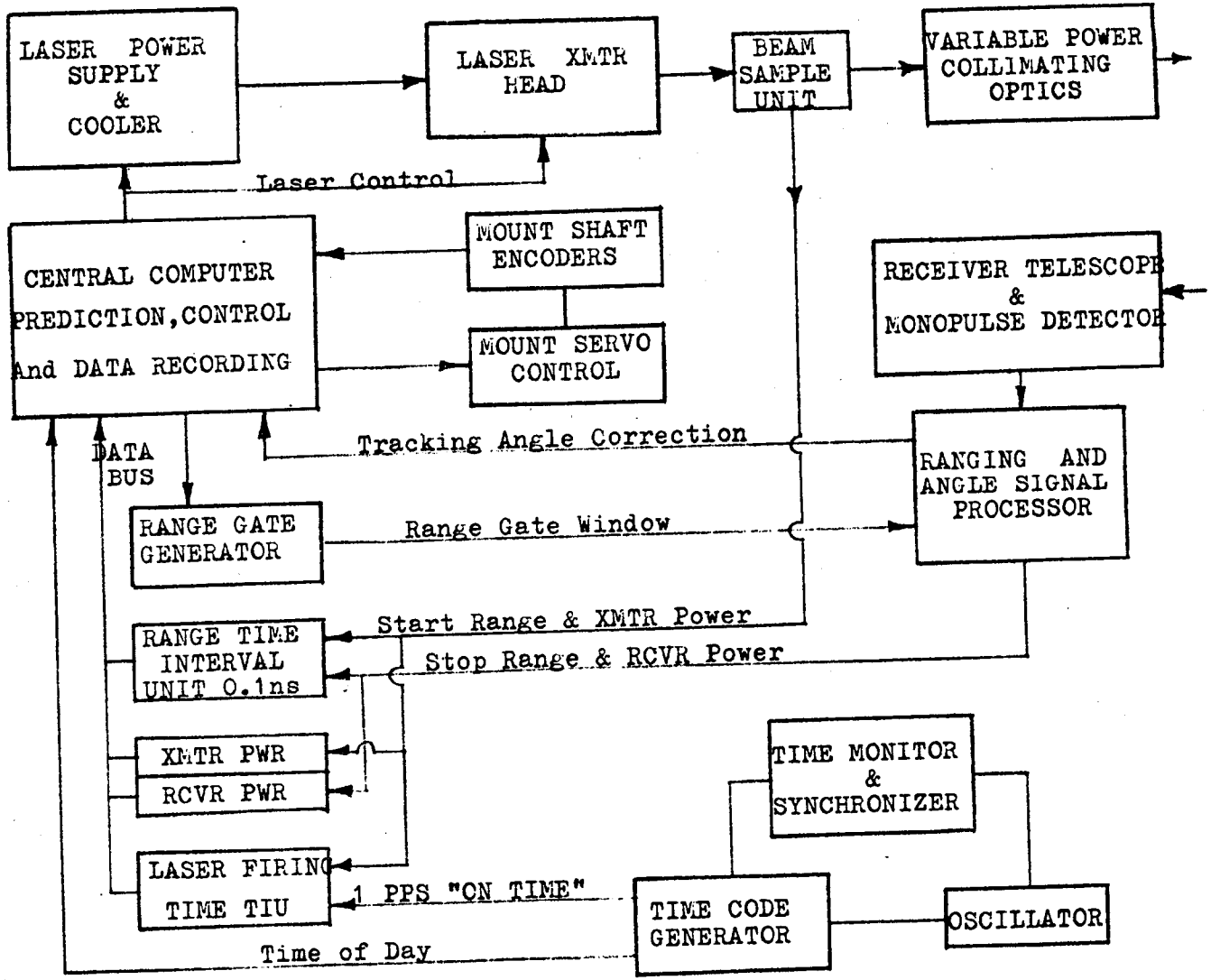

FIGURE 7

In order to appreciate the problems associated with design of a laser altimeter, it may be instructive to review the parameters of the satellite tracking system. Referring to Figure 8, we consider a laser pulse of E_T joules from a ruby laser radiating red light with a wavelength λ of 6943 Angstroms. Ruby lasers are normally not diffraction limited, but radiate into a solid angle determined, in part, by strains in the crystal. The transmitting telescope diminishes the divergence cone to an angle θ_T, which we choose to be compatible with our ability to point confidently to a rapidly moving satellite. The energy which strikes each reflector, of diameter a, at a distance R, is therefore

$$\frac{E_T \alpha}{\Pi/4\ \theta_T^{\ 2}} \cdot \frac{\Pi/4\ a}{R^2} \qquad \text{joules} \qquad (1)$$

where α is the transmission of the atmosphere.

The pattern of the reflected light should be similar to that of radiation through a circular aperture of radius a (even though the entrance aperture is hexagonal rather than circular). The intensity at the center of the pattern (Reference 7), when the total energy is E, is given by

$$I_o = \frac{E \cdot \Pi/4a^2}{\lambda^2} \qquad \text{joule/steradian} \qquad (2)$$

As illustrated in Figure 8, the reflected spot will not be centered around the transmitter, as might be expected from the retro-reflective properties of the cube corner, but will be shifted in the direction of the satellite's velocity v by an angle $2\ v/c$. Since the receiver and transmitter are mounted together, the receiver will see an intensity reduced by a fraction x of the central intensity. The reflected energy thus collected by the telescope, of diameter D_R is

$$\frac{\Pi E_T \alpha^2 a^4}{4\ \theta_T^{\ 2}\ R^2\ \lambda^2} \cdot \frac{\Pi/4\ D_R^{\ 2}}{R^2} \cdot x \qquad \text{joule} \qquad (3)$$

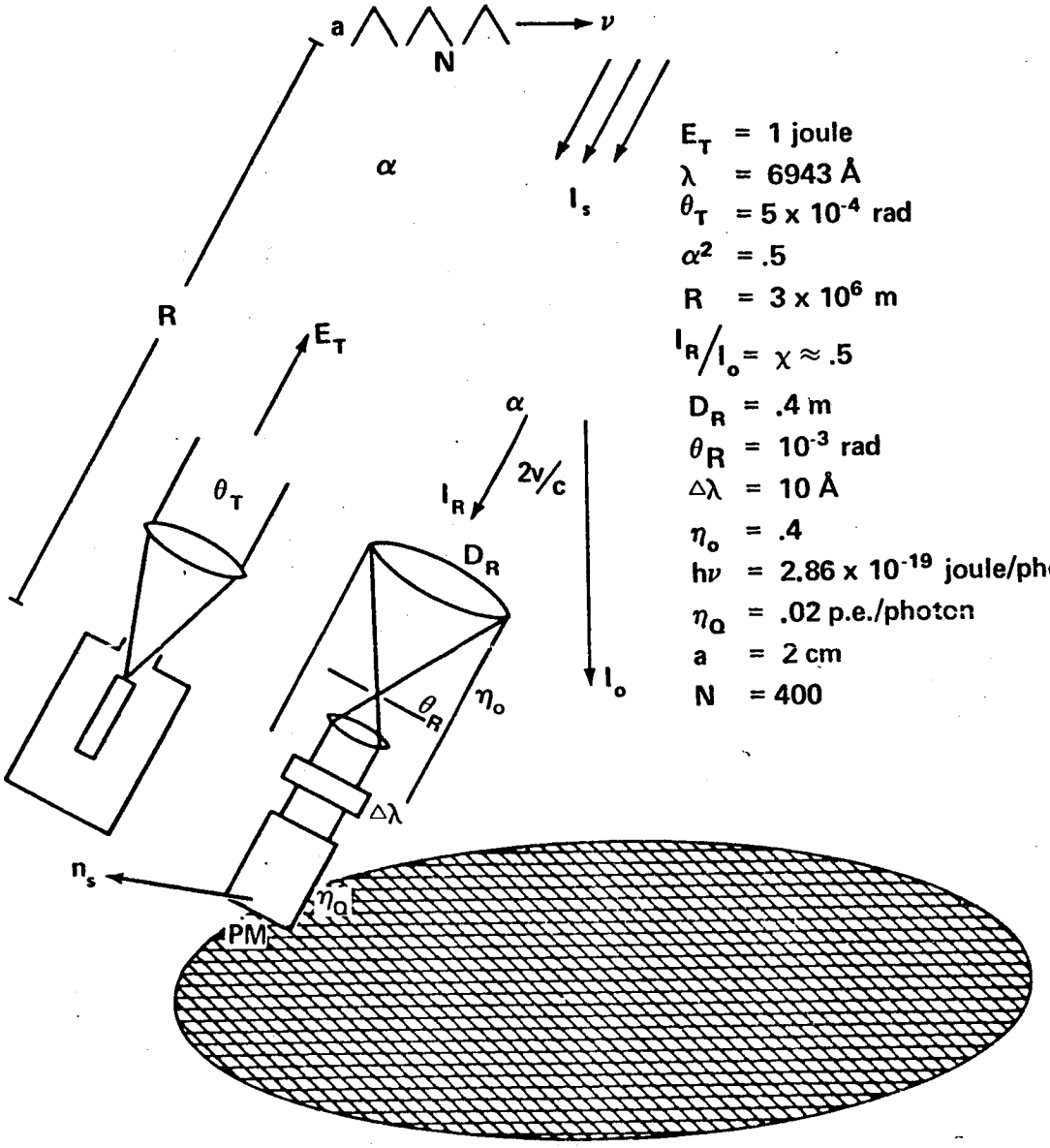

SATELLITE RANGING PARAMETERS

FIGURE 8

The energy received is focused, with optical efficiency η_o, through a filter with passband $\Delta\lambda$, onto a photomultiplier which converts photons into photoelectrons with a quantum efficiency η_Q. Converting the energy given by (3) into photons with energy $h\nu$, and multiplying by the number of satellite reflectors N, the number of signal photoelectrons becomes

$$n_s = N\frac{\Pi^2 E_T \alpha^2 a^4 D_R^2 x \eta_o}{16\ \theta_T^2 R^4 \lambda^2} \cdot \frac{\eta_Q}{h\nu} \qquad (4)$$

Using the hypothetical values for the parameters that are listed in Figure 8, we arrive at a signal of 2000 photoelectrons. This is actually a very good signal. Normally, a signal of 20 photoelectrons is set as the detection threshold. Noise pulses produced by daylight sky background radiation within the milliradian receiver field of view which passes through the wavelength filter very rarely result in false alarms at this threshold level.

If we grant, then, that signals are strong enough to permit confident detection, how shall we use them to measure range in the most precise and accurate manner? Typical ruby laser pulse widths used so far for satellite ranging are 15 nanoseconds (at half-intensity). This would correspond to over 2 meters of range uncertainty. In the ocean surface altimeter, even though we expect to use much shorter laser pulses, the ocean wave structure would introduce similar pulse spreading. How can we achieve 10 cm accuracy?

In Figure 9, we see that a constant threshold level, set to trigger a counter when the leading edge of a received pulse reaches a prefixed value, will result in a measured time which depends upon the height of the received pulse. The larger the pulse, the earlier the trigger will be activated, with respect to the center of the pulse. On the other hand, the figure also shows that, with approximately Gaussian shaped pulses, the half-maximum intensity seems always to occur at the same time. The technique which is now used is to trigger the counter when the pulse reaches half the maximum intensity, in accordance with the block diagram shown. Such an arrangement is necessary because the energy of received signal pulses will vary over orders of magnitude through the course of a satellite pass. Figure 10 is the record of a typical pass. The general trend of signal level results from the inverse R^4 dependence, but the wide scatter in pulse height from shot to shot is due to variable aiming accuracy and

DYNAMIC THRESHOLD COMPENSATION

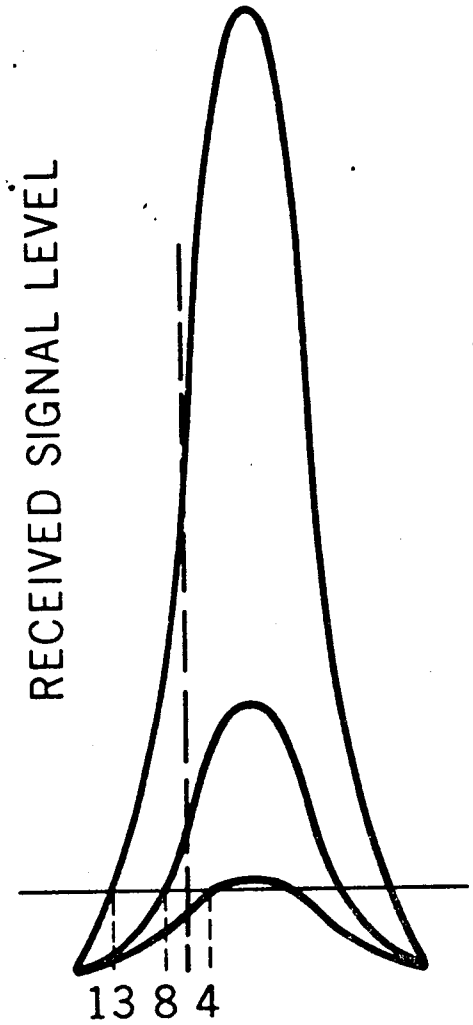

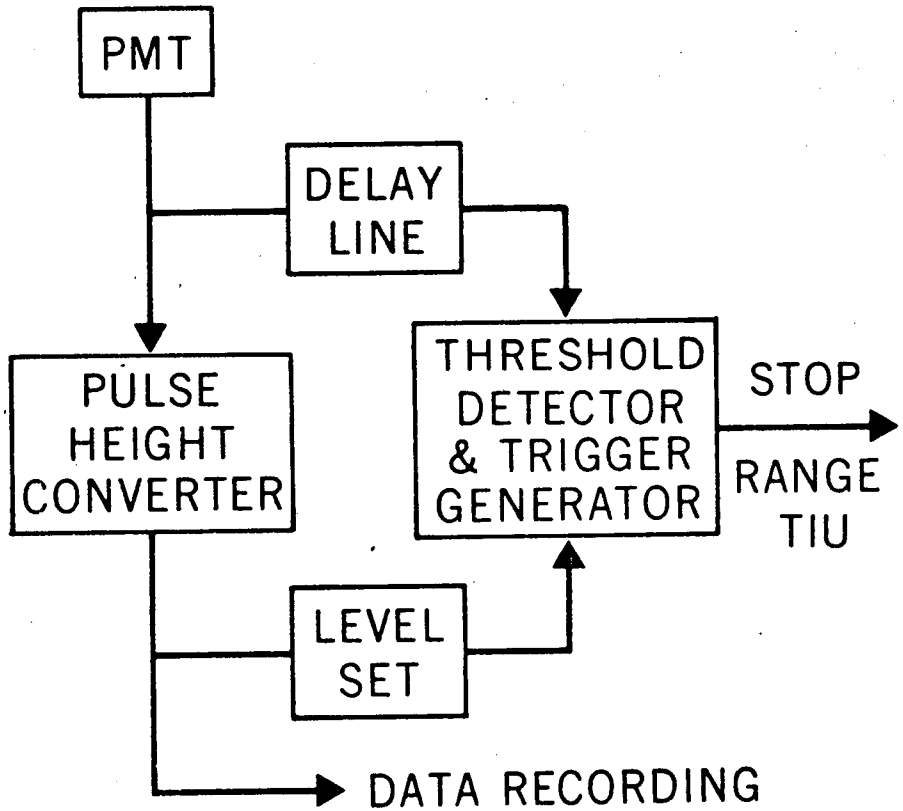

FIGURE 9

SIGNAL LEVEL DISTRIBUTION
RANGE ~ KM
TIME
MEASURED SIGNAL LEVEL
(PHOTO ELECTRONS)

FIGURE 10

scintillation in the intensity of the reflection back to a given spot on the ground. Superposition of reflections from all of the cube-corners in the satellite array gives rise to a random interference pattern with sharp contrast between bright and dark spots.

If a constant trigger level were used to stop the range counter, we could expect a wide variation in measured satellite range. This is illustrated in Figure 11. All of the ranges measured during a single pass are fitted to an orbit. That is, the parameters for an orbit, consistent with the latest SAO model of the earth's gravitational field, are adjusted to yield a least-square fit to the observed ranges from the known ground station. The individual residual difference between each measured range and that calculated from the best-fit orbit is then plotted as shown. The upper curve shows range residuals when a constant trigger threshold level is used, resulting in an rms deviation of 1.4 meters as a measure of scatter. In the lower curve, we have stopped the counter at the half-max time and also applied an analytic calibration correction. The range scatter has been reduced to 24 cm. This technique is now standard in all GSFC laser satellite tracking.

It is interesting to note that the accuracy of laser tracking (i.e., ability to calibrate instrumental delays and to prevent drift) is also commensurate with the precision (or scatter), which is now between 20 and 50 cm on individual short arcs. This has begun to uncover new effects which will probably require refinements in our description of the gravitational field. An example is shown in Figure 12. Recently, BE-C was tracked simultaneously over a period of several months, by two laser stations: the fixed one at Goddard (GODLAS) and the Mobile one in upper New York State at the Seneca Army Depot (SENLAS). If range measurements from any one pass were fit to an orbit, the residuals of individual points would look like those in Figure 11. The orbit parameters could be adjusted well enough so that over a short arc no systematic trend could be noticed in the residuals. However, in Figure 12, the orbit parameters have been adjusted to fit four successive passes from one of the stations. The orbit was made consistent with the latest SAO gravitational model. Yet, even the best fit was not able to remove the obvious short term fluctuation in the residuals. Similar patterns are observed from the second station.

Although the systematic fluctuations from the best-fit four-pass orbit exceed ± 5 meters, the scatter of measurements about the smooth sinusodial curve is on the order of 20 cm rms. Similar results were obtained during all opportunities to track four successive orbits from

LASER RANGE RESIDUALS

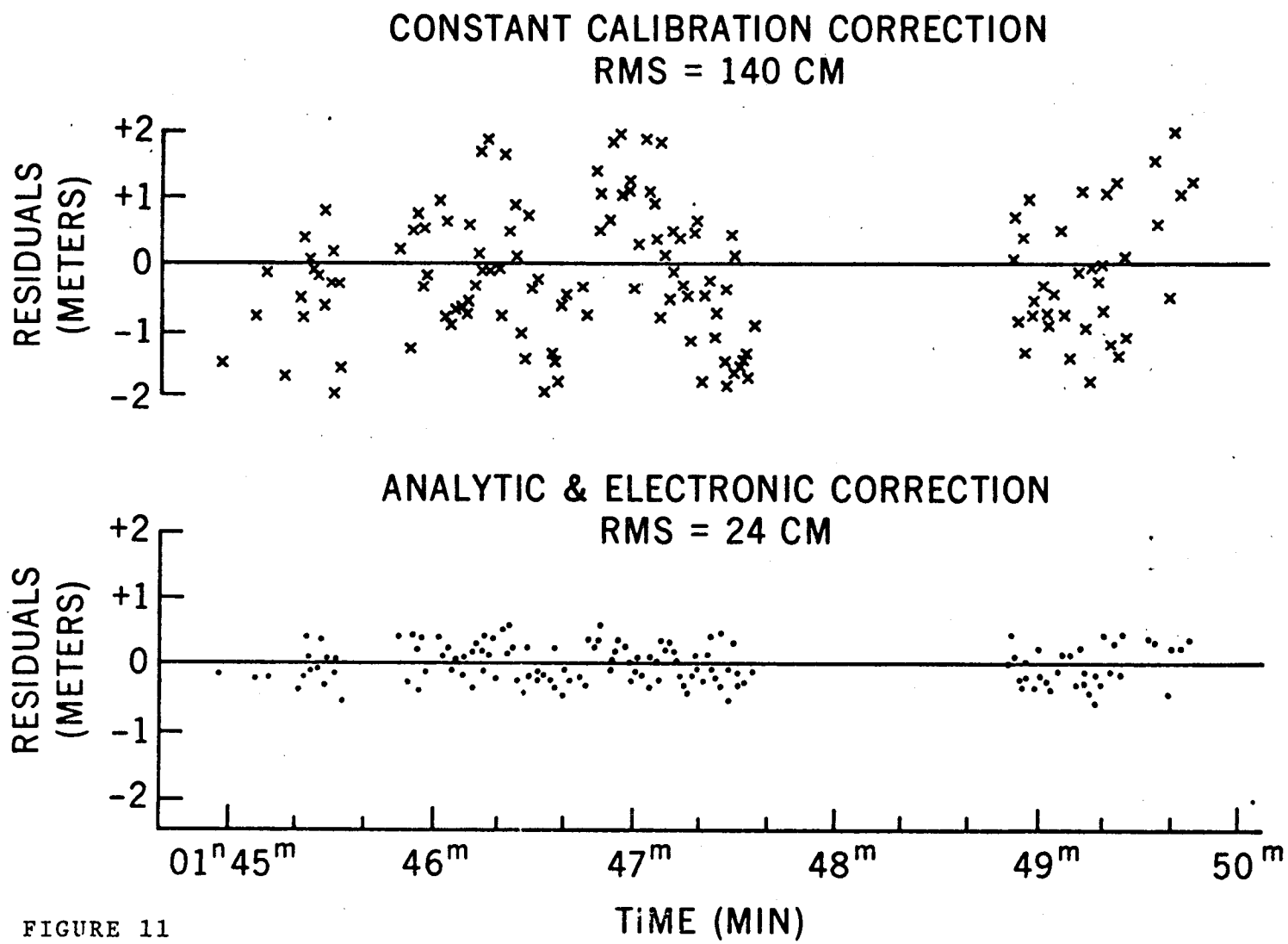

FIGURE 11

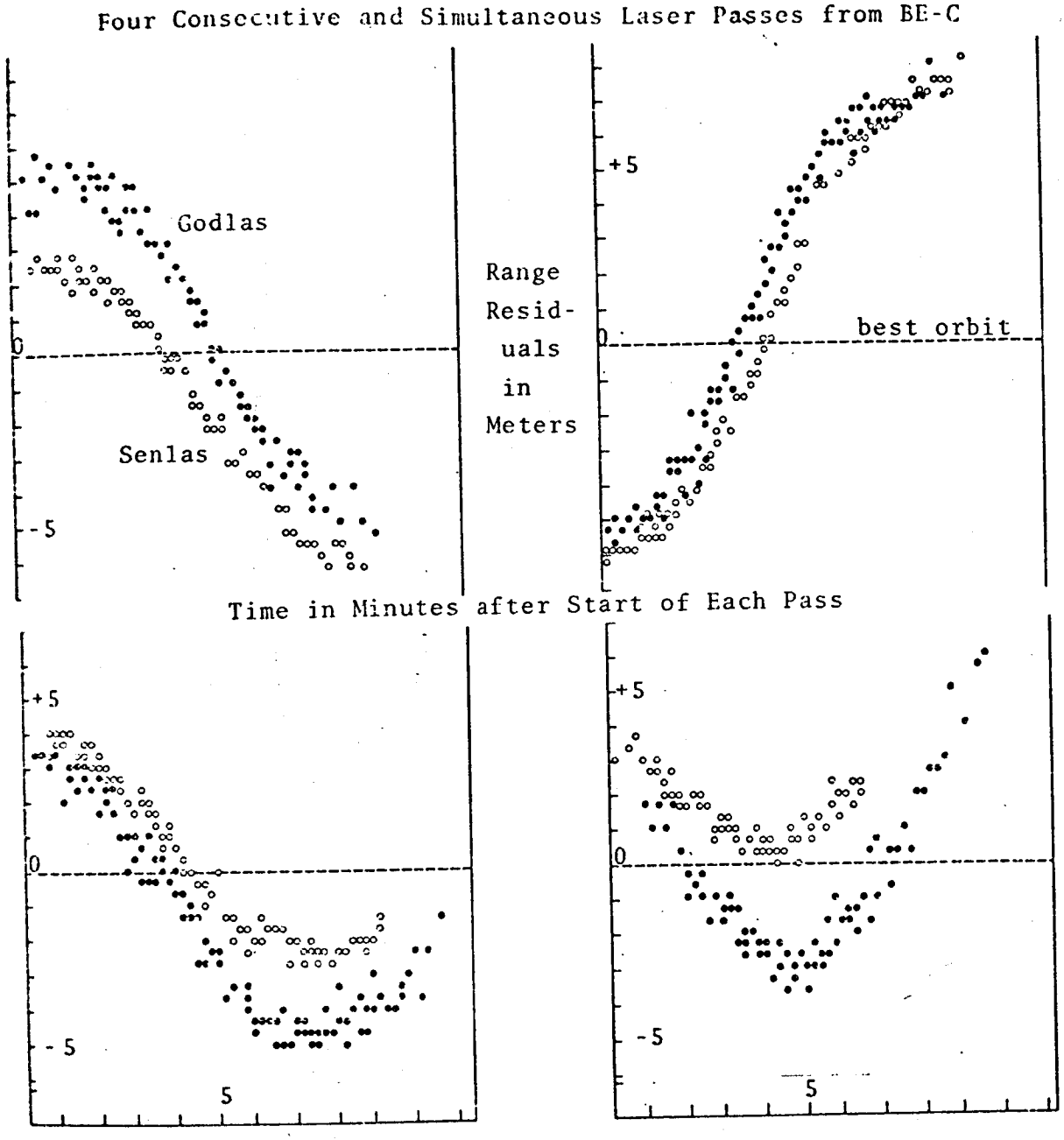
Four Consecutive and Simultaneous Laser Passes from BE-C
Godlas
Senlas
+5
0
-5
Range Residuals in Meters
best orbit
Time in Minutes after Start of Each Pass
5

FIGURE 12

the same station. Although it is not clear which geopotential terms must be corrected to account for this residual pattern, the period of the effect suggests deficiencies in low degree and order terms in the gravity field.

Laser Altimeter Design

We will discuss the simple-minded concept sketched in Figure 13, as an introduction to the significant factors for a space-borne laser altimeter. A neodymium-YAG laser was chosen, with frequency doubling, so that the wavelength of the transmitted radiation is 5300 Angstroms. This seems a reasonable choice, because of the sensitivity of state-of-the-art detectors for green light. Trade-off studies in this and other areas must be performed before choosing a final design. Pulse energy E_T of 0.25 joule and pulse width t_p of 3 nsec implies a Q-switched, but not necessarily mode-locked laser.

The laser collimating antenna will produce a divergence cone with diameter (θ_T) radians, and the spot of illumination on the ocean (footprint) will have a diameter $\theta_T R$. The numerical values we have chosen give rise to a 100 meter circle, which may be awkward because it is close to the length of a typical gravitational wave. However, this parameter is not at all critical, and can be greatly expanded or contracted. It should be noted, however, that 0.25 joules spread over a 100 meter circle produces an intensity of 3.2×10^{-11} joule/mm^2 on the surface, which is far below the danger threshold of 1.25×10^{-7} joule/mm^2 (U.S. Army).

For the reflectivity, ρ, of ocean water, we take the value 2% derived from the Fresnel formula for normal incidence, using an index of refraction of 1.33. Further, we assume that the angular distribution of reflected radiation is that which corresponds to a diffuse reflector. If there is any specularity to the reflection at vertical incidence, then the signal strength will be much greater than the estimate given here. This is a parameter that will probably depend very critically upon "sea state", and should be studied as a preliminary to final system design. We should also expect a good deal of scintillation, similar to that now observed from satellites. For diffuse reflection, then, the intensity reflected vertically up is

$$\frac{E_T \rho \alpha}{\Pi} \qquad \text{joule/steradian} \qquad (5).$$

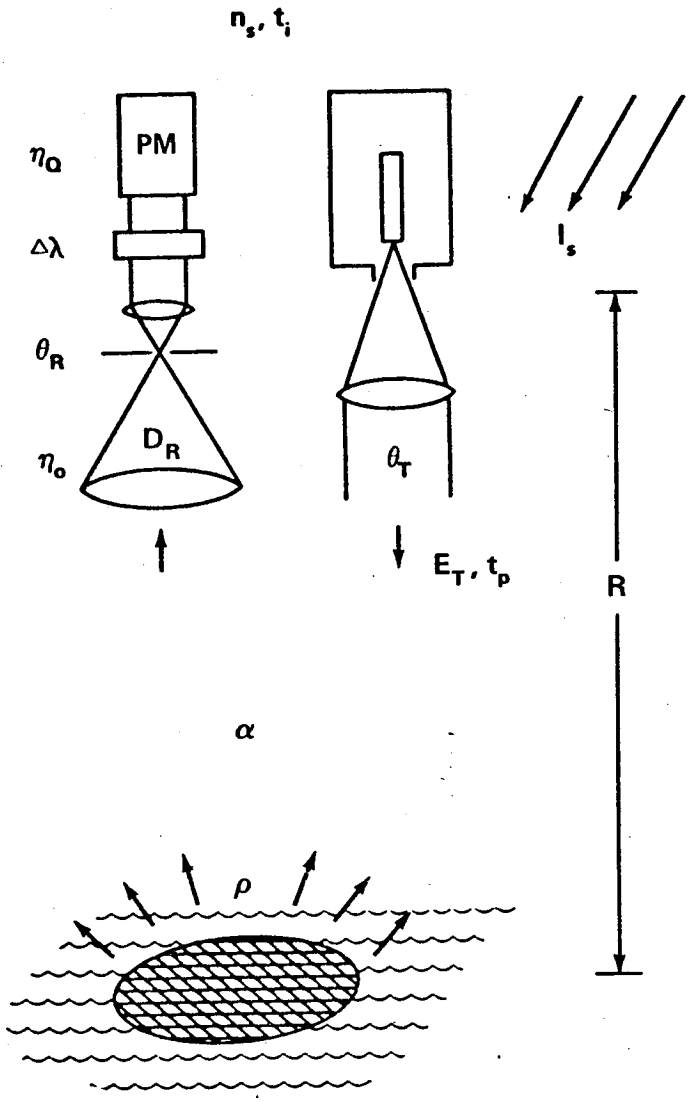

E_T = 0.25 j
λ = 0.53 μm R = 10^6 m
t_p = 3 nsec α^2 = 0.5
θ_t = 10^{-4} rad

ρ = 0.02
D_R = 0.3 m
θ_R = 1.5×10^{-4} rad
$\Delta\lambda$ = 10 Å
η_o = 0.4
η_Q = 0.2 p.e./photon
t_i = 20 nsec
$h\nu$ = 3.75×10^{-19} j/photon
I_s = 0.1842 w/cm^2 - μm

ALTIMETER PARAMETERS

FIGURE 13

The receiving telescope has a field of view θ_R which is large enough to see the entire illuminated spot. It collects the energy

$$\frac{E_T \rho \alpha^2}{\Pi} \cdot \frac{\Pi/4 \; D_R^2}{R^2} \qquad \text{joule} \qquad (6)$$

After passing through the optical system, whose efficiency is η_o, the photons are converted by the detector into n_s photoelectrons, with quantum efficiency η_Q:

$$n_s = \frac{E_T \rho \alpha^2 D_R^2}{4 R^2} \cdot \eta_o \cdot \frac{\eta_Q}{h\nu} \qquad (7)$$

Using the values listed in Figure 13, we arrive at an average signal of 12 photoelectrons per transmitted pulse.

Competing with this, we have various noise sources. We only consider two which appeared most likely to be significant: sunlight and signal fluctuation. Sunlight illuminating the ocean surface within the receiver field of view and within the optical filter passband is given by

$$I_s \Delta\lambda \cdot \frac{\Pi}{4} \theta_R^2 R^2 \alpha \qquad \text{watt} \qquad (8)$$

where I_s (Figure 13) is found in Reference 8.

In order to discriminate against noise sources, Figure 14 shows a post-detection filter and threshold detector. The filter is essentially an integrating circuit which stores the charge received over an interval t_i, and t_i is set to represent the longest pulse we may expect to receive. Assume that t_i is set to 20 nanoseconds, since that is the pulse spreading due to reflection from waves 3 meters high. Then, the threshold detector will determine whether the energy received during any 20 nanosecond interval should be considered a valid signal. The sunlight given by equation (8) which falls within t_i, is then the significant solar background. This is reflected

(diffusely), collected by the receiving telescope, and converted into noise photoelectrons:

$$n_s = I_s t_i \Delta\lambda \cdot \frac{\Pi}{4} \theta_R{}^2 R^2 \alpha \cdot \frac{\rho\alpha}{\Pi} \cdot \frac{\Pi/4 \; D_R{}^2}{R^2} \cdot \eta \cdot \frac{\eta_o}{h\nu}$$

$$= \frac{\Pi I_s t_i \Delta\lambda \theta_R{}^2 \rho\alpha^2 D_R{}^2 \eta_o \eta_o}{16 \; h\nu} \qquad (9)$$

Substituting the numerical parameters from Figure 13 tells us that .04 photoelectrons are collected from reflected sunlight during the integration period t_i. This is clearly not a significant noise background when compared to an expected signal of 12 photoelectrons. (The background computed here is equivalent to 2×10^6 noise photoelectrons per second, which is generally equivalent to the sky background now observed in satellite tracking.)

The second type of noise which we must consider is that arising from fluctuations in the number of signal photoelectrons arriving during each pulse. The statistics of discrete photoelectrons (Reference 9) tells us that if we expect n_s photoelectrons within a measuring interval, the root-mean-square deviation from the average will be $\Delta n_s = \sqrt{n_s}$. Thus, in our case, the ratio of signal-to-rms fluctuations will be

$$\frac{n_s}{\Delta n_s} = \sqrt{n_s} = \sqrt{12} = 3.5 \qquad (10)$$

Such a poor signal-to-noise ratio can have a profound effect in limiting the range measuring precision.

This can be illustrated by considering the block diagram of Figure 14 (taken from Reference 1). In this system, after determining that a pulse is a true laser reflection by satisfying the threshold criterion, the gate is opened and the pulse is sent to an integrator. When the integral is equal to half the total area under the pulse curve, a signal is generated to stop the range gate. Thus, the centroid of the pulse is used for measuring range. This may be the most valid measure for mean sea level when the pulse is spread by

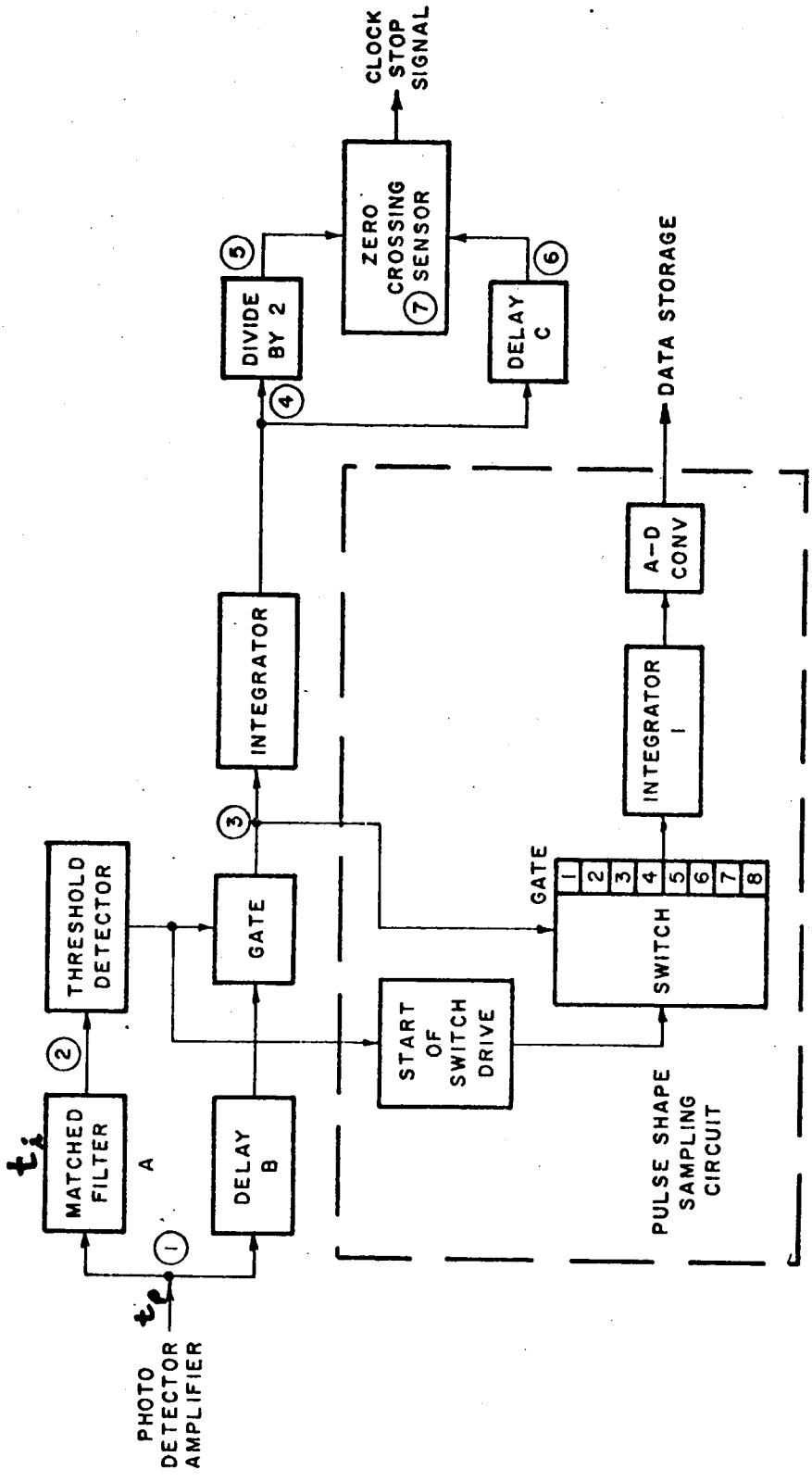
CLOCK STOP SIGNAL
ZERO CROSSING SENSOR
7
DIVIDE BY 2
DELAY C
DATA STORAGE
A-D CONV
INTEGRATOR
INTEGRATOR I
THRESHOLD DETECTOR
GATE
GATE
1 2 3 4 5 6 7 8
SWITCH
START OF SWITCH DRIVE
MATCHED FILTER
A
DELAY B
PULSE SHAPE SAMPLING CIRCUIT
PHOTO DETECTOR AMPLIFIER

FIGURE 14

wave height. Any other point in the pulse may be used, if suggested by a detailed study of ocean wave shapes.

If, however, the random arrival of pulses serves to distort the shape of the pulse, then the measured centroid position will not be a true measure of mean sea level. It can be shown that the fractional error in finding the centroid is given by the ratio of noise to signal. If the pulse were 20 nanoseconds long, corresponding to 3 meter waves, and S/N = 3.5, we could expect an rms error of 85 cm in finding mean sea level. If waves were 2 meters high, and we wanted a precision of 10 cm, we would need $\sqrt{n_s} = 20$, or $n_s = 400$.

Figure 14 also illustrates one technique for studying the shape of the pulse, and thereby inferring ocean wave structure. By dividing the pulse into a number of time-slot channels, each 2 or 3 nanoseconds wide, we can measure the number of photoelectrons in each channel and read them out sequentially.

An additional obvious source of error arises when the rays are not vertical. If we limit the error from this source to 10 cm, then the rays must not deviate by more than 1.5 minutes of arc. This would be satisfied by a divergence cone of 1 miliradian, producing a footprint 1 kilometer in diameter.

The assumptions upon which this paper is based may be quite conservative (especially that of diffuse reflection from the ocean surface). It appears that the present state-of-the-art would make a space-borne laser altimeter practical within a reasonable development cost. Whether or not such a task is undertaken must depend upon its expected value to oceanography and geodesy. It cannot operate through cloud cover, which probably limits it to no more than 50% of the ocean area at a given time. On the other hand, its superior precision and accuracy may justify a laser altimeter as a supplement to a microwave altimeter. While the latter can provide continuous coverage, the former will provide accurate calibration checks and permit possible study of detailed fine structure. The laser could, in addition, measure height above lakes and above small inexpensive retroreflectors placed at critical spots around the globe.

APPENDIX A

Apollo 15 Laser Altimeter

Information about the Apollo 15 Laser Altimeter was obtained in very brief telephone conversations with Mr. J. H. Woodward and Mr. R. C. Guyer, RCA, Aerospace Systems Division, Burlington, Massachusetts. It is presented here to the best of the author's memory and therefore should not be considered reliable.

The altimeter (built by RCA) operated in conjunction with a metric camera (built by Fairchild) taking mapping photos of the lunar surface from the Command and Service Module as it orbited the moon waiting for Ascent Stage to return. Altimeter and camera were boresighted so that a precise range could be found for a well-defined spot on the photograph. From this, one could convert angular distances on the photo into accurate linear distances on the lunar surface.

The altimeter operated continuously for 24 hours at the moon, performing up to specifications. Then several malfunctions occurred which terminated the operation. Apparently, there was a high voltage breakdown in a "safety circuit". There also seemed to be severe contamination of the telescope optics, perhaps because of proximity to a discharge port for waste fluid. RCA engineers believe they can correct the deficiencies and that the malfunctions did not reflect inherent weaknesses in the system itself. It is expected to fly again on Apollo 16 and Apollo 17.

The altimeter operated between altitudes of 40 mi and 80 mi, and had a fixed detector gate corresponding to this range of delays. The laser was a Q-switched ruby laser, operating once every 16 seconds. Transmitter divergence was 300 microradians, receiver field of view was 200 microradians. The receiver was a 16 power reflecting telescope with 4-inch diameter aperture. The range measuring circuitry was built around a 150 MHz counter and had a precision of $\pm$ 1 meter. The package was an irregular shape with a volume of about 1 ft^3 and weight of 50 lb. It consumed about 50 watts when operating. The observed signal strengths implied that the lunar surface had reflectivity between 7 and 18%.

That the Lunar Laser Altimeter is a simpler problem than that presented by an ocean surface altimeter from earth orbit, can be seen by a rapid calculation. Using the formula already developed for the number of signal photoelectrons from a diffuse reflecting surface,

$$n_s = \frac{E_T \rho \alpha^2 D_R^2 \eta_o \eta_Q}{4 R^2 h\nu}$$

We use the following values:

$E_T = 0.25$ joules	$\eta_o = 0.4$
$\rho = 0.1$	$\eta_Q = .02$ p.e./photon
$\alpha^2 = 1$	$R = 100$ km
$D_R = 0.1$ meter	$h\nu = 2.857 \times 10^{-19}$ joule/photon

This results in a signal of 175 photoelectrons per pulse, which is quite comfortable, under the circumstances.

REFERENCES

1. "Space Geodesy Altimetry Study", Raytheon Company, NASA Contract Report, NASA CR-1298, March 1969

2. "Optical Altimeter Receiver Systems Study and Design for a Spaceborne Laser Altimeter", ADCOM Final Report for Contract Number NAS 12-2058, May 31, 1969

3. "Development and Fabrication of a Laser Tracking Receiver System", ADCOM Final Report for Contract NAS 12-2184, October 1970

4. Private communication with Jason Woodward, RCA Corporation, Bulington, Massachusetts

5. P. R. Yoder, Jour. Optical Society of America 48 No. 7, p. 496 (July 1958)

6. R. F. Chang, et al, Jour. Optical Society of America 61, 431, (April 1971)

7. Born and Wolf, Principles of Optics, Pergamon Press, 1959, Page 394

8. "Solar Electromagnetic Radiation", NASA Document No. NASA SP-8005, Space Vehicle Design Criteria (Environment), Revised May 1971

9. "Laser Receivers", M. Ross, John Wiley & Sons, New York, 1966, p. 32

E

OPTIMUM USAGE OF GROUND STATIONS FOR GEOS-C ORBIT DETERMINATION

9

Chreston F. Martin

Wolf Research and Development Corporation
Riverdale, Maryland

The work upon which this report is based was sponsored in part by NASA/Wallops Station under Contract Number NAS6-1942

1.0 INTRODUCTION

The effective utilization of the planned GEOS-C satellite for geoidal mapping will require the determination of the satellite orbit with an accuracy of at least a few meters in the radial coordinate. The measurements made by the GEOS-C altimeter can be used both for orbit and geopotential improvement, but only after the instrument has been well checked out and calibrated and techniques have been developed for effectively using altimeter data for orbit determination. Prior to this stage, it will be necessary to have available a satellite ephemeris based on ground tracking data. Inter-satellite tracking data may also be used, but even here there is a link to a ground tracking station. The scope of this paper will be limited to the conventional type of single satellite tracking data.

The determination of an accurate satellite ephemeris is limited by a number of factors, inlcuding station position errors, measurement biases, tropospheric and ionospheric refraction, station timing errors, and errors in knowledge of the earth's potential field. If we wish to relate altimeter measurements to the geoid, then we require that the satellite orbit be

determined relative to the earth's center of mass and not relative to, say, some particular station. Intuitively, this would suggest that the satellite orbits need to be determined using at least one revolution of tracking and no arcs shorter than this will be considered. Since the altimeter power is limited to approximately one satellite revolution per day, it is therefore suggested that one revolution is the maximum period for which the most accurate orbit is necessary. Accordingly, we will consider the accuracy of orbits of one revolution, but which may be based on more than one revolution of tracking data.

If there were no errors in the geopotential field (or other forces acting on the GEOS-C satellite), then the accuracy of an estimated orbit would be improved with the addition of tracking data over longer and longer periods of time to the orbit estimation process. In this way, the effects of measurement noise and the various systematic errors are minimized. Conversely, if knowledge of the geopotential field were very poor, then the satellite position (and velocity) could be estimated at each time point if at least three (or six) simultaneous measurements were available. The accuracy limitation in this particular situation is due to measurement errors and station position errors. In practice, the true situation is somewhere between these two extremes, and the most accurate orbit is obtained using some finite arc length which depends on the satellite orbital elements, the number and locations of the tracking stations, the measurement type and accuracy, and the accuracy of the geopotential model used.

Two global networks of tracking stations will be considered in this paper and the accuracy of orbits using their data will be compared in a limited set of simulations. The networks will be compared both separately and together, with the objective of determining the amount of tracking beyond which the addition of more data from more stations produces a negligible orbit improvement. This rather ambitious objective cannot, of course, be definitively answered without an extensive study, but the results obtained do have strong implications on the need for extensive tracking of the GEOS-C satellite, particularly with regard to the need for continuous tracking. Currently existing tracking stations are emphasized.

2.0 METHOD OF ANALYSIS

The analysis of orbit determination accuracy was made using a computer program which simulates the normal reduction of satellite tracking data and propagates through this process the expected errors in the data and the station positions, and the model of the geopotential coefficient error. All these errors are propagated into the satellite ephemeris and are then transformed into radial, cross track, and along track components. For the altimeter application, the radial error component is the only one whose accuracy is critical and results only for radial errors will be considered in the following analysis.

With a large number of well distributed tracking stations used in the GEOS-C orbit estimation, individual error sources of measurement biases (for range type measurements), errors in refraction corrections, station position errors, etc., all have small effects if all such errors are independent. Error analysis runs have indeed verified this and for none of the arcs considered did any single systematic error of the expected amplitude have an effect greater than 0.5 meters. In all cases, the dominant error source is geopotential coefficient error. By comparison, all other errors are essentially negligible, with the total radial uncertainty only slightly greater than the geopotential coefficient error effect except at those times when the coefficient errors have very small effects.

The model for geopotential coefficient error is based upon the differences between two gravity models which are basically independent. These models are the Smithsonian Astrophysical Observatory M1 model [Lundquist and Veis, 1966] and the Johns Hopkins Applied Physics Laboratory 3.5 model [Guier and Newton, 1965]. It has been shown [Martin and Roy, 1971] that 25% of the differences between these two models produces a quite valid estimate of the geopotential coefficient error effects on a short arc data reduction using the SAO 1969 Standard Earth gravity model [Gaposchkin and Lambeck, 1969]. Some care must be exercised in the interpretation of results when using this set of differences as an error model, since it can have only a statistical interpretation. However, because of the success in predicting GEOS-B errors, and the relatively small altitude and inclination differences between GEOS-B and the planned GEOS-C, the peak amplitudes and locations of peaks and minima should be reliable with a reasonable degree of confidence.

3.0 GEOS-C SIMULATIONS

The GEOS-C satellite is presently planned for a 115° inclination and an altitude of 500 nm. Ground tracks for three revolutions of such a satellite are shown on Figure 1. Also shown on Figure 1 are the locations of 12 Doppler measurement sites and 8 range measurement sites. The geodetic locations of these stations are shown in Table 1. The Doppler stations are representative of existing Navy Doppler sites, and the range measurement sites are representative of existing C-band radar and laser measurement sites.

The coverage provided by the Doppler sites is shown in Figure 2 for the stations tracking down to 5° elevation angles. For this set of stations, the coverage has good geographic distribution, and would appear to provide satellite coverage for greater than 50% of the time. Coverage provided by C-band radar sites is rather heavily concentrated along the United States east coast and provides little tracking at the high latitudes. Laser trackers are, in most cases, mobile and can be located on most land areas.

Simulations were performed for the Doppler network with tracking from all stations when the satellite was above 5° elevation angle. Arc lengths of 2, 4, and 6 hours were simulated with the 2 hour arc falling in the middle of the 4 hour arc and the 4 hour arc in the middle of the 6 hour arc. A frequency bias was assumed to be adjusted for each Doppler pass of each

GEODETIC LOCATIONS
TABLE 1

DOPPLER SITES

	ϕ	λ (E)
LASHAM, ENGLAND	51° 11′ 10″.6	358° 58′ 30″.5
SAO JOSE DOS CAMPOS, BRAZIL	-23° 13′ 01″.7	314° 07′ 50″.6
SAN MIQUEL, PHILIPPINES	14° 58′ 57″.8	120° 04′ 26″.0
SMITHFIELD, AUSTRALIA	-34° 40′ 31″.4	138° 39′ 12″.4
MISAWA, JAPAN	40° 43′ 04″.6	141° 20′ 04″.7
ANCHORAGE, ALASKA	61° 17′ 02″.0	210° 10′ 37″.5
THULE, GREENLAND	76° 32′ 18″.6	291° 13′ 46″.7
SOUTH POINT, HAWAII	21° 31′ 26″.9	202° 00′ 00″.6
LOS CRUCES, NEW MEXICO	32° 16′ 43″.8	253° 14′ 48″.3
HOWARD COUNTY, MARYLAND	39° 09′ 47″.8	283° 06′ 11″.7
MCMURDO SOUND, ANTARCTICA	-77° 50′ 51″.7	166° 40′ 25″.3
PRETORIA, SOUTH AFRICA	-25° 56′ 46″.1	28° 20′ 53″.0

RANGE MEASURING SITES

CARNARVON, AUSTRALIA	-24° 53′ 47″.5	113° 43′ 02″.1
KOUROU, FRENCH GUIANA	5° 06′ 46″.3	307° 29′ 19″.5
SANTIAGO, CHILE	-33° 00′ 00″.0	289° 00′ 00″.0
ANTIGUA, BRITISH W. INDIES	17° 08′ 37″.6	298° 12′ 25″.8
MERRITT ISLAND, FLORIDA	28° 25′ 29″.0	279° 20′ 07″.5
BERMUDA	32° 20′ 52″.8	295° 20′ 47″.6
WALLOPS ISLAND, VA.	37° 51′ 36″.8	284° 29′ 25″.9
WHITE SANDS, NEW MEXICO	32° 21′ 28″.8	253° 37′ 47″.9

station, with negligible a priori knowledge of the bias. Refraction errors were ignored, but station position errors of 5 meters in each coordinate were propagated.

For the range tracking network, simulations were made for the same 2 hour arc as was the 2 hour Doppler simulation with tracking also down to 5° elevation angle. Each station was considered to have a range bias of 2 meters which was not adjusted but whose effect was propagated through the data reduction. Station position errors of the same magnitude as the Doppler station position uncertainties were propagated.

The 2 hour arc was also simulated with both the range and Doppler networks tracking. Weights for the two data types were chosen in such a way that each network was given approximately equal weight. For the same data rate, this requires that a Doppler sigma of 3cm/sec correspond to about a 12 meter range sigma.

For all simulations, the effects of the geopotential coefficient model error discussed above were propagated into the satellite orbit and the radial component computed. Station position and measurement bias errors produced effects which were, in general, negligible when compared to the geopotential error and will consequently be ignored in the discussion below. With the geopotential error above considered, it will be meaningful to consider the estimated error including sign, rather than as just a sigma. In this manner, expected correlations between errors at different spatial locations can be demonstrated.

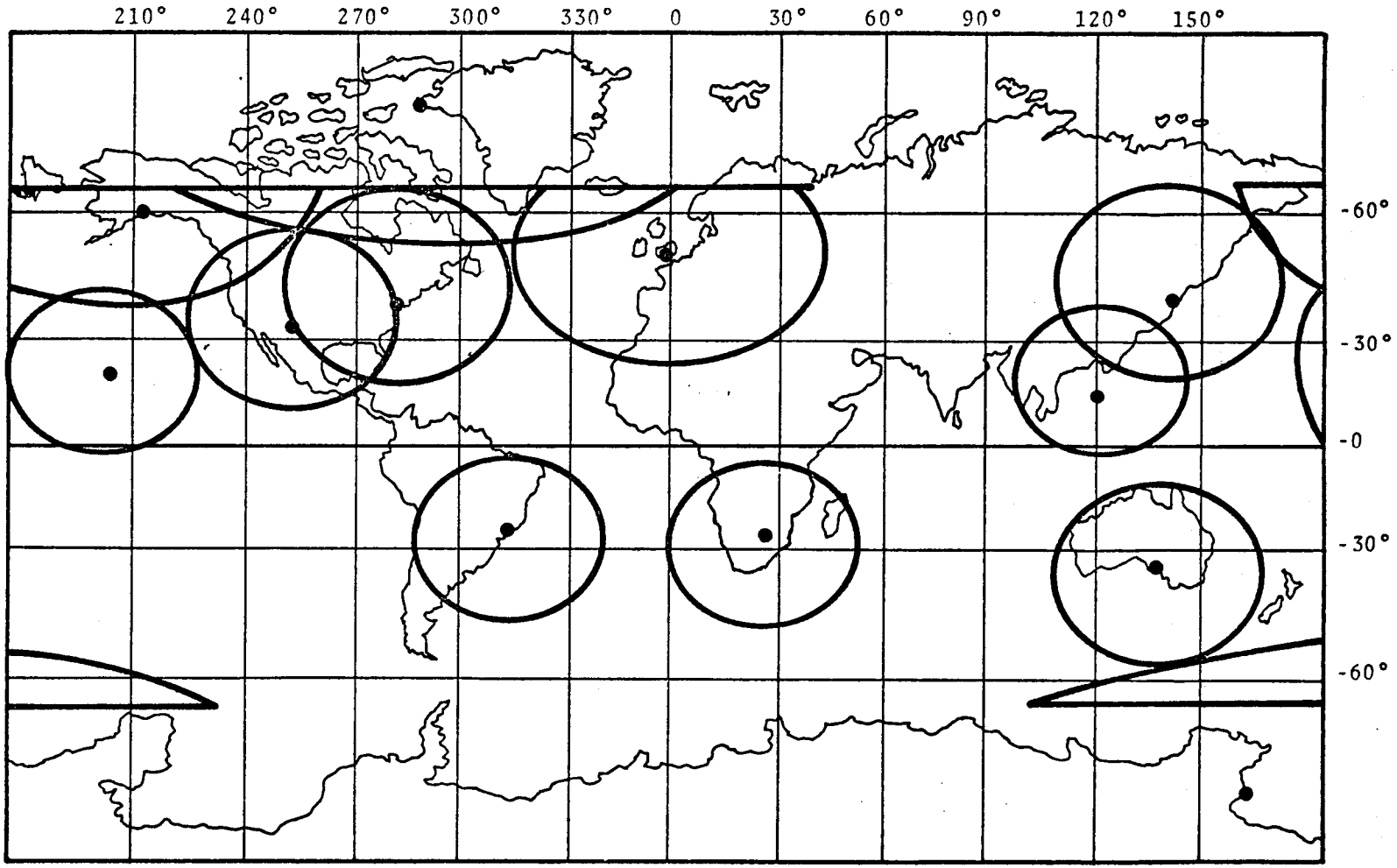

DOPPLER TRACKING COVERAGE OF GEOS–C

5° CUTOFF

FIGURE 1

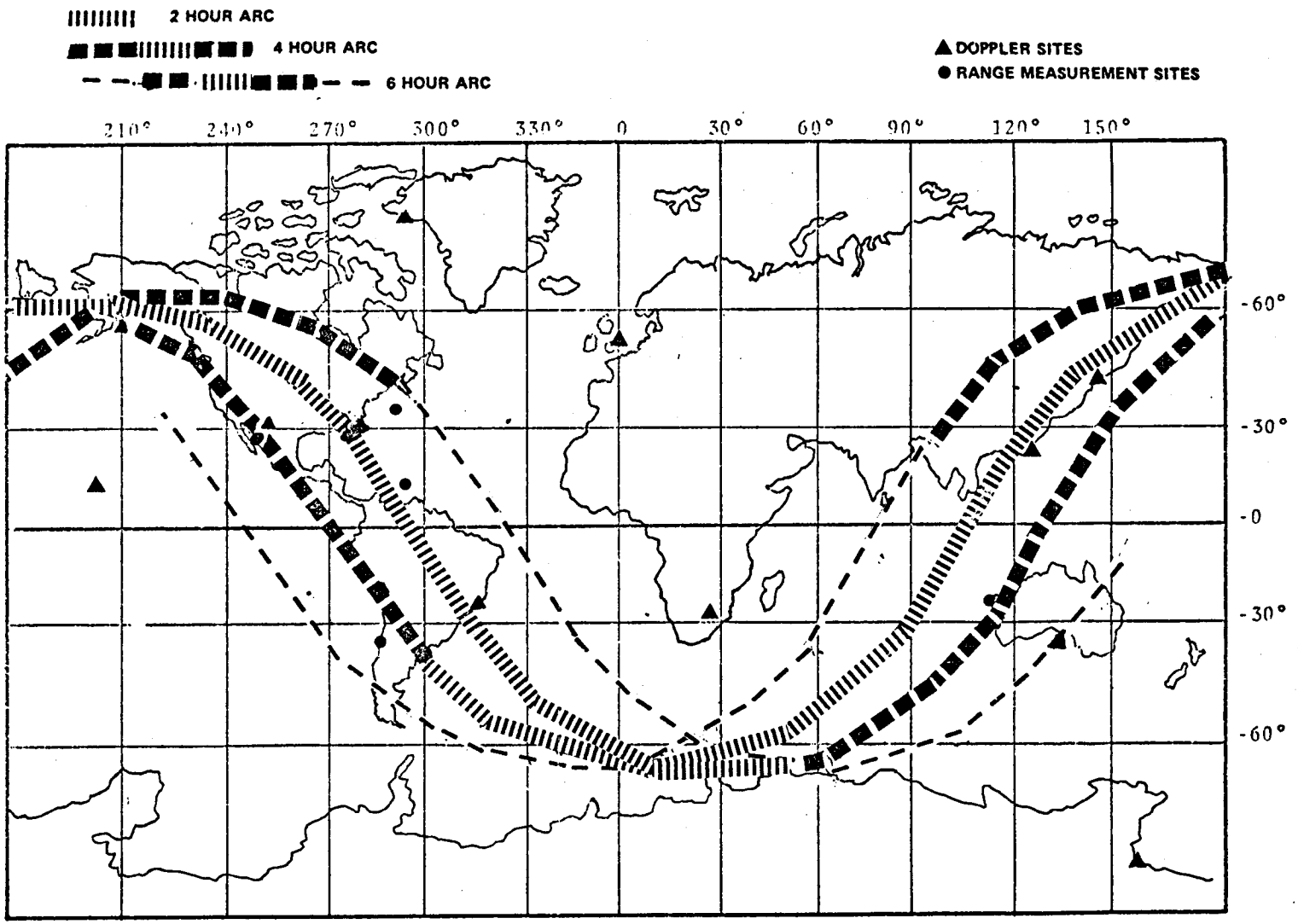
2 HOUR ARC
4 HOUR ARC
6 HOUR ARC
DOPPLER SITES
RANGE MEASUREMENT SITES
210°
240°
270°
300°
330°
0
30°
60°
90°
120°
150°
-60°
-30°
-0
-30°
-60°

FIGURE 2

4.0 ANALYSIS OF RESULTS

For the 2, 4, and 6 hour arcs using Doppler tracking, the effects of the geopotential model error are shown in Figure 3. The 4 and 6 hour orbits appear to be affected in the overlap period by about the same amount, approximately $\pm$7m. Peak errors occur, for the most part, during periods of limited or no tracking. The error tends to be minimum (i.e.,cross zero) during periods of overlapping tracking.

The 2 hour Doppler orbit is affected somewhat less during portions of the arc than are the 4 and 6 hour arcs, apparently indicative that the geopotential model errors can be more absorbed in the orbital elements. The times of minimum error are, however, approximately the same.

The geopotential model error effect for the 2 hour arc is also shown on Figure 4 on an expanded scale. On the same graph is shown the geopotential model error effect on the range tracking network only, and also the geopotential error effect on the combined Doppler plus range orbit. The range orbit error is larger than the Doppler orbit error near the beginning of the arc, but the first tracking is approximately 7 minutes after epoch. However, the maximum orbit error during the tracking period is still at the beginning of track.

The range tracking is heavily concentrated during the 10-30 minute period. There is then a 35 minute break before the

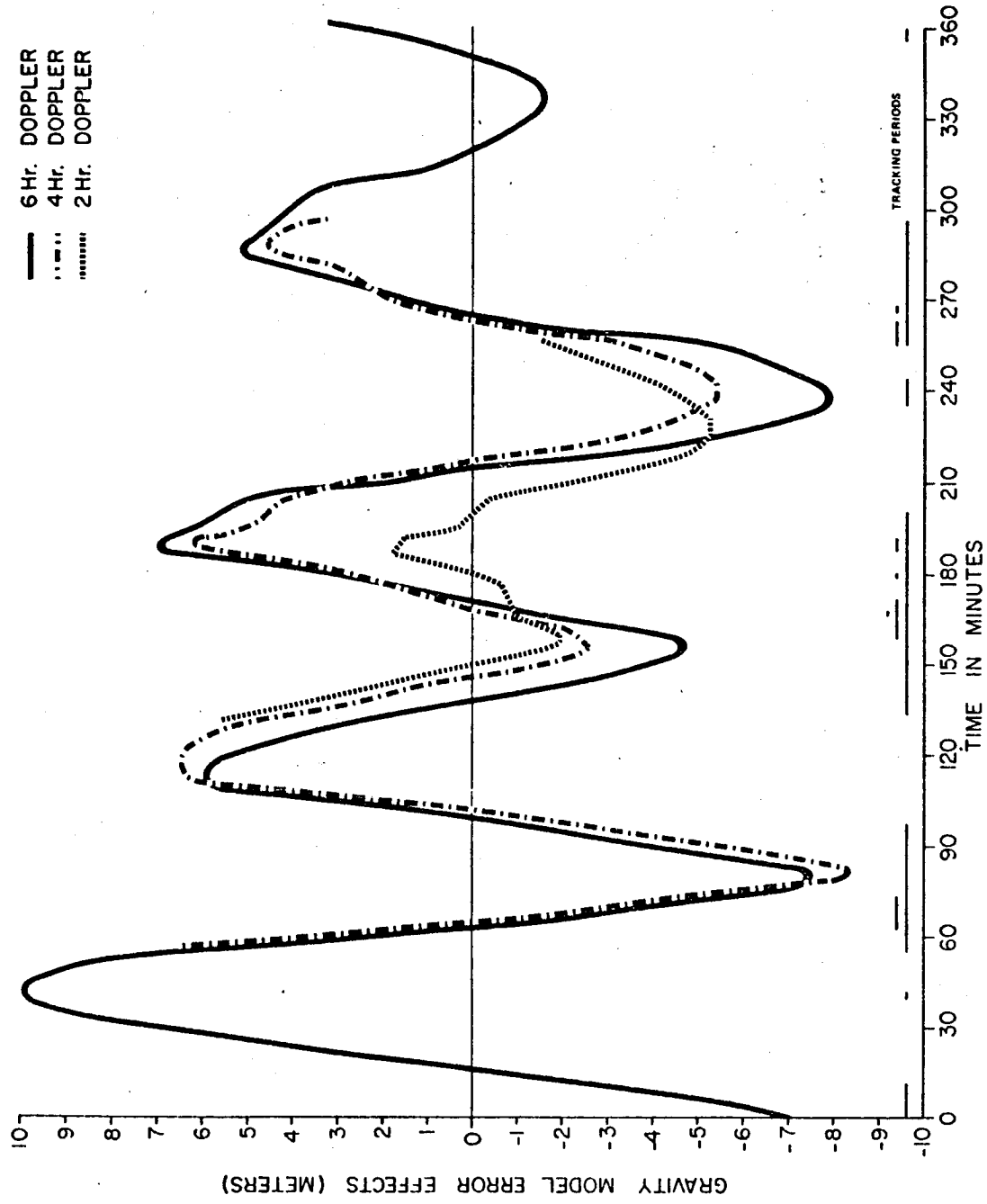

FIGURE 3 Geopotential Model Error Effects on Doppler Determined Orbits

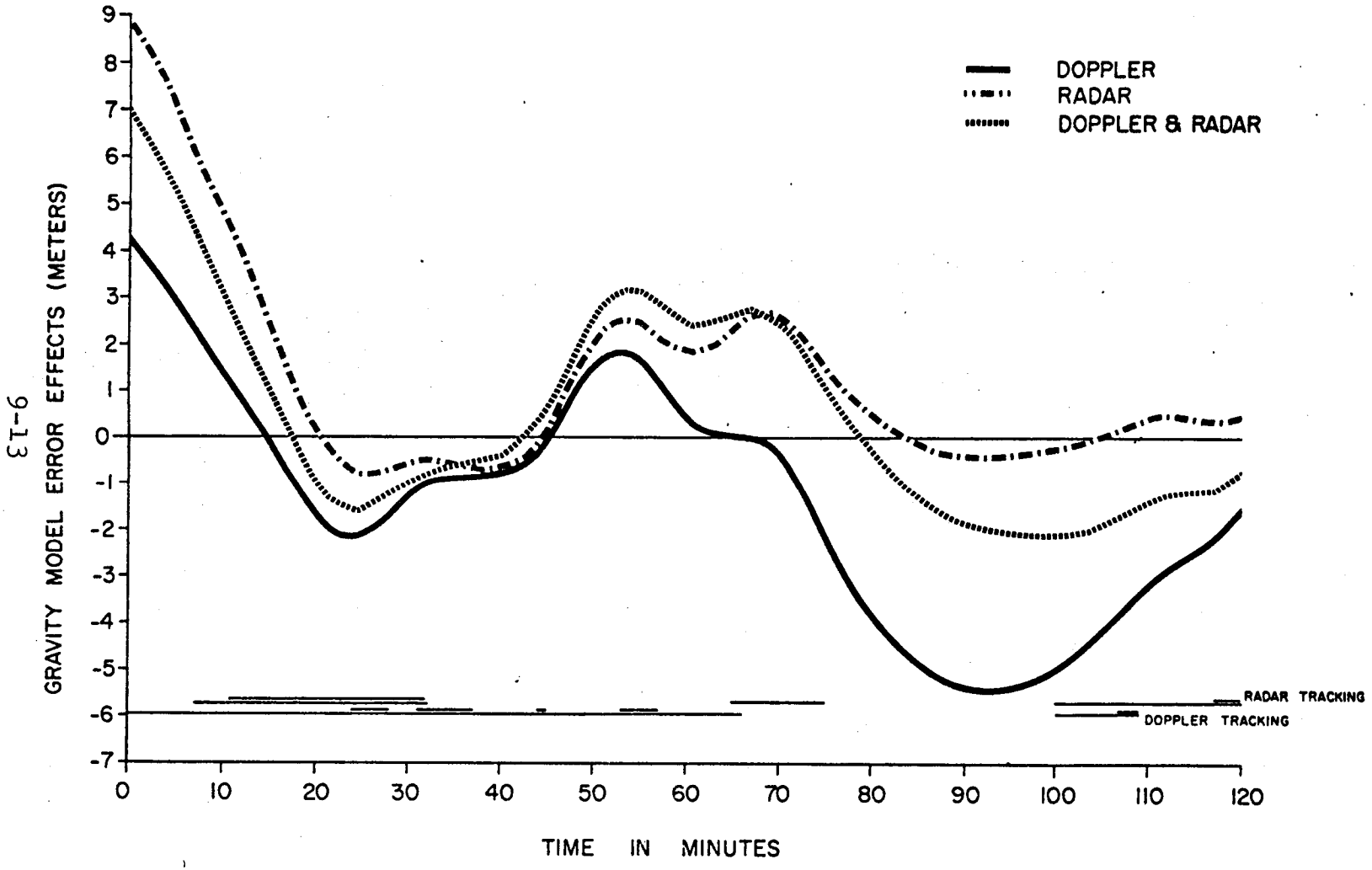

FIGURE 4 Geopotential Model Error Effects on Two Revolution Doppler and Radar Orbits

satellite is seen by Carnarvon, and another 25 minute gap before the satellite is picked up by Santiago. During this time, including the tracking gaps, the maximum orbit radial error only slightly exceeds 2 meters.

As might be expected, the orbital error for the range-Doppler solution is intermediate between that of the range only and Doppler only solutions throughout most of the arc. Unfortunately, the model error effects tend to have the same sign on both the range and Doppler solutions, so the combined solution is always worse than one of the solutions.

The similarity of the geopotential model error effects for the different tracking periods and, to a lesser extent different tracking systems, is indeed striking, and suggests that the reduction in orbit error through the use of more tracking is not easily accomplished. It also suggests that the comparison of orbits generated using different tracking systems but the same geopotential model will be a very poor measure of the actual orbit accuracy.

The extrapolation of the range determined orbit for an excess of 30 minutes without a serious increase in orbit error shows that the orbit error need not grow excessively without continuous tracking. Combining this conclusion with the result that the Doppler orbits are minimum during simultaneous track would suggest that some period of concentrated tracking

combined with some amount of global tracking is adequate for a well determined and accurate global orbit over a single revolution.

It should also be noted that the one revolution solutions, at least for the particular tracking periods used, is significantly less affected by geopotential coefficient error than are multi-revolution solutions.

5.0 CONCLUSIONS

Because of the limited nature of the simulations, conclusions drawn must be considered tentative until additional arcs are investigated and the geopotential model error is more fully validated. The conclusions regarding the amount and type of ground tracking which produces the orbit with the minimum radial error may be summarized as:

1. Minimum orbit error tends to occur during periods of simultaneous ground tracking.
2. Single revolution solutions would be expected to have less error than multiple revolution solutions.
3. No type of tracking instrument has any strong advantage over another type, given a sufficient amount of data.
4. Continuous tracking is not necessary for accurate orbits.
5. With good tracking geometry, radial errors of approximately 2 meters or less appear possible.
6. The Doppler system appears capable of approximately 5 meter height accuracies on a global scale.

ACKNOWLEDGMENT

The author would like to thank Mr. Ronald L. Brooks for his generous assistance in the preparation of this paper.

REFERENCES

Gaposchkin, E.M., and K. Lambeck, 1969 Smithsonian Standard Earth, Smithsonian Astrophysical Observatory Special Report No. 315, May 18, 1970.

Guier, W.H., and R.R. Newton, The earth's gravitational field as deduced from the doppler tracking of five satellites, Journal of Geophysical Research, Vol. 70, No. 18, September 1965.

Lundquist, C.A., and G. Veis, Geodetic parameters for a 1966 Smithsonian Institute Standard Earth, Smithsonian Astrophysical Observatory Special Report No. 200, Vol. 1, Union of Geodesy and Geophysics, October 1967.

Martin, C.F., and N. Roy, An error model for the SAO 1969 Standard Earth, presented at Third International Symposium on the Use of Artificial Satellites for Geodesy, Washington, D.C., April 1971.

PRECISION TRACKING SYSTEMS OF THE IMMEDIATE FUTURE: A DISCUSSION 10

David E. Smith

Geodynamics Branch
Trajectory Analysis and Geodynamics Division
Goddard Space Flight Center
Greenbelt, Maryland

INTRODUCTION

This paper discusses briefly the present status and future expectations of four satellite tracking systems, satellite-to-satellite tracking, lasers, very long baseline interferometry (VLBI) and geoceiver. None of these techniques are being fully exploited at the present time but all can be expected to provide measurements in the next few years of a quality that will contribute extensively to studies of Earth and ocean dynamics.

SATELLITE-TO-SATELLITE TRACKING

This technique has been discussed extensively during the last few years as a possible means of maintaining current orbits on active spacecraft and also as a precision tool for studying the perturbations in satellite motion for Earth physics. In its simplest terms satellite-to-satellite tracking is an electronic tape measure connecting a master satellite, usually depicted in a high stable orbit, with a relatively low altitude, strongly perturbed spacecraft. The big advantage for Earth physics of satellite-to-satellite tracking compared to normal tracking is that extensive coverage both geographically and in time is possible with nearly all proposed systems. Indeed, it has been argued that this technique is probably the only way many of the objectives described in the Williamstown Report on Solid-Earth and Ocean Physics (ref. 1) can be achieved.

Although satellite-to-satellite tracking is not yet a reality the technique has essentially been explored and applied to problems of the lunar gravitational field. The way lunar satellites are tracked from the Earth is essentially the same method and, furthermore, it has been successfully spplied to the mascon problem where the perturbations, of too high a frequency for adequate representation by spherical harmonics, were shown by Muller and Sjogren (ref. 2) to be correllated with topographical features.

The type of spaceborne tracking system that will be used for the Earth physics investigations is expected to be similar to the Goddard Range and Range-Rate System (GRARR) which operates at S-band. The present accuracy of the range-rate measurements based on an averaging time of 10 seconds is about 0.3 mm/sec compared with the 0.03 mm/sec which will be actually required for Earth physics investigations. Improvement of the system to the required level is not expected to be a major problem.

LASER TRACKING

Of the four systems being discussed the laser technique has probably been in operation longer than any of the others. However, only a limited amount of operational experience has been gained with this system, and most of that has been gained during the last year. In concept, the laser is probably the simplest of all measuring devices since, like radar, it sends a pulse of energy towards the spacecraft which is reflected and received back down near the transmitter. The real measurement is the roundtrip travel time which is then turned into a range.

Systems of this kind have been operating in a network configuration only recently and then with only a few stations and with systems not fully tested. Furthermore, the best way of analyzing these data for Earth physics purposes has not yet been determined and, in this respect, puts this system in essentially the same position as the others.

In the United States it is Goddard Space Flight Center and the Smithsonian Astrophysical Observatory who have been the main organizations responsible for the development of laser tracking of artificial satellites and for investigating and fostering the application of these systems to Earth physics. The present systems probably have an accuracy of about 50 cm but this is a rather arbitrary figure because there is no absolute scale by which their quality can be judged and for this reason a laser system tends to be judged by the rms range noise about some reference, such as an orbit. In some respects, however, this is not an undesirable parameter, provided it is not confused with accuracy, because the noise is an indication of the stability, albeit short-term, of the system, and for many investigations this may be even more important than accuracy.

The quality of the laser in the next few years is expected to improve to about the 5 to 10 cm level. This is not a great deal better than is currently being claimed for the present lunar laser ranging system and is, in fact, a little worse than is expected of future lunar systems. The major disadvantage of the laser over competitive techniques is that it is a fair weather instrument. The operation of the systems during both day and night has been routine for several years but little can be done to overcome clouds or heavy fog, except perhaps, by choosing a more favorable site location. This question of site selection is one that can

be expected to be of considerable importance for all the precise tracking systems of the future because their quality will make them sensitive to the very small changes in station position associated with such movements as creep, subsidence, tidal loading and fault slips. The question of weather is just one more factor in an area which can be expected to become increasingly complex.

Finally, a problem that is unique to the laser, and for which very little information is presently available, is the restrictions that may be placed on the operation of the system near highly congested air-traffic lanes. At present, safety regulations require that an observer keep watch for aircraft and that the system cease operation, when necessary. However, the locating of stations on the west coast by GSFC is necessitating the addition of radars to the systems that will detect aircraft at much greater distances and the impact of this may be to reduce the overall effectiveness and efficiency of the system. These questions will only be answerable after a period of operation under these conditions.

VERY LONG BASELINE INTERFEROMETRY (VLBI)

It is only recently that the technique of very long baseline interferometry has been applied to the problems of geodesy, notably, baseline determination. However, VLBI has been successfully demonstrated as a radio astronomical tool as far back as 1967 with many measurements of angular resolutions smaller than a thousandth of a second of arc (ref. 3).

Of the techniques being discussed here this is the only one which has the ability to make measurements in an inertial frame of reference

and this is an important advantage. With this capability VLBI can be used to monitor the motion of the Earth in space and on its axis in addition to the ability to measure chord lengths. However, the prime consideration here is for the interferometer to be used to track a spacecraft. Recently VLBI experiments conducted jointly by SAO and GSFC on an ATS spacecraft from sites at Rosman and Mojave have detected fringe rates that correspond to changes in the velocity of the spacecraft as small as 1 mm/sec and with a resolution of the order 0.1 mm/sec. These velocity measurements can greatly enhance the position determination capability of synchronous spacecraft, thereby enabling the recovery of low degree and order geopotential coefficients to be significantly improved.

One of the major problem areas of VLBI is in the atmospheric distortion of the ray paths to the source. For very short baseline systems, such as Minitrack, the ray paths are almost identical for both antennas and consequently the atmosphere is not of major importance. However, as the baseline increases to inter-continental distances the ray paths through the ionosphere can differ by several meters even at C-band frequencies. Atmospheric modeling can be applied to the measurements but to achieve accuracies of 10 cm will require models accurate to a few percent and this may not be practical.

GEOCEIVER

The Geoceiver is a continuously integrated doppler system, similar in design to the TRANET doppler stations but considerably smaller and simpler yet designed to produce position determinations of equal quality.

The Department of Defense is apparently obtaining over thirty of these systems and the first few production models are already being tested.

One method of using the Geoceiver system is in a small dense network of, say 7 or 8 stations on a continent with baselines of about 1000 km. Studies of the potentialities of such a network (ref. 4) indicate a position determination of the spacecraft to be about 10 cm. Now the Geoceiver is not, inherently, a ranging system but when used in groups the biases for each of the systems can be recovered enabling spacecraft position to be determined with considerable precision. However, individually, the stations cannot be used as ranging systems and this is probably the biggest disadvantage of Geoceiver.

The production models of Geoceiver are reportedly exceeding the specifications (ref. 5) and under test the rms of the deduced range residuals are about 5 cm. These tests suggest that a geometric determination of the spacecraft position with respect to the ground stations is probably of the same order and that the absolute accuracy of the spacecraft position while being tracked is largely due to the errors in the locations of the ground stations and unmodelable atmospheric effects. Furthermore, it seems highly probable that with sufficient data the station positions relative to each other could be improved upon to the level of a few tens of centimeters and in a geocentric system to at least one meter.

The possible application of these systems to the calibration of a spaceborne altimeter are obvious but with our present gravitational models it would be impossible to extend the same quality of calibration

to areas over which the spacecraft was not being continuously tracked by several of these systems.

DISCUSSION

During the next few years the four systems that have been discussed can be expected to approach the quality required for the Earth physics investigations of the kind described in the Williamstown report (ref. 1). However, it is very doubtful at the present time if the software availale for handling these data and our knowledge and ability to model the effects of the atmosphere are anywhere near adequate. Consequently, even if these systems provide measurements of 10 cm precision, it is doubtful that we shall be able to make proper use of the data unless considerable effort is expended on improving orbital perturbation theories, numerical integration systems, atmospheric and gravitational modeling, etc.

Table 1 is an attempt to summarize the present capabilities of the four systems that have been described, together with an estimate of their precision in two or three years time. Some of the advantages and disadvantages of each of these systems are also given but it should not be inferred that the systems should be competitive, but rather complementary. When working at the 10 cm level it will be dangerous to take for granted the results of any one system for very many years until it has been fully proved. The confirmation of geophysical measurements by at least two systems employing different techniques and data handling methods should be a major aim of this new work for many years to come.

References

1. "The Terrestrial Environment: Solid-Earth and Ocean Physics" NASA CR-1579, April 1970.

2. Muller, P. M. and W L. Sjogren, "Mascons: lunar mass concentrations", Science, Vol. 161, p. 680, 1968.

3. Cohen, M. H., D. L. Jauncey, K. I. Kellerman and B. G. Clark, "Radio interferometry at one-thousandth second of arc", Science, Vol. 162, p. 88, 1968.

4. Brown, D. C., "Near term prospects for positional accuracies of 0.1 to 1.0 meters from satellite geodesy", D.B.A. Systems, Inc., Final report on contract number F19628-69-C-0264 for AFCRL, Report Number 70-0501, August 1970.

5. Private communication with Duane C. Brown, D.B.A. Systems, Melbourne, Florida, Sept. 1971.

	PRESENT PRECISION 1971	FUTURE PRECISION 1973	ADVANTAGES	DISADVANTAGES
SATELLITE-TO-SATELLITE TRACKING	0.3 mm/sec	0.05 mm/sec	near continuous coverage	2 active spacecraft
LASERS	35 cm	5 - 10 cm	one station operation, mobile	fair weather instrument, aircraft
VLBI	0.1 mm/sec	0.01 mm/sec(?)	inertial reference frame	large antennas, fixed locations
GEOCEIVER (network)	10 cm	5 cm	cheap, easy to use	large numbers of stations

Fig. 1 Comparison of Systems

RADAR PULSE SHAPE VERSUS OCEAN WAVE HEIGHT

11

A. Shapiro, E.A. Uliana, and B.S. Yaplee

E.O. Hulburt Center for Space Research
Naval Research Laboratory
Washington, D. C. 20390

The radar height distribution of the vertical ocean surface structure has been measured with a 1 ns radar system from a tower platform. It is shown that the reflecting properties of the ocean biases the mean sea level by about 5% of the significant wave height, and that the radar measured water wave height is reduced by about 6% of the significant wave height. For SWH up to 2 m, it can be assumed that the shape of the distribution is normal and that the mean sea level and water wave height of the observed ocean surface can be directly obtained from the convolved pulse, that is obtained from a high flying altimeter, with accuracies of a few centimeters. Measurements of higher sea states and utilization of an aircraft platform for pulse width limited observations are needed to confirm these preliminary results.

INTRODUCTION

A series of radar measurements over the ocean were made in the spring of 1970 to determine the effect of water waves on extremely narrow radar pulses. The objective of the measurements was to obtain from an analysis of the interaction of a 1 nanosecond radar pulse with the vertical water wave structure quantitative information about the electromagnetic (e-m) ocean height distribution. This information is needed to establish the potential height accuracy and resolution which could be attained with a high resolution satellite radar altimeter over the ocean.

OBSERVATION PROCEDURE AND METHOD OF ANALYSIS

The radar system [1] was installed on the Chesapeake Light Tower (Fig. 1) which is located about 15 miles east of Virginia Beach, Virginia. The radar antennas are about 21 meters above the mean sea surface and sampled a 70 cm diameter ocean surface spot 10 times per second. The ocean wave heights were monitored by three wave staffs separated by about 1.5 m and placed in a delta configuration about the radar illuminated spot (Fig. 2). The wave staff outputs were recorded simultaneously with the corresponding radar return on digital magnetic tape at the 10 Hz rate. For range and reflectivity calibrations, a corner reflector was placed about 3 m above the mean sea surface in the center of the radar beam. A raw data record is shown in Fig. 3 where the wave staff record has been superimposed on the radar return, but shifted in delay, so as to allow the pulse shape of the radar return to be seen more clearly. The ocean radar returns provide two independent types of information, the delay variations of the radar echo with time and the amplitude variations for the different delays. These two effects will be analyzed separately.

The radar height of the sea surface is obtained by measuring the differential delay between the peak amplitude of the sea surface and corner reflector radar return with a potential precision of 0.25 ns. It can be seen that the radar height variations correspond very closely to the wave staff record.

The amplitude variations as a function of observed delay is obtained by calibrating and converting each amplitude to a normalized radar cross section and then averaging the normalized radar cross section for each delay. The two effects are then combined to obtain the resultant electromagnetic height distribution or impulse response.

It was found that the observations could be separated into two groups, one representing the lower sea states covering significant wave heights (SWH) from 0.85 to 1.25 m with wind velocities ranging from 0 to 20 knots and higher sea states with SWH from 1.15 to 1.80 m and wind velocities from 20 to 27.5 knots. The basic difference between the two groups was the noticeably increased fine structure in the height distribution for the larger sea state that was superimposed on the basic gaussian distribution.

In the following presentation of the results a typical example of each group will be discussed to indicate the effect of the sea state on the radar returns and their relation to the wave staff data.

WAVE STAFF AND RADAR HEIGHT MEASUREMENTS

When the amplitude variations of the radar return are removed and only the delay of the peak amplitude is plotted as a function of time, the radar and wave staff profiles of the sea surface for a calm and 20 knot wind sea are obtained as shown in Figs. 4a, b. It is seen that for the calm sea (CLT 17) the radar essentially profiles the underlying sea surface due to the small spot size that is produced by the small antenna beam width and the low platform height. For the higher sea state (CLT 7), it is apparent that some of the higher peaks of the water waves are missed by the radar and the peaks are rounded off due to the finite spot size. The effect of this distortion on the height distribution is shown in Fig. 5a, b for the two cases and the corresponding statistical parameters are given in Table 1. For the calm sea, while no significant difference is apparent in the height distribution, there is a decrease of the skewness value from 0.15 to 0.08 for the radar height distribution. For the wind driven sea there is a decrease both in the skewness value and the width of the radar height distribution, which is apparent from the large number of measured heights near the centroid. The reduced skewness and width is probably caused by the finite size of the illuminated spot and the favoring of the lower areas for reflection, as will be shown later. The differential values of the four moments for all the observations are listed in Table 2. It is seen that the shift in height is random, with an average value of less than 1 cm, but that small biases are introduced to the width, skewness, and kurtosis values of the radar height distributions.

The wave spectra for the two cases have been plotted in Figs. 6a, b to provide further comparisons between the radar and wave staff data. The mean frequency and frequency width for the two observations are given in Table 1. Almost no difference is found for the calm sea, but a slight decrease of the mean frequency occurs for the higher sea state with a small higher frequency component appearing in the radar wave spectrum.

OCEAN RADAR IMPULSE RESPONSE

The beam width limited radar response of this experiment can be related to the equivalent pulse width limited radar response from a satellite altimeter through the ocean radar impulse response. This is obtained by multiplying the radar height distribution by the average normalized radar cross section at each height increment. Typical normal radar cross section variations as a function of

delay are shown in Figs. 7a, b and the gradual increase of the normalized radar cross section as the radar wave penetrates the deeper layers of the water wave structure was noted for all the observed sea states. The slope of the reflectivity curve varied between 3 to 10 cross section units per nanosecond, but no relation between slope and significant wave height or wind velocity could be established. Multiplying the normalized radar cross section with the radar height distributions shown previously for the two sea states, and normalizing the resultant distribution for comparison with the wave staff distribution results in Figs. 8a, b. The weighted distribution is defined as the radar impulse response or electromagnetic height distribution and would correspond to a radar return of an impulse, if a large cylindrical antenna beam were available. The shift of the radar impulse response distribution toward the troughs due to the increasing reflectivity is apparent, but the overall shape has not been greatly affected.

ANALYSIS OF IMPULSE RESPONSE AND RESULTS

The impulse response shown above are typical of 16 observations that covered a range of significant wave heights from 0.84 to 1.81 m (2.77 - 6.05 feet) and wind velocities from 0 to 27.5 knots. To obtain quantitative estimates of the changes of the impulse response distribution relative to the wave staff height distribution, the first four moments of the impulse response distribution were compared with the corresponding moments of the wave staff distribution and the differential values are listed in Table 3.

The shift of the first moment (centroid) is plotted as a function of the significant wave height in Fig. 9. The scatter in the measurements may indicate that the bias is not simply related to the significant wave height, but attempts to relate the spread of the bias to wind velocity, wave spectra skewness, and kurtosis have not been successful. It seems at present that, while other unknown factors of the sea surface structure may contribute to the shift of the electromagnetic centroid, the significant water wave heights are still the dominating parameter in the functional relation. A linear least square fit to the data shows that the bias is about 4.7 percent of the significant wave height with an rms error of ± 5 mm. The results indicate that for significant wave heights up to 2 m the error of the radar height measurements should not exceed 10 cm and, if independent water wave height measurements are available, this error could be further reduced by a first order correction.

To evaluate the potential height resolution of the radar measurements, the width of the impulse response distribution was compared with the width of the wave staff distribution in terms of their equivalent SWH. Again the only relation that could be established was an increasing reduction of the impulse response width relative to the wave staff distribution width as the SWH increased. The results are plotted in terms of the SWH shift in Fig. 10. A linear least squares fit indicates that on the average the equivalent radar SWH is reduced by about 6 percent of the geometric SWH with an rms error of ±1.4 cm.

The skewness values appeared to be random with an average value of about 0.15 for the wave staff distribution and 0.1 for the impulse response.

The radar kurtosis values were slightly smaller than the corresponding geometric kurtosis values.

Summarizing the results of the impulse response analysis, it is concluded that for small significant wave heights (up to 2 m)

1. the basic normal height distribution is preserved in the radar measurements,

2. the shift of the electromagnetic centroid is small for low SWH, but increases with SWH and may become significant for larger wave heights, and

3. the narrowing of the impulse response introduces a small error in the derived SWH.

PULSE WIDTH LIMITED PULSE SHAPE

To extrapolate from the beam width limited radar observations to the pulse width limited measurements obtained from satellite heights, the observed impulse responses were convolved with a 1 ns ramp and the resulting pulse rise time is shown in Figs. 11a, b for the two examples of sea state. It is apparent that the fine structure of the impulse response is smoothed out, and that the assumption of a simple gaussian distribution model for the impulse response would introduce little error. For a simple gaussian distribution, the mean delay is obtained at the 50 percent threshold level of the maximum amplitude, and the standard deviation can be obtained by halving the delay difference between the 84 percent and 16 percent threshold level of the pulse rise time. Applying the threshold technique to the observed data, it was found that the fine structure of the impulse response introduces peak errors of less than 1 cm to the radar mean height and radar significant wave height.

MODIFICATION OF SATELLITE ALTIMETER PULSE SHAPE AND DESIGN CRITERIA

The previously shown pulse rise time assumes infinite bandwidth receivers and no noise contribution. The finite bandwidth of a receiver will introduce an additional delay and decrease the slope of the radar return. While the additional delay can be calibrated out, at least to first order, the increased slope will reduce the accuracy if noise is present. While the receiver noise can be reduced by increasing the radar system sensitivity, the basic accuracy is limited by the intrinsic noise due to sea clutter, which is determined by the available integration time for a given spatial resolution. Thus it is desirable to maximize the slope for a given sea state if high accuracy is needed. This means that not only should the receiver bandwidth be larger by at least a factor of 2 than that needed for maximum signal to noise ratio, but also that the transmitted pulse width be small relative to the width of the impulse response or the equivalent significant wave height. The effect of a 10 ns pulse on the slope of the rise time is shown in Figs. 12a, b for the observations shown previously. In this case the pulse width is comparable to the width of the impulse response and the slope is increased by a factor of about 2. Thus for optimum height accuracy, low sea states, narrow pulse widths, and wide receiver bandwidths are necessary.

FUTURE PLANS

Additional measurements are needed to establish whether the behavior of the impulse response as obtained from a fixed platform close to the observed ocean surface can be extended to radar observations from a high moving platform. In addition, data at higher sea states are needed to determine whether the relation between the mean height and significant wave height can be extended to larger significant wave heights and whether the assumption of a simple gaussian model distribution is valid for larger sea states. If the impulse response distribution is sufficiently distorted at higher sea states, it may be possible to discriminate between swell and wind driven waves and thus obtain information on the wind velocity field.

An aircraft experiment is now being planned to fly a 1 nanosecond radar over the observing tower and obtain simultaneous radar measurements so that the assumed ergodic hypothesis, i.e., whether time and spatial water wave distributions are equivalent, can be proven. After the initial calibration of the aircraft data, the moving platform will be used to simulate pulse width limited observations and seek out higher sea states so that the data can be extended to the larger significant wave heights.

ACKNOWLEDGMENTS

The authors wish to thank D. L. Hammond for his helpful discussions on the interpretation of the data and who also designed the radar system. Special thanks are given to K. J. Craig who assembled the radar system and collected the data which made this report possible. The authors also wish to thank J. T. McGoogan and H. R. Stanley of NASA, Wallops Station, Dr. M. Swetnick of NASA Headquarters and J. W. Sherman, III of SPOC for their support of this problem.

REFERENCES

[1] B. S. Yaplee, A. Shapiro, D. L. Hammond, B. D. Au, and E. A. Uliana, "Nanosecond Radar Observations of the Ocean Surface from a Stable Platform," IEEE Transactions on Geoscience Electronics, Vol. GE-9, pp 170-174, July 1971.

TABLE 1

WAVE STAFF AND RADAR HEIGHT PARAMETERS

FOR OBS. 17 (h_w = 3.45′, v_w = 0 knot) AND OBS. 7 (h_w = 5.84′, v_w = 20 knots)

	Obs. 17		Obs. 7	
	Wavestaff	Radar	Wavestaff	Radar
$\overline{t}$ (ns)	32.3	32.4	28.9	28.9
2σ (ns)	3.5	3.5	5.8	5.5
λ	-0.15	-0.08	-0.19	-0.08
μ^4	2.8	2.8	3.1	3.0
$\overline{f}$ (Hz)	0.18	0.18	0.24	0.23
Δ f (Hz)	0.07	0.08	0.13	0.11

TABLE 2

DIFFERENTIAL MEAN HEIGHT, SWH, SKEWNESS AND KURTOSIS

FOR RADAR HEIGHT DISTRIBUTION

SWH (m)	Δh (m)	Δh_w (m)	$\Delta\lambda$	$\Delta\mu^4$	v_w (knots)	Obs.
0.84	0.004	0.018	0.11	0.02	10 NE	22
0.88	0.015	0.006	-0.07	-0.13	5 NE	20
0.88	-0.02	0.024	0.15	--	15 SE	24
0.92	-0.006	-0.006	0.13	0.04	20 SE	25
0.96	-0.008	-0.048	0.19	0.07	14 E	23
1.02	0.014	0	0.02	0.05	20 SSE	27
1.04	0	-0.012	0.1	0	0	2
1.04	0.018	0.012	0.07	0.05	0	17
1.04	-0.003	0.012	0.01	0.12	15 SE	15
1.05	0.02	-0.018	-0.12	-0.11	15 SE	13
1.15	0.01	-0.004	0.06	-0.09	27.5 S	26
1.20	0.02	-0.03	0.07	-0.06	12 NNE	5
1.26	0.016	-0.04	0.08	-0.2	6 ENE	11
1.74	-0.01	-0.09	0.05	-0.02	12 NE	10
1.76	0.009	-0.12	0.11	-0.08	21 NE	7
1.81	0.027	-0.12	0.11	0.02	20 NE	8

TABLE 3

DIFFERENTIAL MEAN HEIGHT, SWH, SKEWNESS

AND KURTOSIS FOR OCEAN RADAR IMPULSE RESPONSE

SWH (m)	Δh (m)	Δh_w (m)	$\Delta\lambda$	$\Delta\mu^4$	v_w (knots)	Obs.
0.84	0.027	0.003	0.13	-0.02	10 NE	22
0.88	0.011	-0.054	-0.1	-0.08	5 NE	20
0.88	0.006	-0.003	0.08	-0.18	15 SE	24
0.92	0.063	-0.036	0.04	-0.16	20 SE	25
0.96	0.080	-0.066	0.09	0.02	14 E	23
1.02	0.057	-0.072	0.01	-0.09	20 SSE	27
1.04	0.014	-0.003	0.07	0.02	0	2
1.04	0.057	0.003	0.07	-0.11	0	17
1.04	0.041	-0.012	0	0.03	15 SE	15
1.05	0.051	-0.102	-0.18	-0.2	15 SE	13
1.15	0.080	-0.036	0.26	-0.04	27.5 S	26
1.20	0.033	-0.042	0	-0.04	12 NNE	5
1.26	0.051	-0.12	0.12	-0.01	6 ENE	11
1.74	0.054	-0.102	0.08	-0.07	12 NE	10
1.76	0.084	-0.132	0.13	-0.13	21 NE	7
1.81	0.12	-0.222	0.14	-0.05	20 NE	8

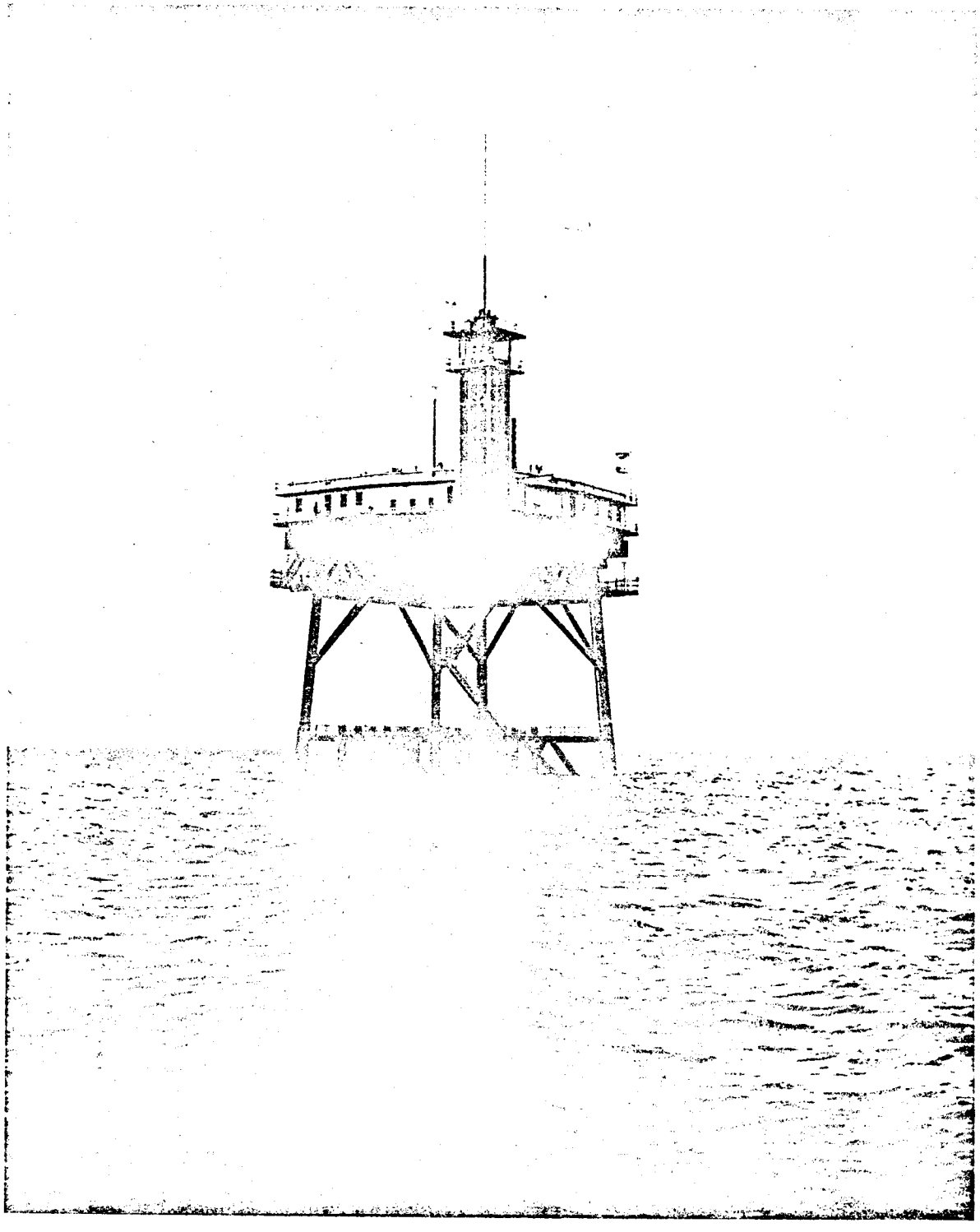

Figure 1. Chesapeake light tower.

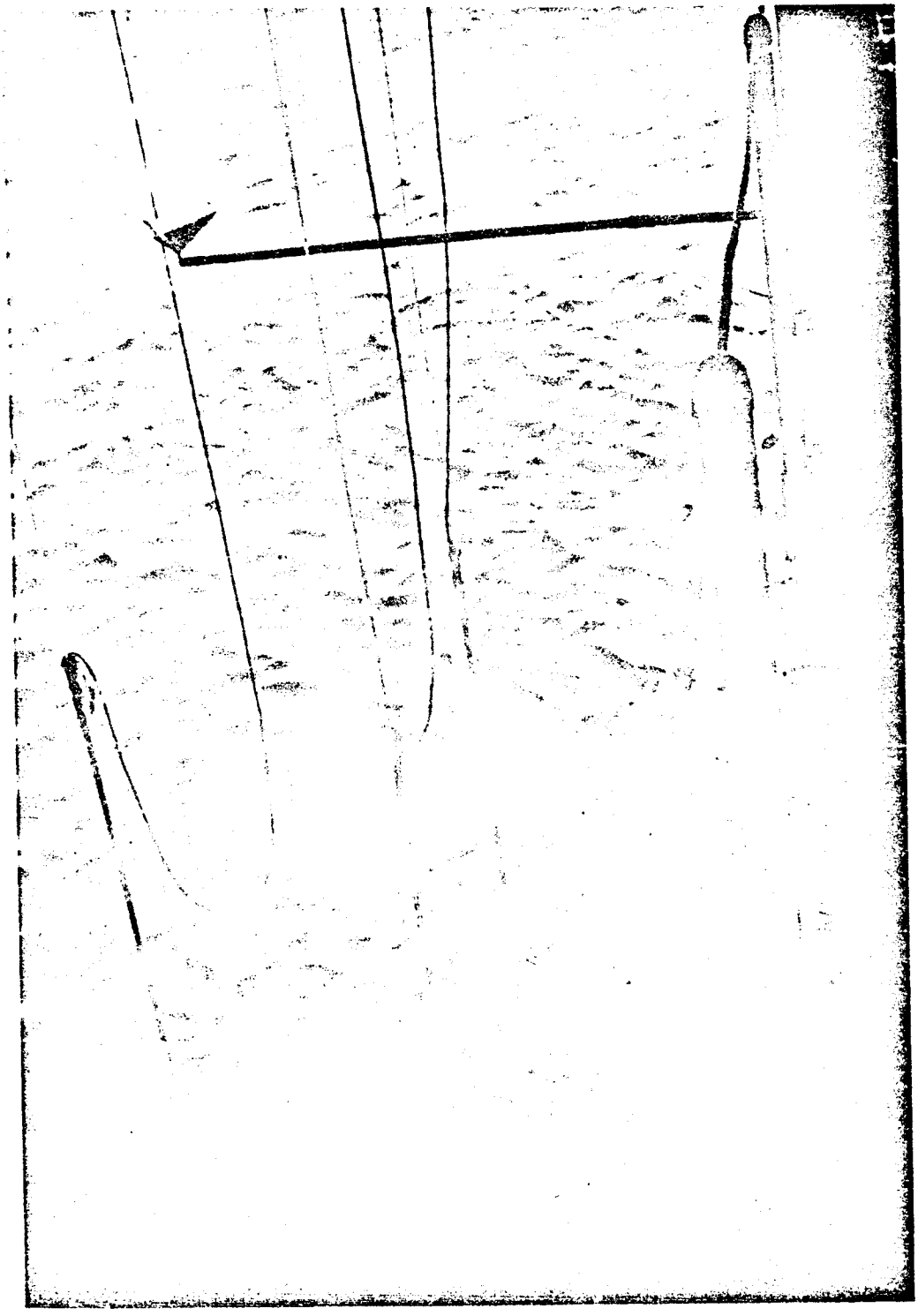

Figure 2. Placement of wave staffs and corner reflector.

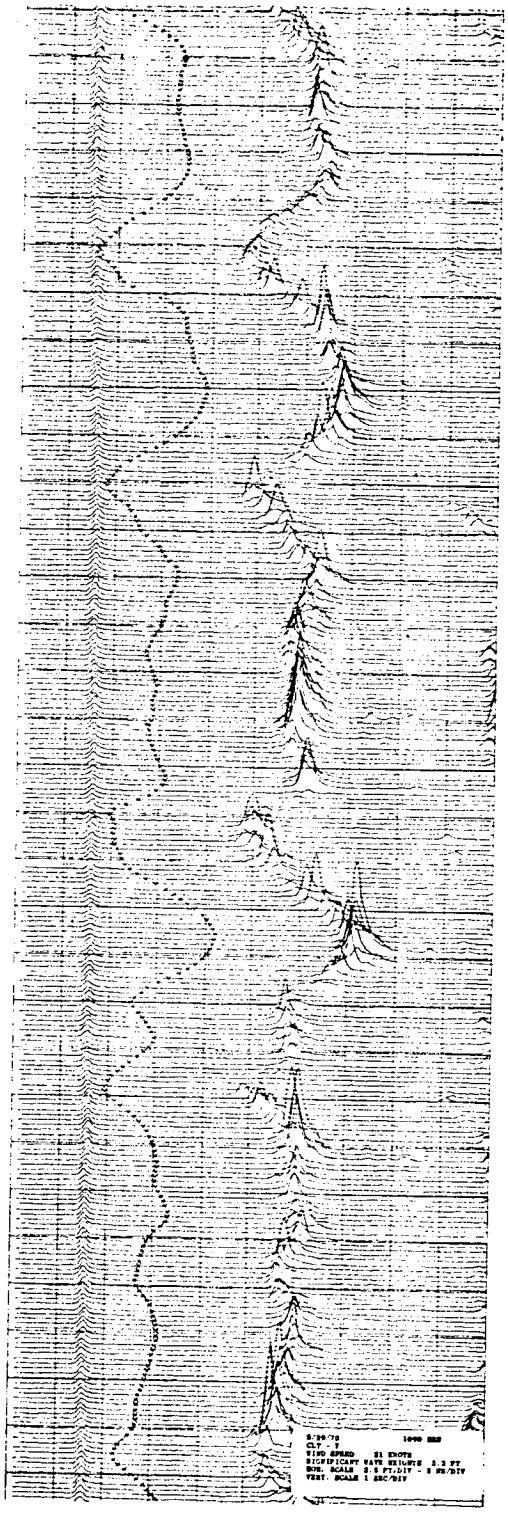

Figure 3. Raw data record for observation 7.

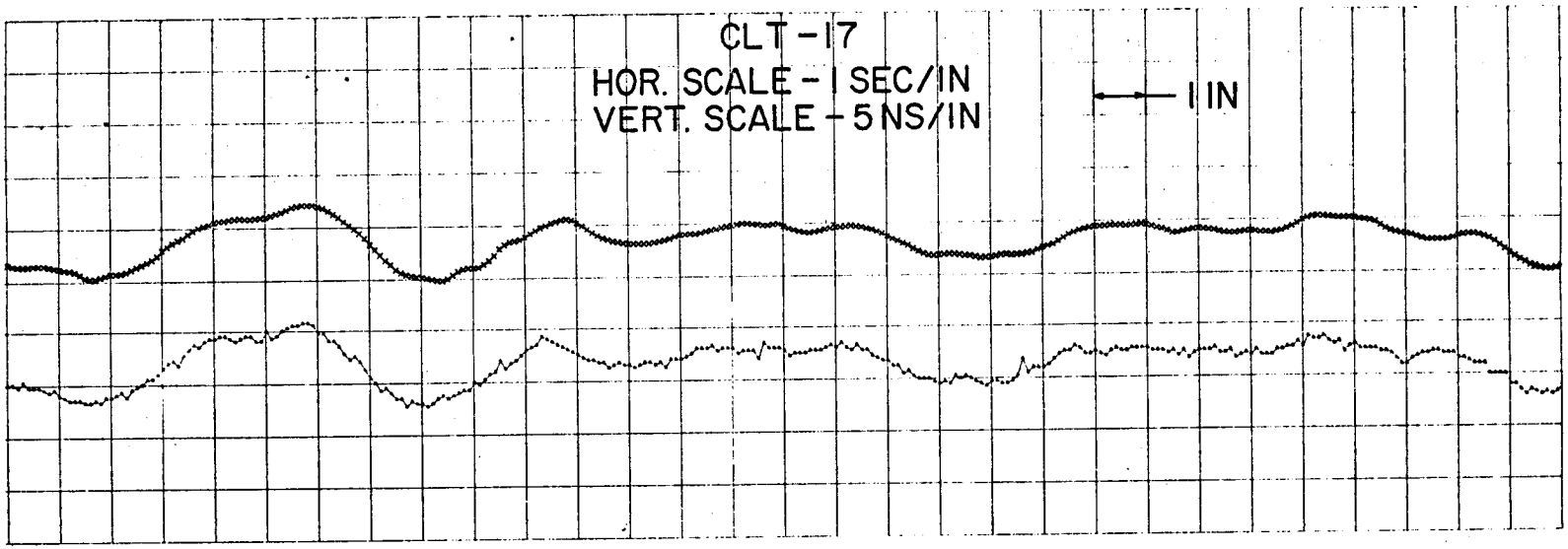

Figure 4a. Water wave profile from wave staff and radar measurements for observations 17 and 7.

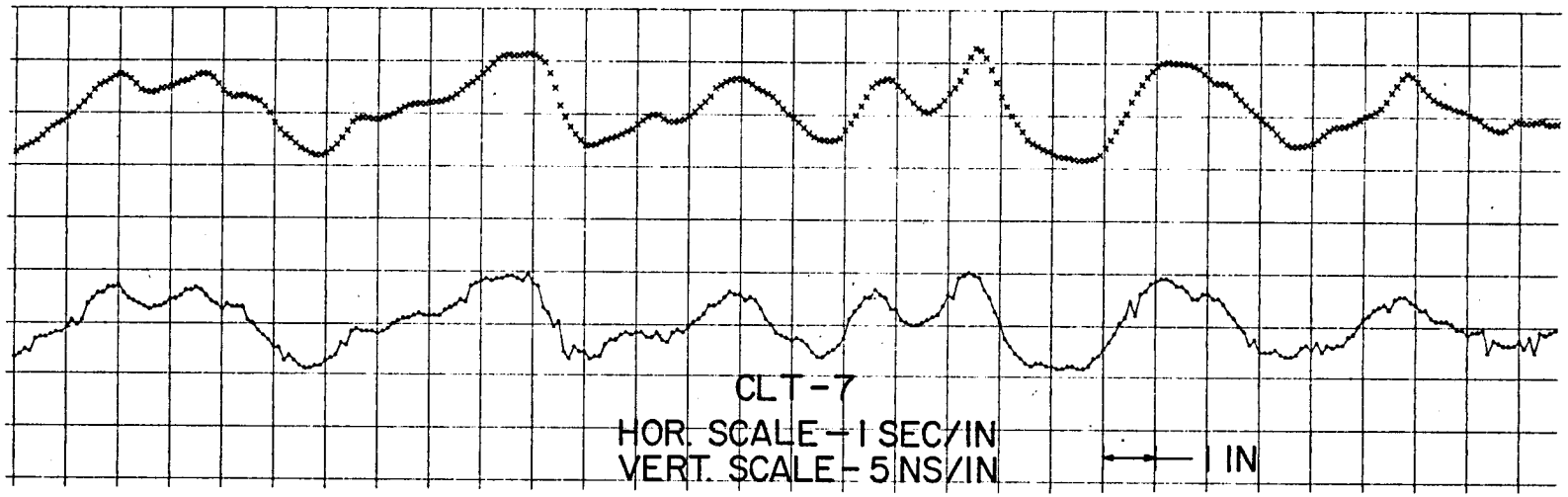

Figure 4b. Water wave profile from wave staff and radar measurements for observations 17 and 7.

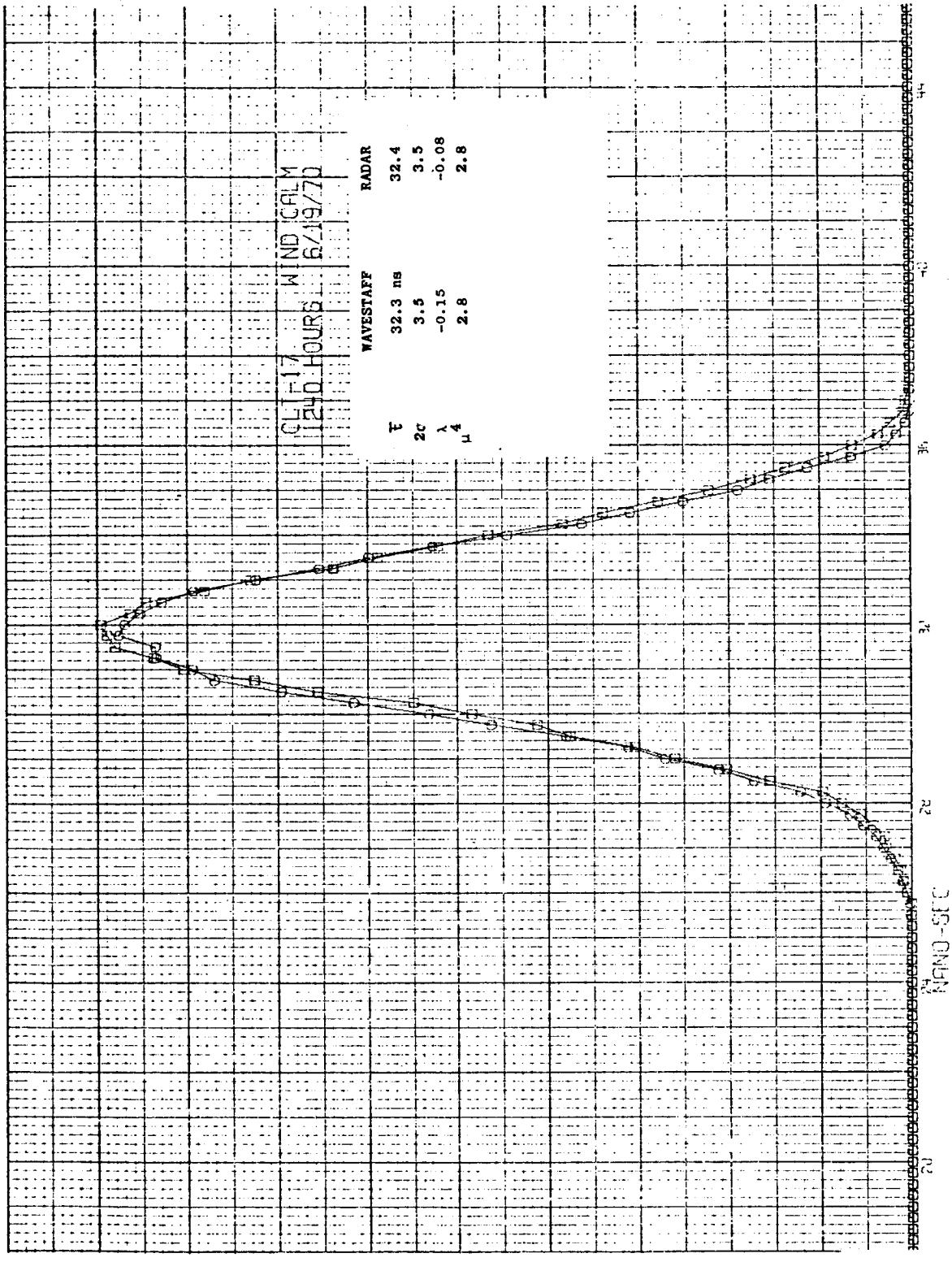

Figure 5a. Wavestaff and direct radar height distribution for observations 17 and 7.

C3

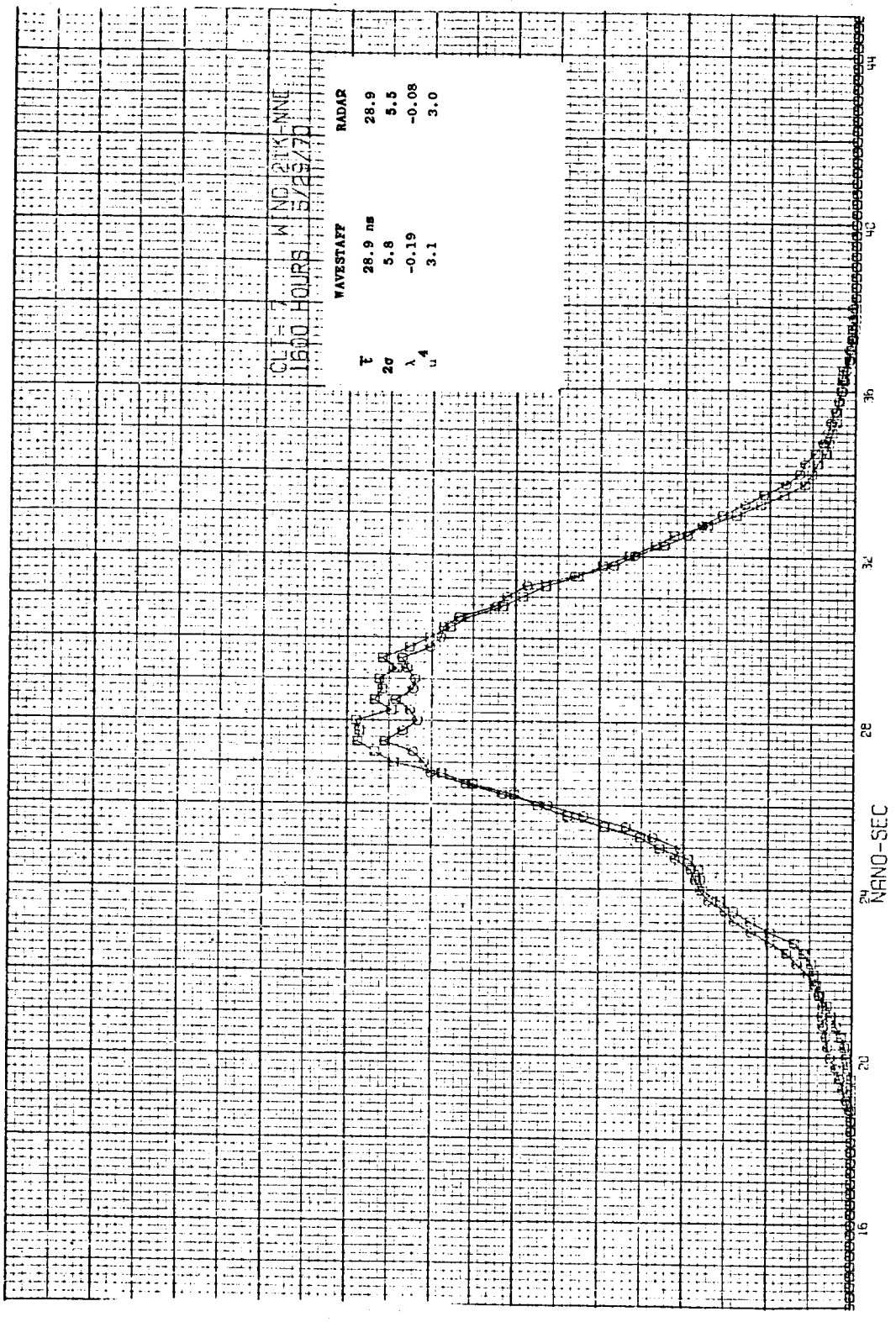

Figure 5b. Wavestaff and direct radar height distribution for observations 17 and 7.

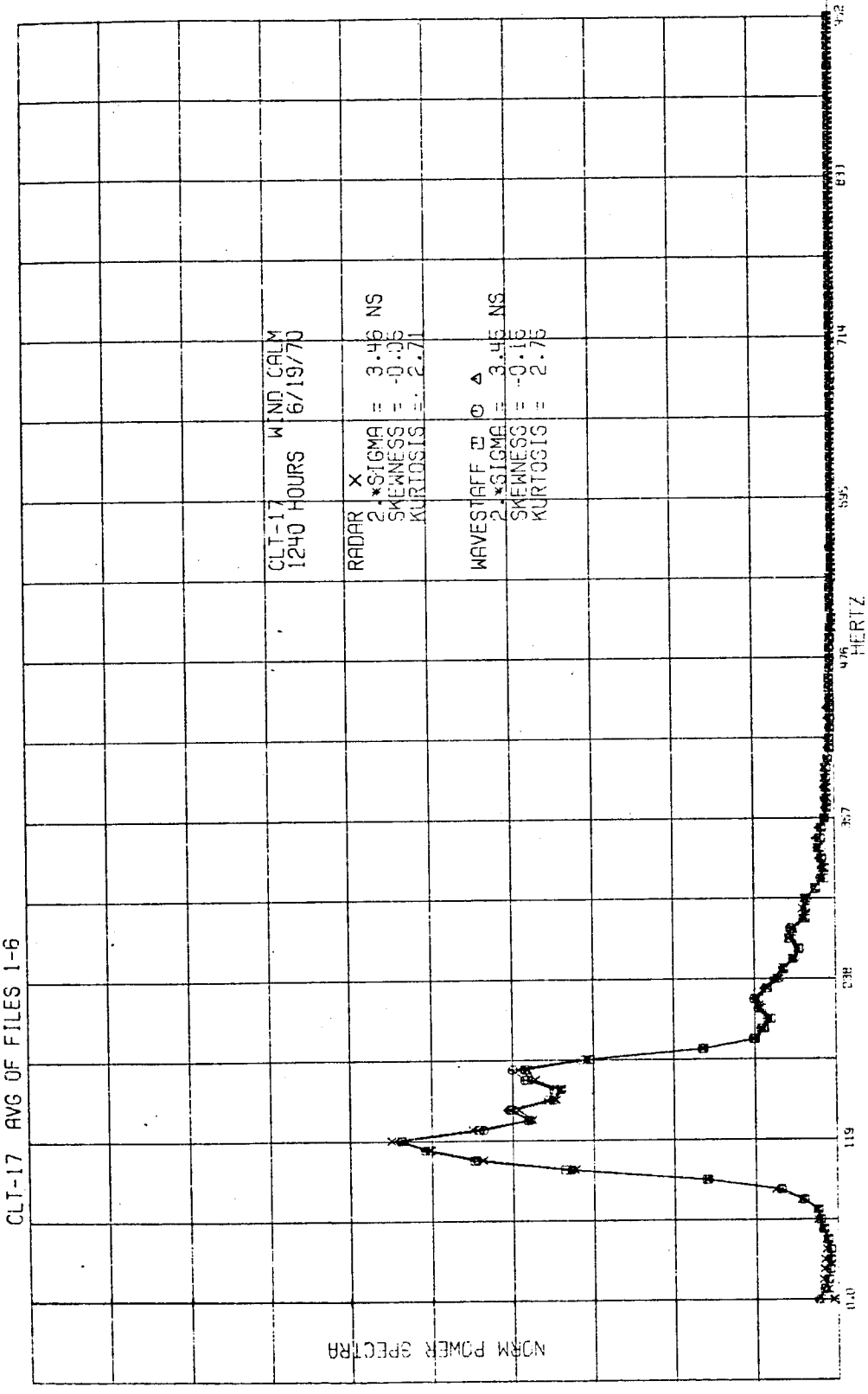

Figure 6a. Wave spectra of observations 17 and 7.

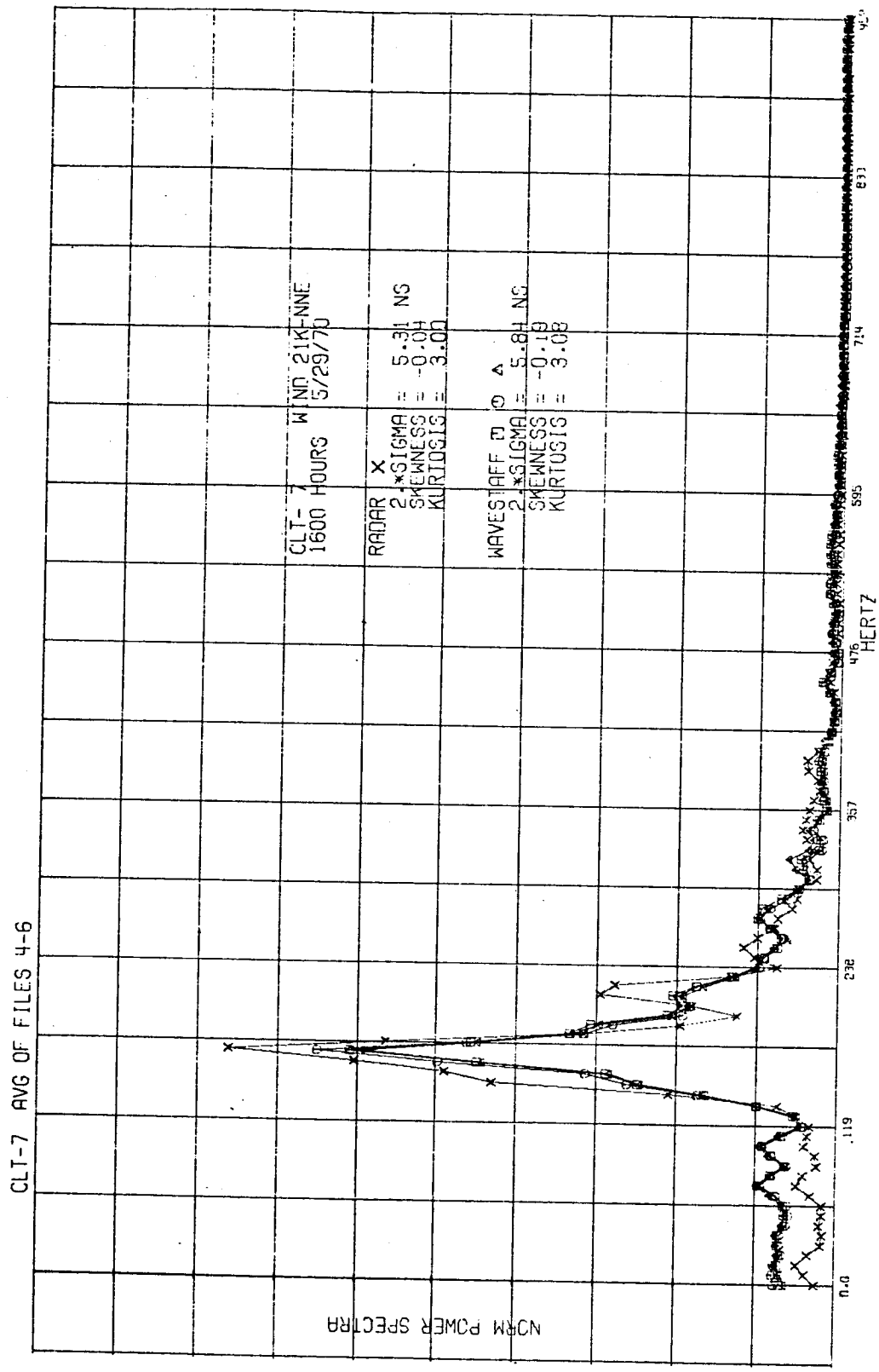

Figure 6b. Wave spectra of observations 17 and 7.

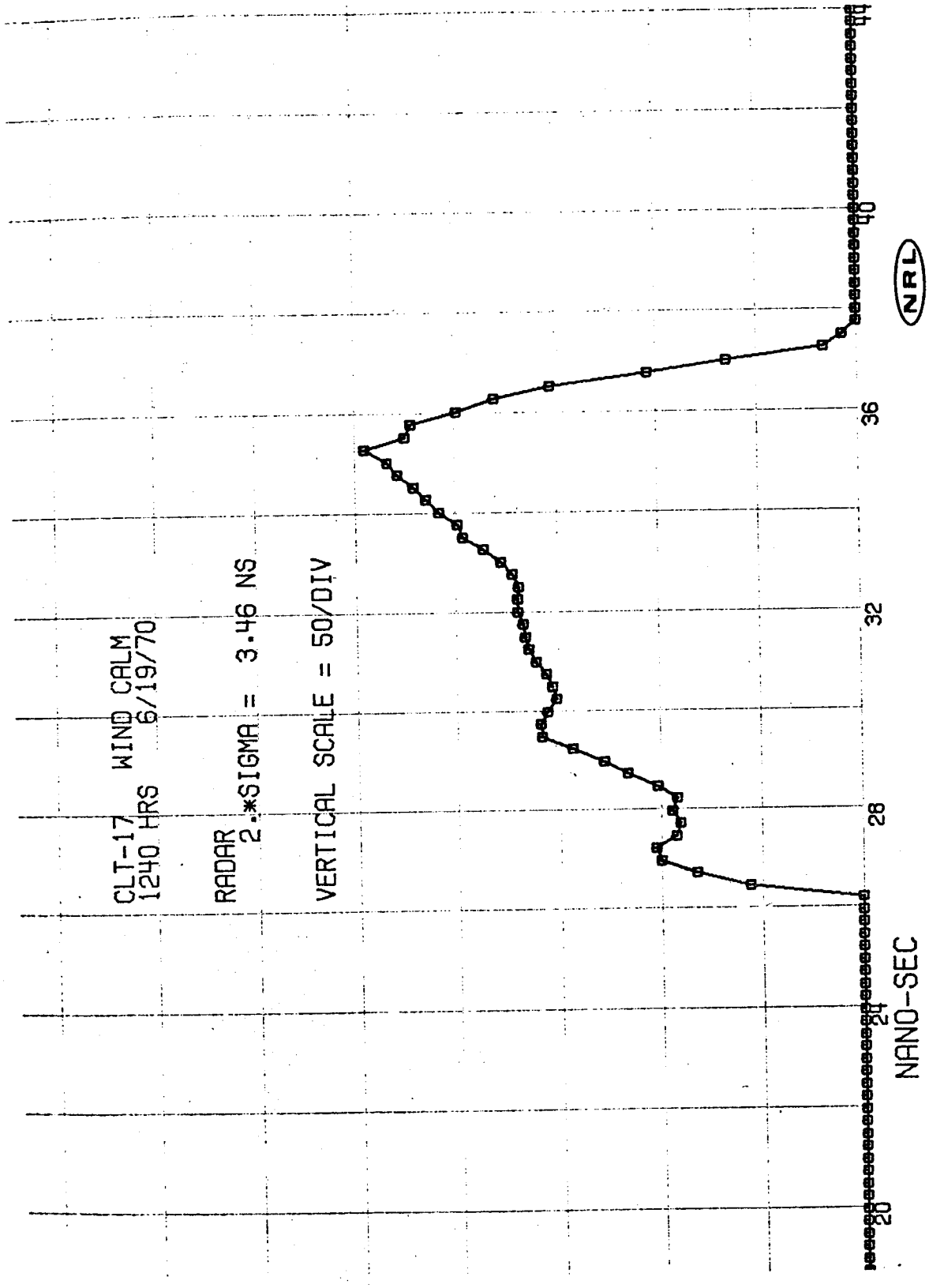

Figure 7a. Reflectivity curve for observations 17 and 7.

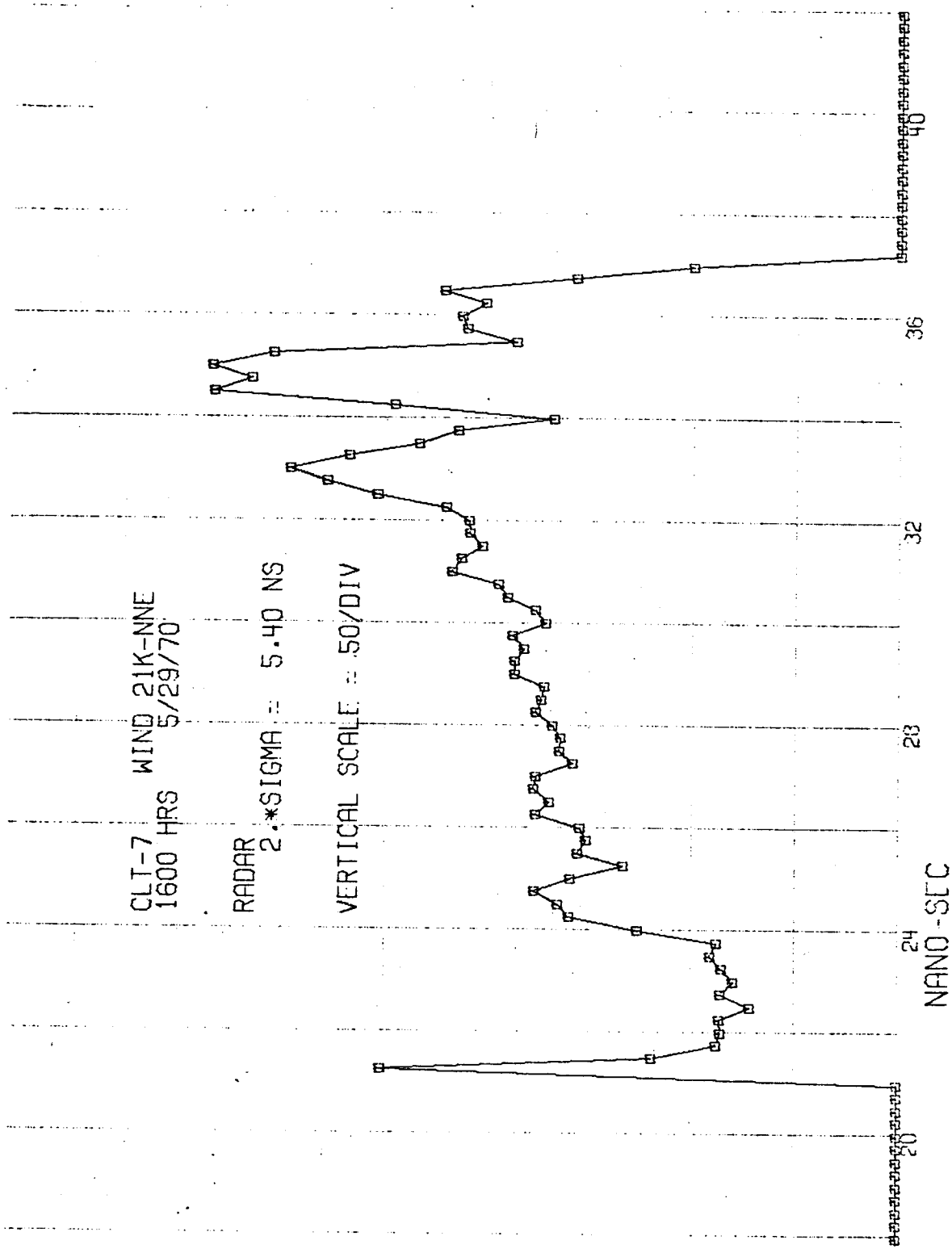

Figure 7b. Reflectivity curve for observations 17 and 7.

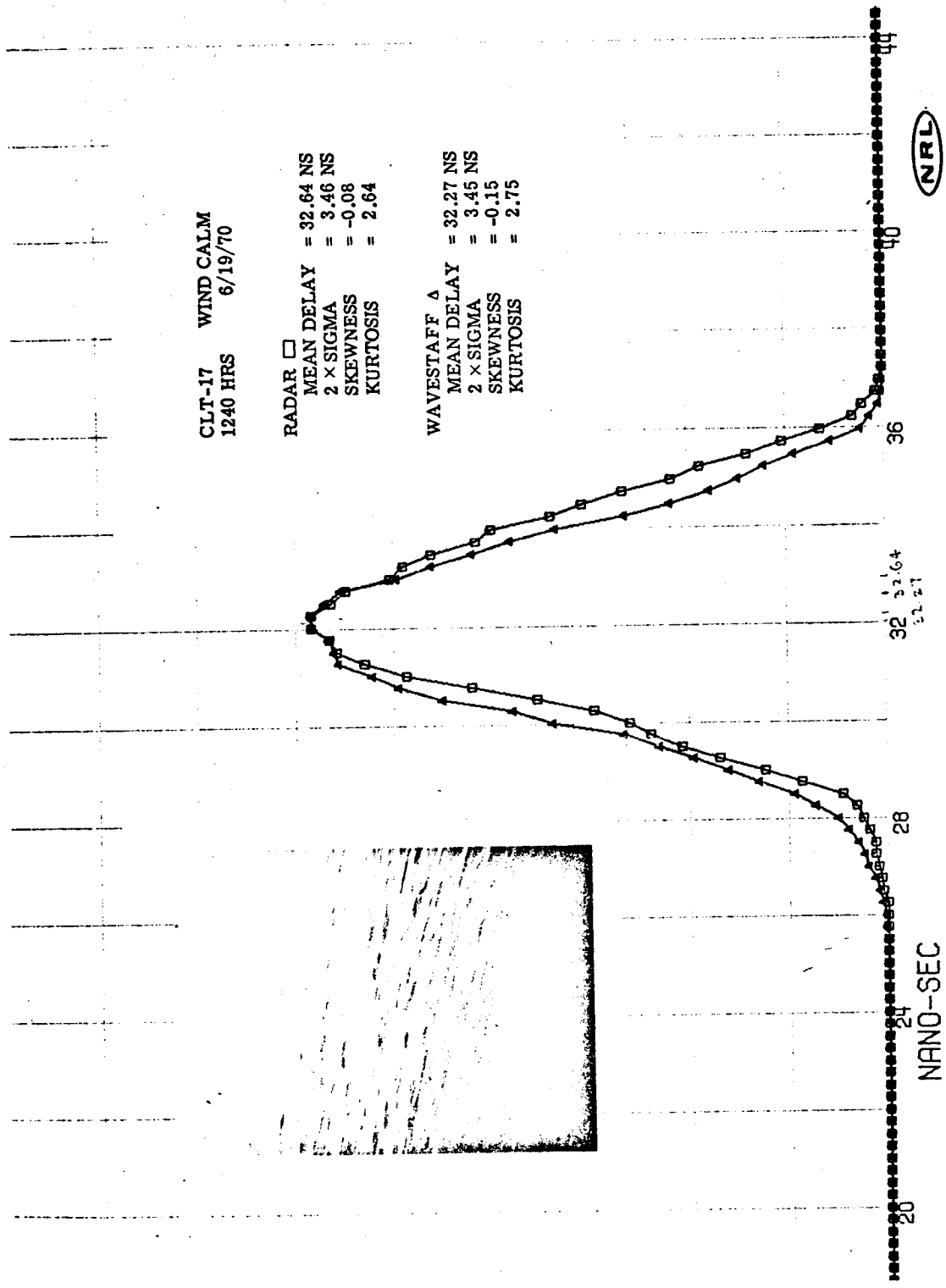

Figure 8a. Radar impulse response for observations 17 and 7.

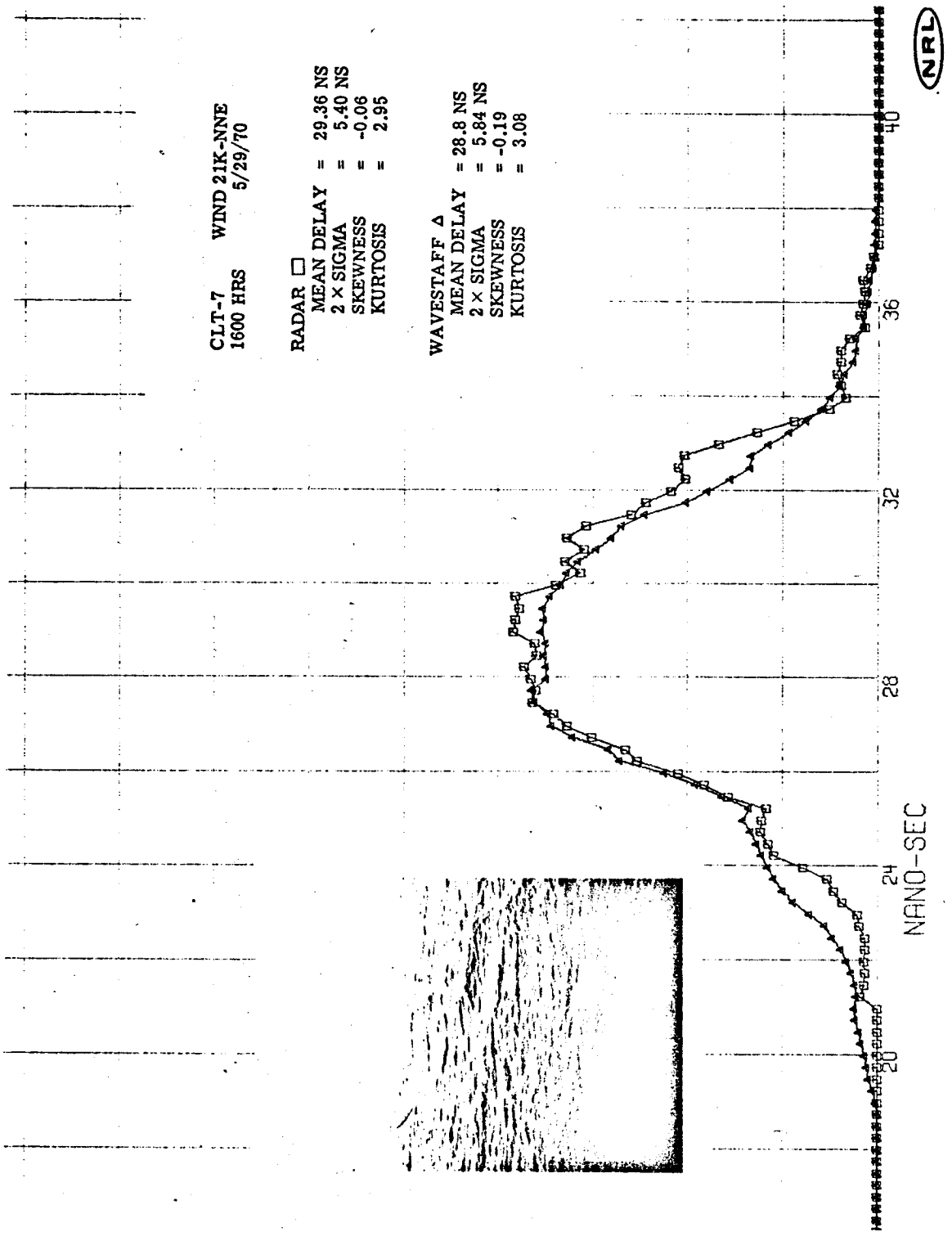

Figure 8b. Radar impulse response for observations 17 and 7.

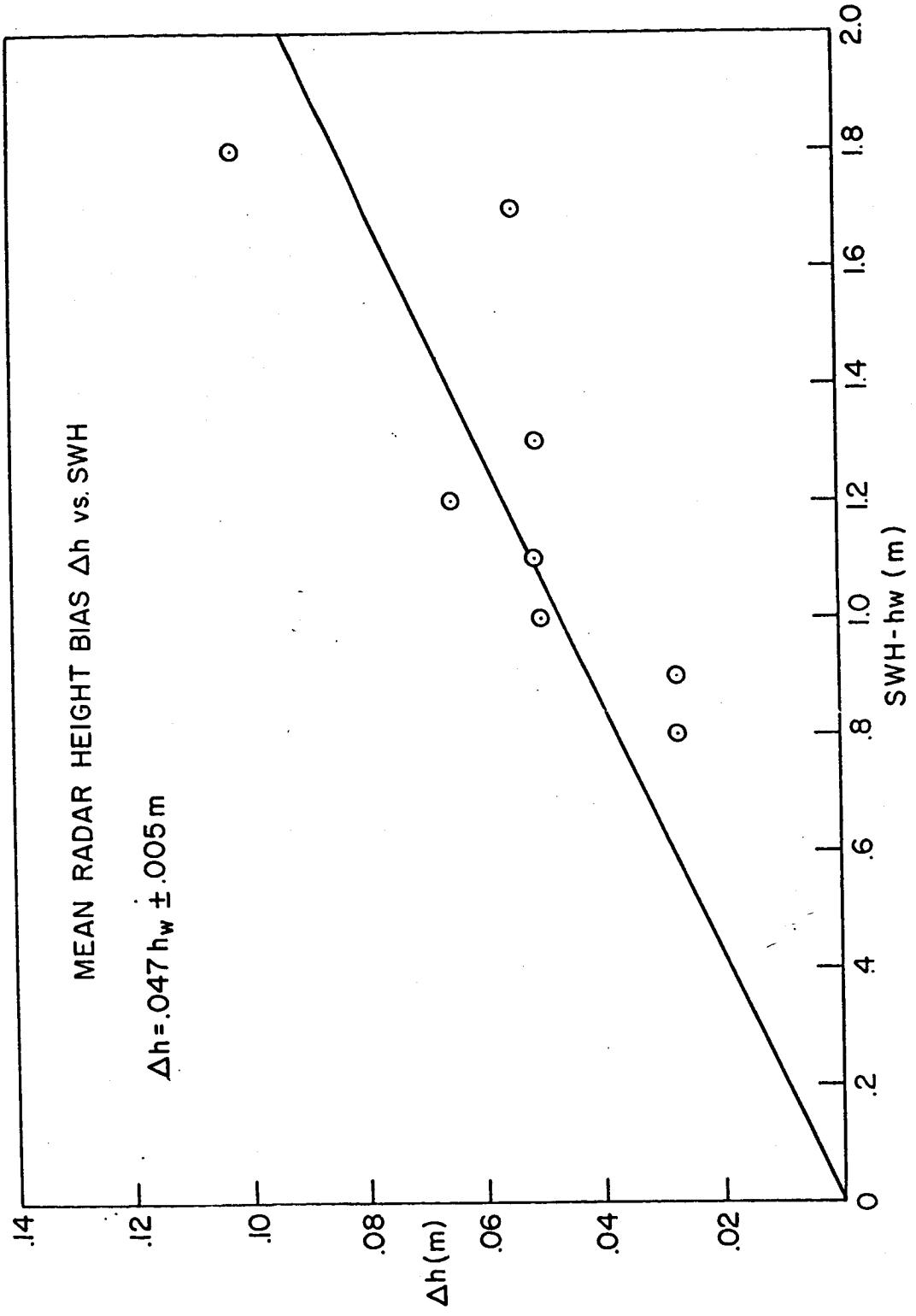

Figure 9. Mean radar height bias versus SWH.

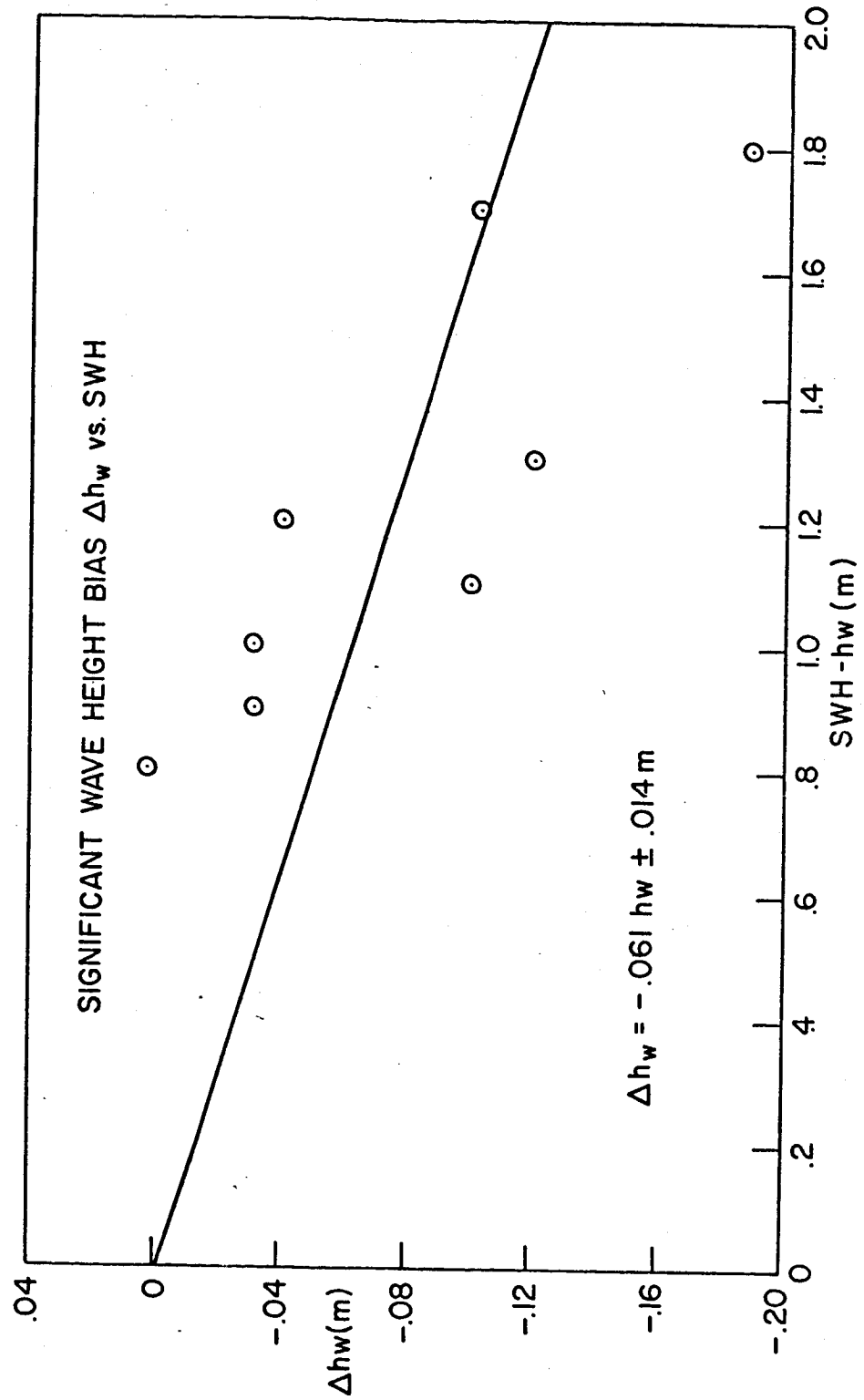

Figure 10. Radar SWH bias versus SWH.

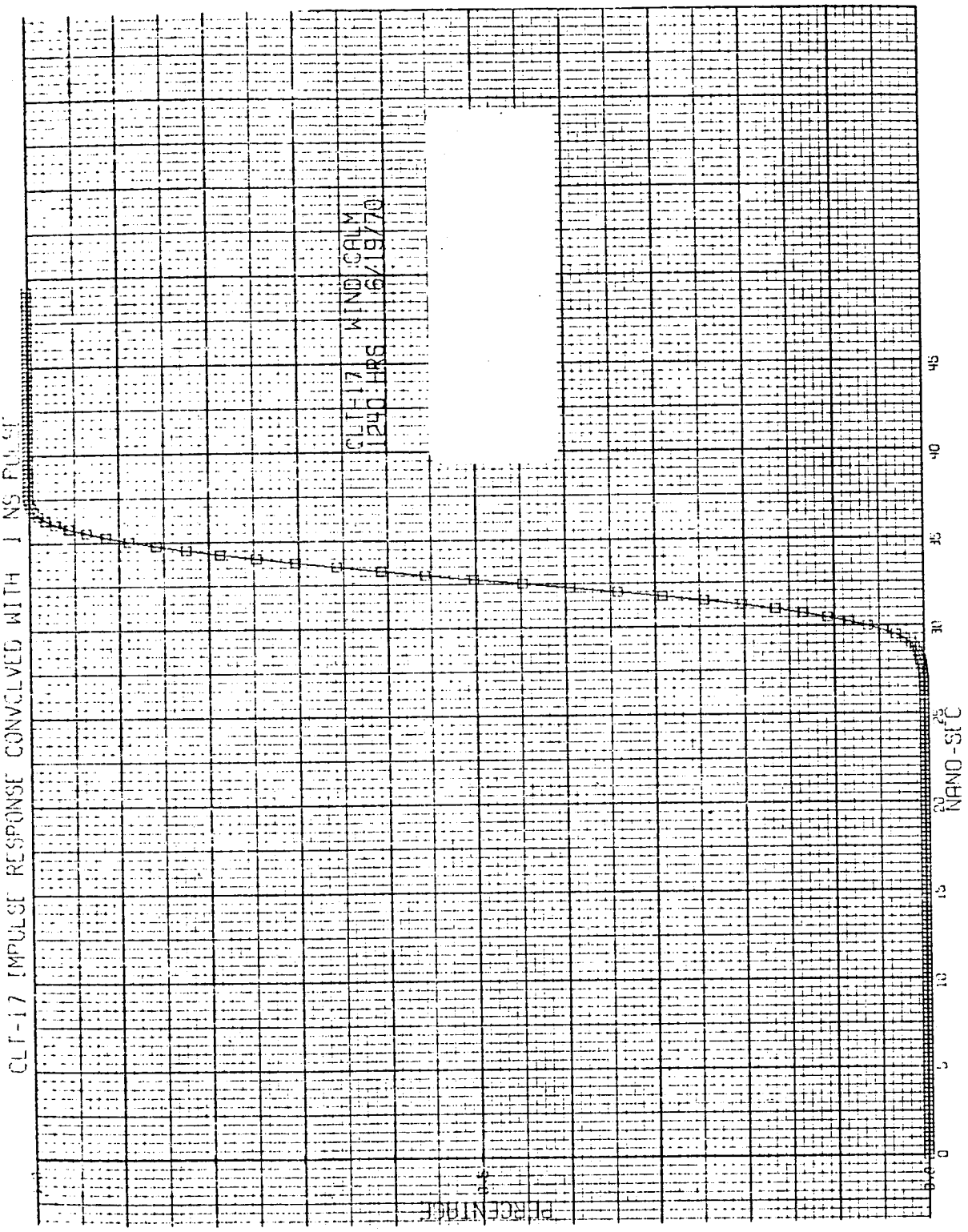

Figure 11a. 1 nanosecond pulse shape for observations 17 and 7.

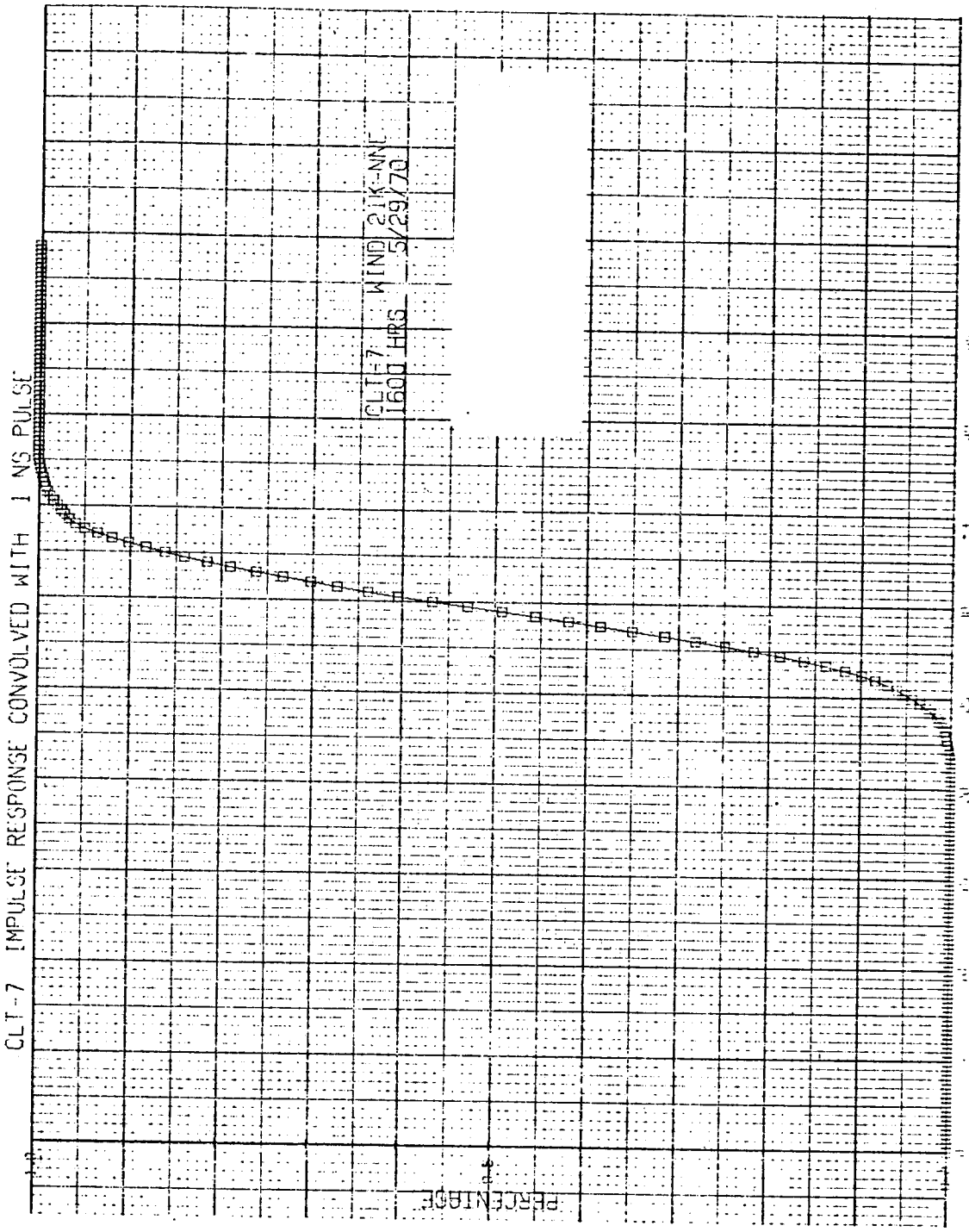

Figure 11b. 1 nanosecond pulse shape for observations 17 and 7.

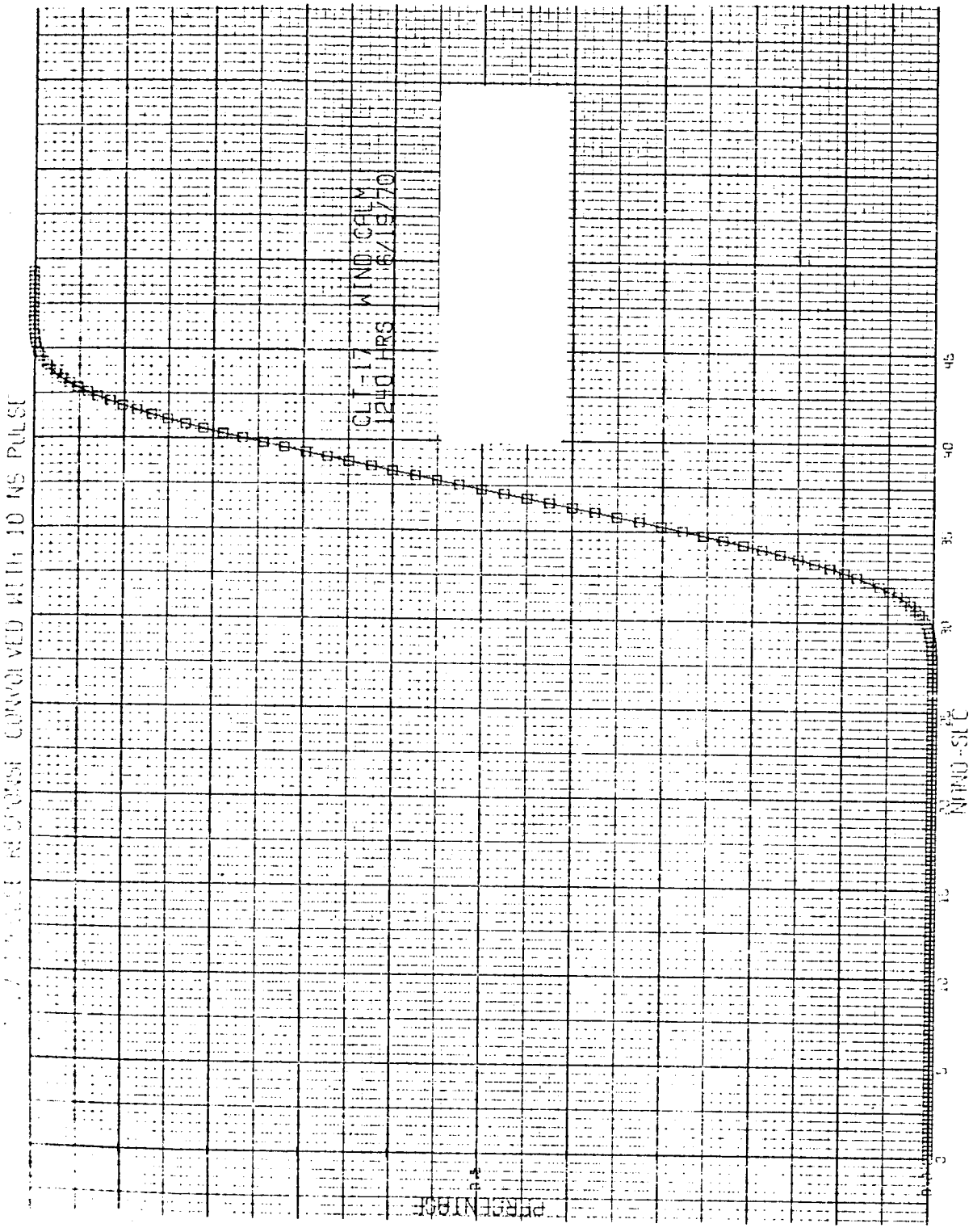

Figure 12a.10 nanosecond pulse shape for observations 17 and 7.

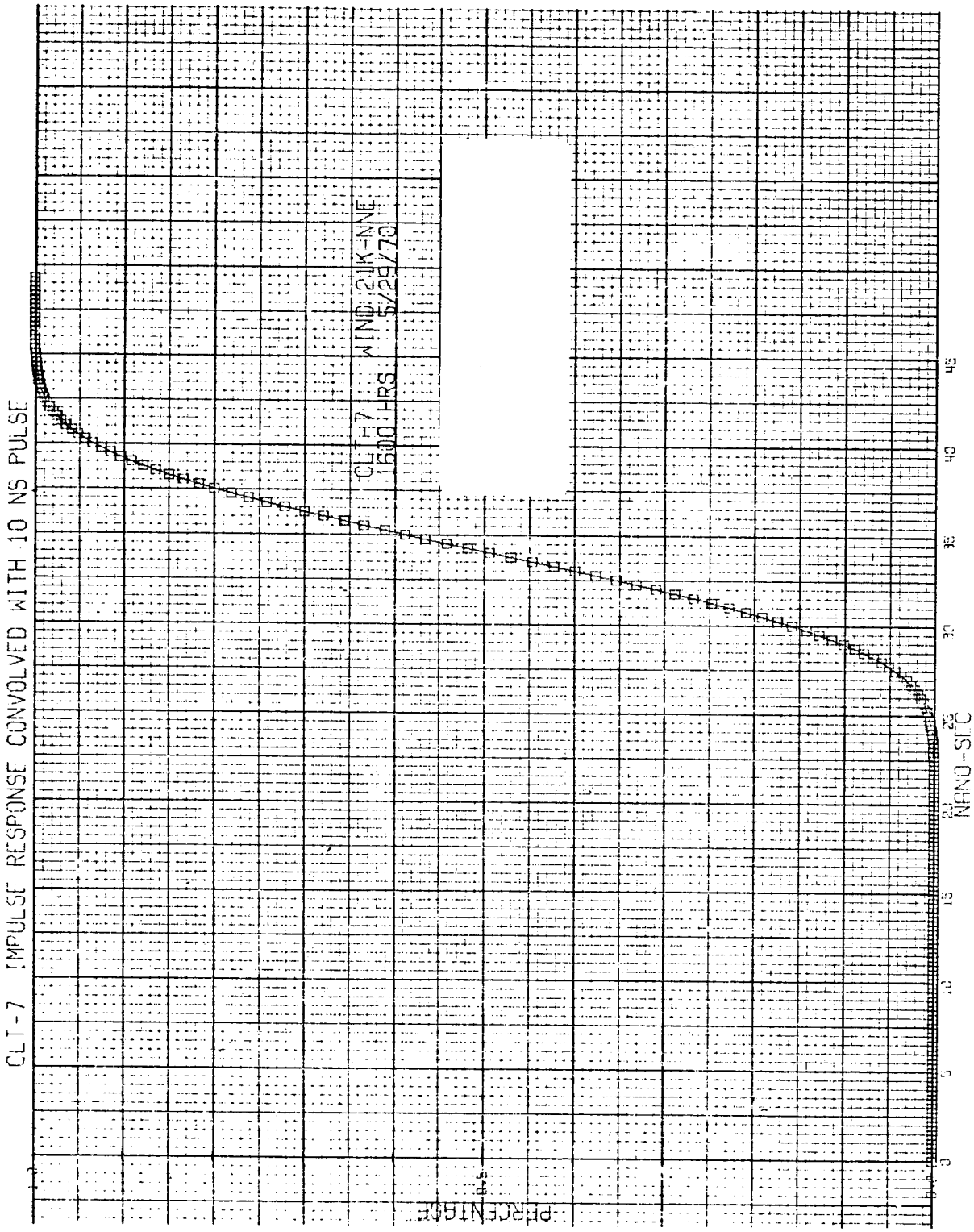

Figure 12b. 10 nanosecond pulse shape for observations 17 and 7.

B

CHARACTERISTICS OF OCEAN-REFLECTED SHORT RADAR PULSES WITH APPLICATION TO ALTIMETRY AND SURFACE ROUGHNESS DETERMINATION

12

N73-15381

Lee S. Miller and George S. Hayne
Research Triangle Institute
Research Triangle Park, North Carolina

The purpose of this paper is to summarize our current work related to geodetic altimetry. Special emphasis is placed on the effects of pulse length on both altimetry and sea-state estimation. Some discussion is also given of system tradeoff parameters and sea truth requirements to support scattering studies. The paper first considers the problem of analyzing signal characteristics and altimeter waveforms arising from rough surface backscattering.

1.0 Rough Sea Effects on the Altimeter Backscattered Waveform

The most frequently used analytical model for describing ocean surface waveform effects on the altimeter signal is based on linear scattering theory [1-3]. With this model, the scattering process may be conceptualized as resulting from the double convolution of the transmitted pulse, the sea scattering impulse response, and the altimeter system impulse response, as shown in Fig. 1. The sea surface ensemble average, temporal impulse response f(t) for this model may be written, for pulse lengths up to a few microseconds, as [2]

$$f(t) = \frac{kc}{\left(\frac{ct}{2}\right)^4} \; I(\theta,t) \int_{\frac{-ct}{2}}^{+\infty} (h-z)\, p(z)\, dz$$

where c is the velocity of light, h is satellite altitude, p(z) is the ocean wave height probability distribution as weighted by the radar observation, and $I(\theta,t)$ describes the altimeter antenna pattern.

The principal assumptions in this theory are:

(1) The radar scattering from the ocean surface occurs as though the surface contained an arbitrarily large number of spatially

stationary, independent, random scattering elements distributed on the ocean surface.

(2) The radar scattering is scalar with no polarization effects, and the return power is proportional to the incremental ocean area illuminated, appropriately weighted by antenna beamwidth and geometry factors. Radar cross-section variation with angle is assumed to be negligible over the antenna beamwidth expanse.

(3) The effect of ocean surface roughness on the radar waveform is derived based upon a model which assumes that the reflection statistics are known a priori. The scattering function is assumed to be distributed in the vertical coordinate in a manner describable by probability density function p(z).

(4) It is assumed that the convolution operations can be interchanged with the waveform expectation operation, for ensemble or mean waveform computations.

The greatest unknown in this model is considered to be the effective wave height probability distribution p(z) and its relationship to the true ocean surface. The work of Yaplee et al. marks the first occasion for which experimental data is available concerning p(z) and the ocean wave height distribution simultaneously [6]. The oceanographic unknowns and statistical complexities of the problem appear to preclude a derivation of the p(z) distribution based on oceanographic variables in the foreseeable future [4]. Longuet-Higgins has given an analysis based on a facet scattering model and use of idealized ocean surface statistics [5]. Attempts to extend this work have been unsuccessful for the following reasons: The two dimensional problem involves ocean spectral moments m_{ij} such as

$$m_{44} \underline{d} \int\int K_x^4 \, S(k_x,k_y) \, dk_x \, dk_y$$

in which $S(k_x,k_y)$ is the directional wave number spectrum. This integral can be shown to be unbounded for frequently used ocean spectral models [4]. Secondly, joint probability distributions of the ocean surface are not known.

In regard to the other assumptions, experimental tests of correctness of the overall model will be available from the Skylab waveform experiment. Item 4 above may be verified and the model improved for particular system configurations via Monte Carlo simulations presently being conducted by the authors or through a time-variant linear system formulation of the problem.

A problem area that is closely associated with waveform modeling is that of sea-state bias. The term "sea-state bias" is used herein to denote differences between mean sea level as sensed by the altimeter and geometrical mean sea level. That is, any discrepancies that arise in the altitude processing operation that results from differences in the radar observed $p(z)$ and the true wave height distribution $q(z)$ will appear as a bias in the altitude measurement. Estimates of sea state bias were first made by Pierson based upon the bias effect arising solely from skewness in $q(z)$ and by equating $p(z)$ to $q(z)$ [1]. (It should be noted that such a model results in larger biases for shorter pulse length altimeters [2]). In the following section we examine the experimental data recently published by Yaplee et al., and present a rationale for the essential time displacements he observed between $p(z)$ and $q(z)$.

2.0 Sea State Bias and Radar Observed Wave Height Distribution

The experimental data recently published by Yaplee et al. on their nanosecond radar measurements shows sea state bias to be much larger than previously estimated for low sea states. While the data base is quite limited and the results are preliminary, it is of interest to examine Yaplee's data in terms of its inferences regarding radar backscattering. On physical grounds we expect the radar wave height profile to be a distorted version of the ocean wave height profile, and the data of Yaplee et al. may be interpreted as indicating that this distortion appears mainly as a relative time shift between the two distributions as shown in Fig. 2. In the following we find that this apparent displacement can be accounted for, within experimental error, by assuming that $p(z)$ is a weighted replica of $q(z)$.

Yaplee's experimental configuration is that of a beamwidth limited exploration of the sea surface. The surface area investigated is that due to an essentially collimated beam. The data we wish to discuss is contained in Figures 9-12 of Ref. 6.

In attempting to model rough sea effects, it has been universally assumed that the cross-section is a function of the area of the ocean surface illuminated. There can be not large quarrel with this assumption; however, there is presently no basis for assuming that the scattering cross-section per unit area is independent of height above "mean sea level", (MSL), and only a function of the projected area. Figures 9 and 10 of [6] can, in fact, be interpreted as showing that radar cross-section of the ocean surface over the range of wave heights increases linearly with increasing distance below the wave crests. For these figures, the slope of the linear increase is approximately

$$m = \frac{.185}{\sigma} \qquad \text{for Figure (9) (calm seas)}$$

$$m = \frac{.141}{\sigma} \qquad \text{for Figure (10)(21 knot wind)}$$

where σ is the rms wave height.

If we take the geometrical centers of the delay expanse in these data as identifying MSL, then the variation of radar cross-section about MSL is given by

$$1 - m\frac{z}{\sigma}$$

where z is measured positive about MSL. Assume for the moment that p(z) can be interpreted as the product of two terms:

$$p(z) = h(z).q(z)$$

where h(z) is the z variation of radar cross-section per unit area and q(z) is the probability of finding a surface element z meters about MSL. We might expect that q(z) may well be of the form proposed by Pierson and Mehr [1]. However, for the conditions at the time that Yaplee's data were taken (calm sea-swell), the skewness parameter λ is expected to be quite small. Accordingly, we take

$$q(z) = \frac{1}{\sqrt{2\pi\sigma^2}} \exp - \frac{z^2}{2\sigma^2} .$$

We are concerned, therefore, with the behavior of p(z) as implied by Yaplee's data.

Three curves are shown in Fig. 3.

$$p(x) = h(x).q(x) = \frac{1}{\sqrt{2\pi}} [1-mx] \exp(-\frac{x^2}{2}) \qquad \text{weighted Gaussian}$$

$$q(x) = \frac{1}{\sqrt{2\pi}} \exp(-\frac{x^2}{2}) \qquad \text{true Gaussian}$$

$$p(x + .175) = \frac{1.02}{\sqrt{2\pi}} \exp(-\frac{(x - .175)^2}{2}). \qquad \text{displaced Gaussian}$$

where m was taken to be 0.115.

Comparison of these curves indicates that p(x) is displaced from the wave height distribution, just as is the data in Yaplee's Figure 11 (see Fig. 2). The x variable used in these calculations is the height normalized by the rms wave height. From Yaplee's Figure (11), we find that the rms wave height expressed in nanoseconds is 1.725. The delay between the peaks of the two curves [p(x) and q(x)] is therefore .3 nanoseconds. The third curve--merely the Gaussian curve shifted and re-normalized--shows the extent to which p(x) can be approximated by a shifted Gaussian curve. The reader may satisfy himself that Yaplee's radar data in Figure 11 can be obtained by simply shifting the wave staff data .3 nanoseconds to the right.

This discussion suggests that one possible explanation of the shift in Yaplee's radar curve is a simple height dependence of the scattering cross-section as provided by the h(z) term. Note that for this sea condition, a skewness parameter λ cannot support the data--it would require a λ of approximately .37 for a calm sea! Note further that the skewness correction to a Gaussian curve is essentially a cubic $[1 + \frac{\lambda x}{6} (x^2 - 3)]$ and that there will be three places at which the Gaussian intercepts the composite curves. Yaplee's data show only one intersection between the radar and wave staff data--which would be expected if the radar data are just shifted wave staff data. This may be taken as further proof that for this sea condition the wave staff data are essentially Gaussian.

Under conditions of a true wind-driven sea, one might expect that the variation of radar cross-section with height above mean sea level may

change. Possibly "m" might decrease. With increasing wind speed, one might also expect the value of λ, the skewness parameter in the wave height distribution, to increase. The overall effect on sea surface bias will still be contained in the formula for p(z)

$$p(z) = \frac{1}{\sqrt{2\pi}} \left[1 + \frac{\lambda}{6}\left(\frac{z}{\sigma}^3 - \frac{3z}{\sigma}\right)\right]\left[1 - m\,\frac{z}{\sigma}\right] \exp\left(-\frac{z^2}{2\sigma^2}\right)$$

These detailed variations with wind speed and sea state are not known and must be measured. In any event, Yaplee has made a clear case for the inclusion of a term which reflects the increasing radar cross-section per unit area with increasing distance below the wave crests.

3.0 Selection of GEOS-C System Parameters Relative to a Sea-State Experiment

In this section we discussed the problem of estimating ocean surface roughness using information available from altimeter normal incidence waveforms. Referring back to Fig. 1, in such an experiment an attempt would be made to measure the width of the p(z) distribution (i.e., its rms value) and thereby infer the surface roughness parameter in the wave height distribution q(z). In order to implement such an experiment, it is necessary to sample a number of points on each incoming waveform and subsequently average (either in the satellite or on the ground) the sample values to extract the ensemble average. The mean waveform can then be examined to derive surface roughness estimates. If it is assumed that p(z) is a symmetrical bell shaped distribution, in an idealized case the sample and hold spacing could be as great as one-half the transmitted pulse length. If it desired to obtain data on the p(z) distribution, then a rather dense collection of sample and hold values would be needed. The problem areas in such an experiment are: 1) Given that satellite constraints place a limit on the sample and hold spacing and signal-to-noise ratio available, and that sea state sensitivity is greatest for short pulses; then an optimum pulse length may exist for sea state measurement. 2) The number of waveform samples available per measurement interval is limited by the homogeneity of the ocean surface during the experiment, the statistical nature of the received signal and other

system constraints. These factors may be seen from an examination of Figs. 4 and 5, which comprise computed* mean waveforms as a function of sea state. These figures show square-law detected waveforms for a matched receiver (i.e. an IF bandwidth equal to the reciprocal of the pulse length) for both 10 and 25 n.s. pulse lengths. RMS surface roughness values are shown on these figures for an assumed Gaussian p(z). To convert these values to significant wave height ($H_{1/3}$) requires multiplication by a factor of four [1].

Figures 4 and 5 also show the one-sigma confidence bounds for the magnitude fluctuations on a waveform containing 1000 sample cases. Based upon an input signal comprising a square-law detected narrow-band, time-varying Gaussian signal, the rms deviation of a sample function about the distribution mean is

$$\sigma_y = \frac{\sqrt{2}\,\sigma_x^2}{\sqrt{n}}$$

where y is the detected process and y the input process. For this model the output will be chi-squared distributed (single degree of freedom) and the average value of y is

$$\bar{y} = \sigma_x^2.$$

This distribution will be modified to some degree, by the presence of the post-detection filter. Our recent work has shown the filter to produce significant departures from the chi-squared distribution for filter bandwidths of approximately the "matched filter" condition. Figure 7 contains a histogram of the filtered distribution, based on simulation results. It shows a standard deviation of very nearly one-half that of the chi-squared distribution. Adding this factor to the above result gives a vertical error component σ_v of

$$\sigma_v = \frac{\text{waveform ensemble average}}{\sqrt{2n}}$$

*These data have been computed by both closed form and hybrid computers simulations; as verification of the interchange of ensemble and convolution operations.

where the waveform ensemble average is taken to be the value of the true mean waveform at the point of interest. For example, σ_v will be $1/\sqrt{2n}$ at the peak of the normalized mean waveform; or $\pm$ 2.2% of the peak for n = 1000.

Figure 6 is a graph of the relative sensitivity of the 10 and 25 nanosecond pulse length altimeters. These data are a re-plotted version of the information contained in Figs. 4 and 5. Note that the shorter pulse length increases sensitivity to the lower sea states.

In summary, the uncertainty in measuring surface roughness, for seas in the range of 1-2 meters rms, for the 25 ns pulse length is ~ 0.2 meter rms for a one second average of 1000 pulses. Table I gives other estimates.

Table I

Estimated uncertainty in measuring surface roughness for a 10 or 25 ns pulse lengths.

Sea Roughness Uncertainty (1-2 rms seas)				
Averaging Period Sec.	25 ns		10 ns	
	rms	$H_{1/3}$	rms	$H_{1/3}$
1	0.21 meters	0.84 meters	0.14	0.56
5	.07	.28 meters	.045	.18

The timing error component in the waveform measurement, which relates to sample and hold jitter is neglected in the above discussion for the following reasons. Assuming that the sample and hold circuits follow the output of a split gate tracker, this error will be approximately 3.6 ns for n = 1000, SNR = 10 db, T = 10 ns and for a tracker bandwidth of 10 Hz (bandwidth is related to orbit eccentricity) [7,15]. If instead the sample and hold circuits are held stationary during the sea-state experiment interval, and adequately spaced to define the mean waveform, this error component will be approximately 14 ns for an orbit ellipticity of 1.05 and for a 1 second averaging interval. As the third option, the sample and hold timing could be programmed, based on orbit parameters or tracker data, thereby reducing

this error component to a fraction of the vertical error. This added complexity appears necessary except for highly circular orbits.

4.0 Altitude Measurement Considerations

At the present time it appears that GEOS-C will utilize a pulse compression mode, which in turn may permit use of pulse lengths as short as 10 n.s. Considerable emphasis has been placed on a 10 n.s. system in past program meetings and the purpose of this section is to briefly indicate other system considerations.

Previous system error analyses have shown that the largest random, instrument error in the altitude measurement is likely to be altitude noise [2,7,8,9]. Based on a pulse repetition frequency (prf) which provides independent waveform samples, the random altitude error σ_a is given by [15]

$$\sigma_a = \frac{0.15\tau}{\sqrt{\frac{prf}{\pi\beta_L}}} \sqrt{\frac{7}{8} + \frac{6}{SNR} + \frac{8}{(SNR)^2}}$$

where β_L is the 3db loop bandwidth, τ is the pulse length in nanoseconds, and SNR is signal-to-noise ratio. For high signal-to-noise ratios, this expression may be approximated as

$$\sigma_a = \frac{.14\tau}{\sqrt{\frac{prf}{\pi\beta_L}}} .$$

As a simple tradeoff situation, assume that it is possible to use an altimeter that either (a) operates at an unambiguous prf of 100 pps and with τ = 10 n.s., or (b) uses an ambiguous prf of 1,000 pps (which necessitates an acquisition mode) and a pulse length of 25 n.s. Use of the above equation shows that the 25 n.s. system will produce a lower σ_a value. Other levels of comparison are possible. If both (a) and (b) operate at an ambiguous prf based on the doppler criterion, σ_a can be shown to be proportional to pulse length to the

three-fourths power. If it is further assumed that the signal pulse signal-to-noise ratio decreases from 10 db to 5 db, the first equation above may be evaluated to show that

$$\frac{\sigma_a(10\text{ n.s.})}{\sigma_a(25\text{ n.s.})} \simeq \left(\frac{\tau_{10}}{\tau_{25}}\right)^{3/4} \sqrt{\frac{\frac{7}{8} + \frac{6}{SNR(10)} + \frac{8}{SNR^2(10)}}{\frac{7}{8} + \frac{6}{SNR(25)} + \frac{8}{SNR^2(25)}}} \simeq 0.8$$

and the 10 n.s. system gives an improvement of $\sim$ 20%.

The purpose of this discussion is to point out the fallacy in assessing altimeter performance solely on the basis of pulse length; careful consideration must also be given to satellite hardware constraints affecting average transmitter power, complexity of sample and hold circuits, logic clock rates, degree of on-board processing available and so forth.

5.0 Ground Truth Needs for a σ^o Experiment

It is often stated that normal incidence, centimeter r-f wavelength scattering is dominated by the short wavelength or capillary range of the ocean spectrum. This statement derives from series approximations or asymptotic expansions of the physical optics scattering integral, in which σ^o is found to be proportional to the mean-squared slope of the ocean surface [10]. This slope dependency coupled with use of popular models of the ocean spectrum forms the basis for this assumed capillary dependency. The work to be summarized below examines in detail the question of what ocean wavelength range dominates the physical optics scattering integral for a Phillips type of spectrum; this question is important in its implications concerning sea truth measurements necessary for validating a σ^o experiment.

The near-normal incidence dependence of σ^o on ocean surface parameters is generally agreed to depend on the integral

$$I_{SC} = \int_o^\infty \int_o^{2\pi} e^{j2\bar{k}_o r\cos\phi\sin\theta - 4\bar{k}_o^2 h_m^2 \cos^2\theta[1-\rho_n(r,\phi)]} r dr d\phi$$

where

$\bar{k}_o$ = rf wavenumber

h_m^2 = mean-squared height of the ocean waves

θ = angle of incidence (measured from the normal to the mean ocean surface)

$\rho_n(r,\phi)$ = normalized surface height correlation function.

In order to verify the relationship between σ^o and sea state, it is necessary to measure the mean-squared ocean height and also obtain the ocean height correlation function, simultaneously with σ^o. One approach to determining $\rho_n(r,\phi)$, the normalized height correlation function, is to measure the ocean height spectrum $S(k,\psi)$ and subsequently to compute $\rho_n(r,\phi)$ from the transform relation,

$$\rho_n(r,\phi) = \frac{1}{2\pi h_m^2} \int_0^{\infty} \int_0^{2\pi} S(k,\psi)\ e^{jkr\cos(\phi-\psi)}\ k\,dk\,d\psi$$

The spectral form chosen for this study is primarily based on the asymptotic behavior of the Phillips equilibrium spectrum [13]. The low wavenumber range, for which the analysis is less sensitive, is based on experimental data given in [15]. The spectral form is

$$S_a(k) = \beta \frac{k^5}{(k^2 + a^2)^4}$$

where $\beta = 4.05 \times 10^{-3}$, $a^2 = 1/(300\ v^4)$, v is the wind speed which has dimensions in knots and k has dimensions in centimeters. These values equate the mean square height derived from $S_a(k)$ to that of the Pierson-Moskowitz spectrum. In accordance with most scattering analyses, the spectrum is taken to be isotropic [10].

The correlation function $\rho_n(r)$ derived from $S_a(k)$ is given by

$$\rho_n(r) = ar\left[-arK_o(ar) + \left(1 + \frac{a^2r^2}{8}\right) K_1(ar)\right]$$

where $K_o(ar)$ and $K_1(ar)$ are modified Bessel functions. A plot of $\rho_n(r)$ and the scattering integrand is shown in Figures 8 and 9. Several unsuccessful attempts were made to obtain an asymptotic expansion which would represent the σ^o behavior as a function of wind speed. The integrand plots in Figure 9 provide a graphic illustration of the difficulty associated with asymptotic techniques. The effective integration range spreads in the r parameter to the extent that it is difficult to obtain a valid point expansion. The scattering integral I_{SC} is shown in Figures 10 and 11 as a function of wind speed and angle of incidence for an r-f wavelength of 3 cm. These figures also show a comparison with experimental data from Ref. 11. Note that a saturation effect at the higher wind speeds is present in Figure 10.

To compute the effect of spectrum truncation on the correlation function, the upper limit on the k-integration was taken to be k_c rather than infinity, i.e.,

$$\tilde{\rho}_n(r) = \frac{1}{h_m^2} \int_0^{k_c} J_o(kr)\, S_a(k)\, kdk$$

In order to avoid a time consuming numerical integration, the following series representations for $\tilde{\rho}_n(r)$ were developed and verified;

$$\tilde{\rho}_n(r) = \frac{\beta}{2} \sum_{m=0}^{2} \frac{\left(-\frac{1}{4} r^2\right)^m b_m}{(m!)^2} + \beta\, \Phi(k_c r)$$

where for $k_c r < 1$,

$$\Phi(k_c r) \simeq 0$$

and for $\left(\frac{k_c}{a}\right)^2 > 9$ and $k_c r < 5$

$$\Phi(k_c r) = \frac{1}{k_c^2} \sum_{m=2}^{\infty} \frac{\left(-\frac{1}{4} r^2 k_c^2\right)^m}{(m!)^2 (2m-2)}$$

and finally for $\left(\frac{k_c}{a}\right)^2 > 9$ and $k_c r \geq 5$,

$$\Phi(k_c r) = \frac{r^2}{2}\left[\frac{1 - J_o(k_c r) + \left(\frac{k_c r}{2}\right) J_1(k_c r)}{(k_c r)^2} + \frac{(\gamma-1)}{2} + \frac{1}{2}\log\left(\frac{k_c r}{2}\right)\right]$$

$$+ \frac{r^2}{4}\left[\frac{2 g_1(k_c r)\, J_o(k_c r)}{(k_c r)^2} - \frac{g_o(k_c r)\, J_1(k_c r)}{(k_c r)}\right]$$

The functions $g_1(k_c r)$ and $g_o(k_c r)$ are given in [14], γ is Stirling's constant and the b_m coefficients are as follows:

$$b_o = \frac{1}{3a^2} - \delta^2 + a^2\delta^2 - \frac{1}{3}a^4\delta^3$$

$$b_1 = -\log(a^2) - \frac{11}{6} + \log(\delta) + 3a^2\delta - \frac{3}{2}a^4\delta^2 + \frac{1}{3}a^6\delta^3$$

$$b_2 = \frac{10}{3}a^2 + 4a^2\log(a^2) - 4a^2\log(\delta) - 6a^4\delta + 2a^6\delta^2 - \frac{1}{3}a^8\delta^3$$

and $\delta = (k_c^2 + a^2)^{-1}$.

When k_c (the upper truncation point) was set equal to one $(cm)^{-1}$, the scattering integral I_{SC} had essentially the same value as when $k_c \to \infty$. To understand how the scattering integral behaves as a function of the spectral truncation point, it is necessary to examine $1-\tilde{\rho}(r)$ as a function of r. Figure 12 is such a plot with $k_c = 1(cm)^{-1}$ and as a function of r and wind

speed. All of the curves have exactly the same shape with a downward translation being the only effect of increasing the velocity. This fact indicates that the correlation function $\tilde{\rho}_n(r)$ is parabolic over the region of interest. The other important point to note from Figure 12 is that $[1 - \tilde{\rho}_n(r)]$ decreases almost uniformly with increasing velocity. In Figure 13, the spectrum interval from 10^{-3} - 1 $(cm)^{-1}$ was taken to represent $\tilde{\rho}_n(r)$. Here it should be noted that $[1 - \tilde{\rho}_n(r)]$ becomes independent of velocity for $v \geq 20$ knots. Since the mean-squared height continues to increase with velocity, this would imply that the scattering integral I_{SC} will exhibit a very rapid roll-off as a function of velocity for greater than 20 knots. Figure 14 shows how the scattering integral behaves when the lower spectrum truncation point is increased from zero to 10^{-2} $(cm)^{-1}$. Figure 15 shows the effect of truncating the spectrum below $k_c = 1.0$ $(cm)^{-1}$. It is most interesting that while varying the lower truncation point drastically changes the shape of the curve, changing the upper truncation point apparently only causes a level shift and not a significant change in the shape of the curve.

The computations presented here indicate that a correlation of spectrally narrow-band sea truth data and experimental values of σ^o with theoretical formulations (for near-normal incidence) will not yield good agreement. Data shown in Figure 15 indicates that sea truth data over a wavenumber range of 0.001 to 1.0 cm^{-1} will be adequate for equilibrium surface winds $\leq$ 8 knots. For higher winds, it is necessary to locate the lower truncation point at a position somewhat below the equilibrium spectral peak.

It must also be concluded that the often-used isotropic assumption is, strictly speaking, not appropriate. However, adequate oceanographic information is not available for an analysis which includes directionality. Also, current work indicates that the conclusions given herein will still hold.

6.0 Summary and Conclusions

We discussed the use of ocean surface impulse response models to obtain radar return waveform expectation values. It was assumed that the ensemble averaging and convolution operations could be interchanged, and preliminary results from our current analog simulation work support this assumption.

We distinguished between the radar-observed height distribution p(z) and the true geometric distribution q(z). Although it has usually been assumed

that p(z) and q(z) are identical, we discussed the experiment of Yaplee et al. as an example of a situation in which experimental data could be explained by assuming that p(z) and q(z) are not identical. We recommend that Yaplee's type of experimental data be obtained from as wide a range of sea conditions as possible and that, because of the difficulty of scaling from near-surface to satellite conditions, direct measurement of satellite altimeter bias be attempted using over-water radar reflectors.

We presented examples to show that sea state resolution and altitude precision did not simply vary inversely as the radar pulse length but were functions of a number of radar system parameters. It is fallacious to assess altimeter performance solely on the basis of pulse length and experimenters should instead state their needs in such terms as: extent of ocean surface over which "sea state" data can be averaged; needed sea-state resolutions and roughness range, or geographic regions of prime interest; specifications of desired altitude noise level, and time or spatial regions over which the data can be averaged. This information can then be used as input data during the altimeter system optimization phase, to select the radar system parameters and to establish different parameter tradeoffs.

Using a physical optics theory for 3 cm rf wavelength scattering at normal incidence from an ocean described by a Phillips type of equilibrium spectrum, we found that σ^o depends heavily on surface wavenumbers in the range .001 - 1.0 cm^{-1}, or ocean surface wavelengths of .06 - 60 meters, for surface winds $\leq$ 8 knots. This means that any σ^o experimentation must include acquisition of gravity wave-range spectral information, not the often-assumed capillary range, as "sea-truth" for σ^o verification. The analysis also predicts negative results for σ^o vs. wind speed experiments since a saturation effect is found in the normal incidence case, similar to the effect noted by Guinard for scatterometer geometry [11]. The Skylab σ^o experiment should provide a most valuable data base for this effect.

7.0 Acknowledgements

The authors wish to acknowledge extensive assistance from W. A. Flood in section 2.0 and Gary S. Brown in section 5.0, in addition to many helpful discussions with participants in the GEOS-C and Skylab programs.

LIST OF REFERENCES

1. Pierson, W. J., and Emanuel Mehr, "The Effects of Wind Waves and Swell on the Ranging Accuracy of a Radar Altimeter," Report on Contract No. N62306-70-A-0075, New York University, School of Engineering and Science, January 1970.

2. Miller, L. S., and G. S. Hayne, System Study of the Geodetic Altimeter Concept, Final Report, Contract No. NAS6-1829. Research Triangle Institute, March 1971.

3. Schindler, John K., Electromagnetic Scattering Phenomena Associated with Extended Surfaces, IEEE International Convention Record, v. 15, part 2, pp. 136-149, 1967.

4. A Study of the Capabilities of the Geodetic Satellite Altimeter to Measure Ocean Surface Characteristics, Final Report, Contract No. NASw-1909, by the Research Triangle Institute, April 1970.

5. Cartwright, D. E., and M. S. Longuet-Higgins, "The Statistical Distribution of Maxima of a Random Function," Proc. Roy. Soc. A-237, pp. 212-232.

6. Yaplee, Benjamin S., et al., "Nanosecond Radar Observation of the Ocean Surface from a Stable Platform," IEEE Trans. on Geoscience Electronics, Vol. GE-9, No. 3, July 1971.

7. Godbey, T. W., et al., Radar Altimetry Study, Phase II Final Report, Contract No. NAS12-683, General Electric Company, Utica, New York, January 1970.

8. Shapiro, A., and B. S. Yaplee, "Satellite Altimetry," Naval Research Laboratory Report No. 7018, February 1970.

9. Kolker, Myer, and Ephraim Weiss, Space Geodesy Altimetry Study, NASA Report No. CR-1298, March 1969.

10. Beckmann, Petr, and Andre Spizzichino, The Scattering of Electromagnetic Waves from Rough Surfaces, The Macmillan Company, New York, 1963.

11. Guinard, N. W., "The Variation of RCS on the Sea with Increasing Roughness," in Microwave Observation of the Ocean Surface, U.S. Naval Oceanographic Office SP-152, June 1969.

12. Hess, G. D., G. M. Hidy and E. J. Plate, "Comparison Between Wind Wave and Sea in the Laboratory," Journal of Marine Research, Vol. 27, No. 2, pp. 216-225, 1969.

13. Phillips, O. M., The Dynamics of the Upper Ocean, Cambridge Press, 1966.

14. Abramowitz, M., and I. A. Stegun, eds., Handbook of Mathematical Functions, pp. 482, U. S. Government Printing Office, Washington, D. C., 1964.

15. Hofmeister, E., and B. N. Kenney, "Radar Altimeter Return Waveform Sampling Study," Final Report, Contract No. NAS6-1823, by the General Electric Company, Utica, New York, May 1971.

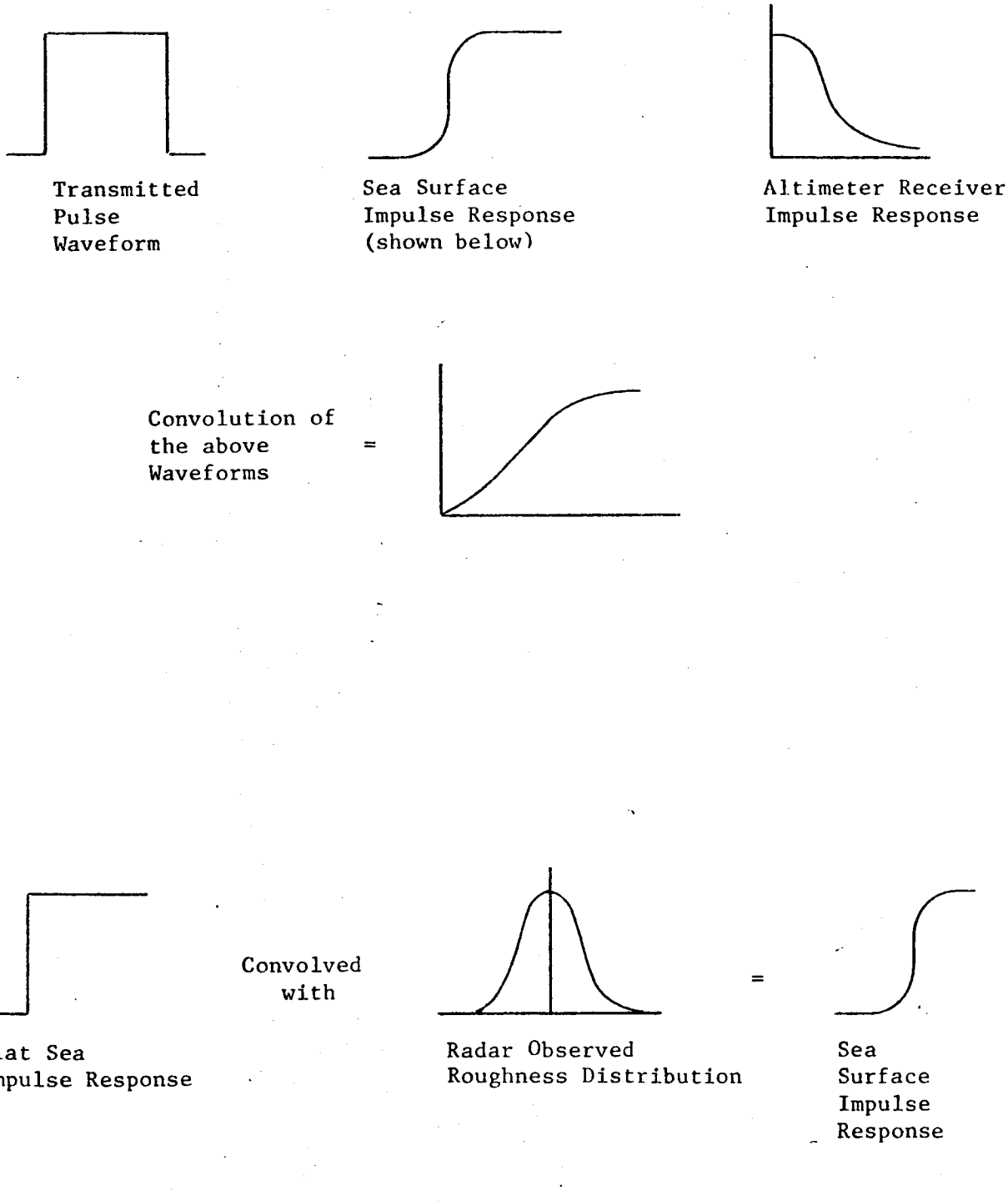

Figure 1. Altimeter Waveforms based on linear scattering theory.

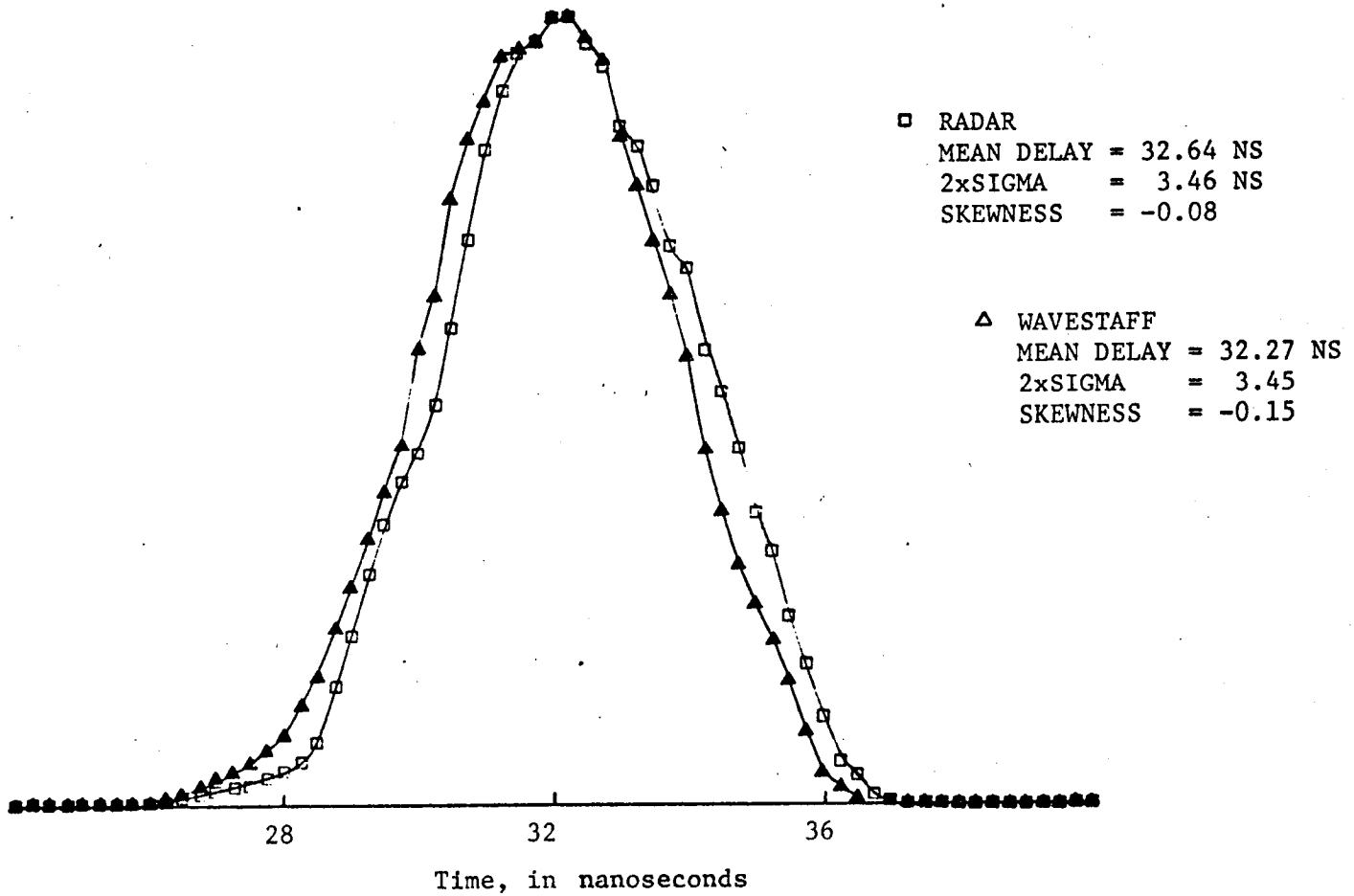

Figure 2. Comparison of Wavestaff and Radar distributions (from Yaplee et al.).

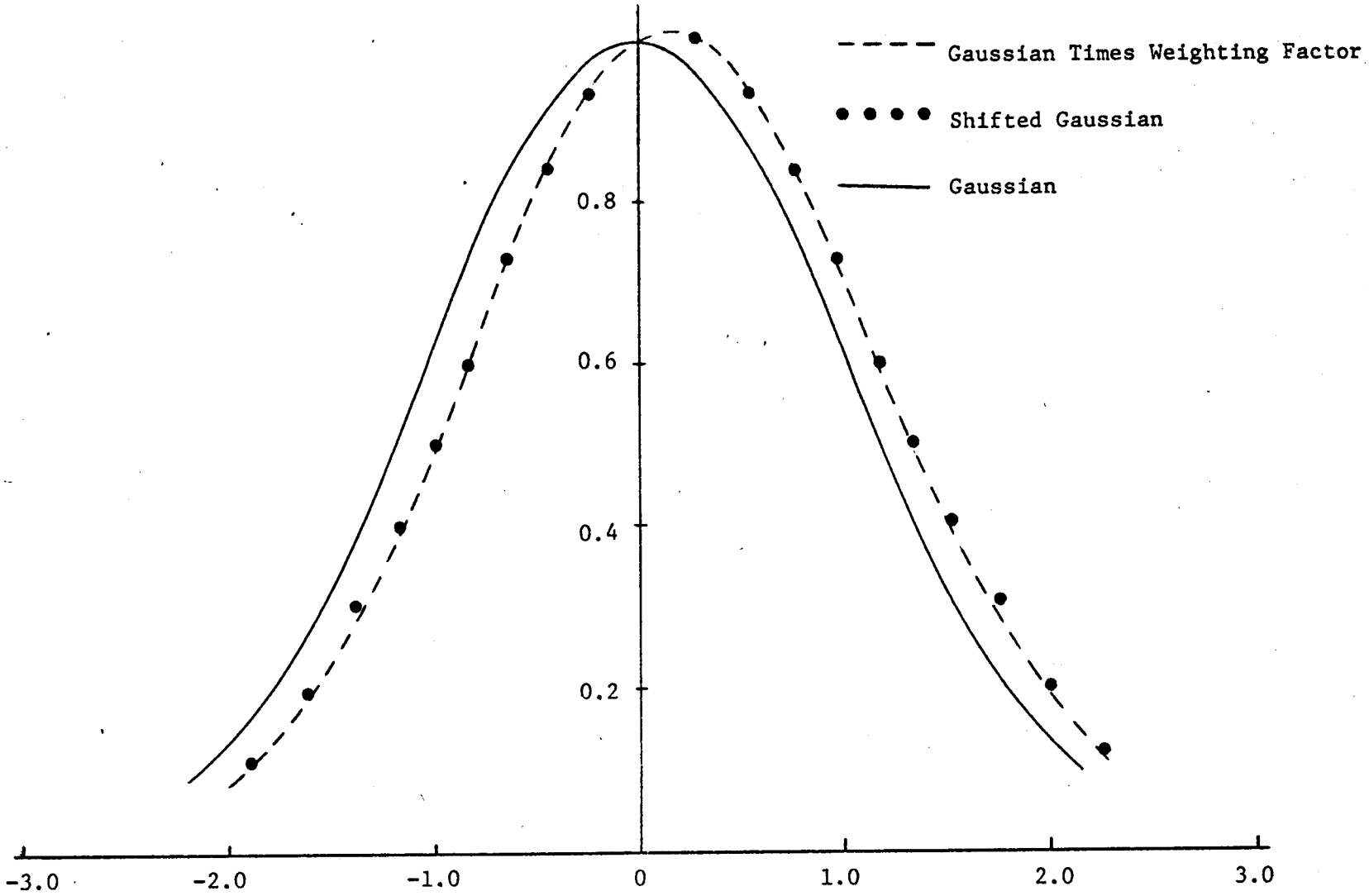

Figure 3. Comparison of linearly weighted Gaussian model of p(z) and a shifted Gaussian curve.

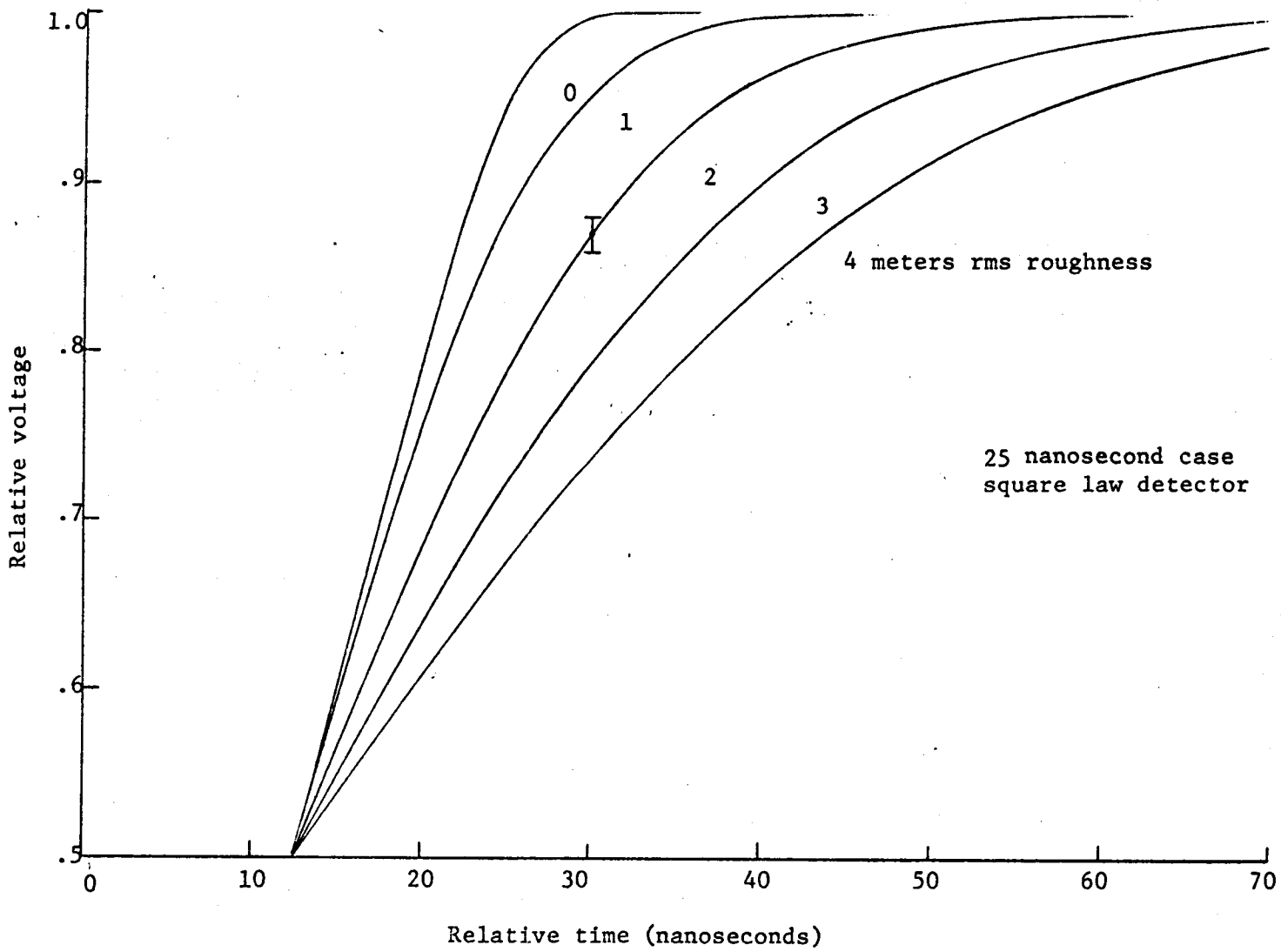

Figure 4. Sensitivity of 25 ns mean waveforms to ocean surface roughness (upper 1/2 of waveform shown).

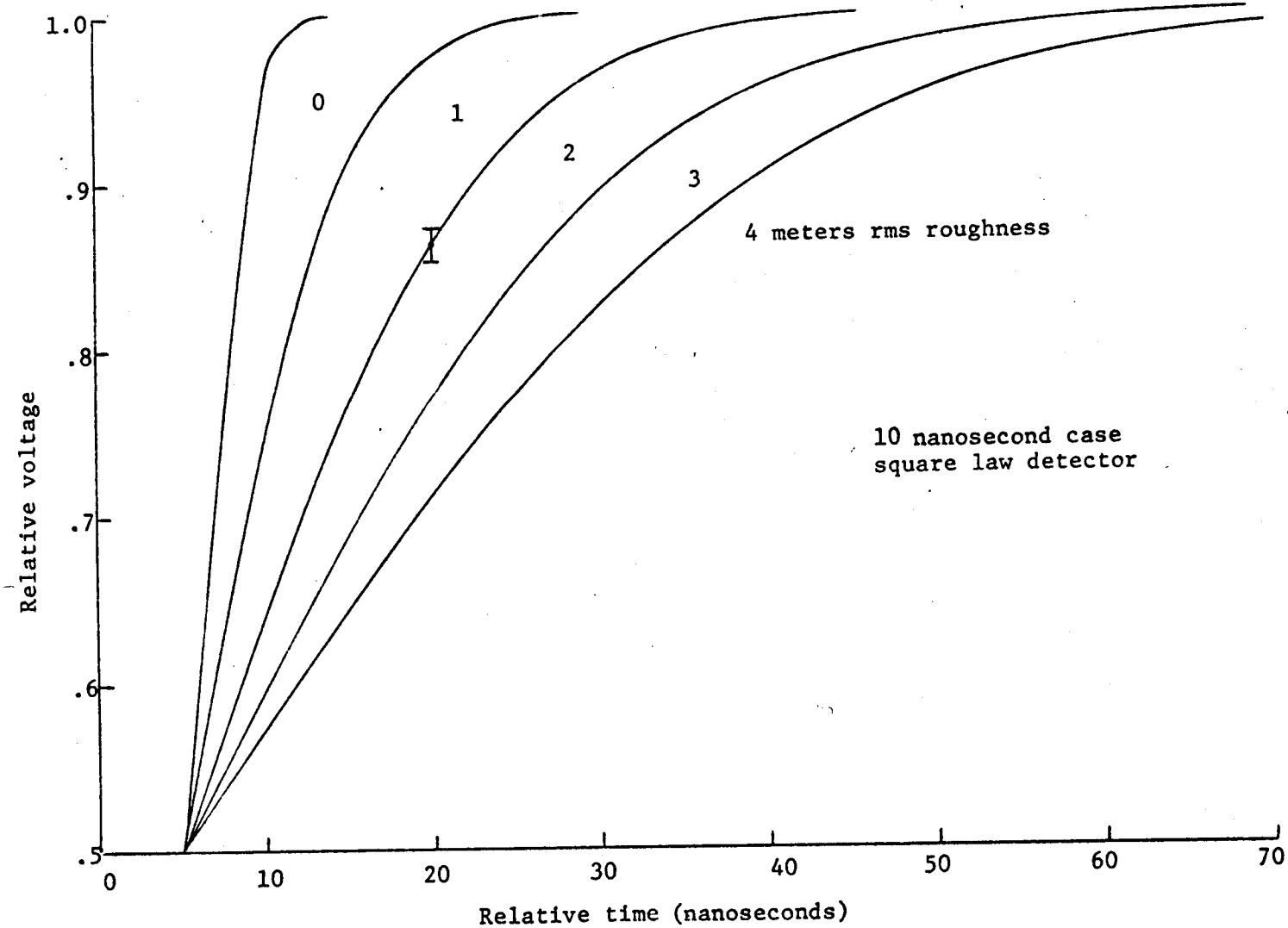

Figure 5. Sensitivity of 10 ns mean waveforms to ocean surface roughness (upper 1/2 of waveforms shown).

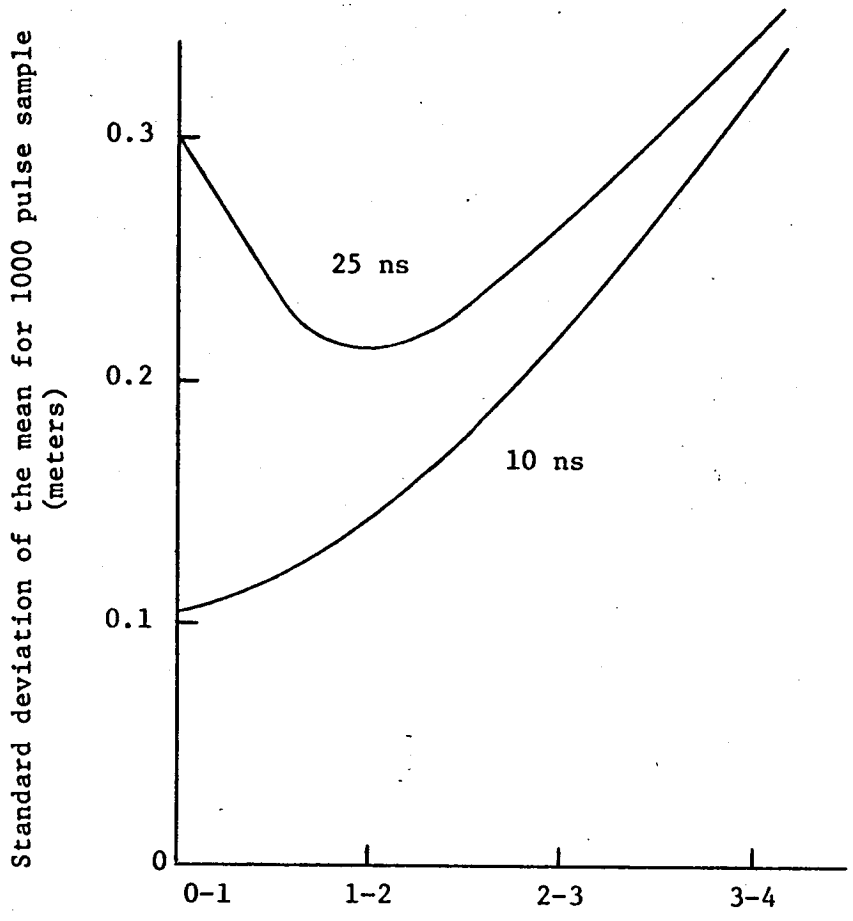

Figure 6. Calculated surface roughness measurement precision as a function of pulse length and sea conditions.

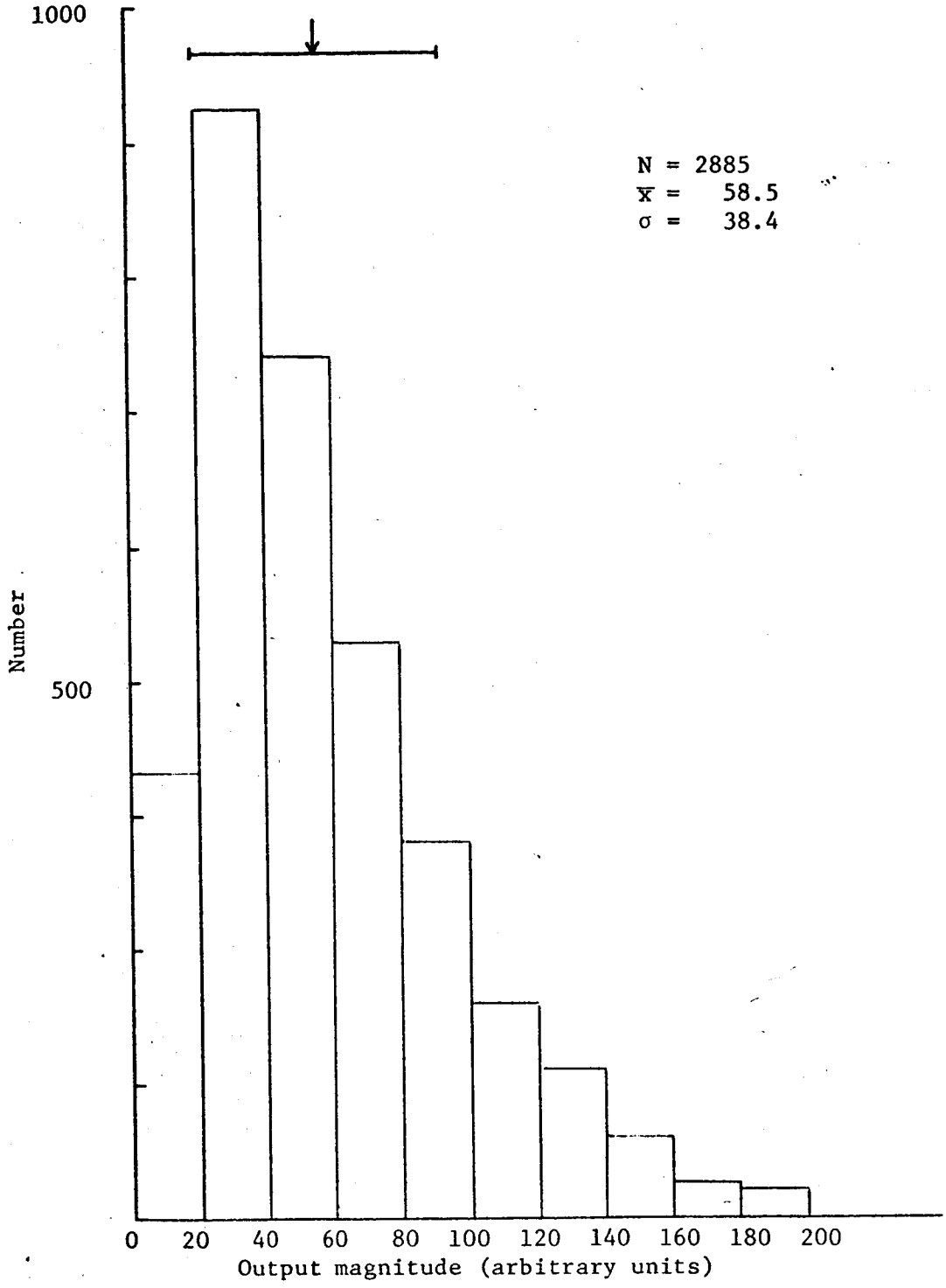

Figure 7. Histogram of simulated video filtered waveforms.

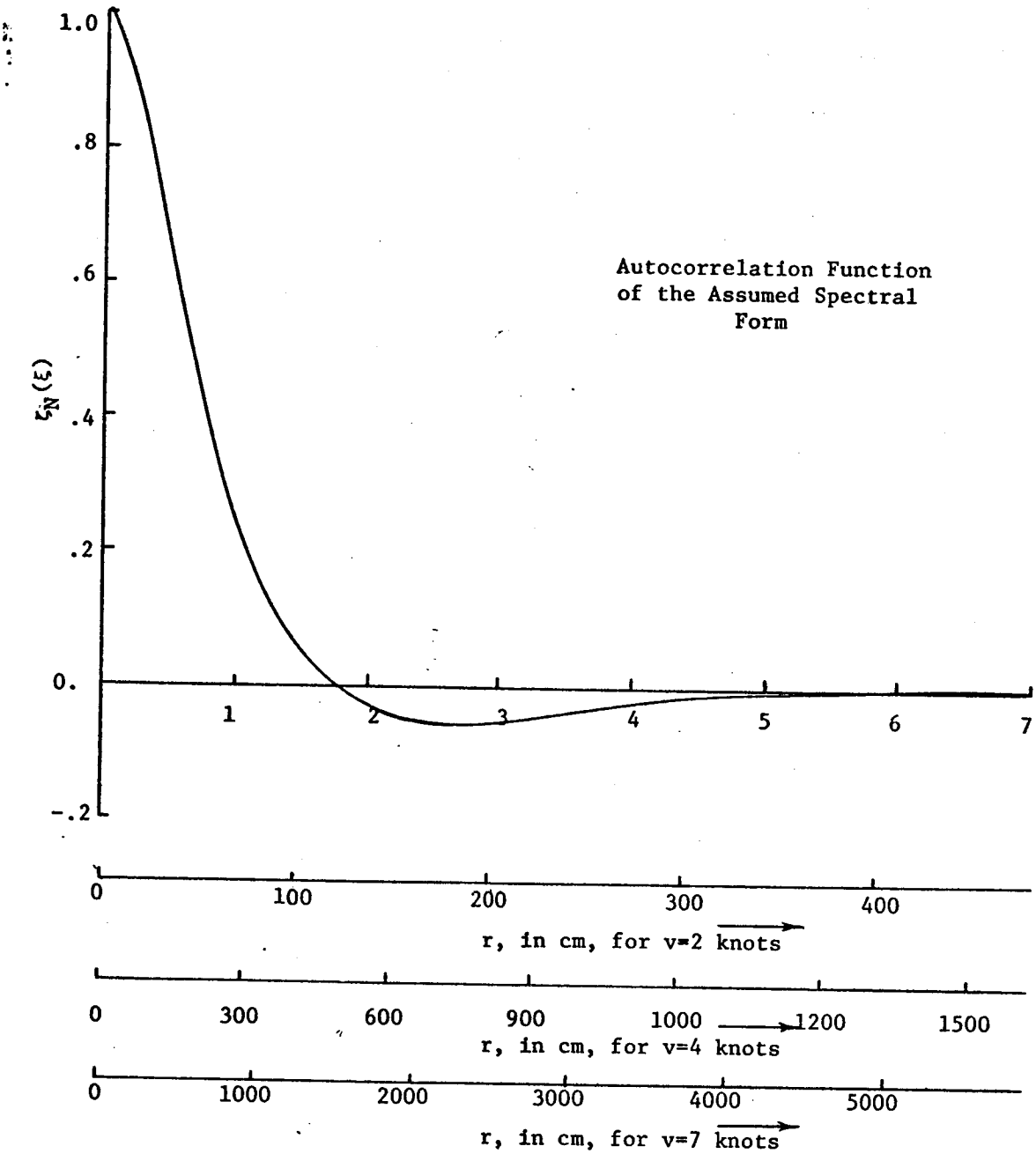

Figure 8. Normalized height correlation function.
(ξ=ar)

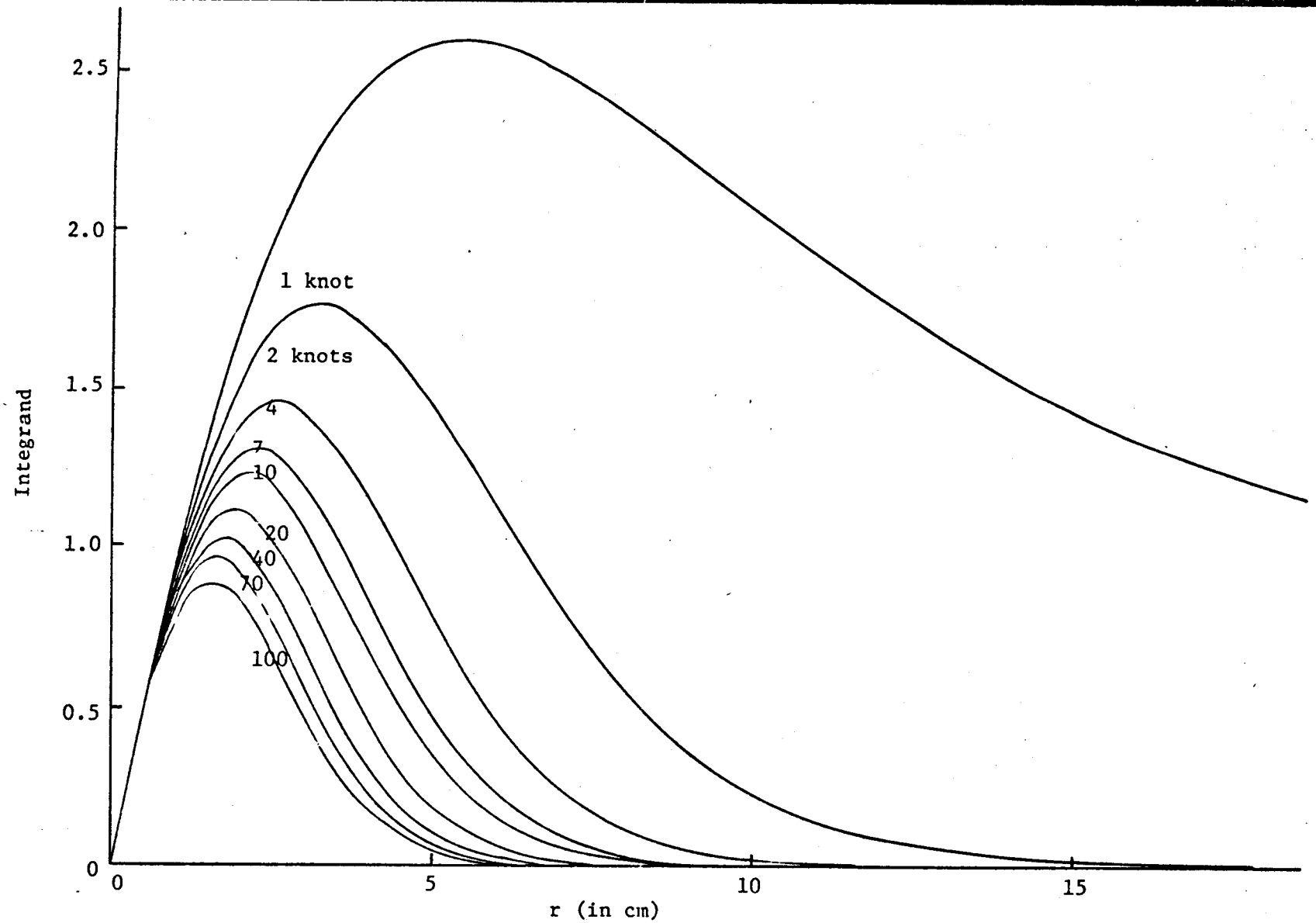

Figure 9. Behavior of the integrand of the scattering equation.

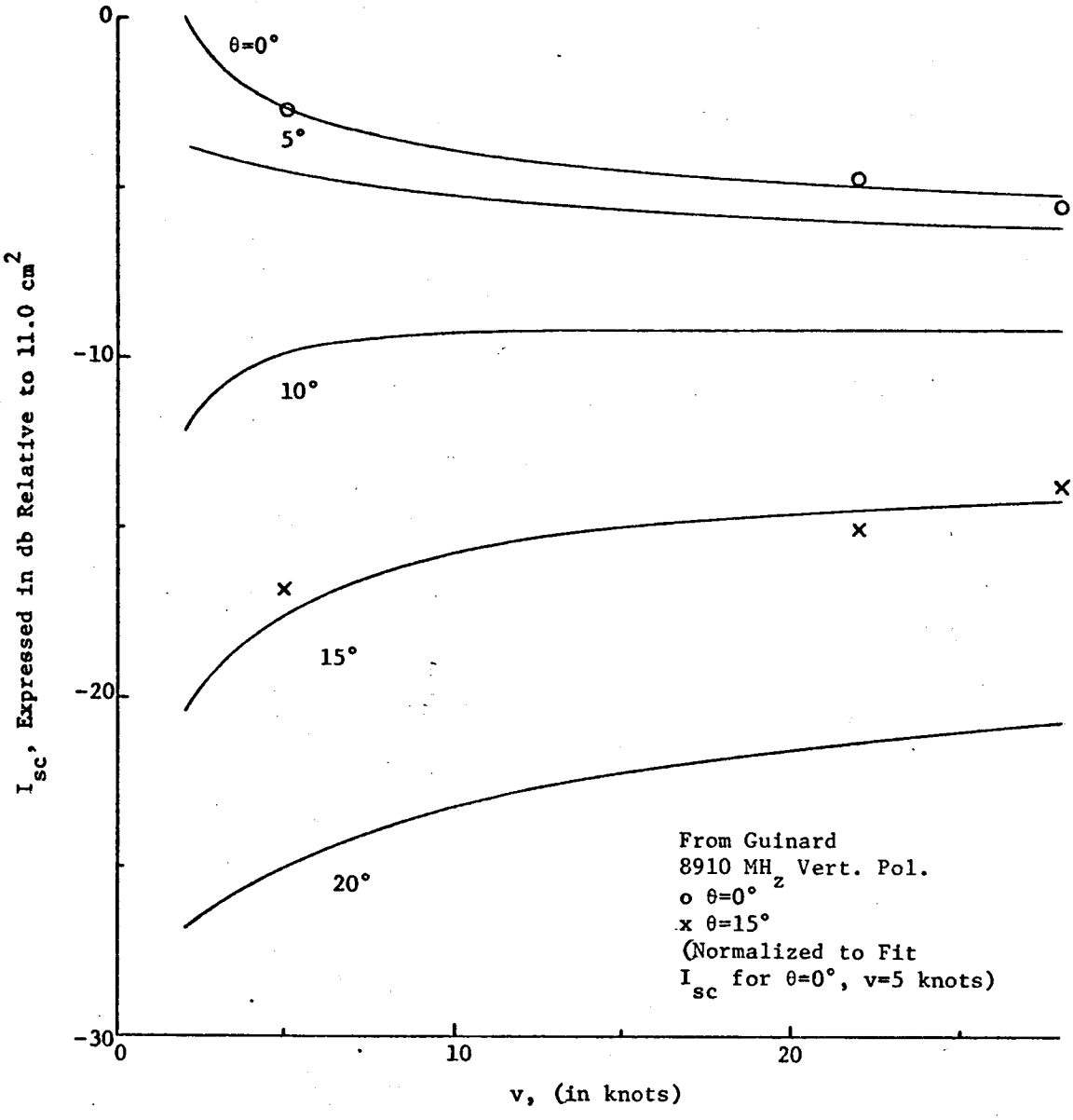

Figure 10. The scattering integral as a function of wind speed (λ_{rf} = 3 cm.).

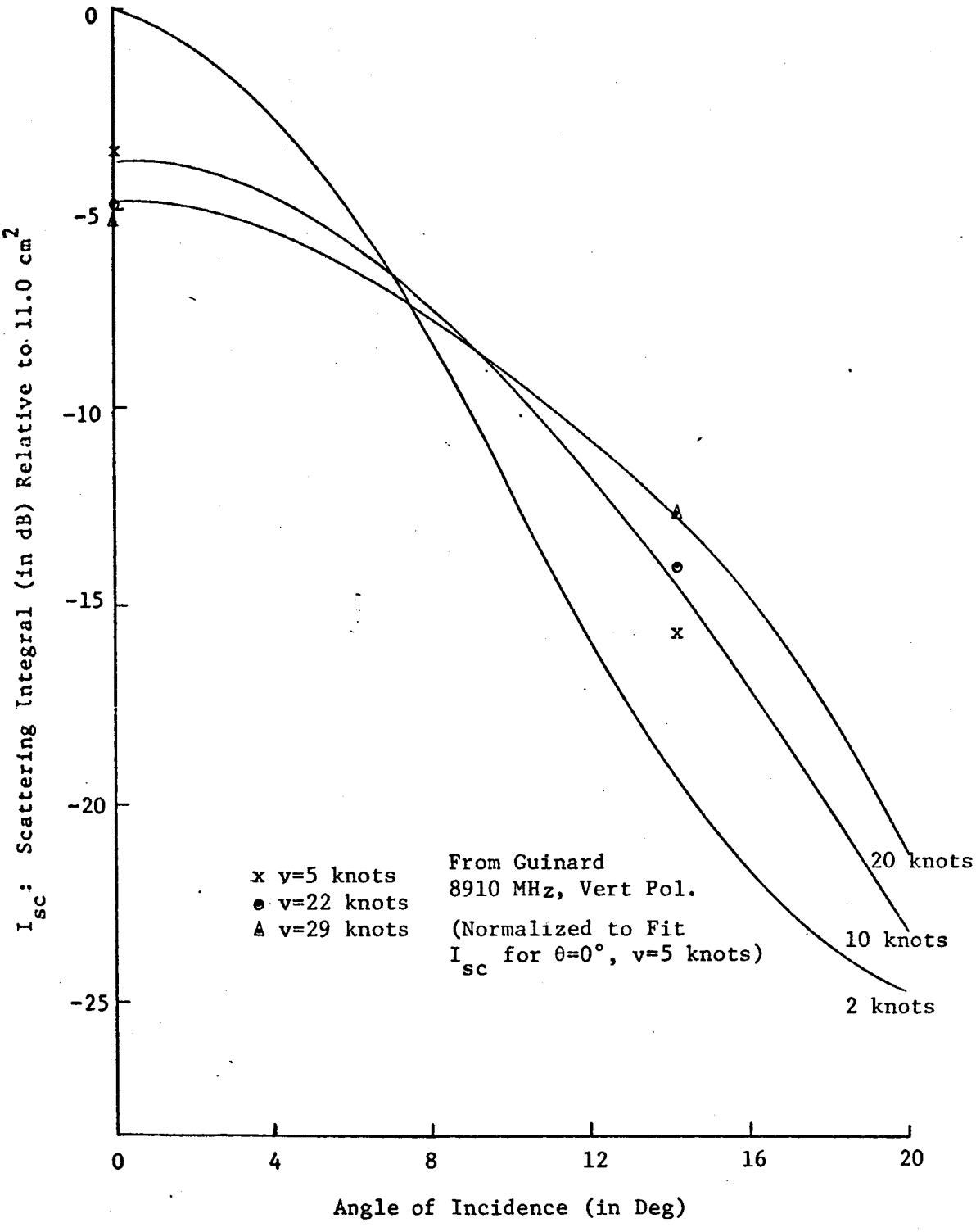

Figure 11. Scattering intergral as a function of angle (λ_{rf} = 3.0 cm)

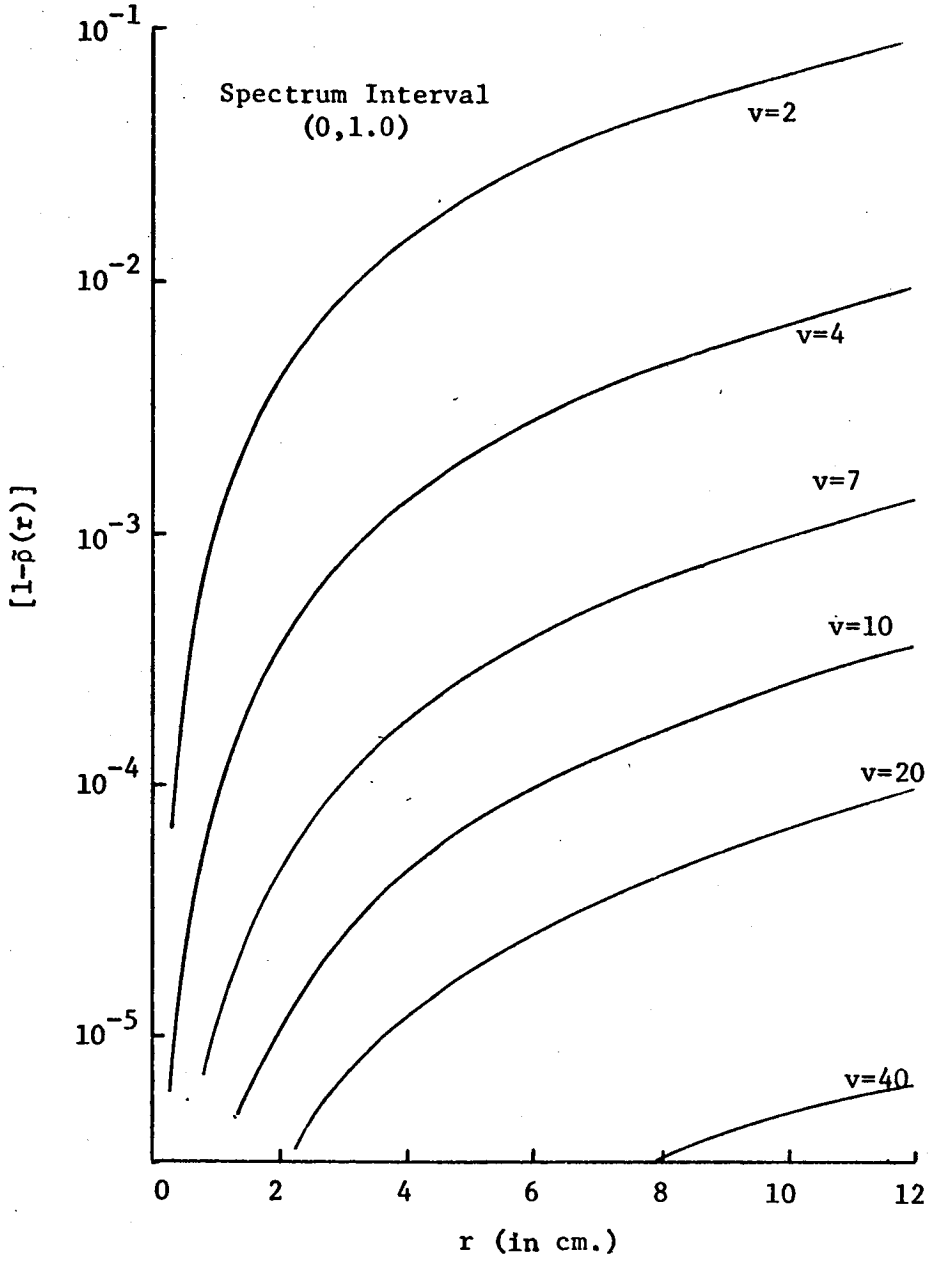

Figure 12. $1-\tilde{\rho}(r)$ as a function of r and v when the spectrum interval is (0,1.0), i.e., essentially the same as $(0,\infty)$.

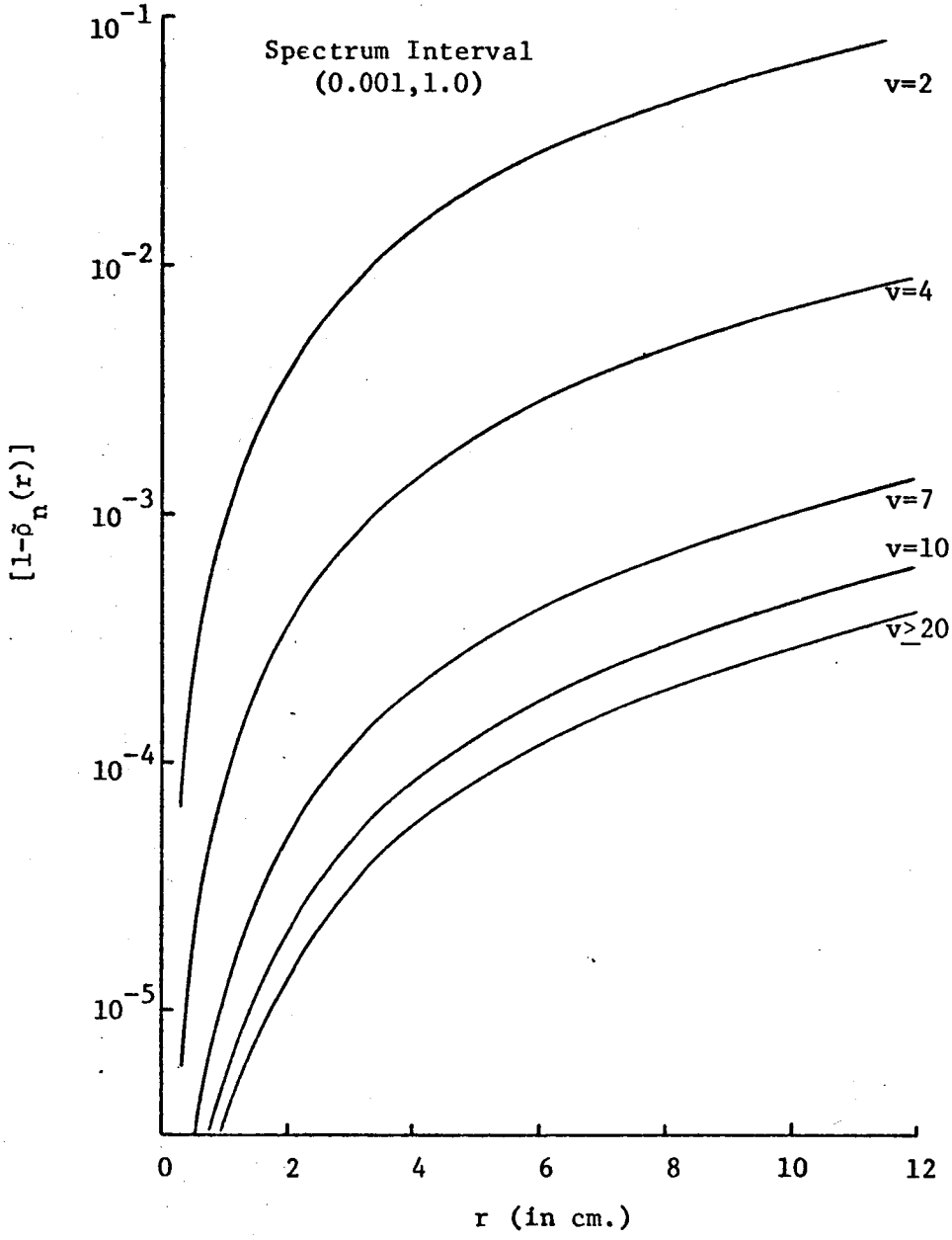

Figure 13. $1-\tilde{\rho}_n(r)$ as a function of r and v when the spectrum interval is $(10^{-3}, 1.0)$.

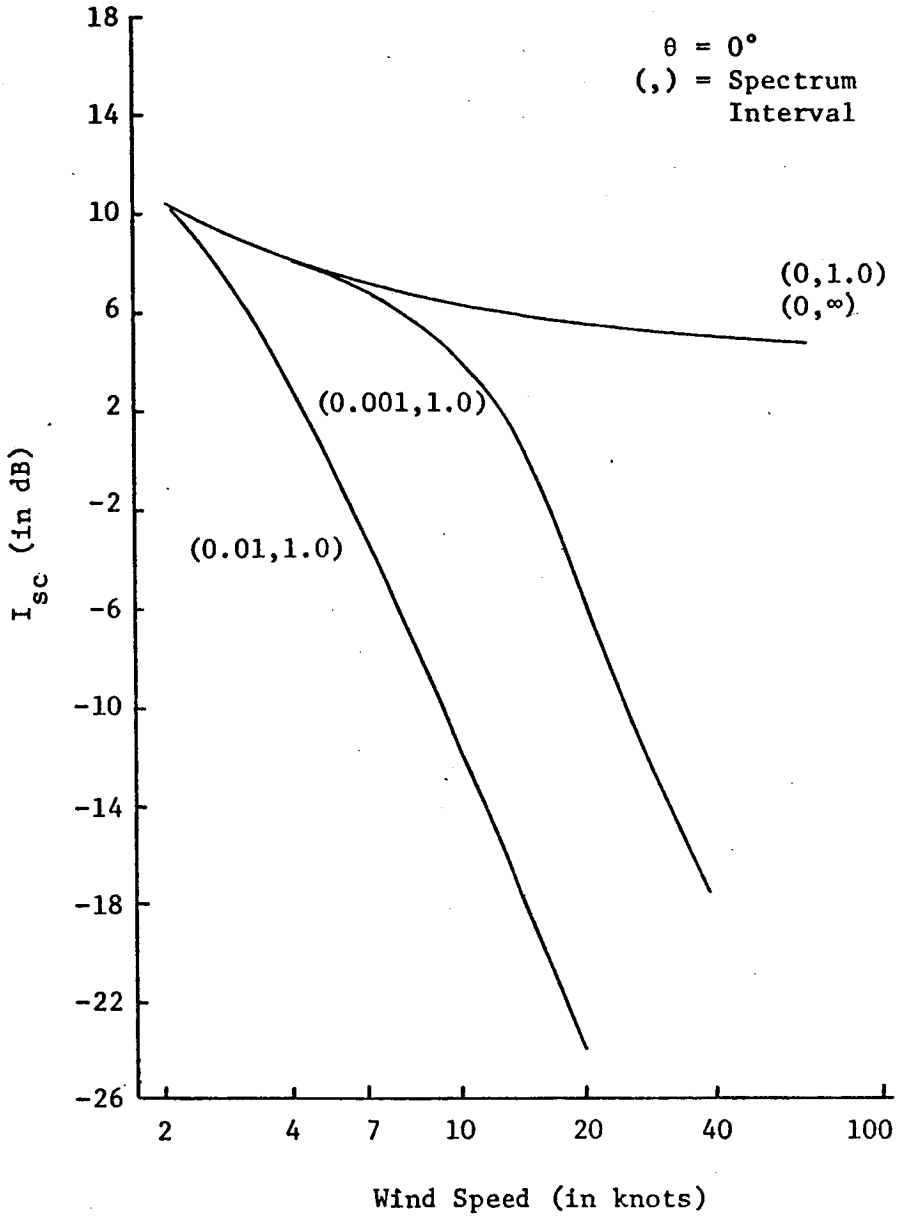

Figure 14. Behavior of scattering integral for various lower spectrum truncation points, λ_{rf} = 3 cm.

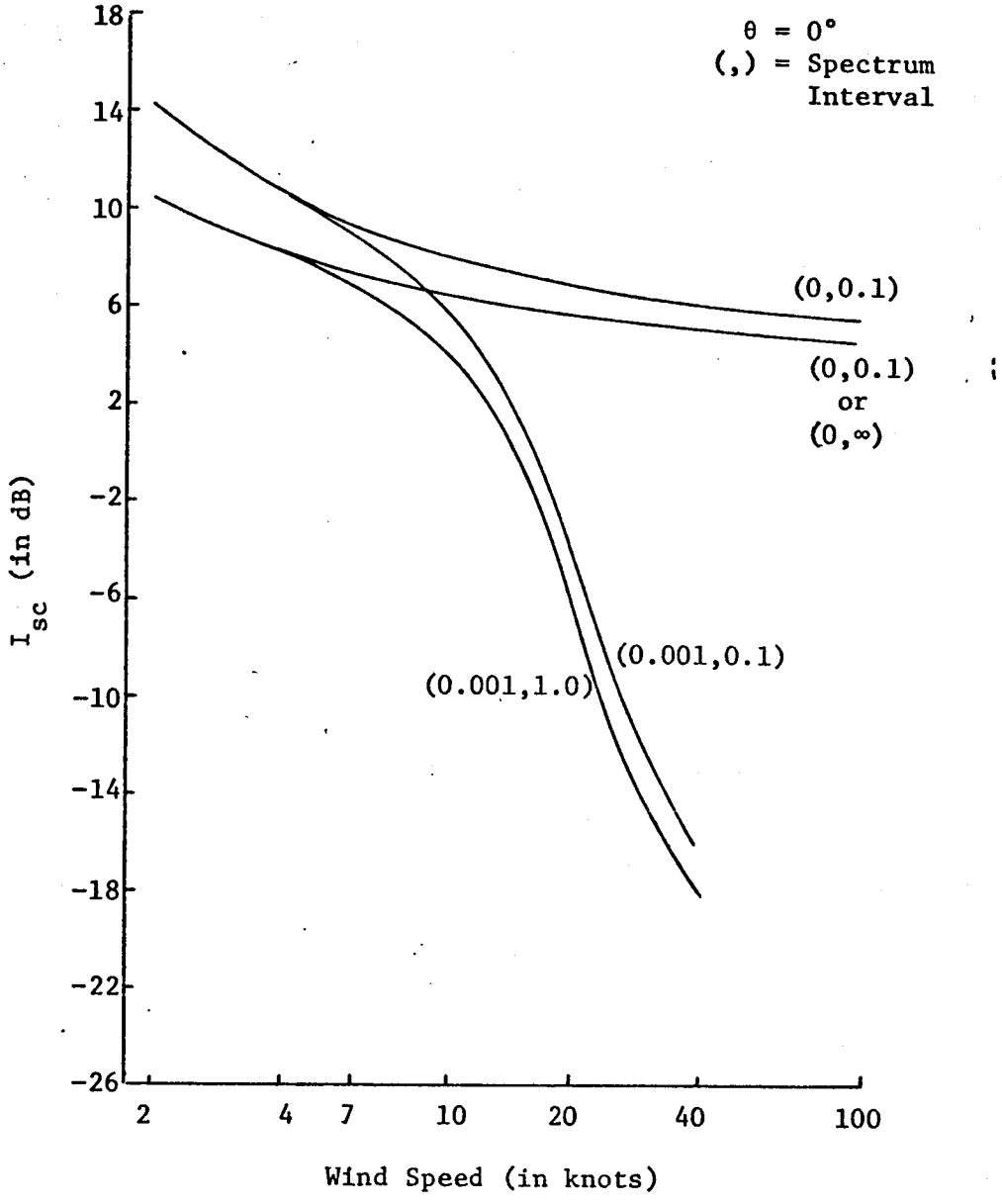

Figure 15. Behavior of scattering integral for various upper spectrum truncation points, λ_{rf} = 3 cm.

Data Requirements in Support of the Marine Weather Service Program

13

J. Travers, R. McCaslin, and M. Mull
NOAA/National Weather Service
Silver Spring, Maryland 20910

I. Introduction

The National Weather Service (NWS) furnishes weather and river forecasts and warnings to the public, and provides specialized services concerned with marine, aviation, agricultural and forestry operations and air pollution control.

Historically, marine weather support was a principal basis for the development of a government weather service, beginning with a Congressional Resolution in 1870. In 1891 the newly established Weather Bureau took over the weather services, and finally, just a year ago with the formation of NOAA we became the National Weather Service, with a constantly growing awareness of, and interest in, serving mariners, boatmen, and all others who work or relax in the marine environment.

Much of the work within the National Weather Service has to do with the description and prediction of weather patterns over most of the globe, and the closely related sea and swell patterns in ocean areas. The operating program is widespread. Its personnel are found at approximately 400 facilities within the 50 states, at 15 overseas stations, 7 ocean stations, and 20 moving ships. To meet our responsibilities for the provision of forecasts and warnings over wide areas of the globe, rapid receipt and processing of global data are required on a continuing and regular basis. Data must be gathered in real-time, within one to three hours or so, from international organized networks covering the land and ocean areas, and extending up through the atmosphere. The inter-relations of the fluid envelope are such that these data are required even for forecasting the state of the ocean.

In order to satisfactorily predict future conditions of the atmosphere and the ocean, it is necessary that we have a running account of these conditions delivered to the forecasters at regular intervals and as soon after the observations as is possible. Any data delayed in delivery may be useful for climatological purposes or for hind-casting, but it simply does not exist as far as the forecaster is concerned. As high-speed communications improve, so our operational weather data base improves. We reached the point about 15 years ago where high-speed computers became necessary to assimilate the vast amount of data. Computers at the National Meteorological Center, aided by human judgment and prompting, calculate the broad-scale weather analyses and predictions, and the results are immediately relayed by teletypewriters and facsimile machine to "the field."

Our field forecast offices use the broadscale predicted patterns and statements as guidance in preparing forecasts for their respective areas of responsibility, and these forecasts in turn are further refined for local use by Weather Service Offices (WSOs) scattered in communities throughout the country. These forecasts include, as applicable, information on wind, waves, weather, air temperature, and visibility. At coastal locations the Weather Service Offices make available the astronomical tide predictions and in some cases also the "surf" temperature. In addition to the general public services, we provide more specialized services to agriculture, aviation and other weather-sensitive endeavors, including, of course, marine interests on the high seas, in coastal waters, and on the Great Lakes. Because of the special threats presented by severe local storms and by hurricanes, expertise and communications necessary to deal with these phenomena are concentrated at a few key locations. The National Severe Storms Forecast Center at Kansas City rides herd on tornadoes, severe thunderstorms and the like, while the wild ocean storms are handled by the National Hurricane Center, Miami, and our forecast offices at San Francisco and Honolulu. Storm surge and high waves are forecast, along with atmospheric phenomena.

Very briefly, the marine service program is concerned with furnishing information on the present state of the marine environment, predictions of future developments, and warnings of expected hazardous conditions. Timely warnings of severe storms, hurricanes, and other marine environmental hazards contribute substantially to the safety and efficiency of marine operations. Ships on the high seas use regularly broadcast warnings and forecasts to navigate around severe storms, to select time-saving routes, and to schedule shipboard operations.

Our present program includes information about anomolous water levels, including sea and swell, surf and breakers, and storm surge. Advisories concerning sea ice on the Great Lakes and Cook Inlet in winter, and in the Bering, Chukchi, and Beaufort Seas in summer, are a part of our existing program. In the future we hope to do more. We think we can deal with ocean currents such as the Gulf Stream, with areas of upwelling, with the thermal structure at least down through the mixed layer, and with the day to day anomolies in the tide height and tidal currents. To gather data necessary for this ambitious program we will look to various methods, including in situ measurements and surface-based remote sensing as well as to satellites.

The NWS is working very closely with the National Data Buoy Project people and other NOAA components in marine instrumentation. Although the NWS is involved in some sensor development, our principal efforts lie in helping to devise methods for rapid data relay, in improving forecast techniques, and in finding ways to reach the people who need our service products.

II. Present Data and Problems

At the present time we have, in addition to observations from coastline points and islands, regularly scheduled observations from seven "stationary" ships in the Atlantic and Eastern Pacific, from 20 moving ships that carry NWS personnel, and from a great many moving ships that have NWS instrumentation. The reports are collected each six hours, averaging about 560 reports each collection period. Unfortunately, only about three-fourths of these arrive at the National Meteorological Center (NMC) in time to be included in the working analyses. In addition to observed weather phenomena and the barometric pressure, the reports include wind speed and direction, wave and swell height, period, and direction, air temperature and dew point, ice information, and sea surface temperature. Unfortunately, these ship reports come almost entirely from ships on well-traveled regular trade routes, leaving very large areas of the oceans unreported.

In addition there are reports from shore stations and a limited number of reports from airlines over the ocean, and while these aircraft reports do not speak directly to surface conditions, we can make large scale inferences from their altimetry and wind calculations. From satellites we already have a limited subjective ocean roughness parameter, in that the sun glint from the ocean surface has different characteristics and brightness with different surface conditions.

We hope to enroll additional ships into the internationally sponsored cooperative ship program, to at least make our data base more dense over the trade routes. Furthermore, these ships and those already in the program provide potential platforms for obtaining bathythermograph data as well as additional ocean surface data. We have some hope for this new data now because of our cooperation, along with other NOAA elements and other government agencies, in the Integrated Global Ocean Stations Systems (IGOSS), a joint effort of the Intergovernmental Oceanographic Commission and the World Meteorological Organization. The first phase of the IGOSS will be to obtain and distribute bathythermograph data in real time. The target date for commencing this new data distribution is January 1972. Satellite observations of sea surface temperature, already available, will be incorporated with those from ships, for a complete analysis of this parameter.

III. Needs For Sea Surface Data

The National Weather Service has agreed in principle to common DOC-DOD requirements for sea state data in the Federal Plan for Meteorological Data from Satellites. As stated in that document they are:

Waves (sea and swell) (global and local)

Frequency of observation	4 obs per day
Timeliness (receipt after obs)	3 hours
Grid spacing	100 n.m. (over open ocean: closer near shores)
Vertical resolution	2 ft. intervals 0-10 ft. 5 ft. intervals 10-30 ft. 10 ft. intervals above 30 ft.

The Federal Plan also states a common requirement for location accuracy of one nautical mile. However, it seems that a location accuracy of 4 or 5 n.m. will meet National Weather Service needs for a few years.

The above requirements are for data over the high seas in the Northern Hemisphere, and will be used to furnish a base line for our numerical wave prediction model. They should be looked on as goals for satellite observation capabilities in the next 5 years or more.

The principal requirement of NWS is for information concerning wave height. In addition, some measure of wave direction and of length or period would be useful. If these requirements cannot be met, it would still be useful to have an indication of roughness or some other parameter that can be related to wave energy, which in turn can be related to wave heights.

Other anomalous water levels are also of interest, such as storm surge, and lesser deviations from astronomical tide calculations, changes in Great Lake levels due to wind set-up or seiche, and surf and breakers along the coast. The above requirements represent the more urgent operational concerns of the Marine Weather Service Program of NWS.

As the satellite's capability to provide more quantitative data grows, we expect to use such data as direct input to the numerical wave prediction model. The availability of such data should result in increased accuracy of sea state predictions. In terms of safety of life and property on the high seas, sea state is one of the most important parameters.

Tide gage observations of wave height are desired to an accuracy of one foot or 10%. However, from the point of view of remote sensors, let us assume that this represents a future research need which might become an operational need several years from now.

Numerical weather analysis programs at the National Meteorological Center are capable of handling input weather data in many forms. Objective

analysis schemes used on the computer to prepare input for numerical weather forecast models can be designed to weight various forms of input data according to accuracy and timeliness. Thus, the derived surface wind speeds in the range from about 5 to 30 knots said to be possible from radar scatterometry data could be integrated into the forecast system. The speed information merged with wind speed and direction observations from ships and islands would be helpful over the broad ocean areas for wind, weather and sea state forecasts.

IV. Summary

One of the greatest responsibilities of the NWS is to provide forecasts of atmospheric and ocean surface conditions over vast areas where data is usually scarce and sometimes unreliable. An improvement in our services would represent a considerable improvement in the safety and efficiency of shipping and fishing industries, and in the safety of the growing population of those who find recreation on the oceans and Great Lakes. Our efforts toward improved services are considerably hampered by lack of information concerning those parameters we hope to forecast. We have traditionally depended largely on our prime users, the ships at sea, for our data. It is a little ironic that the better we get in forecasting, the less data we have from storm areas, rough sea areas, and ice areas. Furthermore, there are large parts of the oceans not usually populated with ships in normal commerce. Therefore our requirements for additional data are immediate and will be of long standing, and hopefully can be met in part by observations from satellites.

THE COMPOSITE SCATTERING MODEL FOR RADAR SEA RETURN 14

K. Krishen

Lockheed Electronics Company, Inc.
Earth Observations Department
Houston Aerospace Systems Division
Houston, Texas

In this paper a composite scattering model, suitable for explaining the behavior of measured scattering cross sections of the ocean surface, will be presented. Furthermore, utilizing this scattering model, the spectrums of the small gravity, gravity-capillary, waves will be predicted for NASA/MSC, 13.3 GHz Scatterometer data.

INTRODUCTION

From the viewpoint of radar scattering at high frequencies, the ocean scene is best described by the composite surface function $\xi(x,y)$ given by

$$\xi = \xi_s + \xi_1 + \xi_2 + \xi_3 + \cdots\cdots , \qquad (1)$$

where ξ_s is the swell, ξ_1 is the sea, ξ_2 is the gravity-capillary structure, and so on. The solution of the electromagnetic scattering from the sea requires the probability density function of the height and the correlation function of each component of ξ, as well as the joint probability densities of the components of ξ. The interaction of the surface wind with each component of ξ must be formulated to study the wind dependence of the scattering cross section. However, a mathematical model of $\xi(x,y)$ as a function of surface wind velocity is not available.

Most of the ocean studies in the past have been devoted to developing models for ocean surface wave forecasts. Toward this goal low frequency gravity wave spectrums for fully developed seas for various windspeeds and fetches have been studied (ref. 1). The dependence of significant wave height, $H_{1/3}$, on surface windspeed has also been reported (ref. 2). The measurement of high frequency gravity-capillary waves has been reported in only a few instances, with the most recent investigation reported by Dobson (ref. 3).

Due to the lack of complete mathematical description of $\xi(x,y)$, the composite model for sea surface scattering will be studied using the NASA/MSC scattering cross section (σ_0) data.

SCATTERING THEORIES AND COMPARISONS

Numerous approaches have been advanced to explain scattering from rough surfaces. The three theories which have received attention and show promise of efficient interpretation of experimental data are as follows:

- The Kirchhoff method
- The small perturbation theory for slightly rough surfaces
- The composite scattering theory

In the Kirchhoff method the field scattered by rough surface is formulated according to Huygen's principle and is given by the Stratton-Chu integral. The total field and its normal derivatives are determined by tangent plane approximation on the surface. These requirements generally restrict this method to locally flat surfaces.

The small perturbation method is valid for large values of the angles of incidence and exhibits meaningful polarization dependence. It is useful in the low frequency limit and can therefore be applied to a class of slightly rough surfaces when very low frequencies are used. A comparison of theoretical and experimental results over slightly rough water surface has been given by Wright (ref. 4). As pointed out in his paper, the measured average backscattering cross sections are in good agreement with the calculated values. The depolarized return from slightly rough ocean surface has been obtained by Valenzuela (ref. 5) by using Rice's small perturbation method. A slightly different approach using the small perturbation theory has also been used for slightly rough surfaces by Bass et al. (refs. 6 and 7).

It is interesting to examine closely what parameters are needed in the formulation of the electromagnetic problem. If only the large-scale structure is considered, the tangent plane approximation can be used. With this theory σ_0 can be expressed as a function of tan β_0, the root-mean-square slope of the surface, in the high frequency limit. Only a few measurements of the sea slope distributions have been reported. The most widely used of these are the optical measurements of Schooley (ref. 8) and Cox and Munk (ref. 9). Figure 1 shows the value of β_0 as a function of windspeed. The curves C(1), C(2) have been calculated using the spectrums of Kitaigorodskii and Pierson and Moskowitz (ref. 10). The lower value of C(1) and C(2), as compared to other curves in figure 1, is attributed to the fact that these curves are not direction dependent (upwind, downwind, etc.) but involve all facets of the sea surface.

For comparison, a value of $\tan \beta_0 = 0.27$ was taken corresponding to a 20.5-knot upwind speed as given in figure 1. The value of σ_{vv} was calculated for the Gaussian height probability function. The calculated value of the scattering cross section (using the Kirchhoff method) given by

$$(\sigma_{vv})_L = \frac{\sec^4 \theta}{\tan^2 \beta_0} |R_{11}(0)|^2 \exp\left(-\frac{\tan^2 \theta}{\tan^2 \beta_0}\right) \qquad (2)$$

for $\epsilon = 55 + j30.25$ is plotted in figure 2. In equation (2), θ is the incidence angle, and $R_{11}(0)$ is the Fresnel reflection coefficient for normal incidence. Also shown in this figure are the NASA/MSC, 13.3-GHz, F4L8R1, 21-knot, forebeam data. The evident disagreement is attributed to the fact that equation (2) is a limiting solution, and only one component of the composite surface is considered.

It has often been suggested that, near the normal direction for backscattering cross sections, scattering of the optics type (Kirchhoff method) predominates. In other directions, however, the slight roughness on top of the large-scale roughness constitutes the major source of scattering. The scattering cross sections are calculated from the scattered component of the field. In view of this, Wright (ref. 11) and Guinard and Daley (ref. 12) ignore the effect of large structure to account for the scattering at higher backscattering angles. The procedure by Wright, Guinard and Daley parallels that of Rice (ref. 13), Barrick and Peake (ref. 14), and Valenzuela. For Rice's method the

backscattering cross sections for a slightly rough surface using first order terms are given in reference 14.

$$(\sigma_{\gamma\delta})_s = 4\pi k_0^4 \cos^4 \theta |\alpha_{\gamma\delta}|^2 W(p,q) \ . \qquad (3)$$

In equation (3)

k_0 = wave number of the incident radar energy

θ = the incident angle

$W(p,q)$ = the roughness spectral density of the surface, and p,q are radian wave numbers

$$\alpha_{HH} = \frac{\varepsilon - 1}{\left[\cos \theta + \sqrt{\varepsilon - \sin^2 \theta}\right]^2}$$

$$\alpha_{vv} = \frac{(\varepsilon - 1)[(\varepsilon - 1) \sin^2 \theta + \varepsilon]}{\left[\varepsilon \cos \theta + \sqrt{\varepsilon - \sin^2 \theta}\right]^2}$$

ε = the complex dielectric constant of the surface.

The scattering cross sections can be computed from equation (3) for the exponential and Gaussian surface height correlation function. For the Gaussian correlated surface, the result is

$$(\sigma_{vv})_s = 4k_0^4 h^2 \ell^2 \cos^4 \theta |\alpha_{vv}|^2 \exp(-k_0^2 \ell^2 \sin^2 \theta) \qquad (4)$$

where ℓ is the surface height correlation distance, and h^2 is the surface-mean-square height.

Several ocean wave spectrums have been proposed over the last few years. However, no experimental spectrums of the fine structure (the capillary waves) have been reported for different wind velocities. In the equilibrium range the isotropic spectrum is of the form

$$W(r) = kr^{-4}$$
$$r = \sqrt{p^2 + q^2} \qquad (5)$$

There is some uncertainty for the value of k, but Phillips (ref. 15) gives the following estimates:

6×10^{-3} for the equilibrium range spectrum for gravity waves

1.5×10^{-2} for the capillary wave spectrum

Evaluating at wave numbers satisfying the Bragg scattering condition (ref. 11) equation (3) yields the limiting form of the cross sections as

$$(\sigma_{\gamma\delta})_s = 1.5\pi \times 10^{-3} |\alpha_{\gamma\delta}|^2 \cot^4 \theta \qquad (6)$$

In the case of the ocean, it is thought that the sea waves, the small gravity waves, and the gravity-capillary structure combined produce the scattering. The swells are assumed absent. To the first order of approximation, the composite scattering cross sections were calculated by adding the average incoherent scattering cross sections from the very rough surface (Kirchhoff method) to that of the slightly

rough surface. The mathematical proof of this is given in papers of Semenov (ref. 16) and Fuks (ref. 17). The comparison of composite scattering cross section and NASA/MSC, 13.3-GHz, F4L8R1, forebeam vv data is shown in figure 3. The theoretical curve is the summation of $(\sigma_{vv})_L$ and $(\sigma_{vv})_s$ as given in equations (2) and (4) respectively. The value of the dielectric constant ϵ is taken as 55+j30.25 and, furthermore, $\tan \beta_0 = 0.27$. The result is encouraging. Comparisons such as shown in figure 3 made it obvious that the scattering by small gravity-capillary structure plays a significant role at higher angles.

A comparison of equation (6) with 13.3GHz, NASA/MSC data in the range of angles $20° \leq \theta \leq 50°$ showed that the angular variation of the data was approximately the same as that given in the equation. It was therefore concluded that the directional spectrums of the small gravity and gravity-capillary structure of the sea could be expressed as

$$W(r) = kr^{-k_3} \tag{7}$$

The values of k and k_3 are wind dependent. After substitution of equation (7), and toward the goal of studying the change of spectrum as a function of wind velocity, an expression of the following form was used.

$$\sigma_0(\theta) = k_1 W_1^{k_2} |\alpha_{vv}|^2 (\cos \theta)^4 (\operatorname{cosec} \theta)^{k_3} \tag{8}$$

In equation (8), W_1 is the wind velocity reduced to a 19.5-meter anemometer height. After using equation (8) it was found that the value of $(\cos \theta)^{4-k_3}$ (in the range of

angles $20° \leq \theta \leq 50°$) could be taken as 1 for most data. Consequently, the following simplified form of equation (8) was also used:

$$\sigma_0(\theta) = k_1 W_1^{k_2} |\alpha_{vv}|^2 (\cot \theta)^{k_3} \qquad (9)$$

By using algorithm 178 "direct search" from ACM communication (ref. 18), a FORTRAN program was used to find the values of k_1, k_2, and k_3 . The program then searches for a minimum value. The value of dielectric constant was taken as $\varepsilon = 55+j30.25$.

Two typical sets of data will be analyzed here. One set consists of NASA/MSC Mission 119, 13.3 GHz data for vertical-transmit vertical-receive polarization combination. The upwind forebeam data, for F9L1R19 (flight 9, line 1 and run 19), F2L1R1 and F3L1R1, the corresponding surface wind velocities are 6 knots, 22.5 knots and 33 knots respectively, were processed. The values for the constants using equation (8) for this set were as follows:

$$k_1 = 0.026$$

$$k_2 = 1.324$$

$$k_3 = 5.47$$

In figure 4, the experimental and calculated data using preceding value of constants is presented. Similar results

were obtained for other sets of Mission 119 data. The same set of data using equation (9) gave the following values:

$$k_1 = 0.043$$

$$k_2 = 1.33$$

$$k_3 = 5.00$$

The second set of data was chosen from NASA/MSC Mission 156 data. The data is the aft beam 13.3 GHz (vertical-transmit vertical-receive) data for upwind conditions. The F2L8R1, F5L4R5 and F6L4R2 data corresponding to 33 knots, 15 knots and 3 knots of average wind speed respectively were processed. The values for constants using equation (8) were:

$$k_1 = 0.0207$$

$$k_2 = 1.1$$

$$k_3 = 6.6$$

Figure 5 shows the comparison of the experimental and calculated data using the preceding values of the constants. It should be pointed out here that the flight 6 data was for very calm conditions with extremely low surface wind velocity.

CONCLUSION

It can be concluded that a theoretical composite model can explain the dependence of the scattering cross section on the angle of incidence θ . The spectrum of the small scale structure is found wind dependent. In general, as the wind velocity increases, the magnitude of the spectrum for high spectrum frequencies increases. The value of the constant k_3 is also a function of the radar incident wave length. Two sets of data (F7L3R1, forebeam Mission 119 data) gathered under identical conditions for a surface wind of 15.5 knots using equation (9) gave the following values for k_3

$$k_3 = 7.3 \quad \text{for} \quad 0.4 \text{ GHz} , \quad \text{and}$$

$$k_3 = 4.7 \quad \text{for} \quad 13.3 \text{ GHz data} .$$

This dependence is expected since 0.4 GHz radar would be relatively insensitive to small gravity-capillary waves.

REFERENCES

1. *Ocean Wave Spectra.* Proceedings of a conference sponsored by the U.S. Naval Oceanographic Office and the Division of Earth Sciences of the National Academy of Sciences, (National Research Council in 1961), Prentice Hall, N. J., 1963.

2. Moskowitz, L.: "Estimates of Power Spectrums for Fully Developed Seas for Wind Speeds of 20 to 40 Knots", *Journal of Geophysical Research,* Vol. 69, No. 24, 1964.

3. Dobson, E. B.: "Measurement of the Fine-Scale Structure of the Sea", *Journal of Geophysical Research,* Vol. 75, No. 15, May 1970.

4. Wright, J. W.: "Backscattering From Capillary Waves With Application to Sea Clutter", IEEE Transactions on Antennas and Propagation, AP-14, No. 6, 1966.

5. Valenzuela, G.: "Depolarization of EM Waves by Slightly Rough Surfaces", IEEE Transactions on Antennas and Propagation, AP-15, No. 4, 1967.

6. Bass, F. G.; and Bocharov, V. G.: "On the Theory of Electromagnetic Wave Scattering From a Statistically Uneven Surface", Radio Engineering and Electronics, Vol. 3, No. 2, 1958.

7. Bass, F. G., et al., "Very High Frequency Radiowave Scattering by a Disturbed Sea Surface", Parts I, II, IEEE Transactions on Antennas and Propagation, AP-16, No. 5, 1968.

8. Schooley, A. H.: "A Simple Optical Method For Measuring the Statistical Distribution of Water Surface Slopes", *Journal Opt. Soc. Amer.,* 44, 1954.

9. Cox, C.; and Munk, W.: Measurement of the Roughness of the Sea Surface From Photographs of Sun's Glitter", *Journal Opt. Soc.*, 44, 1954.

10. Krishen, K.: "Saturation of σ_0 With Increasing Wind Velocity", Lockheed Electronics Company, HASD TR No. 649D.21.007, Houston, Texas, 1969.

11. Wright, J. W.: "A New Model for Sea Clutter", IEEE Transactions on Antenna and Propagation, AP-16, No. 2, 1968.

12. Guinard, N. W.; and Daley, J. C.: "An Experimental Study of a Sea Clutter Model", Proc. IEEE Vol. 58, No. 4, 1970.

13. Rice, S. O.: "Reflection of Electromagnetic Waves From Slightly Rough Surfaces", *Comm. Pure Appl. Math.*, Vol. 4, 1951.

14. Barrick, D. E.; and Peake, W. H.: "Scattering From Surfaces With Different Roughness Scales: Analysis and Interpretation", Research Report, Battelle Memorial Institute, Ohio, 1967.

15. Phillips, O. M.: *The Dynamics of Upper Ocean*, Cambridge University Press, London, 1966.

16. Semenov, B.: "An Approximate Calculation of Scattering of Electromagnetic Waves From a Slightly Rough Surface", Radioteknika i Electronika (USSR), 11 (English Translation).

17. Fuks, I.: "Contribution to the Theory of Radio Wave Scattering on the Perturbed Sea Surface", Izvestia Vyshikh Uchebnikh Zavedeniy Radiofizika, 5 (English Translation).

18. Hooke, R. and T. Jeeves: "Direct Search Solution of Numerical and Statistical Problems", *Journal Assoc. Computing Machinery*, Vol. 8, No. 2, 1961.

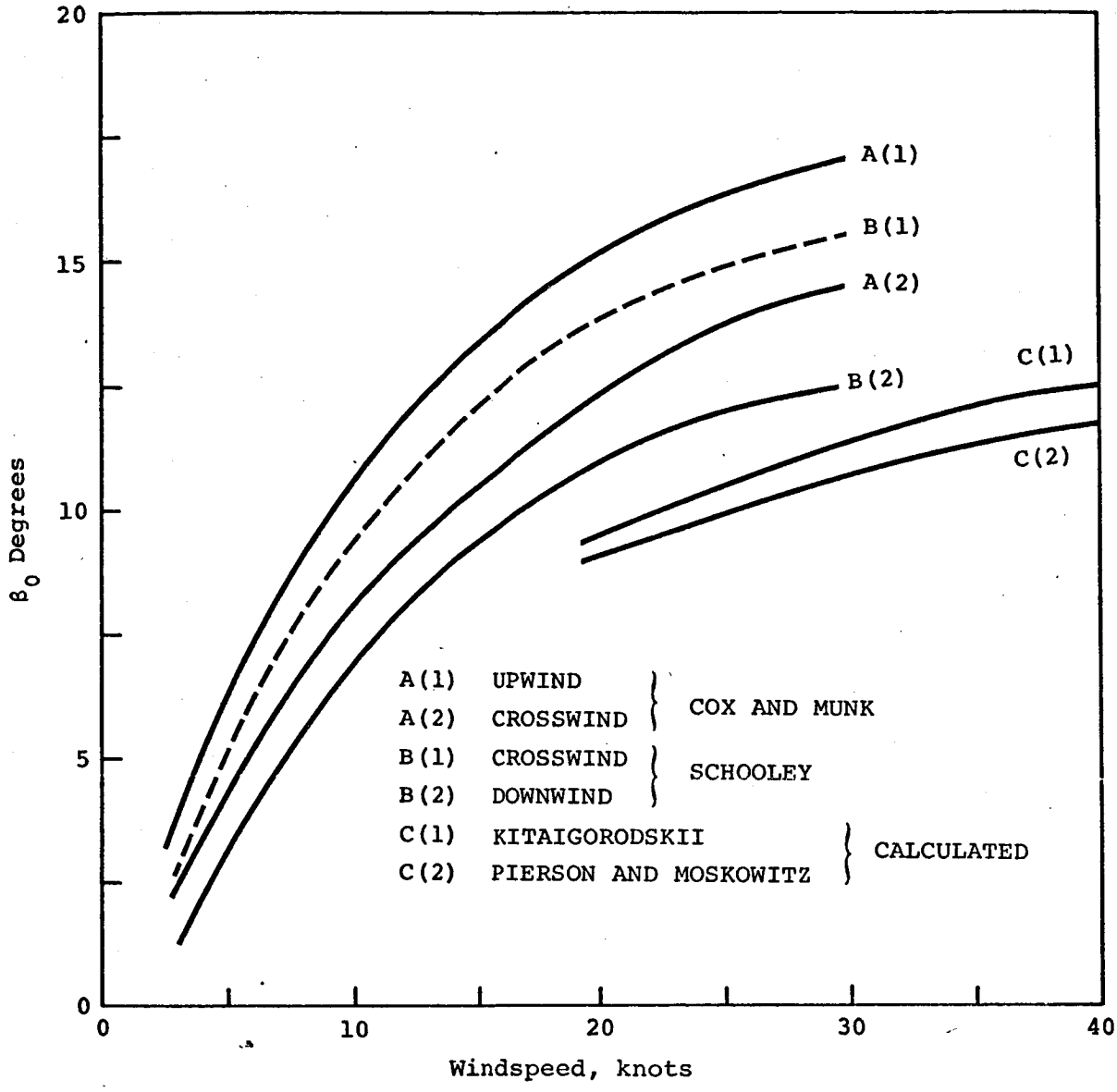

Figure 1. – Values of β_0 as a function of windspeed.

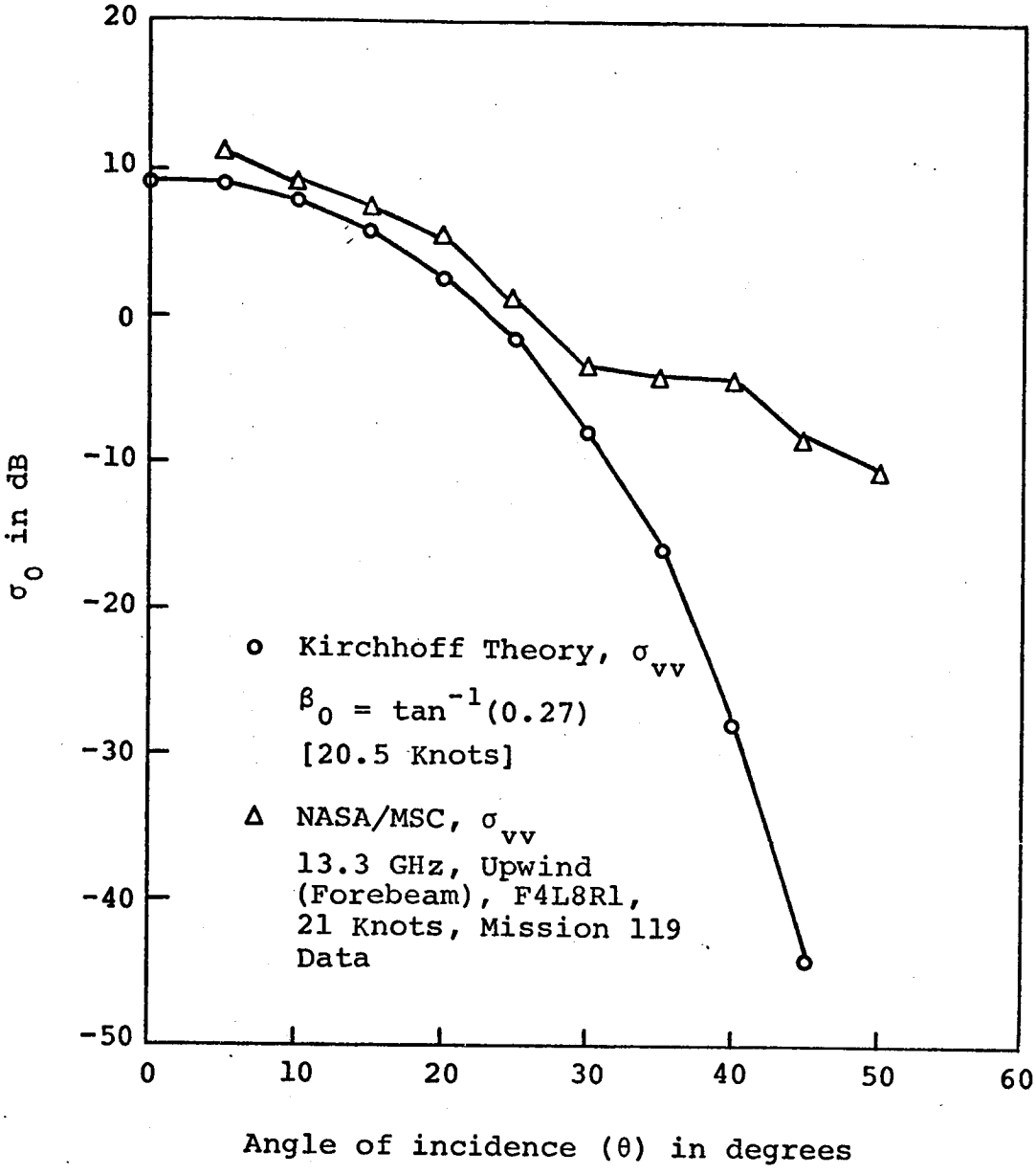

Figure 2. — Comparison of NASA/MSC, 13.3-GHz data with the Kirchhoff theory.

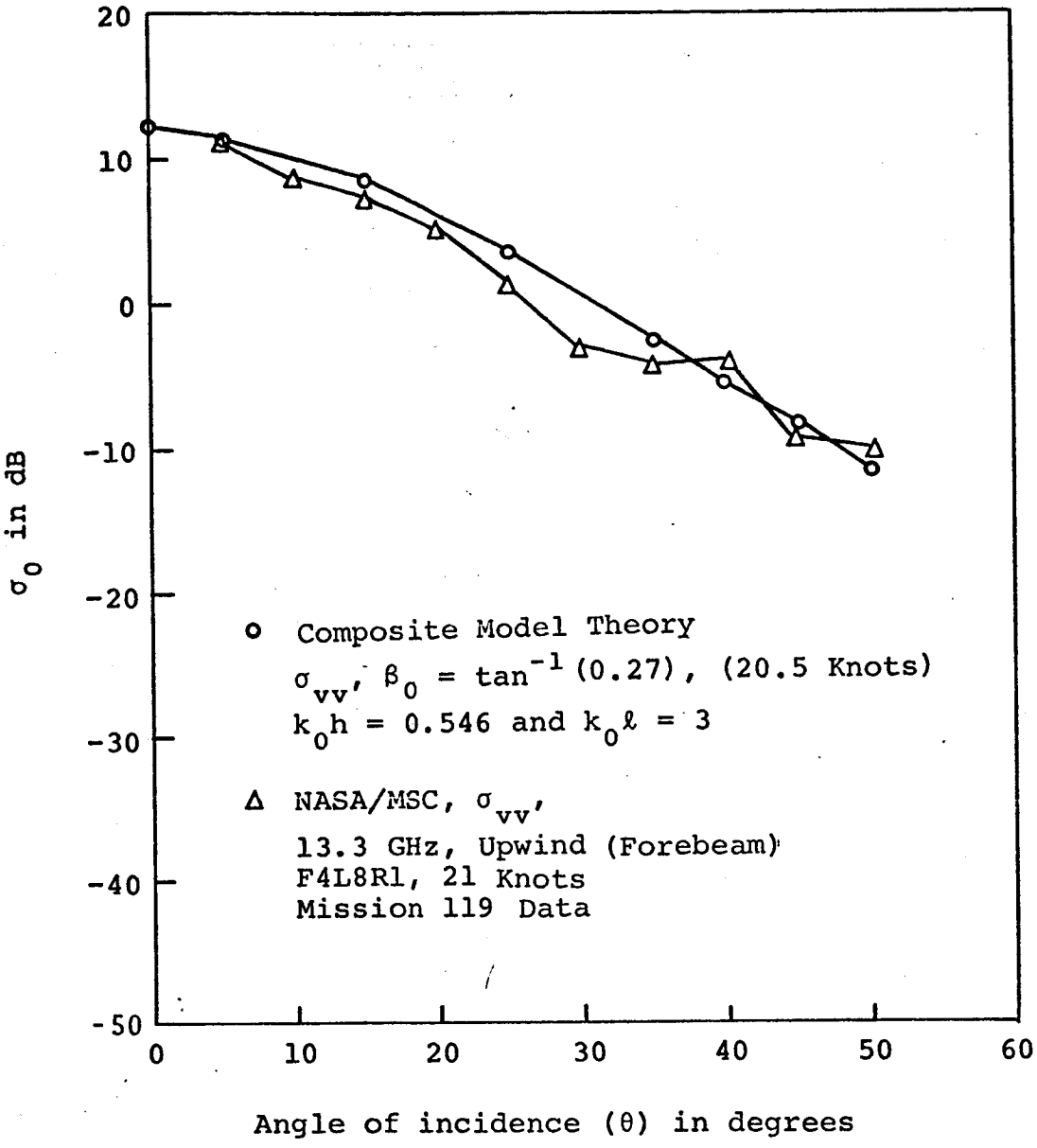

Figure 3. – Comparison of NASA/MSC, 13.3-GHz data with model theory.

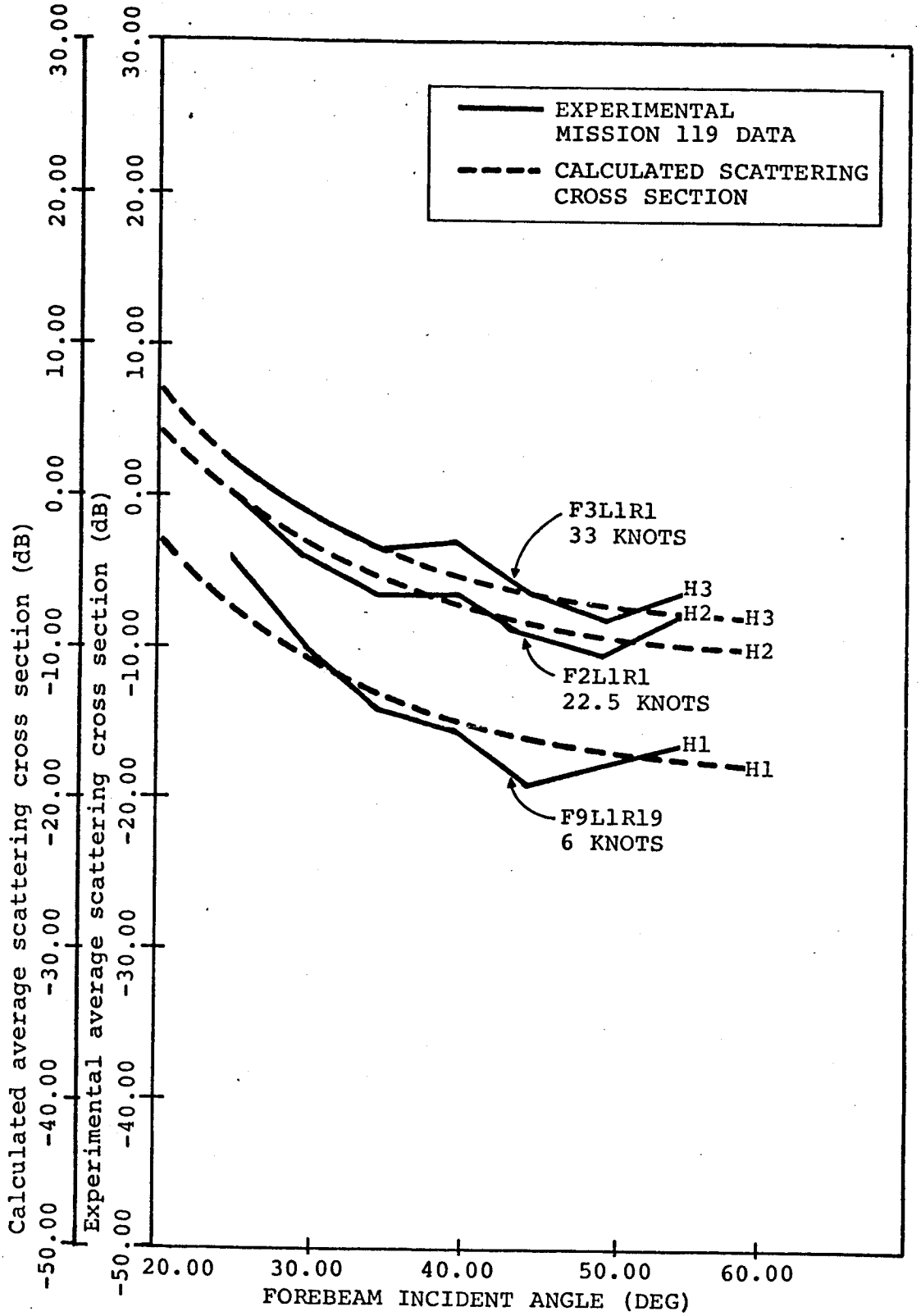

Figure 4. – Comparison of calculated and experimental scattering cross section for Mission 119.

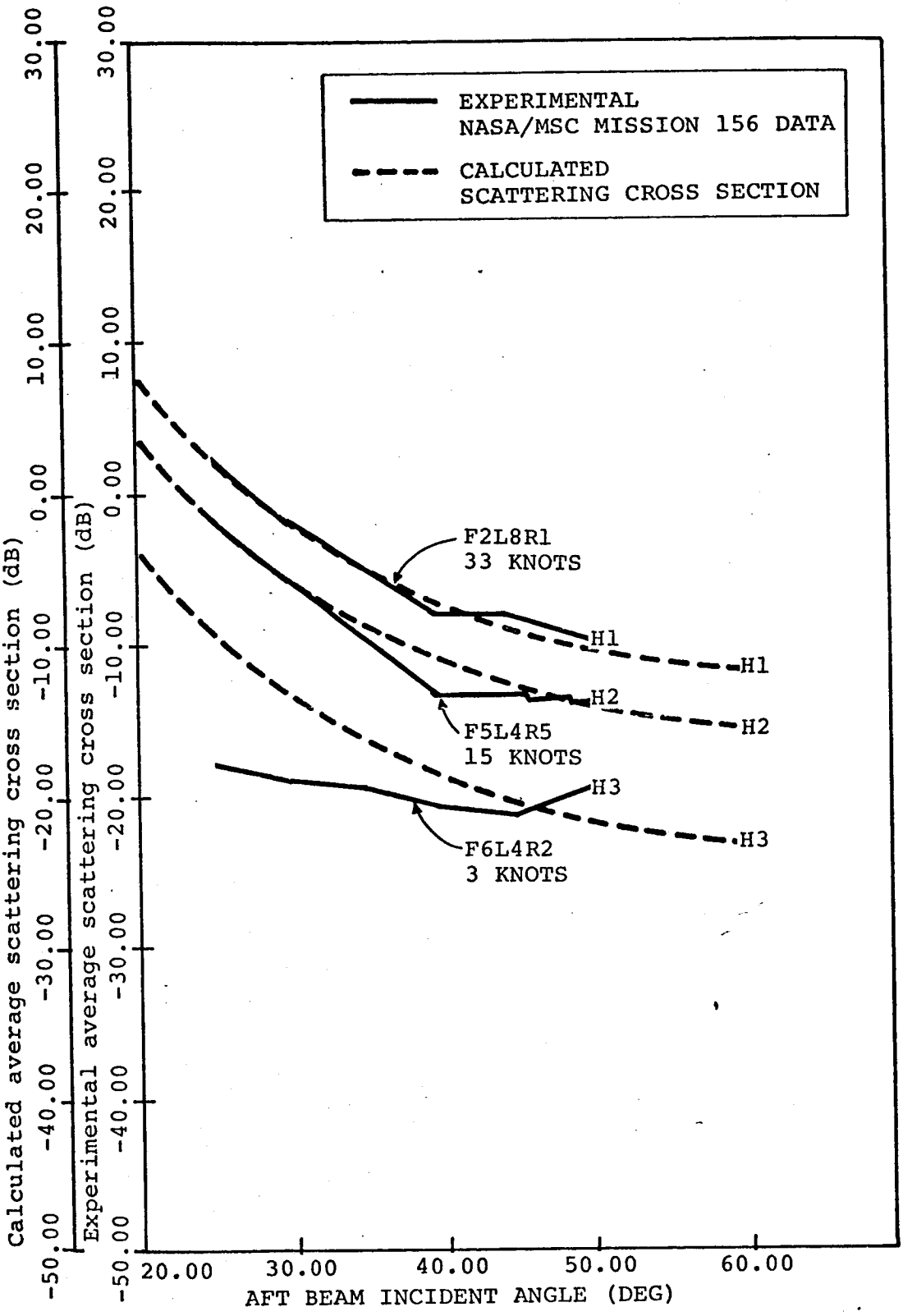

Figure 5. – Comparison of calculated and experimental Mission 156 data.

Skylab S193 and the Analysis of the Wind Field Over the Ocean* 15

N73-15384

Willard J. Pierson, Jr.
Department of Meteorology and Oceanography
New York University

Abstract

The present status of the program to provide proof of concept for the idea that simultaneously observed radar scattering cross section measurements and passive microwave measurements can be used to determine the winds in the planetary boundary layer over the ocean is given. The role of S193 in Skylab is providing the final clinching proof that an operational instrument will obtain data of great value to both meteorology and oceanography is described.

Introduction

A combined program of theoretical and applied research on the problem of determining the winds over the oceans by means of both active and passive microwave measurements has been under way for several years in the Department of Meteorology and Oceanography at New York University and at the Center for Research at the University of Kansas. The overall concept has been described by Moore and Pierson (1971).

The fundamental hypothesis is that the ocean surface gets rougher as the wind increases and that radar backscatter and passive microwave emission vary with this increased roughness. In terms of this conference topic, the sea surface topography for waves with lengths of centimeters to meters changes rapidly in response to the wind. These changes cause changes in radar sea return and in passive microwave emission (especially when whitecaps are considered) that can be interpreted in terms of the wind speed in the planetary boundary layer.

This research as supported by NASA through the Spacecraft Oceanography Project (now called Remote Sensing Oceanography) and through AAFE at Langley has lead to many achievements that fit together into a combined theoretical and observational matrix to provide sound reasons why S193 will prove to be a successful experiment and to give guidance on how the radar radiometer under AAFE development should be used and on how S193 should be operated.

The combined theoretical and observational matrix contains the following results.

*Contribution No. 118 of the Geophysical Sciences Laboratory, Dept. of Meteorology and Oceanography, New York University, Bronx, N. Y.

F

(1) Time histories of capillary gravity waves generated in wind-water tunnels for winds corresponding to anemometer height winds from calm to 60 knots and for a variety of fetches up to 19 or 20 meters as obtained at New York University, Stanford University, and Kyoto University show that the spectral energy in gravity-capillary waves ($f \geq \sim 4$ Hertz) increases with increasing wind speed and does not depend on fetch.

(2) Photographic data from Kyoto University show that this increase in spectral energy at these frequencies is simultaneously accompanied by an increased roughness in the spatial scales of a gravity capillary waves. The instantaneously rough surface as a function of position becomes rougher with increasing wind speed.

(3) Two improved theories of radar sea return have been derived, one at the University of Kansas and another at New York University, that show how knowledge of the spectrum of the waves permits the theoretical calculation of the radar scattering cross section.

(4) Measurements at 13.3 GHz by MSC Earth Resources aircraft for winds from nearly calm to about 50 knots have shown that for both upwind-downwind and crosswind conditions, the radar scattering cross section is a function of wind speed.

(5) Theoretical considerations on the differences to be expected between radar and passive measurements at the sea surface in the presence of clouds and rain compared with the same conditions at the sea surface without clouds and rain have lead to the development of concepts on how to account for the effects of clouds and rain on these measurements.

(6) Since both theory and observation suggest that radar sea return will depend slightly on the larger waves in the wave spectrum and since the observations show that the passive microwave sea surface emission will depend on the amount of foam (as well as on the wave structure), procedures for specifying these features of the sea surface in terms of the gravity wave spectrum and the whitecap production index have been developed.

(7) Numerical models of the wind field in the planetary boundary layer that account for atmospheric stability have been developed.

(8) Simulations of the data that might be obtained by a radar radiometer on a polar orbiting spacecraft have been used to show that such data, plus a few scattered ship reports, permit the analysis of the vector wind in the planetary boundary layer and of the surface pressure field.

(9) Procedures have been developed so that the various scanning modes of S193 can be used to augment and re-verify the variation of sea return with wind speed and to obtain data similar to the data that

would be obtained by an operational spacecraft so as to permit the analysis of the wind field over a large ocean area.

Wave Data and Sea Return Theories

Our work under AAFE sponsorship during the past year has just been reported by Pierson et al. (1971). Summarized quickly, our findings are that the capillary wave spectrum does not saturate. To the contrary, the spectral energy as a given frequency band increased with increasing wind speed for winds up to 60 knots, at least. If the spectrum is given as a function of frequency by

$$S(\omega) = \frac{D(4.05 \times 10^{-3})}{[k(\omega)]^3} \frac{dk(\omega)}{d\omega} \qquad (1)$$

where $k = k(\omega)$ is the equation relating wave number to frequency for all waves; gravity--capillary and in between, it is found that this form for $S(\omega)$ fits a wide range of estimated frequency spectra from the frequency at which the spectrum is a maximum upward.

The quantity D is dominantly a function of wind speed as shown in Fig. 1 from the report by Pierson et al. (1971). The inverse of $k = k(\omega)$ is $\omega = \omega(k)$, and when this inverse is used equation (1) becomes

$$S(k) = \frac{D(4.05 \times 10^{-3})}{k^3} \qquad (2)$$

(which was really the starting point based on the concept of an equilibrium spectrum by Phillips (1966)).

The constant, 4.05×10^{-3} seems well established as an equilibrium range for the gravity wave spectrum with wave periods of 2 seconds or longer. Fig. 1 shows that the capillary spectrum can be 10^{-4} weaker than the gravity spectrum for very low winds and that for winds above a certain threshold value the capillary spectrum is higher than the equilibrium gravity value and shows a strong dependence on wind speed.

Given the observed dependence of the spectrum on wind speed, any theory of radar-sea return would predict a variation with wind speed if the spectrum was changing with wind speed at the Bragg scattering wave numbers.

The newer theories of sea return as given by Fung and Chan (1969) and by Jackson (1971), as extensions of the work by Chia (1968), require knowledge of the full two-dimensional wave number

spectrum as a function of wind speed and would yield changes in sea return caused by effects other than Bragg scattering.

Our goal in this program is to define the full wave number spectrum as a function of wind speed and compute sea return using those new theories.

Measurements of Sea Return at 13.3 GHz

NASA has carried out three remote sensing missions using a 13.3 GHz fan beam doppler scatterometer. The missions were Mission 88 based at Shannon, Ireland, Mission 119 based in Bermuda, and Mission 156 based at Patuxent, Maryland. Data were obtained on radar sea return covering winds from about 7 knots to 49 knots. The data have to be studied in terms of the radar scattering cross section normalized to 10°, but they clearly show that sea return is a well defined function of wind speed over this range of speeds.

A thorough analysis of the instrument and of the data will be given in a forthcoming report by G. Bradley of the University of Kansas. Table 1 summarizes the results of least square fits to all of the available data.

Table 1. Dependence of Radar Scattering Cross Section on Wind Speed

Angle	Wind direction	Dependence	RMS error
15°	upwind	$\sigma^\circ \sim W^{0.37}$	0.68 db
25°	upwind	$\sigma^\circ \sim W^{1.11}$	1.01 db
35°	upwind	$\sigma^\circ \sim W^{1.44}$	1.63 db
15°	crosswind	$\sigma^\circ \sim W^{0.30}$	0.76 db
25°	crosswind	$\sigma^\circ \sim W^{0.98}$	1.39 db
35°	crosswind	$\sigma^\circ \sim W^{1.35}$	1.49 db

Numerical Models for Wind Fields, Waves and Whitecaps

The integration of space obtained data into the total of all conventional data requires computer based procedures. The winds over the oceans in the planetary boundary layer vary with height as a function of atmospheric stability and the thermal wind. Procedures for the analysis of the wind field over the oceans that use conventional ship report data have been developed by Cardone (1969), and the computer products that result for an analysis four times as dense as the NWP grid have been illustrated by Pierson (1970).

Theories of radar sea return in one way or another, and to various degrees, all suggest that the radar scattering cross section is changed by changes in the spectrum of longer waves even if the smaller-scale structures, most responsible for the return, remain unaltered. These longer waves take a while to be generated and can propagate great distances across the ocean. One of the goals of our research has been to produce better wave specification and forecasting computer based procedures, and, as a by-product of this goal, the capability also exists to describe the gravity wave part of the spectrum as a possible "vernier" correction to the sea return measurements.

Several different wave forecasting computer models have been developed. One described by Pierson (1970, 1971) yields 360 numbers at about 4000 points in the North Pacific. This model, though having been run on a test basis, is difficult to run operationally on available facilities.

The model, as first developed, has been made less complicated by doubling the grid spacing so that only about 1000 points cover the North Pacific. This model could also be run.

However, at FNWC the requirement is for coverage of both the South Pacific and the North Pacific and so the spectral angular resolution of the original model has been reduced from 24 direction bands each 15° wide to 12 direction bands each 30° wide so that the number of grid points can be increased.

Some combination of the above wave specification and wave forecasting methods should soon be operational at FNWC. Other larger capacity, higher speed computer complexes would be able to use the smaller grid higher spectral resolution models that have been developed.

Passive microwave measurements of the emission from a wind roughened sea have shown that the whitecaps and foam on a wind sea increase the microwave emission drastically. Whitecaps and the percentage of foam cover on the sea surface are predictable as a part of these numerical wave specification and forecasting procedures. The concepts involved have been described by Cardone (1969), Ross and Cardone (1970), and Pierson (1970).

Simulation of Space Data

Under the assumption that a scanning radar radiometer would gather data that could be used to determine the wind speed on a grid of points, the data that could be obtained by such an instrument have been simulated by Druyan (1971). Analysis procedures based on conventional ship coverage and the simulated space data have been de-

veloped that show that good analyses of the vector wind field and the surface pressure field can be obtained.

A sample analysis based on conventional data coverage and then on only a few ships and simulated data are shown in Figs. 2 and 3.

Plans are under way to study a mix of space data and data buoys such as might be the result of the National Data Buoy System.

Once the surface pressure field is defined over the oceans, measurements of temperature as a function of pressure as obtained by presently operating remote sensing systems of which SIRS was the forerunner (Wark and Hilleary, 1969), make it possible to define the entire atmospheric structure over the oceans as it would be needed for the forward integration in time of the primitive equations defining atmospheric motions. A radar radiometer should prove of great value, combined with an atmospheric sounding device on a spacecraft, as a data source for numerical forecasts in the southern hemisphere. Southern hemisphere numerical models are described by Gauntlett and Hincksman (1961).

Passive Microwave Measurements

Passive microwave measurements of a wind roughened sea have been reported by Hollinger (1970) and others. Clearly, both the change in the small-scale roughness elements and the presence of whitecaps and foam cause an increase in microwave emission with increasing wind speed. If the sea surface is viewed through clear air from spacecraft altitudes, it would be expected that both the radar scattering cross section measurements and the passive measurements would give independent estimates of the wind speed. The radar measurements would be less sensitive to the variations with fetch and duration of the larger gravity waves on the sea surface, whereas the microwave measurements would be affected by whitecaps and foam, which are fetch and duration dependent.

From a spacecraft, measurements will also be made through the clouds of varying thicknesses and water content as well as through clouds with precipitation in the beam. For various reasons no airborne measurements through clouds and clouds and rain have yet been made for varying wind conditions at the surface. Various theories exist as to how clouds and rain affect microwave measurements, but no combined theory is available for simultaneously varying sea surface conditions and clouds and rain.

Efforts to define this problem have been made by Mr. John P. Claassen of CRES and these results have been incorporated in a joint proposal prepared by NYU, CRES, ESG (of NOAA) and Lamont

for the study of S193 data (McClain et al., 1971). The ideal system for such a study is, of course, S193 on Skylab and the results that can be obtained from it are the subject of the following sections of this paper.

Skylab S193

The step from laboratory wind-water tunnel measurements, tower microwave measurements and airborne photographic, laser radar and microwave measurements to space measurements by means of S193 or Skylab introduces a number of important new variables. They are:

1. Increased data rates, compared to past airborne missions, covering a full range of surface wind speeds and wind wave directions relative to the radar beam.

2. A change from the microscale and mesoscale, as encountered during platform and aircraft measurements, to the synoptic scale with resulting measurements that are more representative of the values needed for synoptic meteorological analyses.

3. An opportunity through the scanning mode of S193 to obtain real data for trial computations of the computer based procedures for integrating spacecraft data and conventional data.

4. A variety of intervening atmospheric conditions ranging from clear air, through many types of clouds, finally to clouds with varying amounts of precipitation.

These various new features are illustrated by the simultaneous study of Figs. 4, 5, 6, and 7. Fig. 4 illustrates a typical cloud pattern off the east coast of USA. Fig. 7 illustrates a conventional analysis of the winds at the ocean surface near the time of the cloud imagery. Fig. 5 shows a schematic analysis of the cloud pattern shown in Fig. 4 with indicated areas for showers, rain and drizzle. Fig. 6 illustrates two of many possible Skylab S193 data passes that might have been made over these conditions.

In Fig. 6, the northbound pass illustrates the alternate side scanning mode. At each open ellipse, six quantities are measured, radar scattering cross section in the HH, VV, VH and HV modes and passive microwave emission in the H and V modes, and thus 900 numbers become available in seven minutes of instrument operation. If, at each spot, the data could be used to infer wind speed, the result would be a pattern quite similar, except for orientation, to the pattern that would be scanned by a spacecraft in a 100° retrograde sun synchronous orbit. For the total area scanned, these would be numerous forms of surface truth available, such as conventional ships and, by 1973, buoys of the National Data Buoy System. The area illustrated is one in

which the surface truth should be quite dense compared to most other areas of the world. For such an area, a streamline isotach plus computer based analysis of the wind field based on all available conventional data, as suggested in Fig. 7 then provides a value of wind speed and a wind direction relative to the radar beam for each set of six observations.

The southbound orbit segment shows a second scanning mode. Each black ellipse represents 30 observations, 6 combinations of radar and passive microwave, times five different angles for essentially the same areas of illumination. This particular southbound orbit, if it actually had occurred, might have made measurements for essentially downwind conditions for winds from 20 to 70 knots in just a few minutes.

Each spot on the sea surface scanned by S193 is about 14 by 12 kilometers and represents a large area of the sea surface. Application of the Taylor hypothesis suggests that this brief spacecraft observation would be the equivalent of having about ten duplicate MSC aircraft flying parallel to each other a kilometer apart for a distance of 14 kilometers and averaging radar data recorded by each aircraft to obtain single values for estimates of the scattering cross section and microwave measurements. The instantaneous spatial variability over the area of the scanned spot is the equivalent of several hours of variability in an anemometer record of the turbulent wind at a fixed point above the sea surface. The space average is therefore a very stable measure of a properly averaged wind over an appropriately chosen area suitable for use in synoptic scale analyses.

All of the above are the advantages of making these measurements from space as the next step in the development of an operational instrument. Figures 4 and 5 show, of course, the disadvantage, and the major problem that still has to be overcome. The disadvantage is the clouds, and the problem is to infer wind speed at the sea surface below the clouds from these measurements.

Global cloud mosaics and geostationary cloud imagery show that about 60 to 70% of the ocean surface can be viewed through clear air by a radar radiometer. For these data points there will be no problem.

For the S193 experiment, it will be necessary to obtain an independent decision from other sources of space imagery as to whether or not a particular surface cell is being viewed through clouds. If it is being viewed through clouds, it then becomes important to determine cloud thickness, and whether or not there is precipitation.

If clouds are present in the beam, the effects on the radar and passive microwave measurements are quite different. As pointed out in McClain et al. (1971), the passive measurements soon lose "con-

tact" with the surface, or, stated another way, liquid water in clouds is "hot" compared to the sea surface and the microwave temperature is expected to rise as soon as clouds enter the beam. The radar pulse can, however, pass through the cloud without too much attenuation, be scattered back by the sea surface through the cloud again to the spacecraft, and still contain information on the roughness of the underlying sea surface. As discussed by Moore and Pierson (1971) high microwave temperatures along with reasonable scattering cross section values can be interpreted as a cloud effect and the value of the microwave temperature can be used to correct the sea return value for the slight effect of the clouds on it. It is to be expected that the effects of most non-precipitating stratus decks can be easily removed.

Very thick wet clouds with precipitation are another problem. It may only be possible to identify characteristics of such data points that go with these conditions and eliminate the measurements from further analysis. It is believed, however, that a substantial portion of the measurements through clouds can be interpreted in terms of the winds over the sea surface. Loss of data due to thick clouds and rain should not seriously affect the usefulness of the instrument.

A plan for the stratification and analysis of the radar and passive microwave data in terms of the effects of clouds and precipitation and in terms of the various sources of "sea" truth was given by McClain et al. (1971). The plan essentially proposed proceeding from clear air measurements to thin clouds and finding the effects of the thin clouds to be followed by the increasingly more complex problems of thick clouds and clouds with rain and snow. Airborne measurements with the AAFE radar radiometer below the clouds are an important part of the program. The full scheme is shown in Figs. 8 and 9.

Conclusion

To summarize briefly, various parts of the problem of using a radar radiometer as a remote sensing device to determine the winds over the ocean have been identified and solved. There remains only one real problem connected with going to spacecraft and that is the problem of clouds intervening between the spacecraft and the sea surface. Ways to study this problem are available and suggest that useful data will still be obtainable through many kinds of cloud conditions.

Acknowledgments

The preparation of this paper was sponsored by the Ocean Dynamics Remote Sensing Study Project at NRL under contract N62306-70-A-0075.0007. The work described was sponsored by both the above program and the AAFE program under contract NASA-1-10090.

References

Cardone, V., Specification of the wind distribution in the marine boundary layer for wave forecasting. TR 69-1, Geophysical Sciences Lab., New York University, 1969.

Chia, R.C., The theory of radar backscatter from the sea. Ph.D. thesis, Univ. of Kansas, 1968.

Druyan, L.M., Objective analysis of sea-level winds and pressures derived from simulated observations of a satellite radar-radiometer and actual conventional data. TR 71-7, Geophysical Sciences Lab., New York University, 1971.

Fung, A.K., and H.L. Chan, Backscattering of waves by composite rough surfaces. IEEE Trans. on Ant. and Prop., Vol. AP-17, No. 5, September 1969.

Gauntlett, D.J., and D.R. Hincksman, A six level primitive equation model suitable for extended operational prediction in the Southern Hemisphere. J. Appl. Meteorology, 19(4), 613-625, 1971.

Hollinger, J.P., Passive microwave studies. In Hydrology and Oceanography, Third Annual Earth Resources Program Review, Vol. III, 1970.

Jackson, F.C., A high frequency correction to the Kirchoff approximation, with application to rough surface EM wave scattering. TR 71-8, Geophysical Sciences Lab., New York Univ., 1971.

McClain, E.P., R. Moore, W.J. Pierson, and M. Talwani, A joint meteorological, oceanographic, geodetic, and sensor evaluation program for Experiment S193 on Skylab. Proposal submitted to NASA, 1971.

Moore, R.K., and W.J. Pierson, Worldwide oceanic wind and wave predictions. J. of Hydronautics, 5(2), 52-60, 1971.

Phillips, O.M., The Dynamics of the Upper Ocean. Cambridge University Press, 1966.

Pierson, W.J., The integration of remote sensing data into global weather prediction, wave forecasting, and ocean circulation computer based systems. Hydrology and Oceanography. Third Annual Earth Resources Program Review, Vol. III, 1970.

Pierson, W. J., Spectral wave forecasts. In Eighth U.S. Navy Symposium on Military Oceanography. Vol. I, pp. 394-406. Naval Postgraduate School, Monterey, Calif., 1971.

Pierson, W. J., F. Jackson, R. Stacy, and E. Mehr, Research on the problem of the radar return from a wind roughened sea. (To appear in Proc. of AAFE, Langley, 1971.)

Ross, D. B., and V. Cardone, Laser observations of wave growth and foam density for fetch limited 25 m/s winds. Hydrology and Oceanography. Third Annual Earth Resources Program Review, Vol. III, 1970.

Wark, D., and D. Hilleary, Atmospheric temperature: successful test of remote probing. Science, 165, 1256-1258, 1969.

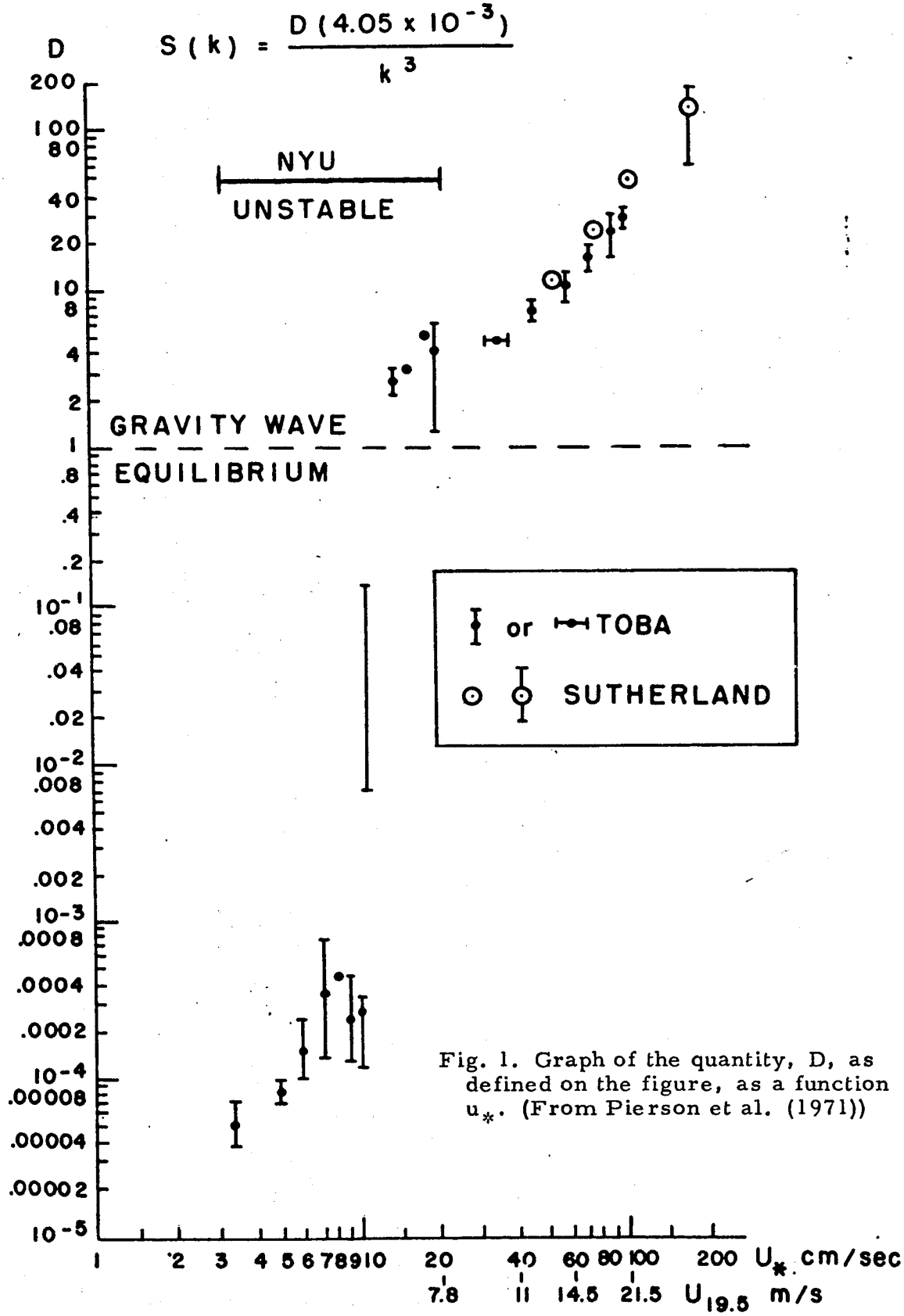

Fig. 1. Graph of the quantity, D, as defined on the figure, as a function u_*. (From Pierson et al. (1971))

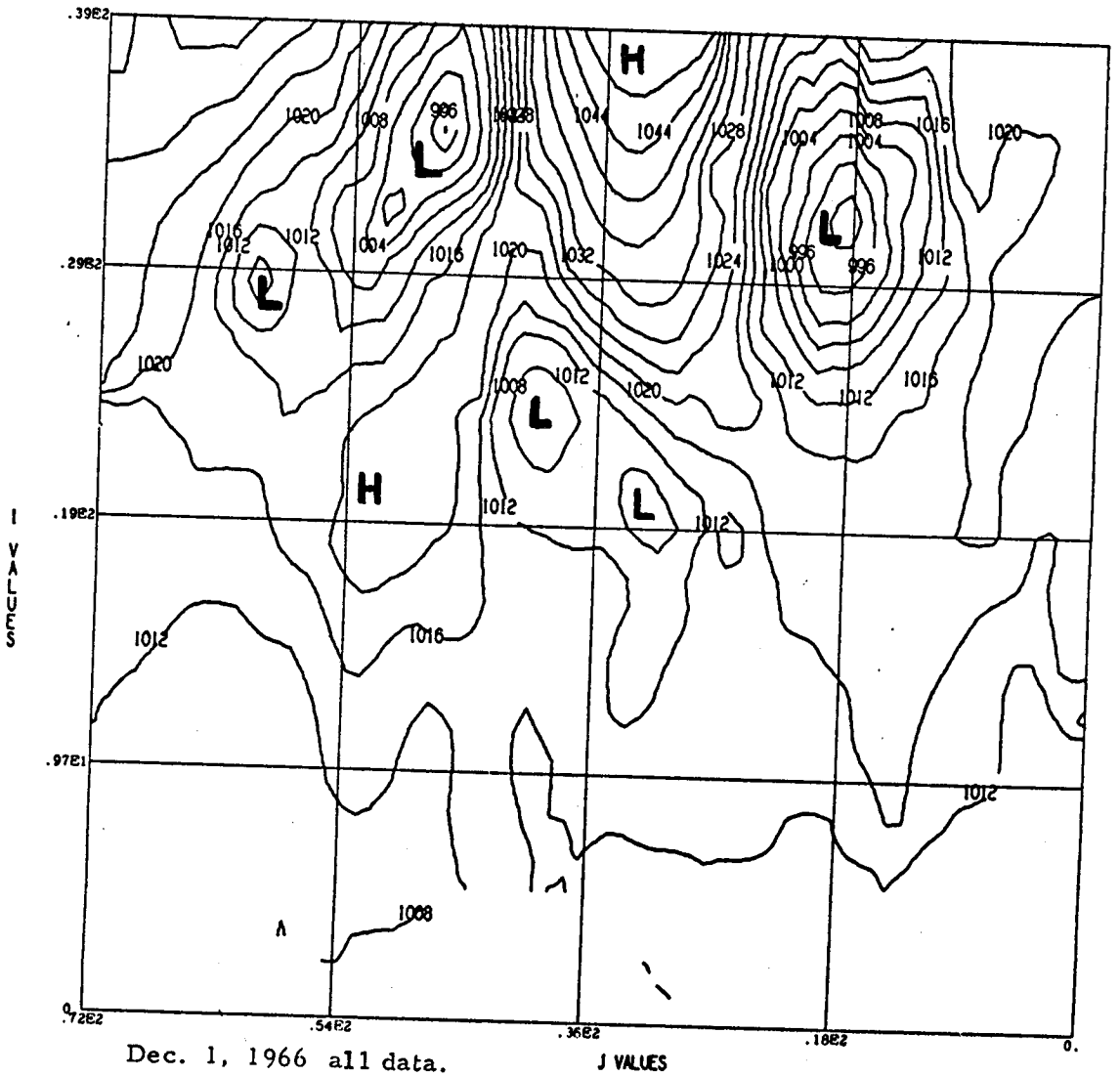

Dec. 1, 1966 all data.

Fig. 2. Analysis of the surface pressure field over the North Pacific Ocean for December 1, 1966 based on all available conventional data. (From Druyan, 1971).

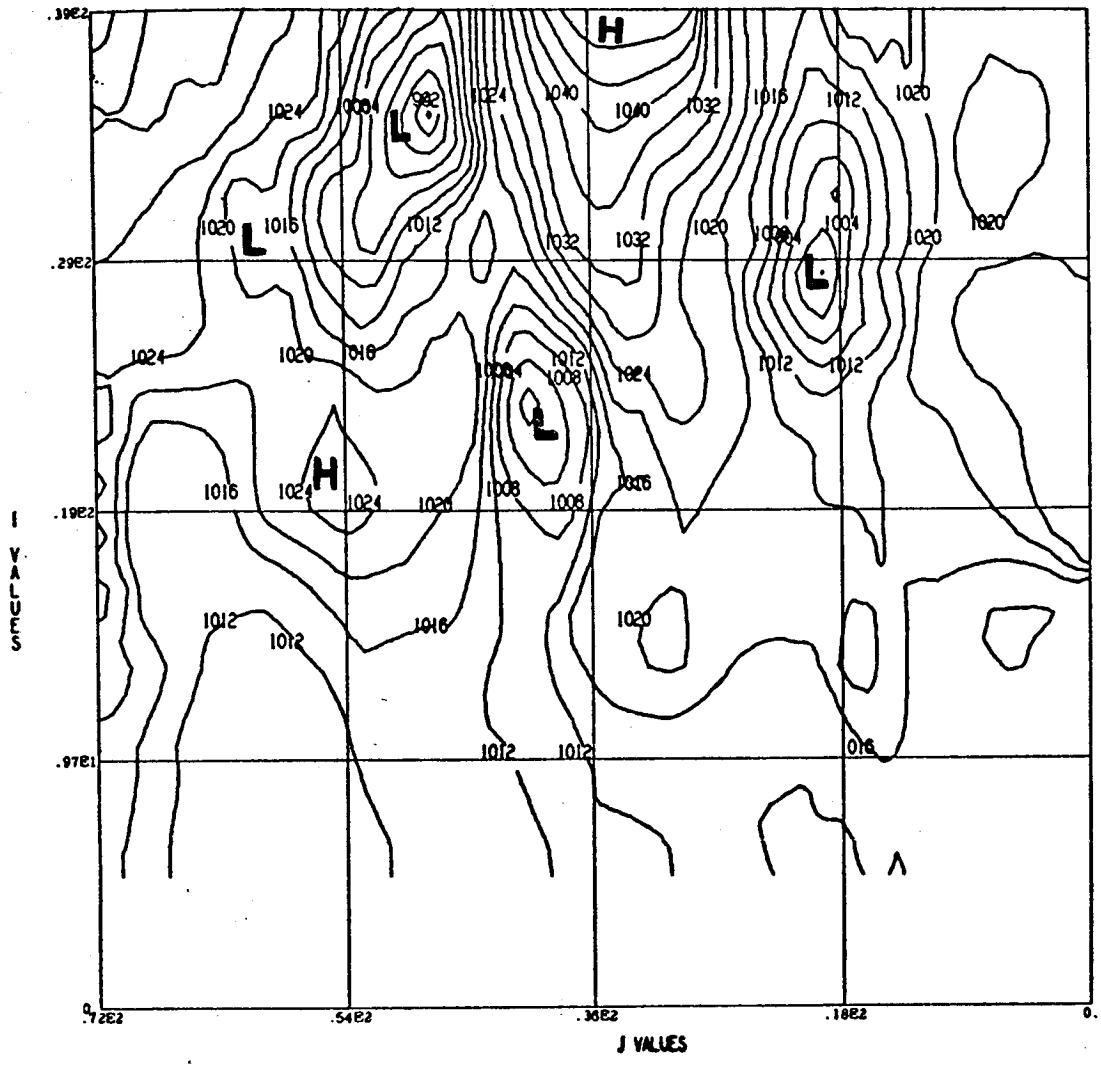

Fig. 3. Analysis of the surface pressure field over the North Pacific Ocean for December 1, 1966 based on 5% of the available conventional ship reports and simulated space data.

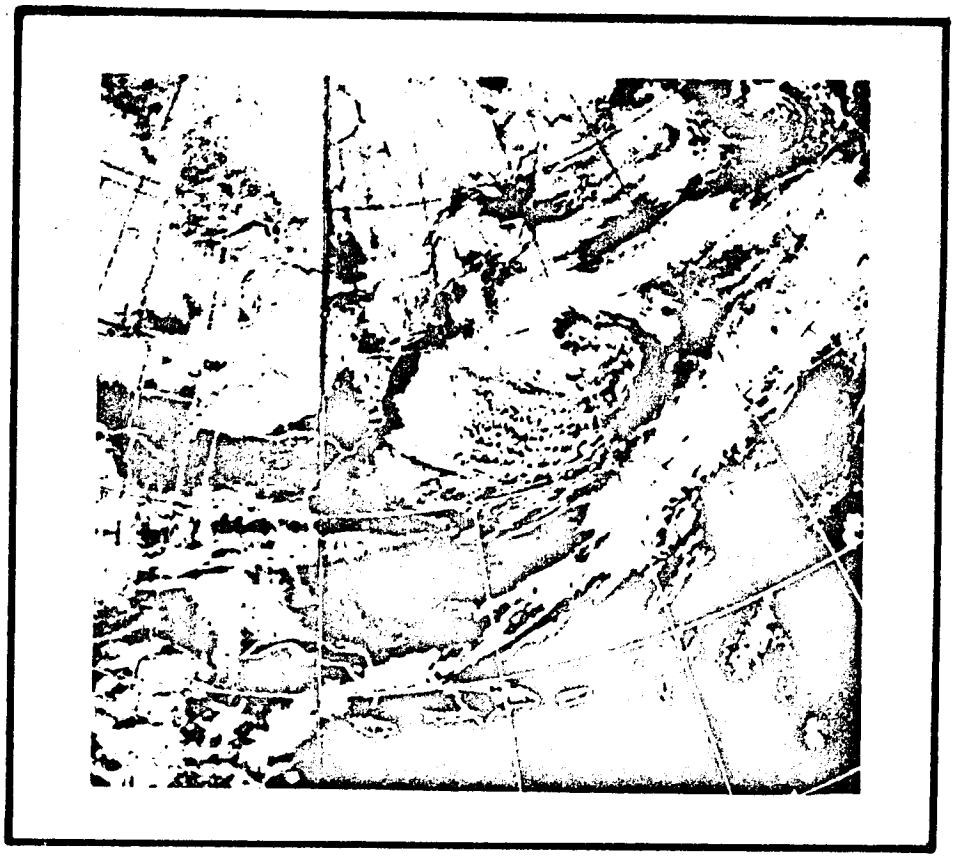

FIG. 4. ESSA SPACECRAFT CLOUD MOSAIC FOR MARCH 10, 1969 1800 GMT.

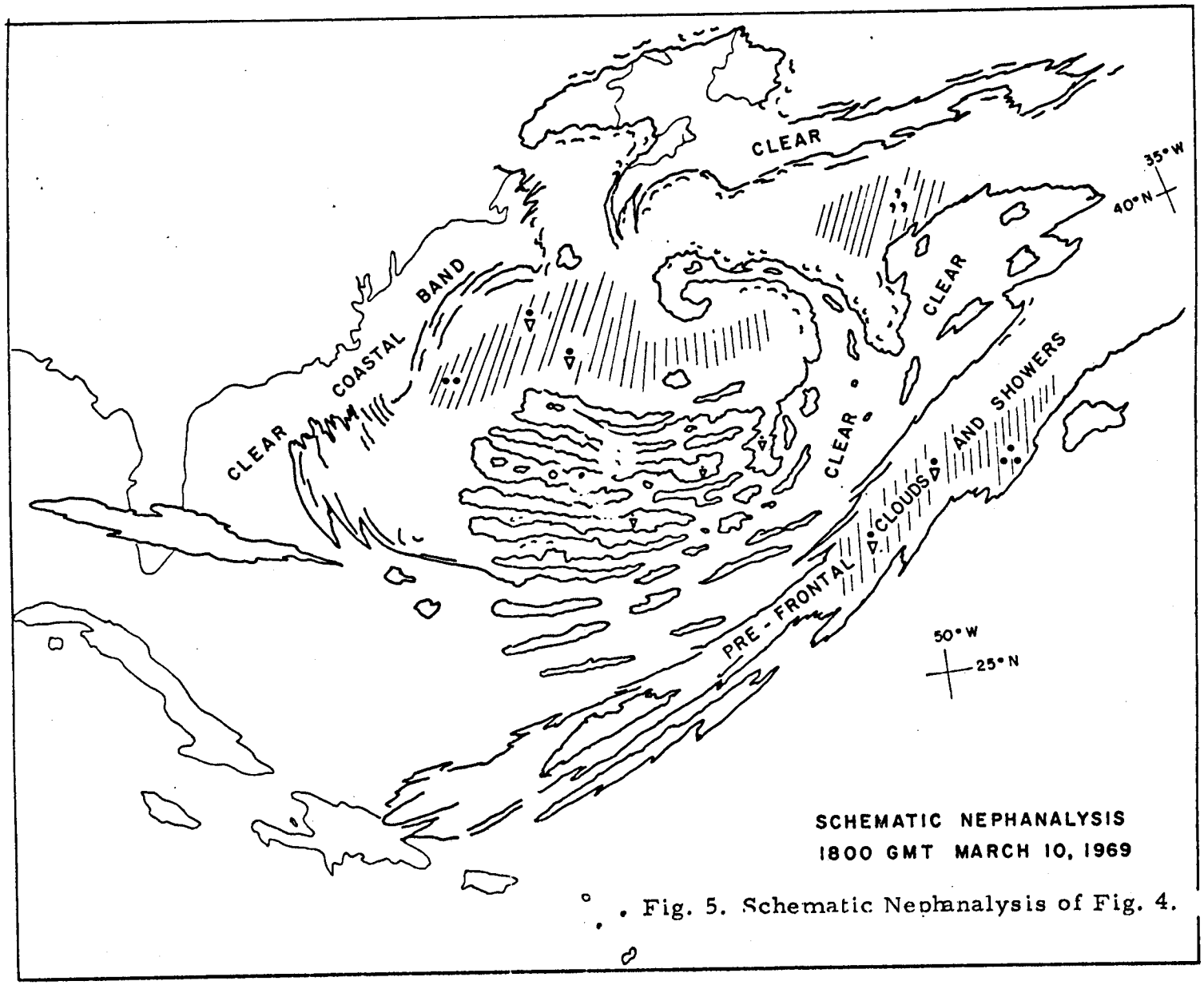

Fig. 5. Schematic Nephanalysis of Fig. 4.

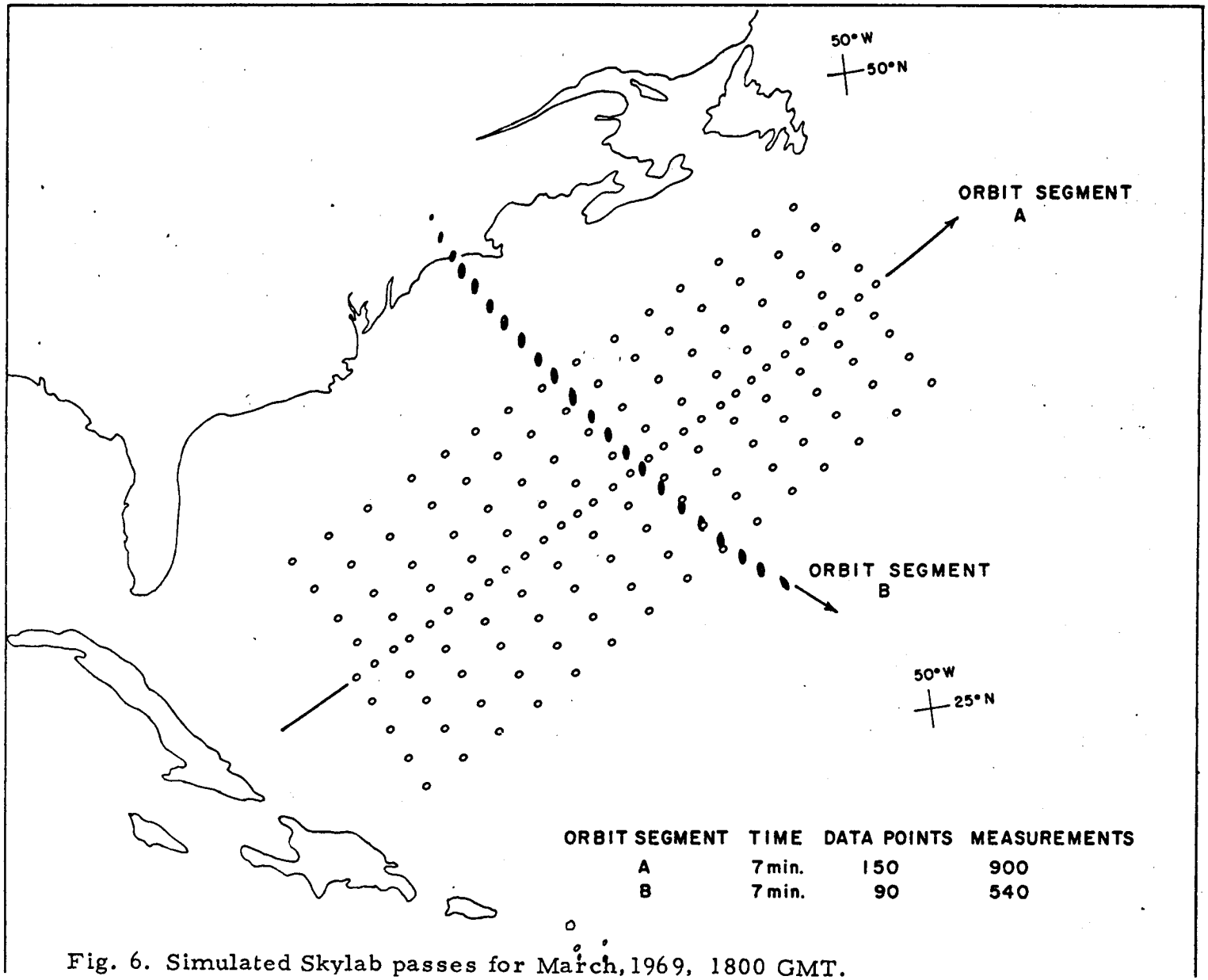

Fig. 6. Simulated Skylab passes for March, 1969, 1800 GMT.

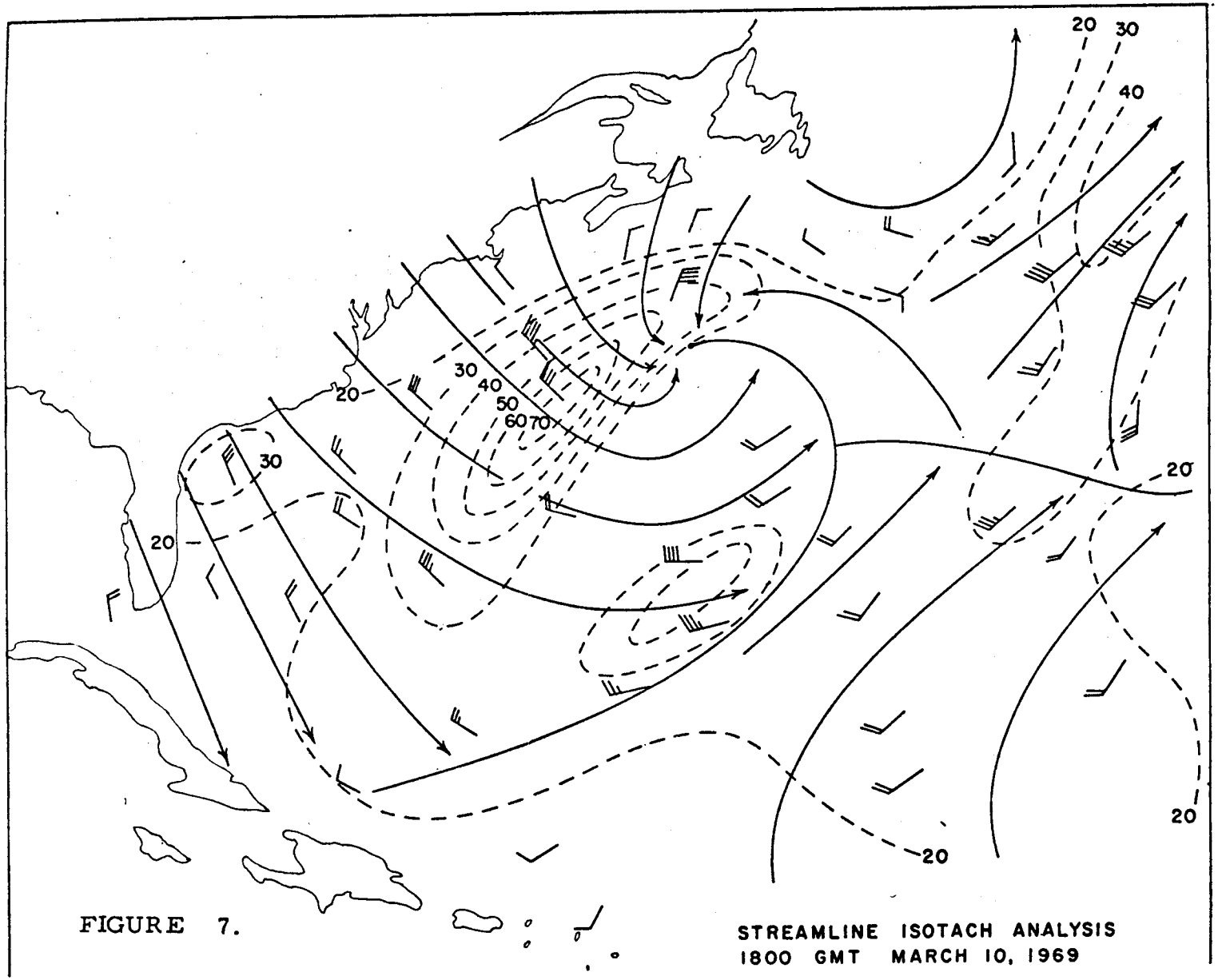

FIGURE 7.

STREAMLINE ISOTACH ANALYSIS
1800 GMT MARCH 10, 1969

FIGURE 8. Schematic flow chart for processing S193 data.

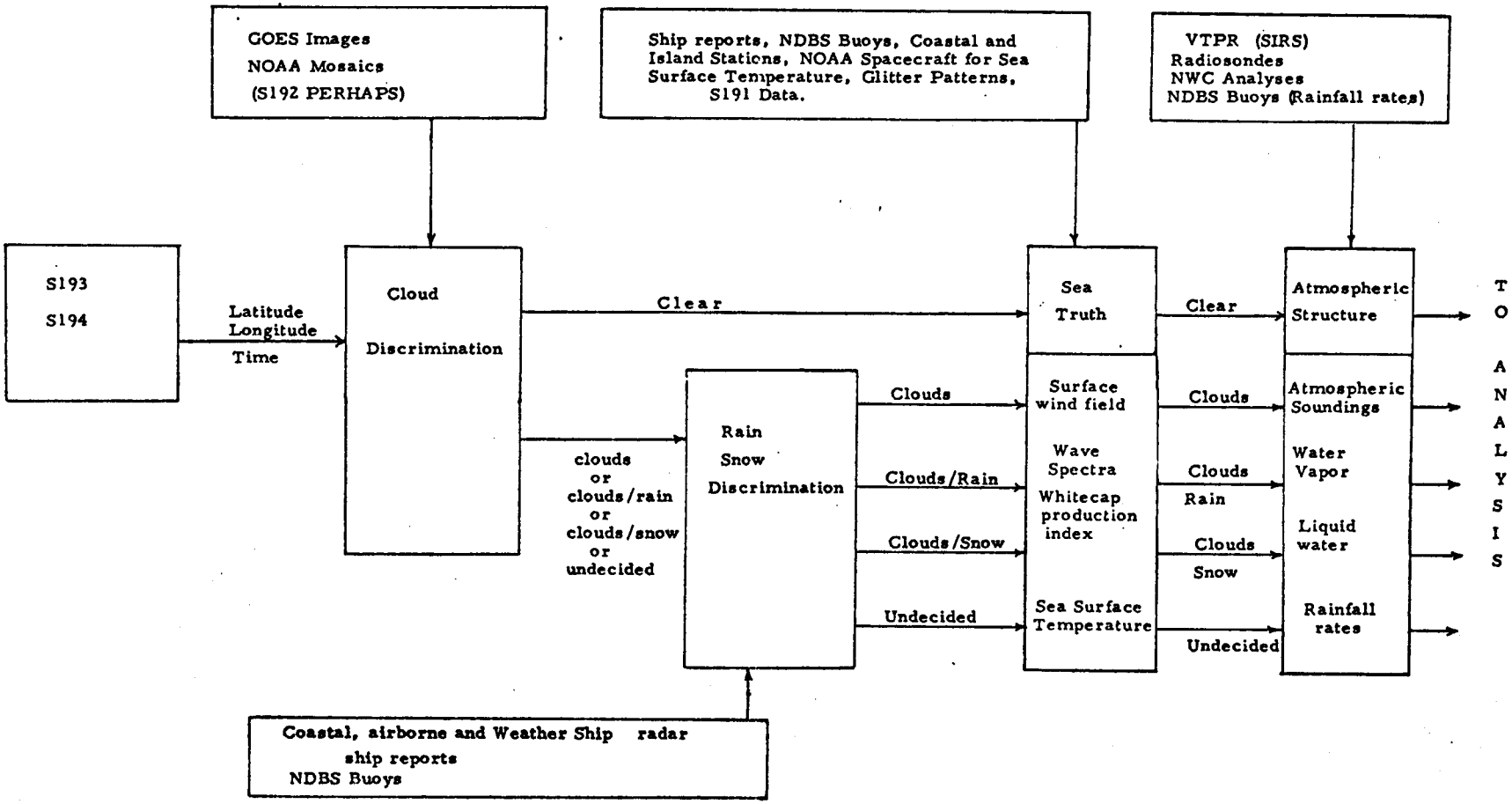

Fig. 9. Schematic flow chart for stratifying S193 data according to cloud and precipitation conditions.

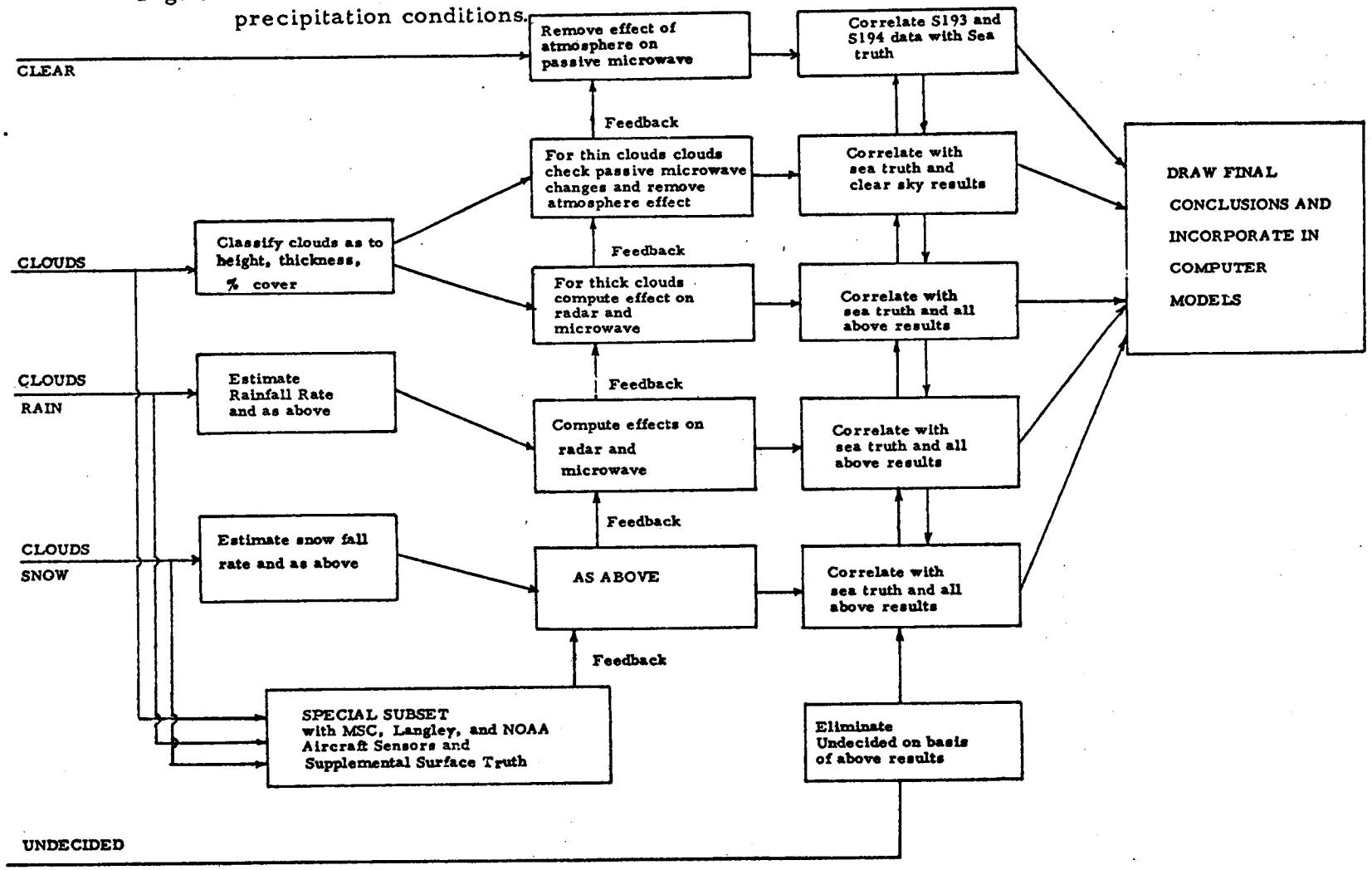

DETERMINATION OF MEAN SURFACE POSITION AND SEA STATE FROM THE RADAR RETURN OF A SHORT-PULSE SATELLITE ALTIMETER

16

Donald E. Barrick
BATTELLE
Columbus Laboratories
505 King Avenue
Columbus, Ohio 43201

Using the specular point theory of scatter from a very rough surface, the average backscatter cross section per unit area per radar cell width is derived for a cell located at a given height above the mean sea surface. This result is then applied to predict the average radar cross section observed by a short-pulse altimeter as a function of time for two modes of operation: pulse-limited and beam-limited configurations. For a pulse-limited satellite altimeter, a family of curves is calculated showing the distortion of the leading edge of the receiver output signal as a function of sea state (i.e., wind speed). A signal processing scheme is discussed that permits an accurate determination of the mean surface position--even in high seas--and, as a by-product, the estimation of the significant seawave height (or wind speed above the surface). Comparison of these analytical results with experimental data for both pulse-limited and beam-limited operation lends credence to the model. Such a model should aid in the design of short-pulse altimeters for accurate determination of the geoid over the oceans, as well as for the use of such altimeters for orbital sea-state monitoring.

INTRODUCTION

Sea surface roughness has always represented an unavoidable degradation to the performance of a satellite radar altimeter[1,2]*. It would be desirable for geodetic purposes to measure the position of the mean sea surface to an accuracy of less than a foot. Sea states over the oceans result in waveheights commonly of the order of six or more feet. It is physically obvious that such waveheights will "stretch" the receiver output pulse in some way, producing an uncertainty in the position of the mean surface of the order of the sea waveheight. Since sea state at any given time and place on the ocean is usually unknown, and since the interaction mechanism of an altimeter pulse with the sea has not yet been fully analyzed, doubt has remained as to the efficacy of an altimeter to determine mean sea level to the precision geodetically desired.

It is the purpose of this paper to show that sea state effects on altimeter performance need not limit its accuracy, primarily because the interaction between the radar pulse and the ocean waves is understood and predictable. Using a physically simple but rigorous theory, we intend to analyze the pulse distortion from wind-driven sea waves. The validity of the results will be established by comparison with two independent sets of experimental data.

Based upon the acceptance of the analysis set forth herein, we feel that mean sea level can be extracted from a satellite altimeter receiver signal. A simple one-step process will be suggested, whereby the incoherent, averaged signal versus time is differentiated, and the mean level is seen immediately as the position of the peak. The rms ocean waveheight and/or wind speed responsible for the ocean waves can then be inferred directly from the width of this signal derivative pulse.

PHYSICAL THEORY RESPONSIBLE FOR SCATTER

For the microwave frequencies at which an altimeter will operate, scatter from the sea within the near-vertical region directly beneath the satellite is quasi-specular in nature. This means that such scatter is produced primarily by specular or glitter points on the surface whose normals point toward the satellite. This is the same mechanism producing the dancing glitter of sunlight or moonlight on a water surface. Such scatter persists only as far as 15-20° from the vertical, since gravity waves can seldom maintain slopes greater than this amount before they break and dissipate energy. A physical picture of the specular points illuminated within a short-pulse radar cell advancing at an angle θ with respect to the mean surface is shown in Figure 1.

This specular point scatter is readily predictable from geometrical and/or physical optics principles, and has been analyzed by this author previously[3]. Here we extend the theory to include the height of the surface, since the short radar pulse will not illuminate the entire surface at a given time, but only those waves whose heights are sufficient to lie within the radar pulse. As the starting point, we note both from elementary geometrical optics principles or from more rigorous

*References are given on page 19.

physical optics derivations[3,4], that the field scattered from N specular points (expressed in terms of the square root of the backscatter cross section) is

$$\sigma_B^{1/2} = \sum_{i=1}^{N} \pi^{1/2} g_i^{1/2} e^{i2k_o h_i \cos\theta} \quad , \tag{1}$$

where g_i is the Gaussian curvature at the i-th specular point, i.e., $g_i = |\rho_{1i}\rho_{2i}|$, with ρ_{1i} and ρ_{2i} as the principal radii of curvature at this point. Also, h_i is the height of the i-th specular point above the mean surface (taken as k = 0), θ is the angle of incidence from the vertical, and $k_o = 2\pi/\lambda$ is the free-space radar wavenumber, λ being the wavelength.

Now, we square the above equation and average with respect to the phase, φ_{ij}, noting that $\varphi_{ij} = 2k_o \cos\theta(h_i + h_j)$ will be uniformly distributed between zero and 2π as long as the sea waveheight is larger than the radar wavelength. Thus the average of the double summation over i and j is zero except where j = -i, reducing the result to a single summation:

$$\langle\sigma_B\rangle_{ph} = \pi \sum_{i=1}^{N} g_i \quad . \tag{2}$$

Now, we rewrite this equation in integral form as a distribution of specular points versus height above the surface, h, and Gaussian curvature, g, as

$$\langle\sigma_B\rangle_{ph} = \pi A \int_{-\infty}^{\infty} dh \int_{0}^{\infty} N(h,g) g \, dg \quad , \tag{3}$$

where AN(h,g) is the number of specular points within a surface patch of area A, within the height interval h to h + dh, and with Gaussian curvatures between g and g + dg.

We now complete the averaging process by defining $n(h,g) \equiv \langle N(h,g)\rangle$ as the average specular point density, and we then denote $\eta_o(h)$ as the average radar cross

section per unit area of the surface per unit height increment, Δh, at a given height h; thus we have

$$\eta^o(h) = \pi \int_0^\infty n(h,g)\ g\ dg \quad . \tag{4}$$

Here we employ the normalization $\sigma^o = \int_{-\infty}^{\infty} \eta^o(h)dh$, where σ^o is the standard average backscatter cross section per unit area. Thus, a short pulse producing a vertical radar resolution cell of width Δh at height h will produce, on the average, a radar cross section per unit area of $\eta^o(h)\Delta h$.

The specular point density, n, can readily be determined (almost by inspection) from the work of Barrick[3] preceding Eq. (7) of that paper; one must merely include height in the probability densities. Thus the density of specular points within area A is

$$n(h,g)\ dg = p(h,\zeta_{xsp},\zeta_{ysp},\zeta_{xx},\zeta_{yy},\zeta_{xy})\,|\zeta_{xx}\zeta_{yy} - \zeta_{xy}^2|\,d\zeta_{xx}d\zeta_{yy}d\zeta_{xy} \quad , \tag{10}$$

where p is the joint probability density function of the surface height h, the surface slopes ζ_x, ζ_y, and the second partial derivatives of the surface at a given surface point. Since it is known a priori that scatter is originating at surface regions with their normals pointing toward the satellite, the slopes which must be used are geometrically known; we denote them ζ_{xsp} and ζ_{ysp}.

Likewise, the Gaussian curvature at a specular point is found from differential geometry to be

$$g = \frac{(1 + \zeta_{xsp}^2 + \zeta_{ysp}^2)^2}{|\zeta_{xx}\zeta_{yy} - \zeta_{xy}^2|} \quad . \tag{11}$$

Hence we arrive at the result

$$\eta^o(h) = \pi \iiint_{-\infty}^{\infty} |\zeta_{xx}\zeta_{yy} - \zeta_{xy}^2|\,p(h,\zeta_{xsp},\zeta_{ysp},\zeta_{xx},\zeta_{xy},\zeta_{yy}) \times$$

$$\frac{(1 + \zeta_{xsp}^2 + \zeta_{ysp}^2)^2}{|\zeta_{xx}\zeta_{yy} - \zeta_{xy}^2|}\, d\zeta_{xx}d\zeta_{yy}d\zeta_{xy}$$

$$= \pi(1 + \zeta_{xsp}^2 + \zeta_{ysp}^2)^2\ p(h,\zeta_{xsp},\zeta_{ysp}) \tag{12}$$

For backscatter, the squared factor in parentheses is merely equal to $\sec^4 \theta$, where θ is the incidence angle from the vertical. Also, it is simple to show that, while the surface height h and second derivatives are correlated, the height and slopes are uncorrelated. Hence, if the surface is Gaussian (or nearly so, which is true for the sea), the height and slopes are statistically independent and we have

$$\mathcal{P}(h) = \pi \sec^4 \theta \; p(h) p(\zeta_{xsp}, \zeta_{ysp}) \quad , \tag{13}$$

where p(h) is the height probability density and $p(\zeta_x, \zeta_y)$ is the joint slope probability density. The above result can now be applied to predict the average radar cross section observed at a short-pulse altimeter as a function of time.

APPLICATION TO SHORT-PULSE SATELLITE ALTIMETER

1. General Development

We now apply Eq. (13) to the problem depicted in Fig. 2: a satellite at altitude H emitting a spherical pulse which in turn sweeps past a spherical earth. The spatial pulse width for a backscatter radar is $c\tau/2$, where c is the velocity of light and τ is the time width of the pulse (compressed, if applicable) at the receiver output. Likewise, the distance of the spherically emanating pulse from the satellite, measured in time at the receiver from transmission of the signal, is ct/2. However, for convenience, we henceforth choose t = 0 as the time that the center of the spherical pulse shell strikes the uppermost cap of the spherical earth. In other words, in the absence of any roughness, the received pulse from the suborbital point will be a replica of the processed transmitter pulse, and we choose its center time position as a reference in order to study the effect of sea state on pulse distortion.

First of all, we note from Fig. 2 that the angle of incidence, θ, at any point on the surface is given by $\theta \approx \psi + \varphi \simeq \psi(1 + H/a)$ for θ small. The incidence angle at the intersection of the mean earth spherical surface and the center of the pulse cell, expressed in terms of receiver time is then $\theta \simeq \sqrt{(ct/H)(1 + H/a)}$. For a short pulse, θ can be considered a constant within the pulse cell width. The height, h, to a point at the center of the cell above the mean sea surface can then be given as

$$h = \frac{H(1 - \cos \psi) + a(1 - \cos \varphi) - (ct/2)\cos \psi}{\cos \varphi} \tag{14}$$

and for ψ small, this reduces to

$$h \simeq \frac{H}{2} \psi^2 \left(1 + \frac{H}{a}\right) - \frac{ct}{2} \quad . \tag{15}$$

At this point, we must make some assumptions about the surface statistics and radar properties in order to perform the integration. For the sake of studying the general nature of the radar return, we make the following assumptions: (i) the signal shape is flat, of width τ, and zero everywhere else, (ii) the antenna beam pattern is uniform out to ψ_B off the axis, and zero everywhere else; ψ_B is thus the half-power half-beamwidth of the antenna*. We assume also that the sea surface height and slope probability distributions are Gaussian, realizing of course that the height distribution to second order is not quite Gaussian, but slightly skewed from the symmetric Gaussian shape, and has less probability in the tails. Furthermore, we assume that the sea is nearly isotropic, making the slopes ζ_x and ζ_y independent of wind direction. This is quite valid for very small incidence angles (and hence specular slopes).

Thus we have

$$p(\zeta_{xsp},\zeta_{ysp}) = p(\tan\theta) = \frac{1}{\pi s^2} e^{-\frac{\tan^2\theta}{s^2}} , \qquad (16)$$

and

$$p(h) = \frac{1}{\sqrt{2\pi}\,\sigma_h} e^{-\frac{h^2}{2\sigma_h^2}} , \qquad (17)$$

where $s^2 = \langle\zeta_x^2\rangle + \langle\zeta_y^2\rangle$ and $\sigma_h^2 = \langle h^2\rangle$.

Later, when relating these quantities to wind-developed waves, we shall use the relationships

$$s^2 = 5.5 \times 10^{-3}\, v \quad \text{and} \quad \sigma_h^2 = 2.55 \times 10^{-4}\, v^4 , \qquad (18)$$

where v is wind velocity in meters per second. The first of these relationships is inferred empirically from slope data versus wind speed presented in Phillips[5], and the second is obtained from integrating the Phillips wind-wave height spectrum.

Thus, the observed average radar cross section as a function of time will be

$$\sigma(t) = 2\pi^2 a^2 \int_0^{\frac{H}{a}\psi_B} p(\tan\theta)\sec^4\theta \sin\varphi \left\{ \int_{h-\frac{\Delta h}{2}}^{h+\frac{\Delta h}{2}} p(h)dh \right\} d\varphi , \qquad (19)$$

where θ and h were related to φ previously.

*Other, possibly more realistic, pulse and beam shapes can be readily inserted into the integral if desired.

For a pulse width sufficiently short that $\Delta h \approx (c\tau/2) < 2\sigma_h$, we can approximate the second integral and obtain a closed-form answer for the remaining integral. Physically, this requires that the spatial pulse width be less than the rms ocean waveheight (peak-to-trough). This is realized on the open ocean with compressed pulse widths less than about 10 ns for waves excited by winds greater than about 10 knots. For simplicity we shall make this assumption here, analyzing the more general case at a later date. The result is then

$$\sigma(t) = \frac{\pi c \tau}{2s^2[(1/a) + (1/H)]} \left\{ \operatorname{erf}\left(\frac{ct}{\sqrt{8}\,\sigma_h}\right) + \operatorname{erf}\left(\frac{H'\psi_B^2 - ct}{\sqrt{8}\,\sigma_h}\right) \right\} , \qquad (20)$$

where $H' = H[1 + (H/a)]$. The quantities in the braces are the error functions; the first one is responsible for the rising leading edge of the radar return, while the second produces the fall-off of the trailing edge.

2. Pulse-Limited Altimeter ($\psi_B \gg \sqrt{c\tau/H'}$)

When the radar is sufficiently high, the beamwidth sufficiently wide, and the pulse length sufficiently short, the response of the altimeter is said to be pulse-limited. This means in effect that the earth area illuminated most of the time lies in a "range ring" of constant surface area, as shown in Fig. (3a). Such a situation will always exist for a short-pulse satellite altimeter, will nearly always exist for aircraft altimeters, but may not exist for tower-based altimeters looking at the sea (an example of the latter will be discussed subsequently). The general form of Eq. (20) is valid for either pulse- or beam-limited operation, under the simplifying assumptions made previously (flat pulse and antenna pattern, short-pulse operation).

In this mode of operation, the mean surface at the suborbital point lies somewhere in the leading, rising edge of the echo. The essence of the problem, however, is that the rise time of the leading edge is not only inversely proportional to the transmitted signal bandwidth (or shape)--a factor which could easily be removed for high signal-to-noise ratios because the signal shape is known a priori--but the rise time varies also with sea state because of temporal dispersion caused by the spatial distribution of specular points.

To study the theoretical shape of the leading edge of the return for the pulse-limited case, we examine Eq. (20). First of all, we note that the return rises rapidly to a maximum, has a flat shape in the middle of duration $t_D = (H'/c)\ \psi_B^2$, and falls off to zero as rapidly as it rose. The shape of the pulse is symmetric about $t_D/2$. In practice, such a flat, symmetric return will not be observed, primarily because the antenna pattern falls off with increasing ψ, rather than remaining constant out to ψ_B and then dropping suddenly to zero, as we assumed here. The shape shown in Fig. 3a is more typical of the overall echo shape. The shape of this latter portion of the signal need not concern us here, however, because it contains no information about the mean surface position and little information about sea state. The maximum value of $\sigma(t)$ is of concern, however; it is readily found from Eq. (20) by noting that the maximum value of the quantity in braces is 2. Hence, $\sigma_{MAX} = \pi\, c\tau/[s^2(1/a + 1/H)]$.

To study the leading edge versus sea state, we use parameters typical of a Skylab satellite altimeter: $H = 435$ km, $\psi_B = 1.5°$, and $\tau < 15$ nsec. In addition, we use Eqs. (18) to relate the statistics of the wind-excited surface to wind speed. The result is the family of normalized curves shown in Fig. (4), showing the leading edge of the return. The mean surface, of course, is located at $t = 0$, which appears at precisely one-half the maximum value. The effect of sea state is as expected; higher wind speeds and hence greater rms roughness heights tend to stretch (i.e., disperse) the leading edge, giving a greater rise time.

3. Beam-Limited Altimeter ($\psi_B \ll \sqrt{c\tau/H'}$)

In less frequent altimeter applications, the configuration may be beam-limited, as shown in Fig. 3(b). In this case, the interaction at the surface directly beneath the altimeter appears planar, i.e., the effects of the spherical earth and spherical pulse front are negligible. This could occur for a low-flying, narrow-beam aircraft altimeter, but would not exist for a satellite altimeter. When this extreme is achieved, the return can best be analyzed by expanding the second term in Eq. (20) in a Taylor series, expanded about argument $ct/(\sqrt{8}\ \sigma_h)$. This gives

$$\sigma(t) \simeq \frac{c\tau H^2 \psi_B^2}{2\sqrt{2\pi}\, s^2 \sigma_h} \left[e^{-\left(\frac{ct}{\sqrt{8}\ \sigma_h}\right)^2} + \cdots \right] , \qquad (21)$$

where the higher-order terms omitted here are of the order of $H'\psi_B^2/\sqrt{8}\ \sigma_h$, which is assumed to be small since we have taken $c\tau/2 < 2\sigma_h$.

The maximum and the Gaussian nature of this return are easily seen from the above equation. The width of the pulse is directly related to the rms surface height, and the mean position of the surface occurs precisely at the pulse peak.

DEDUCTION OF MEAN SURFACE POSITION AND SEA STATE FROM ALTIMETER RETURN

If we can employ a beam-limited short-pulse altimeter, we will have no trouble deducing either the mean surface position or the rms surface height of the ocean. The former is found from the pulse peak position and the latter from its width, as readily observed from Eq. (21). Unfortunately, the parameter requirements for this limiting configuration are such as to preclude its implementation on a satellite.

Restricted, then, to pulse-limited altimeter operation from a satellite, the question remains as to how to find the mean surface position in the leading edge of the extended echo. From Eq. (20) and the curves plotted in Fig. 4, the answer is obvious--in the absence of noise. Merely find the half-power point on the rising edge; this time corresponds to the distance to the mean surface. However, in the presence of additive, independent noise, and with the often-jagged appearance of the echo near its maximum (see measured returns in Fig. 6), finding this half-way point becomes more difficult.

A signal processing technique to be suggested here makes use of the fact that this half-power point defining the mean surface position is also the point of maximum slope. Hence, we suggest that the processor form the time derivative of the altimeter output power--after incoherent averaging (or summing) and band-pass filtering of several pulse returns. Thus, the incoherent averaging and filtering will remove much of the jagged noise, while providing a smooth, clearly recognizable leading edge. The derivative of this signal is easy to form from Eq. (20). It is

$$\sigma'(t) = \sqrt{\frac{\pi}{2}}\,\frac{c\tau}{2s^2}\cdot\frac{c}{\sigma_h\left(\frac{1}{a}+\frac{1}{H}\right)}\,e^{-\left(\frac{ct}{\sqrt{8}\,\sigma_h}\right)^2} \qquad (22)$$

Figure 5 shows a family of normalized curves of this average altimeter leading-edge output differentiated versus time. The pulse center is the mean surface position, and its width is clearly proportional to rms surface height (or the square

C4

of wind velocity, for wind-driven waves). There is no need for absolute measures of signal level, either for mean surface position or for sea state determination; hence, atmospheric attenuation and system power drifts are not critical.

A large amount of noise can, of course, degrade the pulse positioning accuracy of this system, as in any system. However, so long as σ_{MAX} is several decibels above the noise level, the position of the pulse center in the signal derivative should be relatively insensitive to noise. The degradation of altimeter accuracy with sea state and noise level has the desirable attributes of pulse-position modulation (PPM) systems of digital communication theory, but should be the subject of further study.

COMPARISON OF THEORETICAL MODEL WITH GROUND-TRUTH DATA

For verification of the theory and the various assumptions that have gone into it, we choose measured data from two separate altimeter experiments: one pulse-limited and the other beam-limited. The pulse-limited data chosen was measured and reported by Raytheon[6] for aircraft flights at 10,000 ft with a pulse width of 20 ns. The half-beamwidth, ψ_B, is 2.5°, and the surface winds reported during Flights 14 and 16 were 12 and 22 knots, respectively. Their averaged altimeter outputs are shown in Fig. 6. Since there is no precise way of comparing measured surface position with that calculated, we intend to compare the actual sea state effects, as contained in the leading-edge rise time, t_r, with those calculated. We roughly measure rise times of 21 and 30 ns for the two records displayed, and use Eqs. (18) and (20) to calculate the wind speeds required to cause seas producing this rise time. The calculated winds are 14.1 and 21.2 knots, comparing reasonably well with the measured winds. Good comparison on Flight 14 was not expected, because the condition $c\tau/2 > 2\sigma_h$ is barely satisfied for this mild sea condition. When this inequality is not satisfied, Eq. (20) is not applicable, and one must instead go back to Eq. (19). Practically, this means that with a 20 ns pulse, one cannot hope to meaningfully measure sea states which will produce a rise-time stretching of less than 20 ns.

As an example of the comparison of Eq. (21) for beam-limited operation with measurements, we selected data recently reported by Yaplee et al[7]. His measurements were taken from a tower at H = 70 ft above the water and $\psi_B \simeq 1°$. His pulse width $\tau = 1$ ns was long enough to assure beam-limited operation, but short enough to allow

the condition $c\tau/2 < 2\sigma_h$ to be satisfied for the two sets of data reported. We compare the shapes of the curve given by our Eq. (21) with what he has called the impulse response* shown in his Figs. 11 and 12. He plots the responses measured both by radar and by a wavestaff, for two different days on which the significant waveheights (measured by the wavestaff) were 3.1 and 5.2 ft. Since his response heights were relative, we compare the shape of his curves in Fig. 7 with that of our Eq. 21, using rms waveheight, σ_h, corresponding to 3.1 and 5.2 ft. The agreement in width is quite good. The comparison also points out where the Gaussian assumption for the sea height is weak: in the echo tails and in the symmetry about the center. The Gaussian surface has some (small) probability of very large heights, and is always symmetric, whereas the height of real ocean waves can never be infinite, and the surface is not exactly symmetric for positive and negative heights. These differences, while interesting, should not detract from the fact that the simple Gaussian model can be applied adequately well to predict mean surface position and rms waveheight.

CONCLUSIONS

The principal conclusions to be made from this analysis are that a short pulse altimeter can be used--even in the presence of high seas--to measure accurately the mean surface level and also to deduce the sea state. The simple interaction of the microwave altimeter pulse with the sea at near-vertical incidence is separable from the more complex interaction mechanism at larger incidence angles; It follows the straightforward specular point theory derivable from either geometrical or physical optics.

In satellite applications, the altimeter return will be pulse-limited in its nature. For reasonably meaningful measurements of the geoid, the pulse width must be kept small, i.e., less than 20 ns. It is precisely for these short pulses that ocean waveheights can temporally disperse the signal leading edge. We have shown by the specular point theory, however, that this interaction is known and its results are predictable. We have suggested and discussed a signal processing scheme employing the signal derivative, which can locate the mean surface position from the pulse position and the rms surface height from the pulse width.

*The impulse response essentially has the effect "deconvolving" the pulse shape and size from the return to give a result with the same meaning as our Eq. (21).

Comparison of the theory with measurements and ground-truth data for two different altimeter modes (pulse- and beam-limited operation) lend credence to the theory. System noise can and will limit altimeter accuracy, but this can be reckoned with in a systematic manner using principles of PPM communication theory. Other practical effects such as nonrectangular pulse shapes can be accounted for in any further system analysis by including an additional pulse-shape factor in the integrand of Eq. (19).

In short, the pulse-sea interaction is at present sufficiently well understood and verified that a short-pulse altimeter could be built which will provide: (1) accurate determination of mean sea level to a precision much greater than ocean waveheights, and (2) as a by-product, can provide rms ocean wave height (or wind speed) as well.

ACKNOWLEDGMENT

The analytical assistance and constructive comments of T. Kaliszewski are gratefully acknowledged.

REFERENCES

1. J. A. Greenwood, A. Nathan, G. Neumann, W. J. Pierson, F. C. Jackson, and T. E. Pease, "Radar altimetry from a spacecraft and its potential applications to geodesy", Remote Sensing of the Environment, vol. 1. New York: American Elsevier Publishing Co., Inc., 1969, pp. 59-80.

2. T. W. Godbey, "Oceanographic satellite radar altimeter and wind sea sensor", from Oceanography in Space, Proc. of Conference, Woods Hole Oceanographic Institution, Ref. No. 65-10, G. C. Ewing, Ed., Aug. 24, 1964, pp. 21-26.

3. D. E. Barrick, "Rough surface scattering based on the specular point theory", IEEE Trans. Antennas Propagat., vol. AP-16, 1968, pp. 449-454.

4. R. D. Kodis, "A note on the theory of scattering from an irregular surface", IEEE Trans. Antennas Propagat., vol. AP-14, 1966, pp 77-82.

5. O. M. Phillips, Dynamics of the Upper Ocean. London: Cambridge at the Universit Press, 1966, pp. 109-139.

6. ———, "Space geodesy aircraft experiment", Raytheon Co., Wayland Laboratories, Sudbury, Massachusetts, Final Rept., Contract No. NASW 1932, May 1970.

7. B. S. Yaplee, A. Shapiro, D. L. Hammond, B. D. Au, and E. A. Uliana, "Nanosecond radar observations of the ocean surface from a stable platform", IEEE Trans. Geoscience Electronics, vol. GE-9, 1971, pp. 170-174.

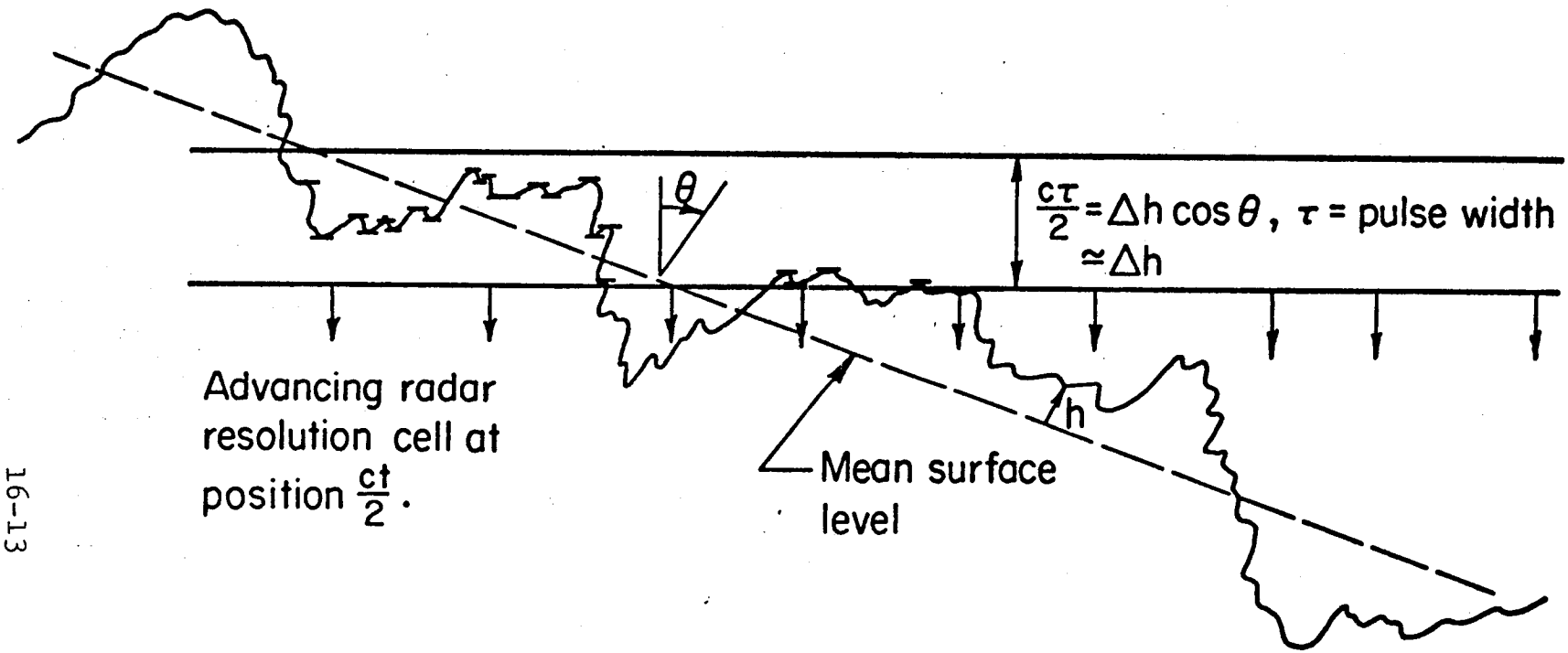

Figure 1. Physical Picture of Specular Point Scatter. Specular Points Within Radar Resolution Cell Are Shown Highlighted.

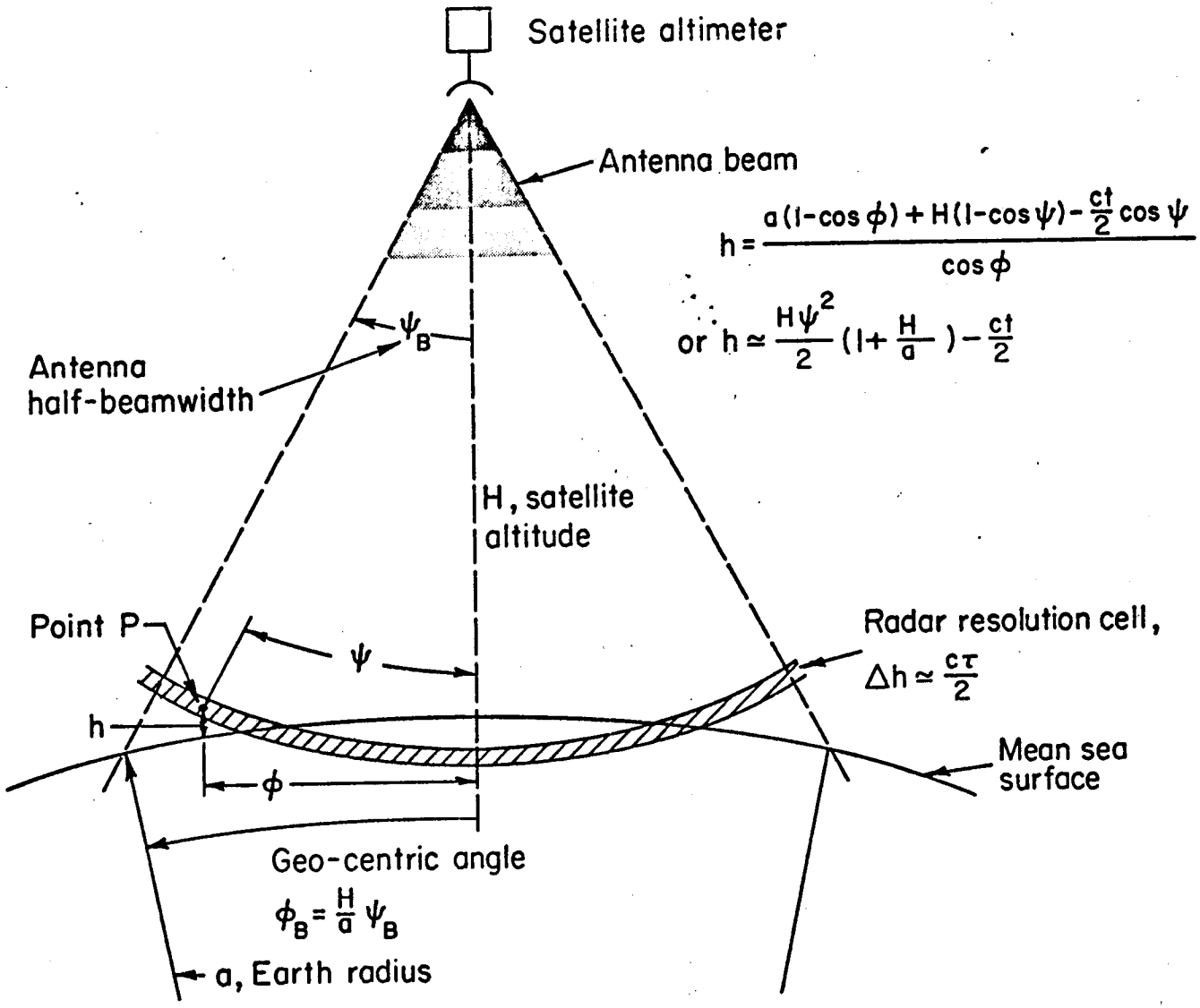

Figure 2. Geometry of Satellite Altimeter

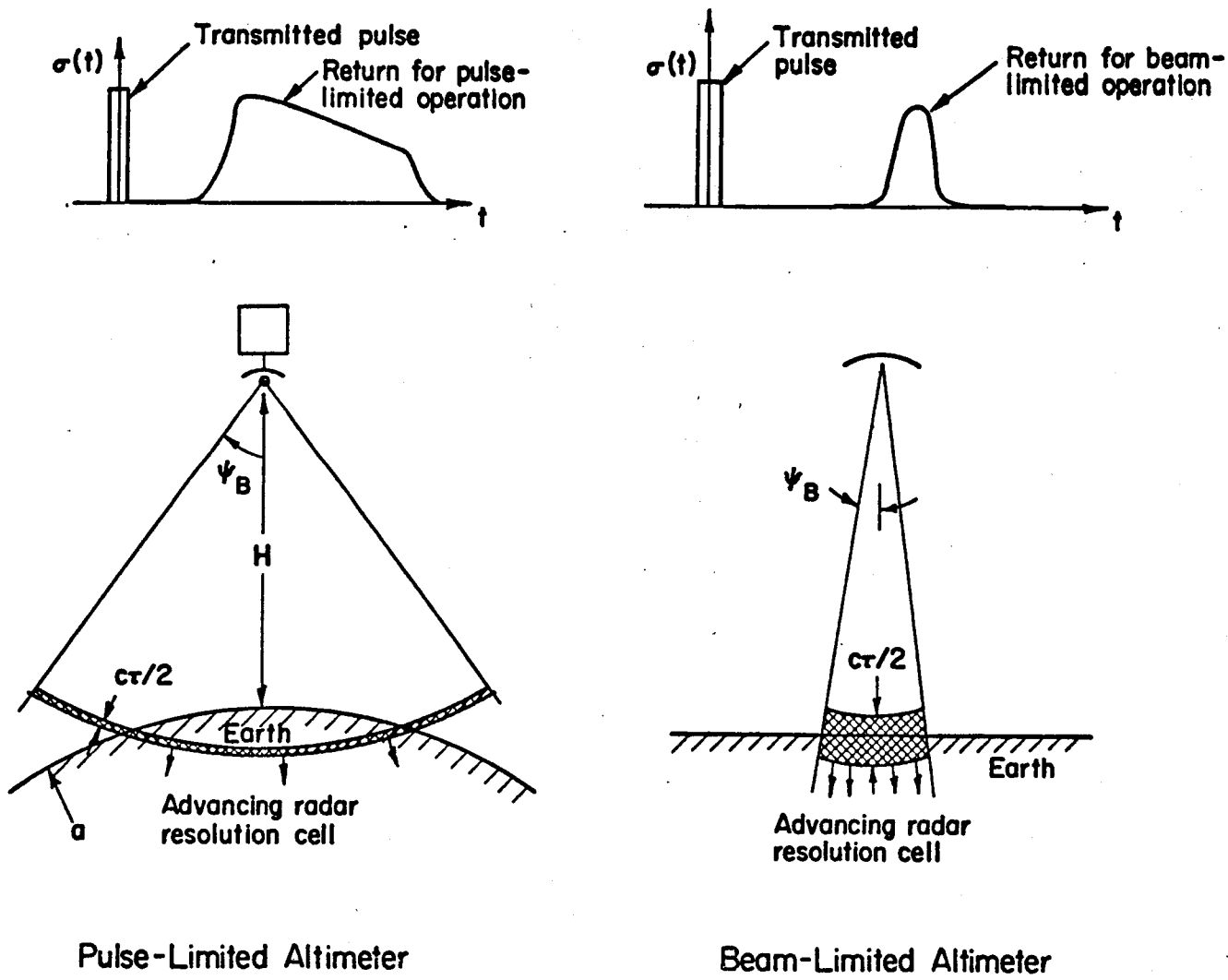

Figure 3. Two Modes of Altimeter Operation and the Resulting Signals

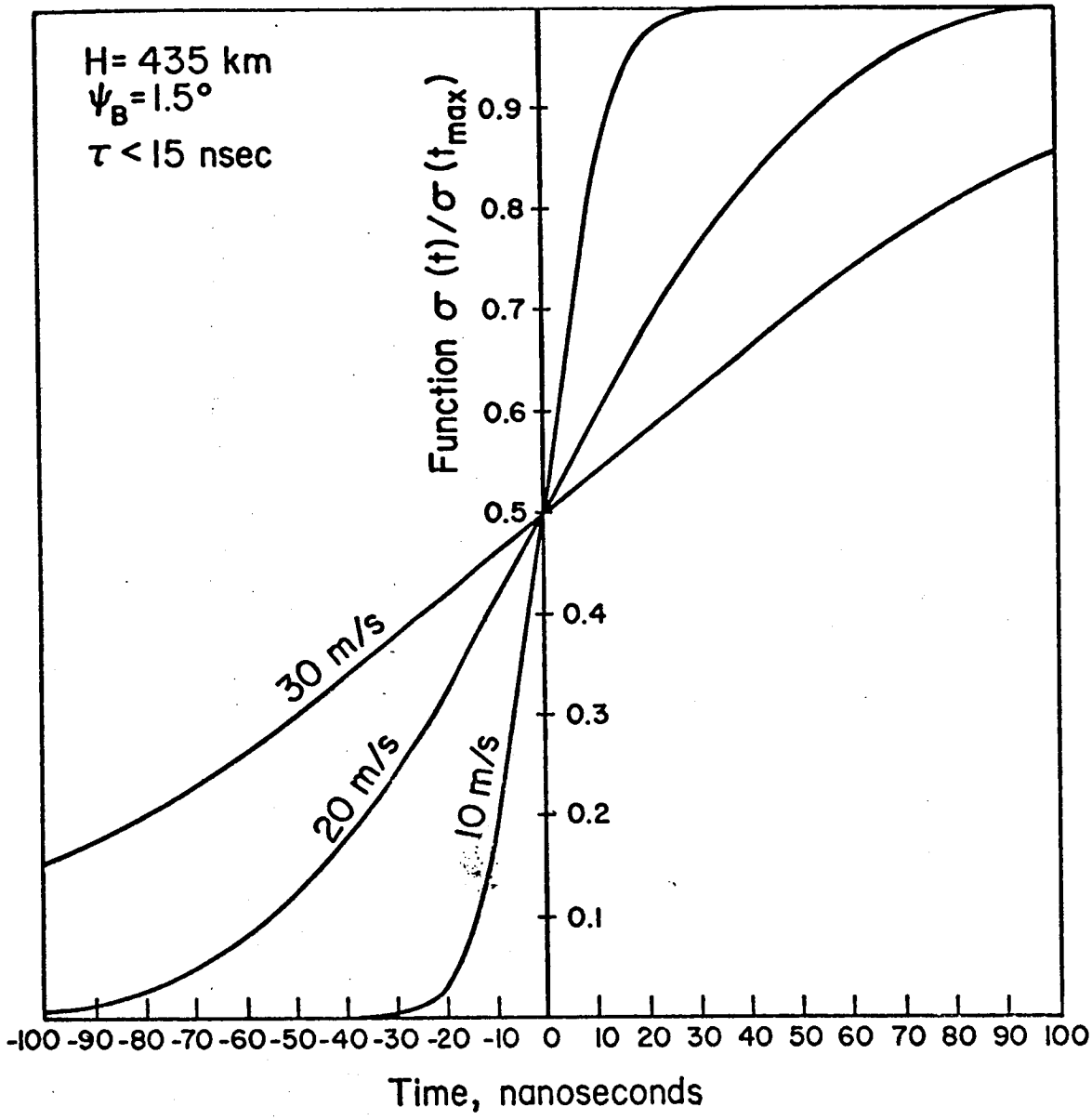

Figure 4. Leading Edge of Averaged Altimeter Output Versus Time for Pulse-Limited Operation

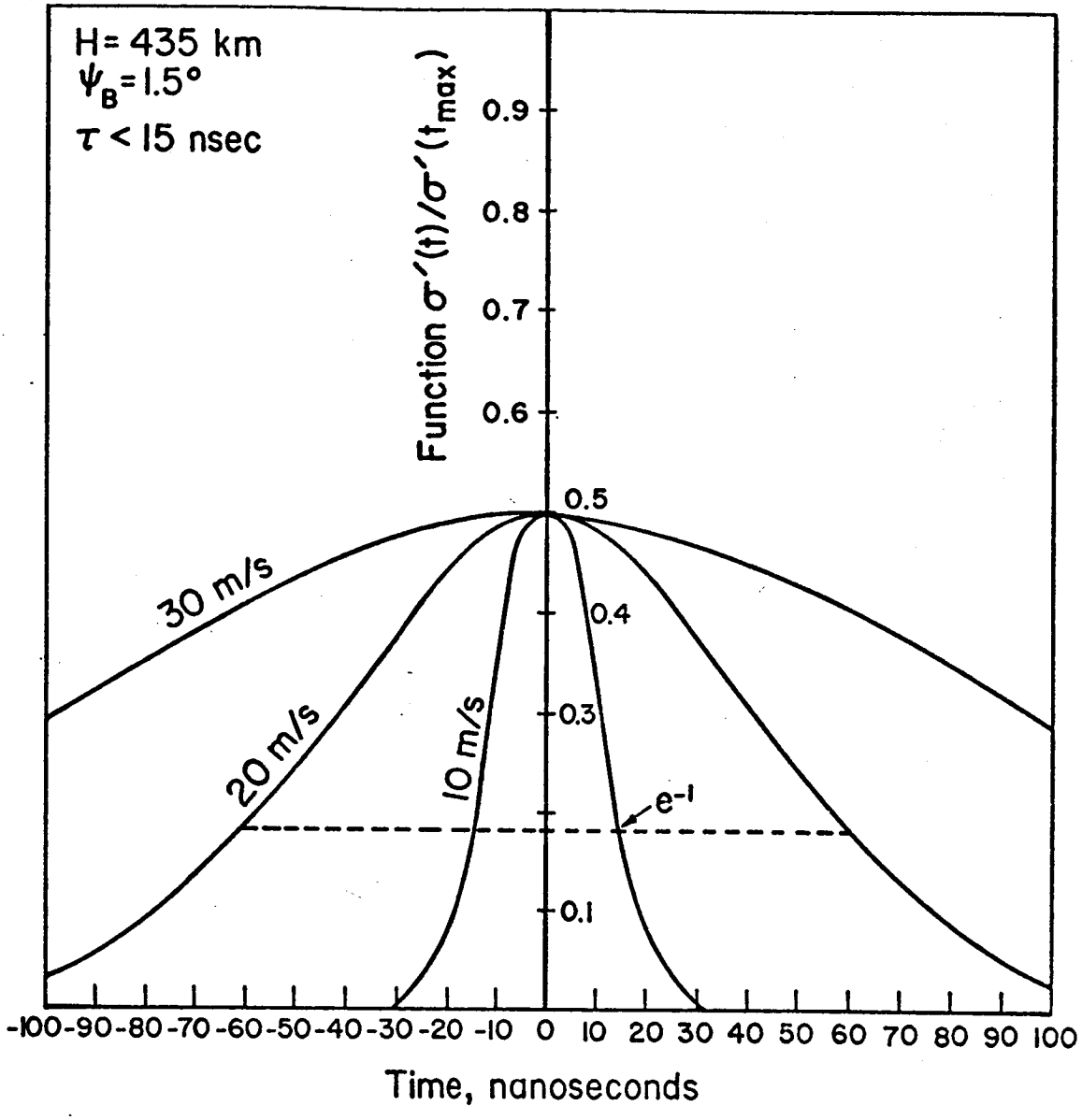

Figure 5. Derivative of Leading Edge of Averaged Altimeter Output Versus Time for Pulse-Limited Operation.

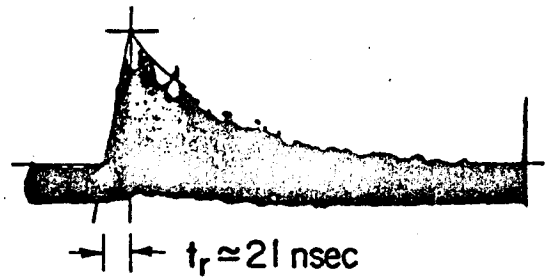

Flight #14
Run #12
H = 10 kft
τ = 20 nsec
$t_r \simeq 21$ nsec
Measured wind = 12 knots
Calculated wind = 14.1 knots

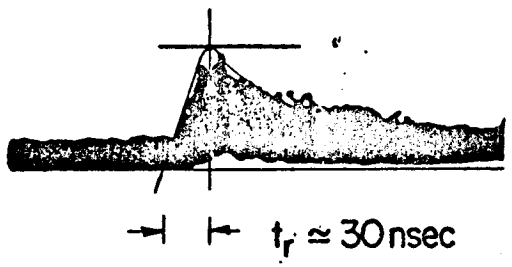

Flight #16
Run #9
H = 10 kft
τ = 20 nsec
$t_r \simeq 30$ nsec
Measured wind = 22 knots
Calculated wind = 21.2 knots

Figure 6. Measured [Raytheon Co., Wayland Laboratories, 1970] Aircraft Altimeter Responses. Wind Speeds Inferred from Rise Time and Pulse-Limited Model Are Compared to Observed Wind Speeds.

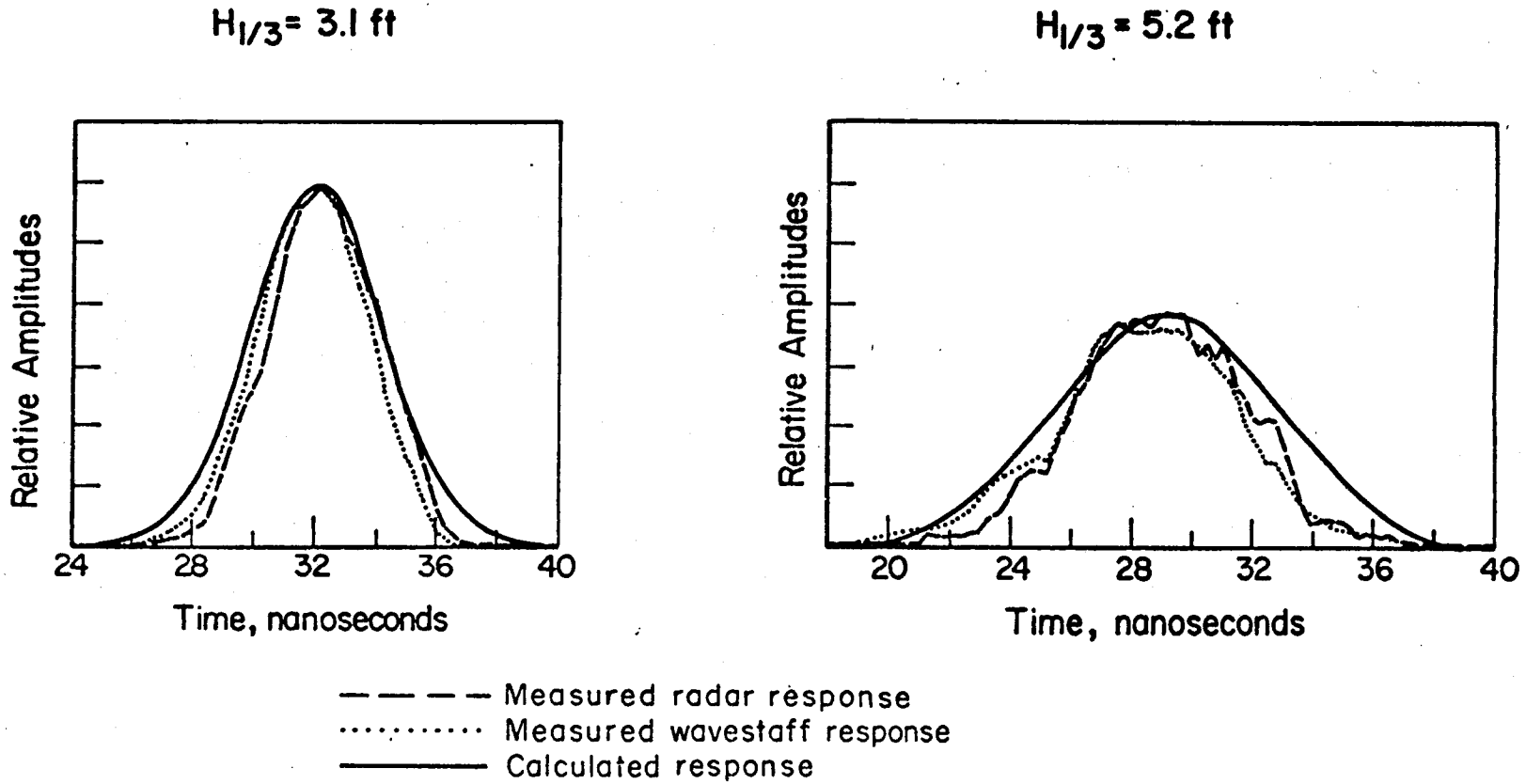

Figure 7. Measured [after Yaplee et al, 1971] Altimeter (Impulse) Responses Versus Calculated Using Beam-Limited Model

THE SKYLAB RADAR ALTIMETER

17

H.R. Stanley
J.T. McGoogan

NASA Wallops Station
Wallops Island, Virginia 23337

A summary of the significant hardware characteristics of the S-193 altimeter experiment portion of the 1973 SKYLAB Mission is presented. A detailed discussion of the Altimetry, Oceanographic, and Instrumentation Technology objectives are presented along with a discussion of the major experiments associated with these objectives.

INTRODUCTION

For a number of years, geodesists, oceanographers, and others have expressed an interest in the scientific possibilities of an orbiting altimeter (1-10). During recent years NASA has sponsored various studies related to the development and implementation of such a system (11-17). The basic concept which has evolved uses the orbit of the satellite as a reference from which direct radar pulse measurements are made of the vertical distance to the ocean surface - The overall objective of satellite altimetry being to synoptically map the dynamic topography of the sea surface with a precision of 10cm (7). Although, altimetry with a precision of only ±2-5 meters would perhaps be of considerable value to the earth physics community (18), the overall usefulness is largely dependent on its ability to ultimately achieve this high resolution. The present state of knowledge concerning the geoid and critical instrumentation design parameters as well as the state of precise orbit determination require that an evolutionary approach be taken. This implies that successive missions are required and that each mission should provide some significant advance in the state of the art. The SKYLAB mission is uniquely suited to be first in line to accept such a challenge.

Good spacecraft stabilization which permits using a high gain antenna and the low orbital height provide good loop gain. The permissible weight, volume, and power drain allow design of an instrument with a high degree of flexibility. This flexibility coupled with the planned low orbital eccentricity not only offers an excellent opportunity for acquisition of short arc geoidal profile information but also permits acquisition of the detailed technical information needed to improve future precision altimeter designs. This will include sensing of oceanographic and surface features, measurement of basic electromagnetic scattering characteristics, and acquisition of detailed statistical information on the characteristics of the backscattered signal. The general applications of altimetry are listed in Table 1.

Table 1

APPLICATIONS OF ALTIMETRY

- o INSTRUMENTATION TECHNOLOGY
- o GEODESY - REFINEMENT OF GEOID/GRAVITY MODEL
- o ORBIT DETERMINATION
- o OCEANOGRAPHY
- o METEOROLOGY
- o NAVIGATION

Some of the investigations actually planned for the SKYLAB experiment in the areas of Geodetic and Oceanographic Investigations are listed in Table 2 and 3 respectively. The Instrumentation Technology Investigations are discussed later in detail.

Table 2

GEODETIC & OCEANOGRAPHIC INVESTIGATIONS

- o GEOID MAPPING
- o TOPOGRAPHY
- o SEA STATE
- o RAIN
- o CLOUDS
- o SCATTEROMETRY
- o ALTITUDE PRECISION
- o SPATIAL DECAY TIME OF PRECISION
- o CALIBRATION

B

Table 3

INSTRUMENTATION TECHNOLOGY INVESTIGATIONS

- o IMPULSE RESPONSE
- o RESOLUTION
- o σo (LOOP GAIN DESIGN)
- o STABILIZATION EVALUATION
- o CORRELATION TEMPORAL (OR SPATIAL LENGTH) MAXIMUM COMPRESSION CODE & PRF
- o PULSE COMPRESSION

INSTRUMENTATION CHARACTERISTICS

The S-193 altimeter experiment is one of three microwave experiments to be conducted aboard the 1973 SKYLAB mission. The other two experiments are the S-193 Radiometer/Scatterometer experiment and the S-194 L-Band Radiometer experiment. Since the three portions of the S-193 experiment share common R.F. circuits, the altimeter portion of the system cannot be operated simultaneously with the RADSCAT portion.

A summary of the basic electrical characteristics of the altimeter system are listed in Table 4. The flexibility of the instrument allows selection of several groups of characteristics into five basic modes of operation. These five modes are listed in Table 5 along with the pertinent characteristics of each mode.

Table 4

SKYLAB ALTIMETER ELECTRICAL CHARACTERISTICS

Transmitter type	TwT
peak power	2 Kw
PRF	250 pps
pulse code	single or dual pulse
frequency	13.9 GHz
Receiver type	coherent
IF center frequency	350 MHz
noise figure	5.5 db
pre-amplifier	tunnel diode
Antenna type	parabolic
diameter	44 inch
gain	42 db
beamwidth	1.5
Experiment Data Rate	10 K bits per sec (max)
Altimeter Signal Processor	threshold & split gate
tracking loop type	digital, 200 MHz logic
loop bandwidth	1 Hz
altitude output	32 pulse average of 2-way delay
altitude granularity	1.25 feet
acquisition time	less than 6 sec. (with initial altitude set to with ±4000 yds)
no. of sample & hold gates	8
sampling gate width	10 & 25 nsec
gate spacing	10 & 25 nsec

Sub Modes	100 nsec	10 nsec	10 nsec comp.
Rx Bandwidth	10 MHz	100 MHz	100 MHz
Altitude Noise	2 M	1.5 M	1 M
Signal to Noise Ratio	28 db	10 db	18 db
Pulse Footprint	3.5 n. miles	1.5 n. miles	1.5 n. miles

Pulse Compression	selectable
type	binary phase code
code	13 bit Barker code

Table 5

SKYLAB ALTIMETER MODES

Mode Number	Unique Features	Prime Data Sources
1. PULSE SHAPE	.5° Step Wide Bandwidth	Sample & Hold Altitude AGC
2. σo (RADAR-CROSS SECTION)	12 db Step (AGC Calibration) Antenna Positions 0°, 1/2°, 15.6°, 8°, 3°, 1.5°, 0°	Sample & Hold AGC
3. TIME CORRELATION	Two Pulsewidths Double Pulse Operation Spacings 1, 19.2, 17.8, 153.6, 409.6, 819.2 (Micro Seconds)	Sample & Hold Altitude
5. PULSE COMPRESSION	Three Pulsewidths 10ns 10ns (Compressed) 100ns	Sample & Hold AGC Altitude
6. NADIR ALIGNMENT	Slow Spiral Drive	AGC

The reasoning behind these five modes, or their scientific objectives, are discussed below along with their relation to altimetry and their various ground truth and calibration requirements.

Mode 1 - Waveform Experiment

The waveform experiment has been designed to collect statistical information concerning the backscattered signal, which will be used to experimentally verify the various signal models and error sources involved in both altitude and sea-state measurements. During this mode of operation, detailed pulse-by-pulse waveform information on the backscattered signal will be recorded. Each received pulse will be sampled at eight points within the received waveform with sample spacings of 10 and 25nsec for transmitted pulse lengths of 10 and 100nsec respectively. In the case of mean value waveforms which can be constructed from these measurements the square law detected signal is related to the power impulse response. Impulse response measurements are of considerable interest in the design of altimeters since the manner in which the fluctuating signal converges to a mean value strongly influences altitude tracker design and defines the degree to which surface parameters can be extracted (13, 17).

Mode 2 - Radar Cross-Section and Altimeter Experiment

This mode will provide measurement of the radar cross-section (σ^o) for land, sea, and ice returns at both normal incidence and as a function of angle up to 15 degrees off nadir. This cross-section information will be very useful in the design of future altimeters and useful for comparison purposes with the other SKYLAB experiments. Data will also be collected in this mode and analyzed to investigate the accuracy, precision and overall capability of satellite altimeters to determine mean sea level, monitor mean surface slopes, and measure small scale departure of the ocean surface from overall mean sea level.

For this mode of operation, ground truth information is especially critical.

Mode 3 - Time Correlation Experiment

In this mode a pair of pulses will be transmitted, with spacing between pulses variable from approximately 1μsec to one millisecond. Examination of the sampled return waveform data should yield the maximum PRF at which statistically independent samples of altitude data can be obtained, characteristics of the signal correlation properties as a function of surface conditions, and the maximum time interval over which the reflecting surface appears motionless and therefore suitable for use of pulse compression systems that do not contain doppler compensation.

Mode 5 - Pulse Compression Experiment

This mode consists of both 10 nanosecond uncompressed pulse operation and a 10 nanosecond phase reversal pulse compression operation using a 13 bit Barker code. Direct comparison of the two techniques will be possible, establishing the capability of phase reversal pulse compression techniques to measure detailed information on extended targets. It should be noted that 10 nanosecond altimetry (height data) cannot be obtained since the altitude tracker is designed to operate only on the 100 nanosecond pulse length. During the 10 nanosecond pulse mode the pulses are narrow-band filtered to equivalently stretch the 10nsec pulses up to 100nsec. This will not, however, affect the 10 nanosecond waveform data gathering process.

Mode 6 - Nadir Alignment Experiment

The objective of this experiment is to evaluate the feasibility and accuracy of an on-board nadir seeker to supplement or complement the normal stabilization systems required for altimeter pointing. In the nadir seeker mode the antenna is automatically moved in pitch and roll to a position at which the gated AGC control voltage is a maximum.

OPERATIONS

Present plans call for three periods of time in which the altimeter experiments can be conducted; the first two periods will be for a duration of 28 days each and the last period for a duration of 58 days. Each experiment data collection mode is expected to last approximately 3 minutes. All experimental data obtained will be stored on digital magnetic tape at a maximum rate of 10 K bits per second and returned to earth with the astronaut crews. Sufficient time exists between flights to allow some examination of the data and planning of subsequent measurements.

GROUND TRUTH

In the planned experiments, both surface and aircraft sensors will be utilized to measure parameters such as surface winds, temperature, and wave height spectrum. In addition to the nominal aircraft complement of instrumentation (nanosecond radar, laser profilometer, Stilwell photography) it is hoped that the engineering model of the SKYLAB altimeter can be installed and used for ground truth data collection.

REFERENCES

1. "Satellite Radar Oceanography, An Introduction" R. Moore University of Kansas, appearing in the Woods Hole Oceanographic Institution Report Oceanography from Space April 1965.

2. "Oceanographic Satellite Radar Altimeter and Wind Sea Sensor" T. Godbey, General Electric, appearing in the WHOI Report Oceanography from Space April 1965.

3. "A Study of Satellite Altimetry for Geophysical and Oceanographic Measurement" E. Frey, J. Harrington, W. von Arx, MIT, proceedings of the XVI Congress of the International Astronautical Federation, September 1965.

4. "Radar Altimetry from a Spacecraft and its Potential Applications to Geodesy and Oceanography" J. Greenwood, A. Nathan, G. Neumann, W. Pierson, F. Jackson, T. Pease, NYU May 1967.

5. "Possible Geopotential Improvement from Satellite Altimetry", C. Lundquist, SAO Special Report 294 February 1969.

6. "Satellite Altimetry" A. Shapiro, B. Yaplee, Naval Research Laboratory, NRL Report 7018, February 1970.

7. "The Terrestrial Environment: Solid-Earth and Ocean Physics" MIT, NASA CR-1579 April 1970.

8. "Utilization of a Radar Altimeter for Determining Ocean Roughness" I. Ketz, APL, Proceedings of the IEEE 1970 EASCON.

9. "Global Geoid Mapping Using Satellite Altimetry", H. Stanley, NASA Wallops Station, N. Roy Wolf R & D, 3 International Symposium on the Use of Artificial Satellites for Geodesy, April 1971.

10. "A Geodetic and Oceanographic Satellite Altimeter System", E. Hudson, Raytheon, AIAA Space Systems Meeting, July 1971.

11. "Definition of GEOS-C Mission" Geonautics Inc., Technical Report No. 184-7/1, December 1968.

12. "Space Geodesy Altimetry" M. Kolker, E. Weiss, Raytheon, NASA CR-1298, March 1969.

13. "Radar Altimeter Study Phase II", T. Godbey, E. Hofmeister, B. Keeney, W. Kelly, G.E., January 1970.

14. "A Study of the Capabilities of the Geodetic Satellite Altimeter to Measure Ocean Surface Characteristics" L. Miller, Research Triangle Institute, April 1970.

15. "Space Geodesy Altimetry Aircraft Experiment", E. Genest, M. Kolker, C. Mundo, Raytheon, May 1970.

16. "Nanosecond Radar Observations of the Ocean Surface from a Stable Platform" B.S. Yaplee, A. Shaprio, D. Hammond, B. Au, E. Vliana, NRL, IEEE Trans. Geoscience Electronics, vol. GE-9 pp 170-174, July 1971.

17. "System Study of the Geodetic Altimeter Concept", L. Miller, G. Hayne, Research Triangle Institute, Final Report NASA Contract NAS6-1829 March 1971.

18. "Potential Applications of Satellite Geodetic Techniques to Geoscience". G. Woollard, ed., NASA sp-158, 1968.

GEOS-C RADAR ALTIMETER CHARACTERISTICS

18

J. B. Oakes

The Johns Hopkins University
Applied Physics Laboratory
Silver Spring, Maryland

I. INTRODUCTION

GEOS-C is the third in a series of spacecraft to be designed and built by the Applied Physics Laboratory for NASA. The first two of these spacecraft, GEOS-A and B, have successfully operated in orbit for a number of years and have become important components of the National Geodetic Satellite Program. The GEOS-C spacecraft will fulfill a dual mission; it will carry on the work of the GEOS series in satellite geodesy, and it will also carry equipment to gather data of significance in earth physics research. A primary experiment of GEOS-C will be a K-band radar altimeter, employed to gather data for both of these research areas. This paper will describe the characteristics of this radar altimeter and will discuss the rationale behind the choice of its operating parameters.

An artist's concept of the multi-purpose GEOS-C spacecraft is shown in Figure 1. The octagonally shaped body will carry solar cells arranged in an array designed for maximum efficiency in the collection of solar power. Gravity gradient stabilization will be employed in order to keep the flat face of the satellite facing the earth at all times. The weight of the spacecraft will be approximately 600 pounds. Present plans call for launch during the last quarter of 1973.

As with previous GEOS spacecraft, several of the equipments carried will provide precision data for determining the shape of the earth. These include the doppler beacon, the unified S-band transponder, the range and range rate transponder, the ATS relay experiment, the flashing lights, and the laser reflectors. All of these experiments, with the exception of the ATS relay, will have their antennas located on the earth-facing side of the satellite.

II. EXPERIMENT OBJECTIVES

Two general objectives guide the design of GEOS-C radar altimeter experiment. It is a requirement that height measurements and other supporting data necessary to evaluate the feasibility and value of altimetry on a global basis be obtained. It is also a design goal that data be obtained on which the design of a dedicated altimetry spacecraft can be based. It is necessary that a design approach be chosen such that mission objectives be met within the constraints imposed by the previous spacecraft design effort and by the dual nature of the mission itself.

III. SPACECRAFT CONSTRAINTS

As in most unmanned spacecraft, power represents a major constraint in the design of the on-board experiments. In GEOS-C, weight and volume also represent less stringent but still important constraints. In addition, all electronic packages must meet orbital temperature restrictions, and certain specific constraints, such as radiated peak power and magnetic compatibility.

Figure 2 is a cross sectional drawing of the GEOS-C spacecraft structure. Space reserved for the radar altimeter is indicated on this drawing. The antenna is visualized as either a paraboloid or a phased array; in either case, it can occupy a volume bounded by a 24 inch diameter cylinder 4.6 inches high. Two electronic packages have also been allowed for. One of these, attached directly to the antenna itself, would contain the altimeter transmitter and receiver. A volume of 6" x 6" x 7" has been set aside for this package. A second package, having a volume of 5" x 9" x 10", has been set aside for additional remote electronics which will be used to process the radar signals as they return from the earth.

Two basic operating modes are visualized for the altimeter. One of these, the global mode, will be used in gathering data over substantial portions of a satellite orbit. In this mode the altimeter experiment can consume a maximum of 40 watts for a duration of two hours. Six non-operating hours are then required to recharge the spacecraft batteries associated with the altimeter experiment. In the intensive mode, ground truth experiments and other data gathering experiments of use in determining some of the characteristics of the ocean surface, will be obtained. In this mode, a maximum of 80 watts can be consumed for a one hour period; seven hours are then required for recharge.

A weight of 60 pounds is allowed for the required global mode altimeter system. The intensive mode system, which is intended to satisfy the design goals of the program, is allowed 25 pounds additional. In order to keep rf interference at a minimum, a maximum radiated peak power of 10 kW is allowed in either the global or the intensive mode. Since the spacecraft will be gravity gradient stabilized, residual magnetic moments must be kept small in order to minimize overturning forces. A maximum of 100 pole-centimeters residual moment is allowed for each altimeter package. In addition, the use of nonmagnetic materials is suggested to keep in-orbit magnetization of the altimeter components to a minimum.

For the approximate orbit of the GEOS-C spacecraft, the temperature extremes of the three altimeter packages have been calculated. The antenna must meet its design characteristics over a range from -130 to +90°F. The attached electronics package must meet its specifications over a temperature range from +20 to +105°F. The remote electronics package will be subjected to a temperature ranging from +10 to +104°F.

IV. OPERATIONAL CONSTRAINTS

In addition to the constraints on the radar altimeter imposed by the spacecraft design itself, a number of operational constraints exist. For example, the orbit must be chosen to maximize both the geodetic and the earth sciences data gathering capabilities of the spacecraft. Tentatively, the following orbit parameters have been chosen; spacecraft eccentricity, .005 maximum; spacecraft inclination, between 40° and 65° retrograde; spacecraft altitude, between 750 and 950 km. Inclination and altitude figures will be refined and finalized in the near future. The radar altimeter frequency is limited by international agreement; in our case, an operating frequency of 13.9 GHz has been chosen. The altimeter will be designed to survive 1500 hours of on-time over an 18 month satellite lifetime. In order to meet its objectives over a wide range sea-state conditions, the altimeter must be designed to operate for sea surface reflectivities between +3 to +16dB. In addition to this, a small amount of satellite libration is expected. With the orbit parameters mentioned above, the maximum value of this libration is not expected to exceed one degree. Therefore, all the objectives of the altimeter experiment must be met for off-vertical librations up to one degree maximum.

V. FEASIBILITY CALCULATIONS

The design of a useful radar altimeter meeting these constraints is an exacting task. The first phase of this task will result in an extremely detailed design study, in which the feasibility of the design will be examined from all aspects. At present, a number of simplified calculations have been completed in an attempt to provide guidance for the detailed study. As an example of one of these calculations, it is interesting to examine the effect of various combinations of radar pulse length, peak power, pulse repetition frequency, average power, and received signal-to-noise ratio on the rms error in the altitude measurement. Figures 3 and 4 indicate the results of such calculations. The first equation in Figure 3 expresses the rms noise of the altitude measurement in terms of pulse length, received signal-to-receiver noise ratio, and the number of pulse integrated, for a three gate range tracker. A Raleigh-type sea return is assumed. The second equation in Figure 3 is the receiver signal-to-noise ratio given by the standard radar range equation. In this equation, the constants have been adjusted to be consistent with the units given below the equation. To make meaningful use of these two equations, we also impose the spacecraft peak power constraint of 10 kW and a maximum PRF constraint which results if one demands complete decorrelation between successive received pulses, as the spacecraft moves over the earth's surface. The results of some sample calculations are shown in Figure 4. The first set of data assumes a maximum peak transmitted power of 2 kW, and varies the pulse length from 100 to 50 nanoseconds. The value of n given corresponds to zero correlation between successive received pulses, in accordance with the Van Cittert-Zernike theorem, and can be thought of as the limiting PRF for the altimeter footprint represented by the pulse. An averaging time of one second has been assumed. The average power level, the signal-to-noise ratio at the front end of the radar receiver, and the rms noise level of the resulting altitude measurement, are shown in the three remaining columns. It is interesting to note that with the parameters employed, a minimum in the noise level occurs at a pulse length of approximately 70 nanoseconds. The noise level of 0.82 meters obtained under these conditions is the noise due to the statistical character of the reflecting surface; it does not take into account either sources of noise within the altimeter tracking loops, or digitizing noise which may result from the range measurement process itself.

It is interesting to see what happens as the peak power is varied and an optimum pulse length is sought for

each value of peak power. This calculation is shown in the bottom part of Figure 4. The second column, τ_{opt}, is the pulse length for which the noise level in the measured altitude is a minimum. For example, if one were to choose a 10 kW peak power, the optimum pulse length would be approximately 30 nanoseconds, and the resulting statistical noise in the received altitude measurement for a one second averaging time would be approximately 0.45 meters. The signal-to-noise ratio for each pulse arriving at the front end of the radar receiver would be approximately 2.85, and the average radiated power under this condition would be 0.36 watts.

VI. ALTIMETER CHARACTERISTICS

The desired characteristics of the GEOS-C radar altimeter are given in Figure 5. Based on simplified feasibility calculations of the type outlined above, the characteristics of the global mode appear to represent a consistent set, achievable within the spacecraft and operational constraints of the program. The intensive mode design goals also appear to be achievable, although greater circuit and system sophistication will obviously be required.

The GEOS-C radar altimeter represents an important first step in the design of dedicated altimetry spacecraft. As such, it can supply information of great importance to geodesists. It can supply some information of interest to oceanographers and can provide a means for establishing design criteria useful in future altimeters.

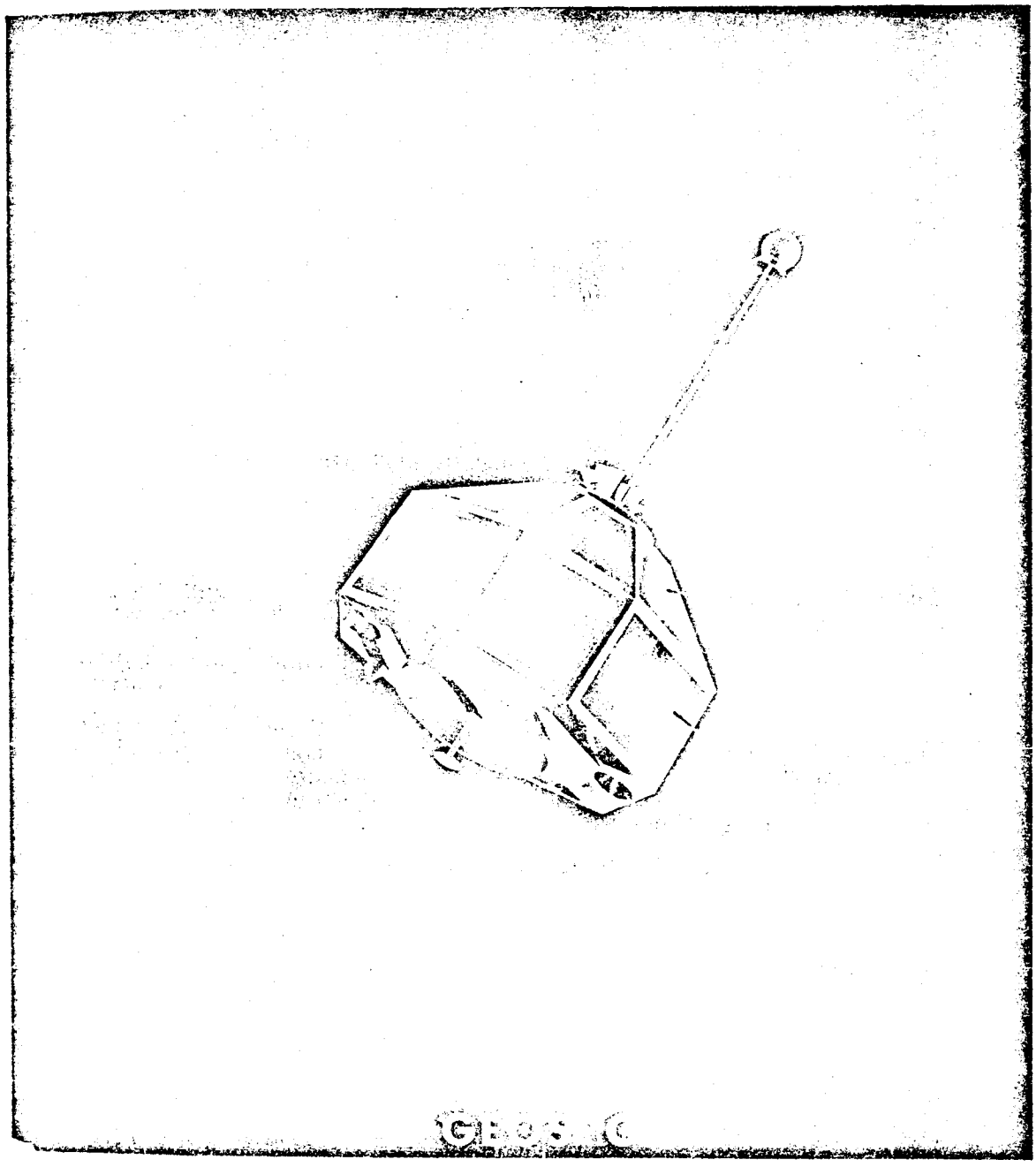

FIGURE 1

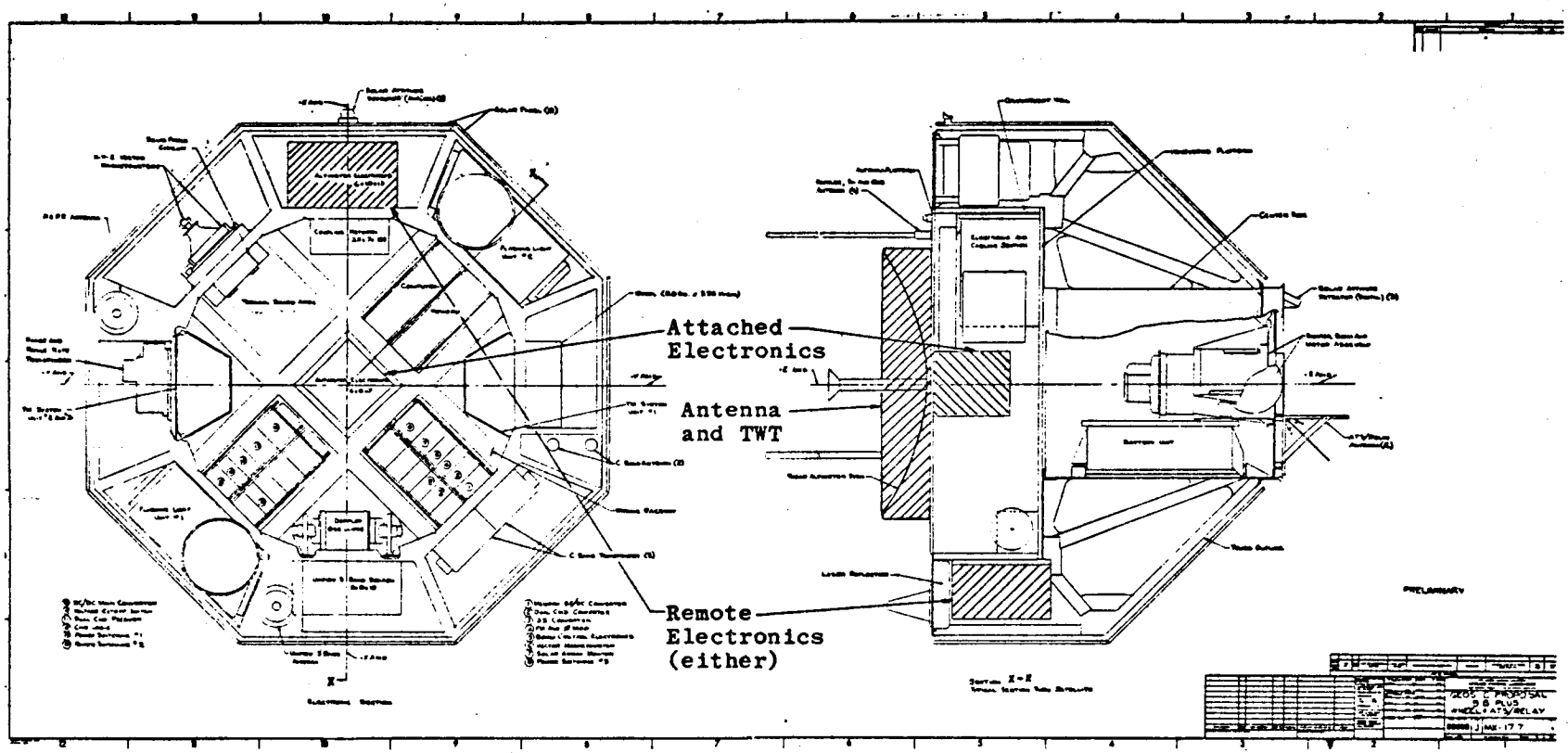

OUTLINE DRAWING

Figure 2

FEASIBILITY CALCULATION

GLOBAL MODE ALTIMETER

$$\sigma_{h_{meters}} = \frac{\tau}{6}\sqrt{\frac{4 + \frac{18}{(S/N)} + \frac{9}{(S/N)^2}}{n}} \quad \text{- 3 Gate Tracker}$$

$$(S/N) = \frac{P_t\, G^2\, \lambda^2\, \sigma_0\, A_r}{4\, h^4\, BNL}$$

Where:

P_t = transmitted peak power, watts

G = antenna gain (= 2800 for 24" parabola 1° off center)

λ = wavelength, cm(= 2.16 for 13.9 GHz)

σ_0 = ocean reflectivity (= 2, worst case)

A_r = illuminated ocean area, m^2(= $2\pi h \times 0.3\tau$)

h = satellite altitude, n.mi. (= 513, worst case)

B = receiver IF bandwidth, Hz (= $1.2/\tau$, matched filter)

N = receiver noise figure (= 10, assumed)

L = two way plumbing loss (= 1.6, assumed)

n = number of received pulses integrated over the one second sampling time

τ = pulse length, nanoseconds

Impose the following limits:

$P_t \leq 10^4$ watts

$$n \leq \frac{1.5V}{\lambda}\sqrt{\frac{\tau}{h}} \quad \text{(Van Cittert - Zernike)}$$

Where V = orbital velocity in meters per second.

Figure 3

FEASIBILITY CALCULATION

GLOBAL MODE ALTIMETER (Continued)

RESULTS:

τ(ns)	P(w)	n	P_{av}(w)	S/N	σ_h(m)
350	2000	4003	2.8	6.9	2.18
300	2000	3706	2.22	5.1	2.09
250	2000	3383	1.69	3.5	2.04
150	2000	2621	0.79	1.3	2.16

P(w)	τ_{opt}(ns)	P_{av}(w)	S/N	σ_h(m)
2000	225	1.44	2.9	2.03
4000	160	1.73	2.9	1.57
7000	120	1.97	2.8	1.27
10000	100	2.14	2.8	1.11
20000	70	2.51	2.8	0.86

Figure 4

GLOBAL MODE REQUIREMENTS

1.	ALTITUDE MEASUREMENT	
	OUTPUT DATA RATE	1 DATA POINT PER SECOND
	OUTPUT NOISE LEVEL	90% OF DATA POINTS LIE WITHIN ± 2 METERS OF THE MEAN
2.	INSTRUMENT DRIFT RATE	LESS THAN 5 METERS PER HOUR, IN ORBITAL ENVIRONMENT
3.	BUILT-IN CALIBRATION	ABSOLUTE ACCURACY ± 1 METER, IN ORBITAL ENVIRONMENT, FOR LIFE OF SPACECRAFT

INTENSIVE MODE GOALS

1.	ALTITUDE MEASUREMENT	
	OUTPUT DATA RATE	1 DATA POINT PER SECOND
	OUTPUT NOISE LEVEL	90% OF DATA POINTS LIE WITHIN ± 0.5 METERS OF THE MEAN
2.	INSTRUMENT DRIFT RATE	LESS THAN 2 METERS PER HOUR, IN ORBITAL ENVIRONMENT
3.	BUILT-IN CALIBRATION	ABSOLUTE ACCURACY ± 0.5 METER, IN ORBITAL ENVIRONMENT, FOR LIFE OF SPACECRAFT
4.	IMPULSE RESPONSE OF OCEAN	DATA DESIRABLE; AS A GOAL, MEASURE WAVES 2 METERS CREST-TO-TROUGH, TO A PRECISION OF 0.6 METERS rms, WITH AN AVERAGING TIME OF 10 SECONDS.
5.	AMPLITUDE PROBABILITY DISTRIBUTION	DATA DESIRABLE
6.	TIME CORRELATION FUNCTION OF BACKSCATTER	DATA DESIRABLE

Figure 5

SATELLITE ALTIMETERS AFTER SKYLAB AND GEOS-C --- SHOULD THEY UTILIZE A SINGLE TRANSMITTER OR AN ARRAY OF PULSED AMPLIFIERS?

Alan H. Greene and Edward F. Hudson
Raytheon Company
Equipment Division
Wayland, Massachusetts 01778

Introduction

The first spacecraft radar altimeters to operate over the ocean were those which flew on the Saturn I launch vehicles in 1964 and 1965 (reference 1). These radars, which were used to measure the altitude of the vehicles during their ascent, operated at 1.6 GHz (L-Band) and transmitted 5-kw pulses of 1-μsec duration. A brief summary of the results is given in Table 1.

The first altimeter to fly in Earth orbit will be the one in the Skylab S-193 Microwave Experiment in 1973. This radar will operate at 13.9 GHz (K_u-Band) and transmit 2-kw pulses of 10-ns, 100-ns, and 130-ns compressed to 10-ns. The second altimeter planned for Earth orbital operation is the one for the GEOS-C satellite scheduled for late 1973 or early 1974. This altimeter will also operate at 13.9 GHz and will transmit pulses of about the same length and peak power as the Skylab altimeter.

Table 1

Saturn Radar Altimeter Flights

(Source: Reference 1)

Flight Number	SA-4	SA-5	SA-6	SA-7	SA-9
Date of Flight	3/28/64	1/29/64	5/28/64	9/18/64	2/16/65
Peak Altitude to which altimeter was operated	62 km	264 km	195 km	210 km	499 km
Amount of Data	120 sec	157 sec	184 sec	629 sec	592 sec
Quality of Data	+20m bias	Noisy	+90m bias	+100m bias	+100m bias

One of the things all these altimeters have in common is their reliance on a single transmitter having a single microwave power tube. The Saturn altimeter utilized a L-Band Triode. The Skylab altimeter utilizes a K_u-Band Traveling Wave Tube (TWT). The GEOS-C altimeter is expected to utilize a K_u-Band Magnetron, or a K_u-Band TWT, or possibly a combination of both in order to have two modes of operation, a global mode at low power for extended periods and an intensive data mode at high power for short periods.

The question addressed by this paper is: should the Earth observation satellite altimeters that come after Skylab and GEOS-C continue to use the single transmitter and microwave tube approach, or should they be designed as an array of solid-state K_u-Band transmit/receive modules?

If the choice had to be made today, it would have to be the single transmitter designed around a TWT or Magnetron. Solid-state module technology at K_u-Band for the output power levels required for these radars is not yet available. However, the choice does not have to be made today. The design of the altimeters for the dedicated satellites should await the return of the design data from the Skylab and GEOS-C experiments and that data will not be available for another two to three years. By that time, the state-of-the-art in K_u-Band solid-state technology hopefully will have advanced to the point where the radar designer will have a choice.

System Requirements

The radar designer will be faced with the task of designing a pulsed radar that, like its predecessors, will operate as a pulsewidth limited system. For this condition, the signal-to-noise ratio per pulse, S/N, is given by:

$$S/N = \frac{y\, P_t\, G^2\, \lambda^2\, \sigma^o\, c\, T^2\, \pi\, r_e}{h^3\, N_F\, L_S\, k\, T_a\, (4\pi)^3\, (r_e + h)} \qquad (1)$$

Table 2 defines each term and gives the values used in subsequent calculations.

Table 2

Pulse Limited Radar S/N Equation Terms

Term	Value	Definition
y	-	Pulse compression ratio
P_t	-	Transmitted pulse peak power
G	36.4 dB	Antenna gain. Assumes constant illumination over a circular aperture 60-cm in diameter having a 3-dB beamwidth of approximately 2^o and antenna efficiency of approximately 0.6.
λ	2.16 cm	R-f wavelength equivalent to a frequency of 13.9 GHz
σ^o	+3.0 dB	Ocean backscatter coefficient at vertical incidence for sea-state 5.
c	$3x10^8$ m/sec	Velocity of light
T	-	Compressed pulsewidth
r_e	6370 km	Radius of the Earth
h	1000 km	Height of the satellite above the ocean
k	$1.38x10^{-23}$ joules/^oK	Boltzman constant
T_a	290^oK	Absolute reference temperature of the receiver
N_F	5.5 dB	Noise figure referred to T_a
L_S	4.1 dB	Sum of all system losses including those projected for the radar equipment and attenuation due to propagation through the troposphere.

Accuracy studies have shown that rms altitude errors reduce as T is narrowed and as S/N is increased, up to a point. T cannot usefully be narrowed below the wave height, and higher S/N ratios yield little improvement if increased above 12 dB. Since the radar should provide the desired accuracy of 10-cm over most ocean conditions, a wave height corresponding to sea-state 5 is taken to limit the minimum value of T which sets T at 20-ns.

For a three gate tracker, the 20-ns pulsewidth results in an rms error of about 6.2-cm and a bias uncertainty of about $\pm$ 5.5-cm. The radar is assumed to have a prf of 1000 Hz, and the tracker time constant is set at 0.5 seconds. Raising the prf will not be effective because of pulse-to-pulse correlation which will occur, and the integration time must be kept low enough to provide sufficient resolution of surface topographical features, given a satellite horizontal velocity in the neighborhood of 7 km/sec.

Substituting the S/N of 12 dB and the compressed pulsewidth of 20-ns into equation (1) gives a value for yP_t equal to 200 kw.

The radar designer may now consider what pulse compression ratio to employ in order to reduce the pulse peak power requirements. For the purposes of this paper, a compression ratio of 500:1 will be used and then two systems will be examined, first a single transmitter system utilizing a TWT, and second a system based on an array of solid-state T/R modules. Both systems will transmit 400-watt 10-μsec long pulses compressed to 20-ns. The prf will be 1000 Hz.

Single Transmitter System

A block diagram for a single transmitter system using a TWT power amplifier, a high voltage power supply and modulator, and pulse compression is shown in Figure 1. Upon receipt of a trigger from the logic and control circuits, the impulse generator will provide a signal to the pulse compression network. The output of the network will be switched, filtered, gated, frequency converted, and finally amplified in a high powered TWT stage. The transmitted signal is then fed through a duplexer to the antenna.

The received signals will be directed by the duplexer to a tunnel diode amplifier, converted in frequency, amplified, and then compressed in a pulse compression network and processed to produce range, pulse shape, and AGC data.

The reliability and life of such a system will depend to a large extent on the Traveling Wave Tube and its associated high voltage power supply. The HVPS will operate at several kilovolts, and in the space environment this can present problems with electrical breakdown, corona, arcing, and electromagnetic interference. With a single transmitter in the system, it is estimated that system life will be on the order of 10^3 hours of assured operation. With an extra transmitter which can be switched in if the primary unit fails, the system life expectancy would be almost doubled.

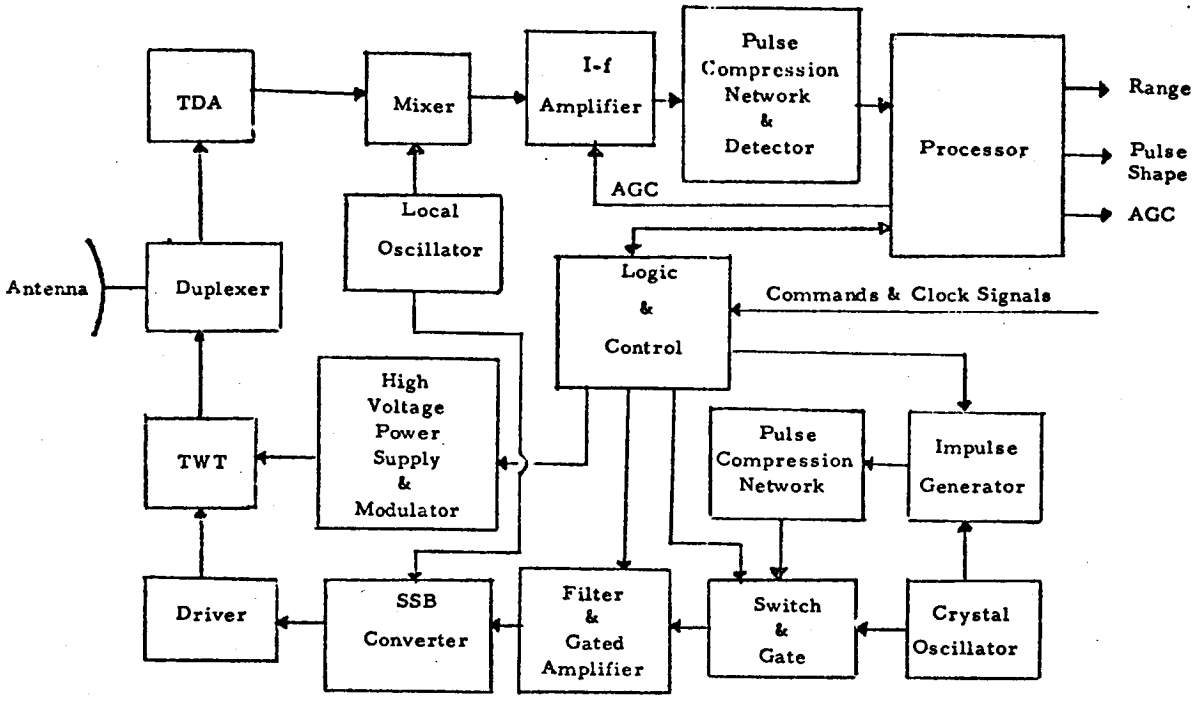

Figure 1 - Block Diagram of Single Transmitter System

It is estimated the system would require about 70 watts of dc power, exclusive of the power required to reposition the antenna in the event the radar senses it is more than 0.5^{o} off the vertical. It may also be desirable for the antenna to scan to either side every so often so that the sea-state can be measured over a swath instead of just along the ground track. System weight, including the second transmitter, is estimated to be approximately 60 lbs.

Array of Solid-State T/R Modules

A block diagram of an altimeter that would use a modular array, with a large number of solid-state low power amplifiers in place of the high power TWT, is shown in Figure 2. Each of the transmit/receive modules would contain several of the elements shown in Figure 1, such as a power amplifier, duplexer or circulator, low noise amplifier, and switching circuits. The output of the impulse generator would be fed through the pulse compression network and the wide pulse would be switched, filtered, gated, and frequency converted. A feed system would distribute the signal to the T/R modules. The received signals from the modules would be combined in a feed system and the single output converted to the I-f, compressed and processed.

In order to estimate the number of T/R modules, it will be assumed that each radiating element in the antenna is fed directly by a module.

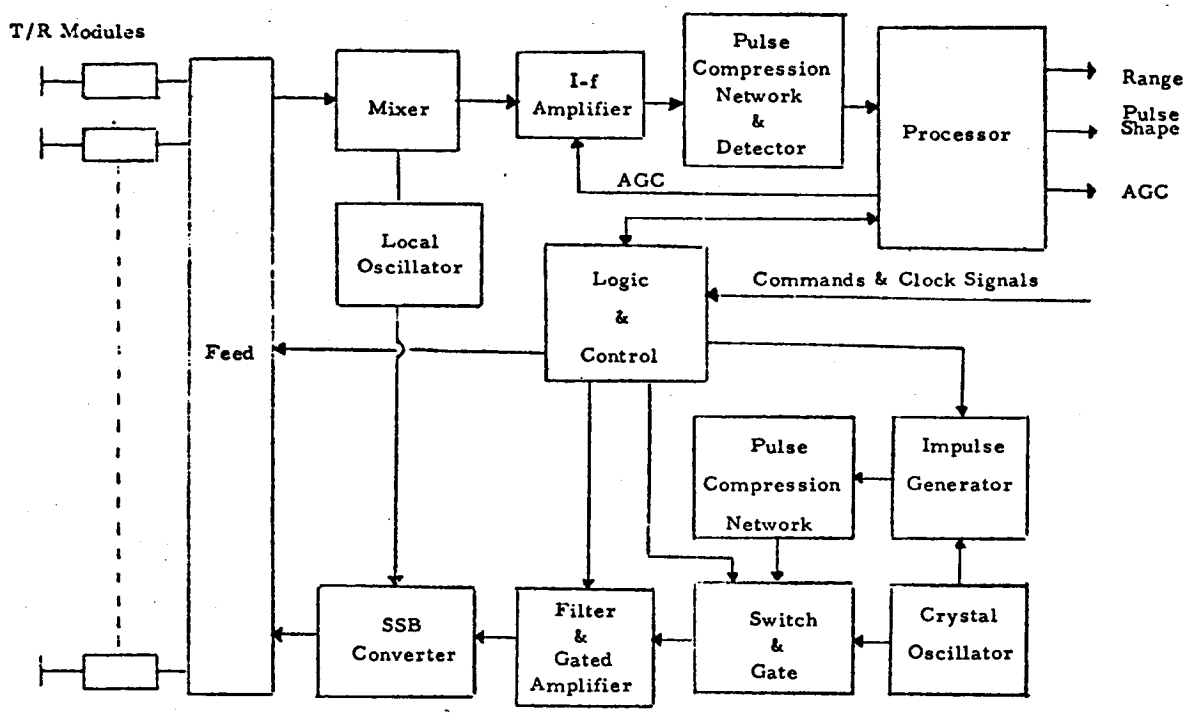

Figure 2 - Block Diagram of Solid-State Module System

In an equilateral-triangular arrangement of radiating elements, the maximum area, A_e, allowed per element if grating lobes are to be avoided is:

$$A_e = \frac{2\lambda^2}{\sqrt{3}\left(1 + \sin\theta_m\right)^2} \qquad (2)$$

where θ_m is the maximum scan angle away from boresight (reference 2).

Therefore, the minimum number of elements is:

$$n = \frac{A_a}{A_e} \qquad (3)$$

where A_a is the antenna aperture area.

Since $A_a = \frac{\pi D^2}{4}$

$$n = \frac{\pi\sqrt{3}}{2}\left[\frac{D\left(1 + \sin\theta_m\right)}{2\lambda}\right]^2 \qquad (4)$$

A 2° beamwidth is desirable to minimize satellite pitch and roll control requirements, and since λ = 2.16-cm, D is selected as 60-cm, as indicated in Table 2. θ_m is selected as 10° so it will be possible to

scan the beam at times out to 10^{o} off the vertical in order to measure sea-state to either side of the satellite ground track. Substituting these values for λ, D, and θ_m in equation (4) gives n = 700 elements. Since P_t is 400-watts, the output required of each module becomes approximately 570-milliwatts per module.

An example of where the K_u-Band state-of-the-art is today is the module recently built and tested by Sylvania under an Air Force contract (reference 3). This module provides 100-milliwatts using a two-stage avalanche diode as the power amplifier in the module.

The life of the solid-state T/R modules is expected to be on the order of 10^5 hours per module, and the system life in this case should be about 5×10^4 hours of assured operation. The high voltages of the single transmitter system have been eliminated, and the highest voltages will be well under 100 volts.

However, system power requirements will be significantly greater than those for the single transmitter system. It is estimated that system power, exclusive of beam steering, will be approximately 120 watts. System weight will also be higher. It is estimated the array system will weigh approximately 100 lbs.

Summary and Conclusions

A summary of the reliability, power, and weight estimates for the two system approaches is given in Table 3.

D

If progress is made in avalanche diodes and microwave hybrid integrated circuit fabrication techniques at K_u-Band, the use of the modular array approach should be considered carefully. Although it will require more power and be substantially heavier, its advantages in life and reliability may more than outweigh these disadvantages. When sufficient progress has been made, this question should be rigorously examined in detail, rather than the cursory way it has been examined here, so that a sound decision may be made on the system approach that should be adopted for the altimeters that come after Skylab and GEOS-C.

Table 3

Summary

	Single Transmitter System	Array Solid-State T/R Modules
System Life (Estimated)	2×10^3 hours	5×10^4 hours
System Power (Estimated)	70 watts	120 watts
System Weight (Estimated)	60 lbs.	100 lbs.

References

1. Performance of Saturn Radar Altimeter M. Coleman, NASA MSFC, NASA TM X-53277, 10 June 1965

2. Array Antennas T. Cheston and J. Frank, APL, Chapter 11 in Radar Handbook M. Skolnik, NRL, McGraw-Hill 1970

3. Integrated K-Band Transceiver Report No. AFAL-TR-71-26 prepared under Air Force Contract F33615-67-C-1896, A. Solomon, Sylvania, January 1971

RADAR PULSE COMPRESSION AND HIGH RESOLUTION SEA REFLECTIVITY 20

F. E. Nathanson, Manager Washington Operations
Technology Service Corporation, Silver Spring, Md. 20910

Abstract

The first part of this paper summarizes the state-of-the-art in radar pulse compression as it applies to spacecraft altimetry. It is illustrated how in the next few years vertical resolutions of 0.5 to 2.0 ft. can be obtained with relative accuracies of 5 to 10% of these values if the nature of the sea surface is known. The second part of the paper shows that when high accuracy is desired, second order effects such as the assymetries in the sea surface reflectivity may be taken into account.

Pulse Compression

In simple terms "pulse compression" is the term applied to radar techniques where it is desired to transmit a long duration waveform but retain the resolution and accuracy characteristics of short pulse waveforms. A long duration waveform is desirable since it can be easily shown (Ref. [1] and others) that the ability to "detect" or "acquire" a target with a given antenna and receiver is soley dependent on the energy (E) in the waveform. Most of the more advanced radar transmitters considered for spacecraft such as the SKYLAB traveling-wave-tube are limited in the peak power that they can transmit. However, their average power (energy) is currently limited only by power supply considerations.

The general expression for radar range accuracy is

$$\sigma_\tau \approx \frac{1}{B(2E/N_o)^{\frac{1}{2}} n^{\frac{1}{2}}}$$

assuming optimum processing as with a maximum likelihood estimator.

where σ_τ = the standard deviation of the time delay error

B = the effective bandwidth of the transmission waveform

N_o = noise power density

n = number of independent samples

While there are some additional terms in the altimetry equations, it can be seen that the error is inversely proportional to the waveform bandwidth and the square root of the transmit energy and number of samples. Thus, for a given energy, accuracy improves with bandwidth. Practical considerations usually limit σ_τ to $0.05/B$ to $0.1/B$ for $(2E/N_o)^{\frac{1}{2}}(n)^{\frac{1}{2}} \geq 100$. A typical example calculation is given below. In active radar $\sigma_r = c\sigma_\tau/2$, where σ_r is the standard deviation in distance units and c is the velocity of propagation. For a standard deviation of altitude of 10 cm (0.1 m) in distance units, $c = 3 \times 10^8$ meters/sec, and $\sigma_\tau = 0.1/B$

$$\sigma_r = 0.1 = \frac{3 \times 10^8 (0.1)}{2B}$$

Then $B \geq 1.5 \times 10^8$ Hz = 150 MHz.

Transmit energy considerations for a satellite of the general size and altitude of GEOS-C call for transmit pulse durations of the order of 1 microsecond. Thus, the "pulse compression ratio" equals the time-bandwidth product = $(1.5 \times 10^8)(10^{-6}) = 150$, in the ideal case.

Implementation

There are several possible implementations of this technique. The most widely used is the linear FM or "Chirp" technique. A typical block diagram is shown as Fig. 1A [1]. An impulse at the intermediate frequency with the appropriate bandwidth is inserted into a dispersive

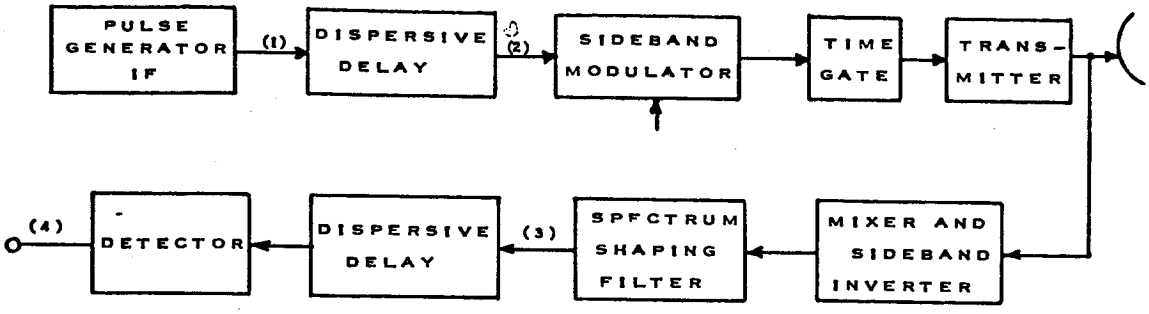

(A) GENERATOR AND DECODER

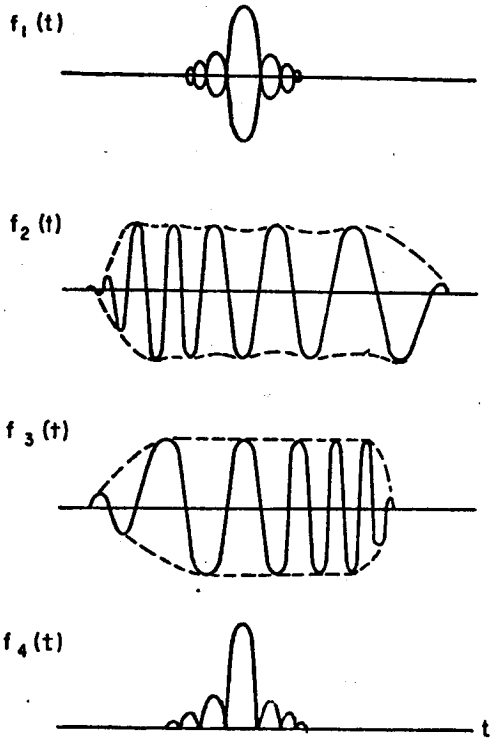

(B) WAVEFORMS (ARBITRARY TIME SCALE)

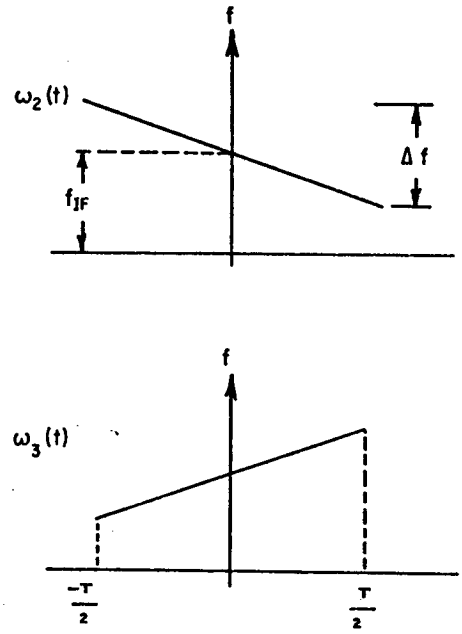

(C) FREQUENCY VS TIME

FIG. 1 PASSIVE SYSTEM FOR LINEAR F.M. PULSE COMPRESSION

device which has a linear time delay vs frequency characteristic as shown on Fig. 1B. The signal is amplified, mixed to the transmit frequency, time gated to the desired duration (i.e., 1 microsecond), and transmitted. The received signal is mixed back to the intermediate frequency, shaped to reduce time sidelobes, and the appropriate sideband is inserted into an identical dispersive device (it can be the same one as on transmit). The resultant signal has the same general shape as the input impulse.

In the past 15 years of use of this technique, the main advance has been in the nature of the dispersive device. For the parameters discussed here, the newer surface wave techniques seem to be the most applicable. A sample of the current and planned devices from two of the leading suppliers in the field are shown on Table I.

The rows show the obtainable resolution in meters, the center frequency of the device (lower frequencies are somewhat easier to work with) the pulse compression ratio, the waveform bandwidth, the pulse envelope duration, the insertion loss which can be a problem if it exceeds about 55 db, the weight of the device and transducers, excluding any over the sidelobes or spurious levels in db down from the peak (25 db or less may be a problem when high accuracy is desired), the type of structure, status and price for a single unit or to develop a single unit.

The first column is an existing item by Autonetics, Anaheim, California. For a 100 mHz bandwidth, it seems acceptable for some applications except for a somewhat marginal spurious level specification. The second column is a unit built by Andersen Labs, Bloomfield, Connecticut. It has 250mHz bandwidth, but in this form it most likely has an unacceptable insertion loss for most applications. The last three columns give characteristic of devices that can be built in the near future with a reasonable development cost. It can be seen that bandwidths of 200 to 500 mHz

TABLE I STATUS OF WIDEBAND PULSE COMPRESSION LINES

	PARAMETER	AUTONETICS	ANDERSEN			
1.	Resolution (M)	1.5	0.6	0.5-0.75	0.5	0.3
2.	Center Frequency (GHz)	0.3	0.5	~ 1.25	0.8	1.0-1.5
3.	Compression Ratio (before weighting)	100	250	200-600	300	500
4.	Bandwidth (mHz)	100	250	200-300	300	500
5.	Transmit Pulse (μsec)	1.0	1.0	1.0-2.0	1.0	1.0
6.	Insertion Loss (db)	42-50	68-75	45-65	45-50	45-50
7.	Weight with Filter (oz)	5	< 8	< 8	< 8	< 8
8.	Sidelobe Supression (db)	> 25	~ 30	30-35	> 25	> 25
9.	Type of Structure	Surface Wave	Wedge	Surface Wave	Quartz Surface Wave	Sapphire
10.	Status	Shelf	5 Built	~ .5 year	95% Conf.	
11.	Price * (Small Quantity)	$1700 +		$50-100 K Devp. $5 K Quant.	~ $20K	~ $50K

*Not including driver amplifiers.

can be obtained in the near future with acceptable spurious levels. The only problem areas involve temperature variations that will limit absolute accuracy, the conversion of wideband video into digital form for further processing or retransmission to earth, and the lack of flexibility.

A second and more flexible technique involves a step frequency approximation to the FM waveform. As an example, let the transmit waveform be a contiguous transmission of N(sixteen in this example) 0.1 microsecond pulse segments. Each segment is a pulse of sine wave on a different carrier frequency spaced Δf = 10 mHz apart as shown on Fig. 2. The frequencies must all be derived by mixing or multiplying from a single coherent stable oscillator. The spectrum of this waveform is $N\Delta f$ = 160 mHz, and since they are "coherent" they can be added vectorially by adjustment of their phases after time realignment with a tapped delay line of 16 segments of 0.1 microsecond delay. To achieve low spurious levels the frequency spacing must equal the inverse of the segment duration. The compression ratio of this type of waveform is N^2 and extremely wideland signals have been generated. Since each segment may be processed through a filter having only a 10 mHz bandwidth, the transition to digital form is made simpler if multiple parallel channels are used. Analog to digital converters of 6-8 bits are currently limited to this bandwidth. Various weighting functions can be used to control the time sidelobes resulting from the transmission of a rectangular spectrum. The primary disadvantage is the relative complexity of this multi-channel approach probably resulting in several times the hardware of the dispersive line system.

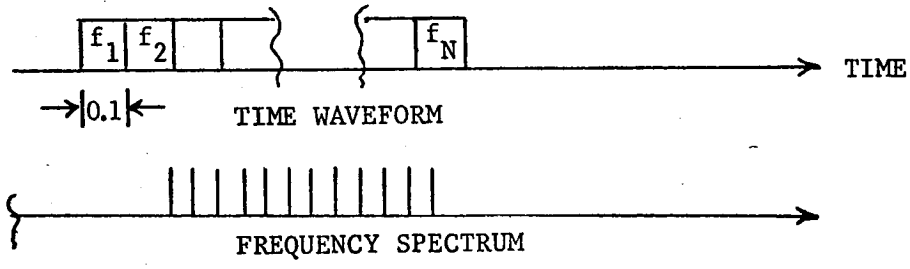

FIG. 2 STEP FREQUENCY PULSE COMPRESSION

A third technique with more flexibility than the single dispersive line, but less complexity than the step frequency approximation, was developed by Airborne Instrument Laboratory, and called STRETCH. It is recently been declassified and is described in Ref. [3]. The basic elements are the same as the linear FM system on Fig. 1 except that the slope of the frequency-vs-time characteristic is made different between transmission and reception yielding either a time expansion (bandwidth reduction) of a portion of the received waveform or a time compression. Time expansion is more appropriate to the study of sea surface topography.

Referring to the previous example of a 1-2 microsecond (T) pulse envelope and a 150 mHz bandwidth (B), information theory shows that 2BT or 300 to 600 samples of information describes the received signal. Since 2 mircroseconds of echo describe 300 meters (ΔR) of altitude ($\Delta R = c\tau/2$) and after acquisition wave heights are rarely over $\pm$ 15 meters, we can afford to throw away all the information greater than 15 meters from the "mean" sea surface altitude and "stretch" the echoes in that vicinity by a factor of about 10. The output signal bandwidth would be reduced to 15 mHz, detected, and analog-to-digital converters used to store the information for further processing and later transmission to ground stations on a narrow band communication link.

A fourth technique is the use of binary phase coded waveforms. Unfortunately the best codes are limited to a length of 13 (pulse compression ratio) and low relative sidelobe level codes are not available again until the code length exceeds about 256. Broadband analog processing is not practical much beyond the 100 mHz, 13:1 code used in SKYLAB, and broadband digital processing requires hard limiting and hence distortion of the sea surface echoes.

The choice of technique is dependent on the system requirements, allowable size, weight and cost and the nature of the recording or retransmission of the signals to earth.

Anomalies in High Resolution Sea Backscatter at Vertical Incidence

If a resolution of a few nanoseconds is employed it will become increasingly important to have a better model of the radar backscatter of the sea at vertical incidence. This section describes what I believe to be an important "second order" effect that I have not seen taken into account.

In radar altimetry from satellites and aircraft, the statistics of the radar sea return at vertical incidence affect the quality of the altitude data and the surface conditions inferred from this data. The parameter of interest is σ_o, which is usually defined as the mean backscatter cross section per unit illuminated area of a reflecting surface.

Since the reflectivity is highest for a specular surface at perpendicular incidence σ_o is greatest for a calm sea, and is predicted to be as high as + 25 db. For very rough seas, the ocean surface consists of numerous scatterers, and the value of σ_o drops to near 0 db. The trend of data taken near grazing incidence would be expected to follow the general curves of Fig. 3. However, this has not been the general case. There have been numerous measurements at vertical incidence by NRL, Sandia, Ohio State and others which show 5-10 db variations from each other as well as from the predictions. Only a portion of these variations can be explained by calibration errors, broad beamwidths, various definitions, etc.

This note suggests that there may be another factor that has been overlooked. I am questioning the symmetry of σ_o near the vertical in the upwind-downwind direction. Schooley [3] has shown that the distribution of slopes of wind driven waves is not symmetrical near the vertical but is centered about 4^o upwind. I have illustrated this with an idealized cross section of ocean waves on Fig. 4A and the resultant contours of constant reflectivity from a Satellite on Fig. 4B. Figs. 5A, B, show that the larger facets tend to peak somewhat in this direction. As a result,

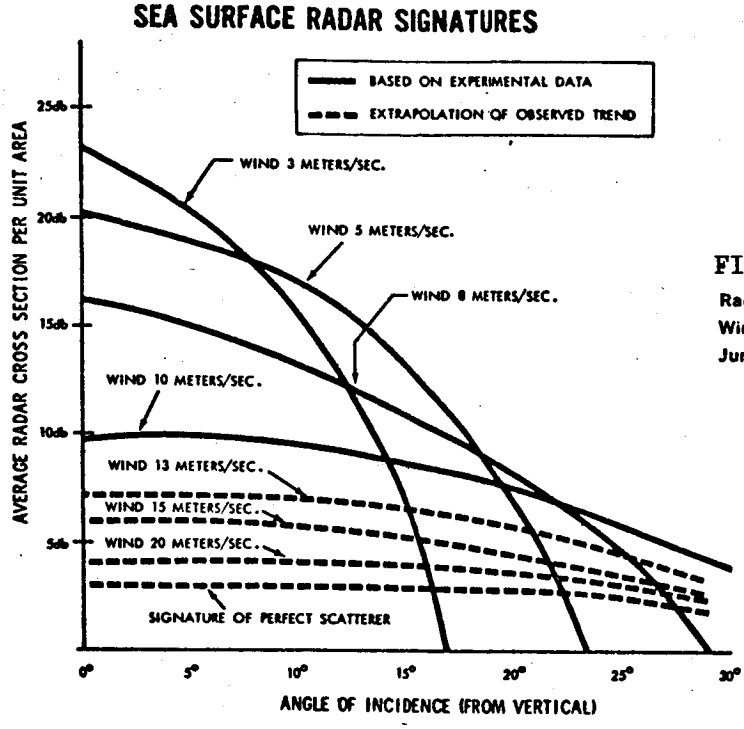

FIG. 3

Radar Reflectivity for Sea Conditions at Various Wind Speeds as a Function of Incidence Angle; June 1967, Pierson, New York University

I would predict that the peak value of σ_o might occur as much as 4^o from the vertical. The implications are;

1. In radar altimetry, with short or compressed pulses, it is assumed that σ_o is symmetrical about the vertical and hence the radar return vs time (altitude) consists of a linear rise plus a flat top portion. The true altitude is found by an interpolation method based on this assumption. Assymetry may cause a small error in the absolute accuracy.

2. In satellite work, the local vertical is sometimes derived by looking for the peak backscatter angle as the beam is scanned in angle near the vertical (a nadir seeker). This may not be an optimum technique.

3. Early data on σ_o at vertical incidence should be used with caution.

Before completely defining the instrumentation for a high resolution satellite altimeter I would suggest that older data should be examined to determine if this anomaly has been observed and further information can be extracted. Also, any bridge or satellite-borne altimeter experiments should be performed with careful calibration of incidence angle.

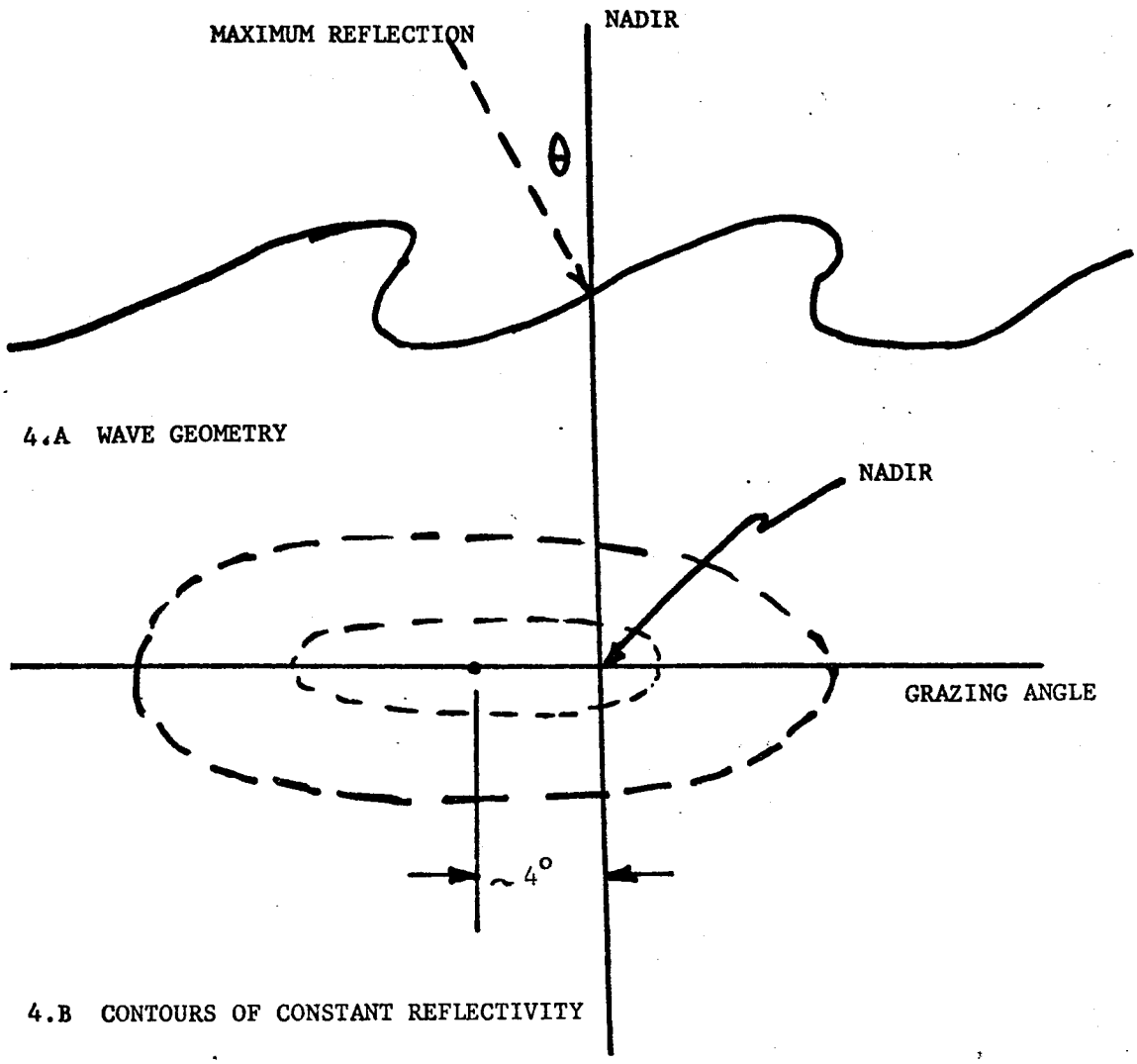

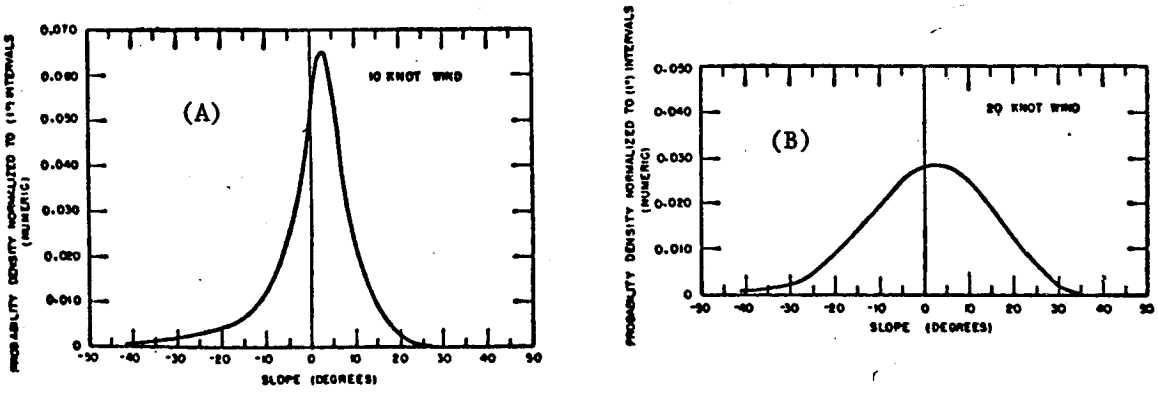

FIG. 5 SLOPE PROBABILITIES FOR 10 AND 20-KNOT WINDS [3]

References

[1] Nathanson, F. E., Radar Design Principles, McGraw-Hill Book Company, New York, October 1969.

[2] Caputi, Jr., William J., "Stretch: A Time-Transformation Technique," IEEE Trans., AES, Vol. AES-7, No. 2, March 1971, pp 269-278.

[3] Schooley, A. H., "Upwind-Downwind Ratio of Radar Return Calculated from Facet Size Statistics of a Wind-Disturbed Water Surface," Proceedings of the IRE, April 1972, pp 455-461.

ALTITUDE ERRORS ARISING FROM ANTENNA/SATELLITE ATTITUDE ERRORS - RECOGNITION AND REDUCTION

21

N73-15390

Tom Godbey, Ron Lambert, Gary Milano
General Electric Co., Aerospace Electronic Systems Department
Utica, New York

The goals of satellite altimetry are to achieve a standard deviation accuracy of less than $\pm$ 1 meter (for Geodesy) and $\pm$ 0.1 meter (for Physical Oceanography) when operated over ocean.

Recognition and reduction to a minimum of every possible source of error is mandatory if these goals are to be reached.

Antenna/Satellite altitude errors can generate significant bias errors on altitude measurements. Whether precise antenna pointing (or equivalently) satellite attitude control is required to reduce the residual (unknown) bias errors depends on the altimeter design implemented.

Specifically, our analysis shows that of the three basic types of Pulsed Radar Altimeter design:

The "Pulse Width Limited Altimeter" design results in negligible residual altitude bias error, $e_h(\phi_E)$, if the antenna 3 db beam width $\theta_A \geq 5\phi_{MAX}$ and $\theta_A \geq 10\theta_T$, where ϕ_{MAX} = Satellite Maximum Attitude Error with respect to Nadir and $\theta_T = 2\sqrt{\frac{cT}{h}}$ = the pulse beamwidth (i.e. the angle subtended by the area illuminated by the pulse at Nadir);

E

- The "Beamwidth Limited Altimeter" design, which occurs when $\theta_A < \phi_M$, $\theta_A < \theta_T$, will require antenna pointing to an accuracy of about $\pm$ 1 milliradian to reduce the residual altitude bias error, $e_h(\phi_E)$, to an acceptable level;

- Between these extremes, the "Antenna Effects Altimeter" design, will require antenna pointing to arrive at an acceptable residual bias error, $\theta_A < \frac{4}{3}\phi_M$. If $\theta_A > \frac{4}{3}\phi_{MAX}$, then two siutably positioned samples of the average return waveform will measure the attitude error, ϕ_E , well enough to reduce the residual error, $e_h(\phi_E)$, to an acceptable level.

The two statements, "negligible residual altitude bias error" and "acceptable residual altitude bias error" are certainly not quantitative, however, they do have a quantitative meaning in this paper. "Negligible residual altitude bias error" means that the residual uncertainty of this bias error is on the order of one-tenth the total specified error performance of the satellite altimeter system. "Acceptable residual altitude bias error" means that this error combined with all the other system errors still allows the satellite altimeter system to meet the specified error performance.

After a narrative and pictorial description of each of the three types of altimeter design and the source and form of the altitude bias errors arising from Antenna/Satellite attitude errors in each design type a quantitative comparison of the three systems is made in a typical satellite altimeter application.

Pulsewidth Limited Altimetry - The essential features of this type of altimeter design are shown in Figure 1. In Figure 1a, a side view of the pulse altimeter geometry is shown. Note that the antenna 3 db beamwidth, θ_A, is larger than the maximum satellite attitude error ϕ MAX. Also note that θ_A is much larger than the pulse beamwidth, θ_T. Note that the pulse beamwidth, θ_T, is defined as the angle subtended by the radar area illuminated at Nadir, N, by the transmitted pulse of duration T. The pulse beamwidth is thus:

1) $$\theta_T \equiv 2\sqrt{\frac{cT}{h}} \quad \text{radians}$$

where T = pulse duration in seconds

C = speed of light

h = altitude

Figure 1b shows a plan view of the radar area illuminated at time T as a circular spot with radius r(T).

2) $$A(T)=\Pi r^2(T)$$

and from geometry with $h>>\frac{cT}{2}$;

3) $$r^2(T)=cTh$$

Also shown in Figure 1b is the radar area illuminated at a time NT after the first return from Nadir as a thin ring with an effective radius of,

4) $$r_E(NT)=\frac{1}{2}\left[r(NT)+r\left[(N-1)T\right]\right]$$

and a thickness of,

5) $$\Delta r(NT)=r(NT)-r\left[(N-1)T\right].$$

The radar area illuminated at time NT is,

6) $$A(NT)=2\Pi r_E(NT)\Delta r(NT).$$

Equation 6) reduces to,

7) $$A(NT)=\Pi cTh\left[1+\left(\frac{2N-1}{2}\right)\frac{cT}{2}\right].$$

The range R(NT) from the altimeter to the ring illuminated at NT has increased from the altitude, h, to an effective range of,

8) $$R_E(NT)=h+\left(\frac{2N-1}{2}\right)\frac{cT}{2}$$

And, since the average power returned to the altimeter at NT is directly proportional to the radar illuminated area and inversely proportional to the fourth power of the range to the illuminated area, the average power returned at NT is:

9) $$\overline{P_R(NT)}=\left[\frac{P_T\ G^2(\phi)\lambda^2\sigma^2(\phi)}{(4\Pi)^3}\right]\frac{A(NT)}{R_E^4(NT)}$$

Where P_T = Transmitted Power

$G(\phi)$ = Antenna Gain Vs. Angle From Antenna Boresight

λ = Transmitted Wavelength

$\sigma^0(\phi)$ = Average Radar Backscattering Cross-section Vs. Incidence Angle of the Illuminated Surface.

Carrying out the indicated operations on Area and Range, equation 9) reduces to:

10) $$\overline{P_R(NT)}=\left[\frac{P_TG^2(\phi)\lambda^2\sigma^0(\phi)}{(4\Pi)^3}\right]\frac{\Pi cT}{h^3}\left[1-3\left(\frac{2N-1}{2}\right)\frac{cT}{2h}\right]$$

The solid curve of Figure 1c shows the waveform of the power return with no antenna/attitude error. The ramp rises from zero to maximum at time T and decays according to equation 10 after time T. The effect of the off center antenna gain due to a small error, ϕ_E, on this average waveform is to decrease the peak, at T, and to decrease the rate of trailing edge fall off slightly. This is shown by the dashed line trailing edge where the peak value has been normalized so the trailing edge effect will stand out.

Because the Satellite Altimeter over ocean is expected to measure altitude to the instantaneous mean sea level averaged over the illuminated area A(T) then optimum tracking should be insensitive to variations in surface roughness.

Figure 1d shows the dispersive effect of sea state on the rising portion of the radar return. The solid line curve shows the waveform expected from a gaussian distribution of radar backscattering area about mean sea level with a standard deviation σ_z. The significant wave height $\overline{H}_{1/3} = 4\,\sigma_z$, so a sea state with $H_{1/3} = 4/3$ CT would give radar return starting at about t = -T and display the form of a probability distribution function until the pulse trailing edge has penetrated to $3\sigma_z$ below the mean sea level which occurs at t = 2T. The dashed line of Figure 1d shows the return from ocean with significant wave heights of approximately CT/100. Note that the rising portion of both returns is symetrical about the time point t = T/2 so that a split gate energy tracker which balanced the average energy seen in the early

gate, E, with one half the average energy seen in a later gate, L, will position the early gate to start at t = 0 and end at t = T for any sea state so long as the separation between gates is large enough to not see dispersion effects. The position and separation of the gates for such a tracker are shown above the waveform of Figure 1d. The idea of time separated tracking gates to give mean sea level tracking independent of sea state was first advanced by George Bush of Applied Physics Laboratory/John Hopkins University. We are indebted to him and to Professor Willard Pierson of New York University who has showed that of a number of possible tracking laws modeled, this one is the least sensitive to expected sea states and departures of the surface distribution from gaussian.

With the split gate energy tracker of Figure 1d, the altitude error arising from Antenna/Satellite attitude error has the form shown in Figure 1e. Note that with $\phi_E = 0$ there will be a slight negative error proportional to the pulse width and the ratio of antenna beam width to pulse beamwidth. If the antenna were always pointed exactly at Nadir, the bias error would constant at:

$$\varepsilon_h(\phi_E=0) = -k_o\left(\frac{\theta_T}{\theta_A}\right)\frac{cT}{2} \quad . \tag{11}$$

Bias error reduction would simply consist of adding this precomputed (or measured) error to all altitude reading which would result in a residual altitude bias error, $e_h(\phi_E)$, equal to zero. If the Antenna/Satellite attitude maximum error, ϕ_M, is small compared to θ_A, as shown in Figure 1e, then the bias error at $\phi_E=\phi_M$

change is small. The form of the error function, $\varepsilon_h(\phi_E)$, is:

$$\varepsilon_h(\phi_E) \doteq \left[\left(\frac{\phi_E}{\theta_A}\right)^2 - k_o\right] \frac{cT}{2} \left(\frac{\theta_T}{\theta_A}\right) * \quad . \tag{12}$$

Optimum error reduction in this case might consist of simply adding the average of the errors at $\phi_E = 0$ and $\phi_E = \phi_{MAX}$ which limits the residual bias uncertainty to:

$$|e_h(\phi_E)| \leq \frac{1}{2}\left(\varepsilon_h(\phi_M) - \varepsilon_h(o)\right) \tag{13}$$

with the probability density between these limits dependent on the probability distribution of ϕ_E.

Figure 1f shows essentially the limits of altitude tracking error as a function of sea state for the split gate tracker of Fig. 1d. If the distribution of area above and below mean sea level is symmetrical and if the average radar backscattering cross-section is the same for every unit of area, then there will be zero error from sea state. If the distribution of area is not symmetrical and/or if the area below mean sea level (troughs) gives a larger radar return on the average than the area above mean sea level (crests) this would generate a positive error increasing as a function of wave height.

*We use ko = 0.225 which was obtained from an "empirical" fit to many computer solutions for tracking error versus attitude error with Altitude, Antenna beamwidth and pulsewidth varied over a wide range.

If the converse (E/M crests > troughs) were true the error would be negative proportional to wave height. To get a feeling for the magnitude and form of tracking error arising from E/M troughs > crests, a linearly weighted backscattering with crests giving 0.75 σ^o_{MSL} and troughs giving 1.25 σ^o_{MSL}. This operation has the effect of shifting the Radar Altimeter observed Mean Sea Level to $e_h(H_{1/3})$ below the Geometric Mean Sea Level. The approximate equation for $\varepsilon_h(H_{1/3})$ obtained from analysis of the altimeter tracking error vs. sea state buildup is:

$$\varepsilon_h(H_{1/3}) \doteq 0.025\sqrt{\frac{H_{1/3}}{cT}}\left[\frac{cT}{2}\right] \quad \text{METERS} \tag{14}$$

If the significant wave height can be hind cast to ±20%, then reduction of this error source to a residual sea state bias error, $e_h(H_{1/3})$, would give a final uncertainty of:

$$e_h(H_{1/3}) = \frac{\partial\left[\varepsilon_h(H_{1/3})\right]}{\partial H_{1/3}} \times \left[\pm 0.2 H_{1/3}\right] = 0.125\sqrt{cTH_{1/3}} \text{ CM.} \tag{15}$$

Solution of 15 for CT = 30 meters, $H_{1/3}$ = 30 meters gives a residual error of $\varepsilon_h(H_{1/3}) = 3.75$ cm.

Ben Yaplee's experimental data on the differential radar backscattering cross-section versus surface depth indicates a linear increase in σ^o from crests to troughs.

Lee Miller's* analysis of Yaplee's data gives the following equation for the variation of radar cross-section about MSL:

*Second Quarterly Report on Contract No. NAS6-1952, Research Triangle Institute North Carolina; L. S. Miller.

(16) $$\sigma^0(z) = \sigma^0(z=o)\left[1 - m\frac{z}{o_z}\right]$$

Where the value of m lies between:

m = 0.141 for 20 knot winds

and

m = 0.185 for calm seas.

Assuming that these are essentially correct, the residual bias error on altitude due to sea state, $e_h(H_{1/3})$, given either 20% $H_{1/3}$ measurements or hind casts will be no greater than $\pm$ 5 cm, with a standard deviation of about $\pm$2 cm, which would probably be an acceptable part of the error budget for even a $\pm$ 10 cm satellite radar altimeter.

Beamwidth Limited Altimetry - Figure 2, shows the significant features of Beamwidth Limited Satellite altimetry. In comparing Figures 2a & 2b with Figures 1a & 1b, note that the antenna beamwidth, θ_A, is less than the maximum satellite attitude error ϕ_M and much less than the pulse beamwidth, θ_T, and therefore the total area illuminated at Nadir is reduced to only that area subtended by θ_A. This is the defining feature of beamwidth limited altimetry. Note also in Figure 2b that even at fairly small angles off Nadir the portion of the expanding ring area does not completely fill the area subtended by θ_A. This fact will cause a decrease in the peak amplitude of the return off Nadir compared to that at Nadir and also a time dispersion (i.e. a widening) of the return pulses as shown in Figure 2c.

This return pulse widening off Nadir could easily be confused with the expected time dispersion due to increasing wave heights (Figure 2d) which has been proposed as an absolutely foolproof method of measuring sea state directly. Figures 2c and d show that for both Altimetry and Sea State measurement by return pulse time dispersion, it would be necessary to point the antenna very accurately toward Nadir in the beamwidth limited type of altimeter.

Selection of a tracking law for beamwidth limited altimetry is illustrated in Figure 2d. The average return waveshape will be an almost symmetrical pulse with a width equal to the transmitted pulse T for low sea states and a larger width for higher sea states. The tracking law selected is shown above the return waveform as an adjacent split gate energy tracker. The slight assymmetry arises from the fast rise from zero, asymtotic approach to maximum value of the leading edge with just the opposite occurring on the trailing edge. This causes a constant tracking bias error whose magnitude is a function of how beamwidth limited the design actually is, (i.e. on the ratio θ_A/θ_T). An approximate equation for this bias is:

$$\varepsilon_h(\phi_E=o) \doteq 0.31 \frac{cT}{2}\left(\frac{\theta_A}{\theta_T}\right)^2 \quad \text{METERS} \tag{17}$$

The Altitude Tracking Error arising from Antenna/Satellite attitude error for beamwidth limited altimetry is shown in Figure 2e. Note that because the return is centered about the area illuminated at the error angle, the tracked range to that return will increase directly with altitude, h, and directly with the square of the error angle, ϕ_E.

The equation for tracking error versus pointing error is thus:

(18) $$\varepsilon_h(\phi_E) = {}_h(\phi_E=o)+\frac{1}{2}h\phi_E{}^2$$

To further illustrate the absolute requirement for accurate antenna pointing in beamwidth limited altimetry (or laser altimetry) put a typical value of h = 1000 KM for satellite altitude and an exceptional satellite attitude control capability of ± 15 arc minutes 3σ with respect to local vertical into equation 18. The tracking error is bounded at ± 20 meters! With this type of altimetry, perhaps the only answer is to point the antenna as nearly as possible to the vertical, set up an oscillation about this direction and take the nearest altitudes observed as the best actual altitude to mean sea level.

The tracking error versus sea state of beamwidth limited altimetry has essentially the same form as that for pulse width limited altimetry as shown in Figure 2f and for the same reasons. That is, if the radar sea surface is symmetrical about mean sea level there will be zero altitude error versus wave height but if troughs give back more average radar return than crests (as seems likely) then the time error tracked will be in the positive direction and proportional to some function of the ratio of significant wave height to the radar pulse length, This is reasonable because the percentage distortion due to sea state will be less for long radar pulse lengths, CT, than for short ones. To translate altitude time errors into altitude errors, use the factor CT/2 (the basic pulse radar range resolution capability) to arrive at

an equation for tracking error versus sea state of the form:

$$\varepsilon_h(H_{1/3}) = k\frac{cT}{2}\left(\frac{H_{1/3}}{cT}\right)^A \tag{19}$$

where the exponent A is probably a fraction between 1/4 and 1/2.

As in the case of pulsewidth limited altimetry, a 20% accurate $H_{1/3}$ by hind cast or measurement will probably suffice to reduce the residual uncertainty due to sea state, $e_h(H_{1/3})$ to less than ± 5 cm with a standard deviation less than ± 2 cm.

Antenna Effects Radar Altimetry - As shown in Figure 3, antenna effects altimetry includes the design options which lie between strictly pulsewidth limited and strictly beamwidth limited altimetry designs. As shown in Figure 3a, the antenna beamwidth θ_A is on the order of the maximum satellite attitude error, ϕ_M, and the pulse beamwidth, θ_T, however, a point can be made here:

- If $\phi_M \leq \frac{5}{8}\theta_A$, then antenna pointing will not be required to achieve acceptable residual altitude bias errors arising from antenna/satellite attitude errors because these errors can be measured directly from suitable sampling of the radar return waveform.

Figure 3b illustrates how this extreme sensitivity of the return waveshape with respect to pointing error, ϕ_E, comes about.

Note that when the antenna is pointed directly at Nadir, $\phi_E = 0$, the area illuminated from $0 \leq t \leq T$ is centered on the gain center of the antenna. Because the increasing area is weighted by decreasing antenna gain, the linear buildup of area will result in a return leading edge resembling an RC step response until t = T, as shown in Figure 3c - solid curve.

Also note that after reaching a peak at t = T, the return falls off in an RC time constant fashion.

Now refer back to Figure 3b and the effective antenna contour when $\phi_E = \theta_A/2$. Note that the portion of the increasing area illuminated from $0 \leq t \leq T$ is less than 1/2 contained within the effective beamwidth and that less than 1/2 A(T) which is contained is illuminated with about 2 db less than boresite antenna gain. This results in a return rise time resembling an RC response to a ramp input until t + T. Note in Figure 3c (the dashed curve) that the amplitude of the return at t = T, when $\phi_E = 1/2\ \theta_A$, is about 1/4 the amplitude reached @ t = T for $\phi_E = 0$. Also note that for t > T the return is almost flat so that the average return waveform for $\phi_E = \theta_A/2$ resembles the average return waveform for strictly pulsewidth limited altimetry; thus, the split gate energy tracker shown in Figure 3d which would track with almost zero error for a pulsewidth limited antenna design will also track with near zero error at $\phi_E = \theta_A/2$ in the antenna effects altimeter design, (see the error curve of Figure 3e).

In Figure 3e, note that the error curve is negative for pointing errors between $\phi_E = 0$ and ϕ_E just less than $\theta_A/2$. At and beyond $\phi_E = \theta_A/2$ the tracking error is positive and growing exponentially. An approximate equation for altitude error vs. antenna/satellite attitude error is:

$$\varepsilon_h(\phi_E) \doteq \left[\left(\frac{\phi_E}{\theta_A}\right)^2 - 0.225\right] \frac{cT}{2}\left(\frac{\theta_T}{\theta_A}\right) \quad \text{METERS} \tag{20}$$

One feature of the action of the split gate energy tracker shown here is that as ϕ_E approaches θ_A the tracker cannot acquire or track the radar returns. This is simply because this tracker requires an initial rapid rise on the order of T or it cannot find a balance point. It is this feature which minimizes the attitude error generated tracking error when compared to the strictly beamwidth limited altimeter design and it also serves as an indicator that $\phi_M < \theta_A$ if an altimeter with this tracking rule does acquire and track.*

*Note - The Skylab Altimeter falls in the category of an antenna effects altimeter design with $\theta_A \doteq 1.4^o$, θ_T (T = 100Nsec) $\doteq 0.95^o$ and ϕ_M which initially may be as high as $\pm 2^o$. This is the reason an initial antenna alignment mode is included in the altimeter experiment. This initial on-orbit antenna alignment consists of a "spiral scan" which settles into a square about the point where the peak of the radar return is maximized then is shut off because, once found, the satellite attitude control will maintain this pointing direction within the requirements of the immediately following altimeter experiment(s).

Dispersion due to increased wave heights for antenna effects altimetry, (see Figure 3d & f) would not be symmetrical in time about $t = T/2$ even with an E/M ocean symmetrical about the mean sea level. We have not yet found the error curves for sea state for any particular antenna effects altimeter design but it would not be surprising if it had the form of the curve shown in Figure 3f which shows an increasingly negative altitude error as sea state builds up to $H_{1/3}=\frac{4}{3}cT$.

This is pointed out as a problem area because if the form and magnitude of the error curve for a symmetrical E/M ocean were just right, then (as shown in Figure 3f), the error curve for the expected asymmetrical E/M ocean could lie on zero. We don't want any such thing to happen by dumb luck although it would be perfect if it could be made to happen by design based on knowing what we were doing. At any rate, with proper care in our experiments, we will one day know what the altitude error vs. sea state should be for any altimeter design and the process of reducing that error to an acceptable level will depend on hind cast and/or measured sea state as discussed before.

Comparison of the three types of Altimeter Systems in a typical satellite application is shown in Figures 4 and 5. Each T = 100 Nsec altimeter system is assumed to operate in a manner which allows 5000 independent returns per second to be tracked. Under this assumption, the standard deviation jitter error, σ_h , of altitude readouts averaged over one second will be approximately ± 22 cm for both the "Pulse Width Limited" and the "Antenna Effects" Altimeters, but will only be about ± 2 cm for the "Beamwidth Limited" design.

F

This difference of 10/1 in jitter error performance comes about entirely from the fact that the returns seen by the beamwidth limited adjacent split gate tracker are almost unity correlated in each gate even though the amplitude distribution of the returns is Rayleigh (or Exponential) distributed depending on whether envelope (or Square Law) detection is employed. Compare this to the split gate energy tracker of the "Pulsewidth" and "Antenna Effects" altimeters where there is essentially complete decorrelation of the returns between the "early" and the "late" gates.

In this comparison, we are looking at altimeter designs which would be satisfactory for a Satellite Altimeter System whose goal was to achieve an overall one sigma accuracy of 50 cm on the position of mean sea level over the Geoid.

A reasonable choice of orbit parameters is given in Figure 4a as a nearly circular, 825 kilometer,nearly polar orbit.

Given a satellite attitude control capability of one degree about the vertical Figure 4b shows the altitude error range expected for the "Pulsewidth Limited" altimeter design to be from -23.5 cm at ϕ_E = 0 to -22.5 cm @ $\phi_E = 1^o$. The residual uncertainty, $e_h(\phi_E)$, obtained from merely assuming -23 cm error regardless of ϕ_E actual is contained within ± 0.5 cm, which is a negligible part of a system with a ± 50 cm one sigma error budget as stated in Figure 5a.

The altitude error due to satellite attitude error, $\varepsilon_h(\phi_E)$, for the "Antenna Effects" altimeter of Figure 4c is (from equation 20) minus about 1.2 meters @ $\phi_E = 0$ and goes to plus about 0.2 meters @ $\phi_E = 1^o$. Error reduction to an uncertainty of about ± 20 cm maximum residual uncertainty can be done (as shown in Figure 5b) by obtaining a measure of the error angle ϕ_E from the difference, Δ, between the averaged sample voltages V_1 and V_2 taken at the sample times S_1 and S_2. This level of maximum residual bias uncertainty is almost negligible in a ± 50 cm one sigma system error budget.

Figure 4d shows the error for a (reasonable?) "Beamwidth Limited" Altimeter design as going from positive 0.825 Meters at $\phi_E = 0$ to positive 126 meters at $\phi_E = 1^o$. This shows the absolute necessity for antenna pointing control to as close as possible to the Nadir.

Figure 5c shows the error reduction possible if the antenna can be pointed and maintained within 10% of its beamwidth with respect to Nadir. In this case, the residual uncertainty due to $\phi_A \leq \theta_A/10$ is:

$$e_h(\phi_A) \leq \pm 11.5 \text{ CM.}$$

As stated earlier, this might be done by a hill climb routine which continuously searched for minimum tracked altitude. The altitude record would look like a cycloid and with proper processing might yield acceptable altitude best estimates.

A more certain method of pointing control is by "Time Difference Monopulse".* The geometry and timing of this system is shown in Figure 5c. The system can consist of a four hour monopulse feed which creates one sum beam, Σ , and four difference beams $\Delta_1, \Delta_2, \Delta_3, \& \Delta_4$ separated in foresite by $1/2\ \theta_\Sigma$ as shown. The returns thru each beam are individually centroid tracked. When the tracked Δ beam returns all lag the tracked Σ beam return equally in time the Σ beam is pointed at Nadir. If a pointing error exists, the direction and amount of the error in the Δ_1-Δ_2 plane is measured by the difference in tracked return time, $t\Delta_1 - t\Delta_2 = k\phi_{1-2}$, and by steering to null this difference the error is corrected out. The same is true for an error developed in the Δ_3-Δ_4 direction.

Maximum reduction of residual error could be obtained post flight if the differences $k\phi_{1-2}$ & $k\phi_{3-4}$ were included with each altitude report.

* Invention of Dr. Kiyo Tomiyasu, General Electric Co., Satellite System Operation, King of Prussia and Tom Godbey.

Conclusions - Prior presentations and papers on Satellite Altimetry presented either the Pulsewidth Limited or the Beamwidth Limited altimeter designs, the former as presenting "no problem" with reasonable satellite attitude control, the latter as having only two problems - that of satellite attitude measurement and control and that of maintaining boresite of the large antenna with respect to the satellite. The claims for Pulsewidth Limited Altimetry have been verified. The problems of Beamwidth Limited Altimetry probably can't be solved with Satellite Attitude Control, but appear soluable with antenna pointing in which the radar seeks and maintains Nadir.

The satellite altimeter systems presently being built and/or being conceived are of the Antenna Effects type which do have a Satellite Attitude Control problem.

It is hoped that this review and examination of the basic altimeter design choices available will stimulate and challenge satellite altimeter system designers to re-examine the "practical limitations of satellites." These mundane matters are forcing us into Antenna Effects Altimetry designs.

Is the added complexity compared to Pulsewidth Limited Altimetry justified? Should we go all the way to the sophistication and complexity of Beamwidth Limited Altimetry and what would be the added capability of this type of design?

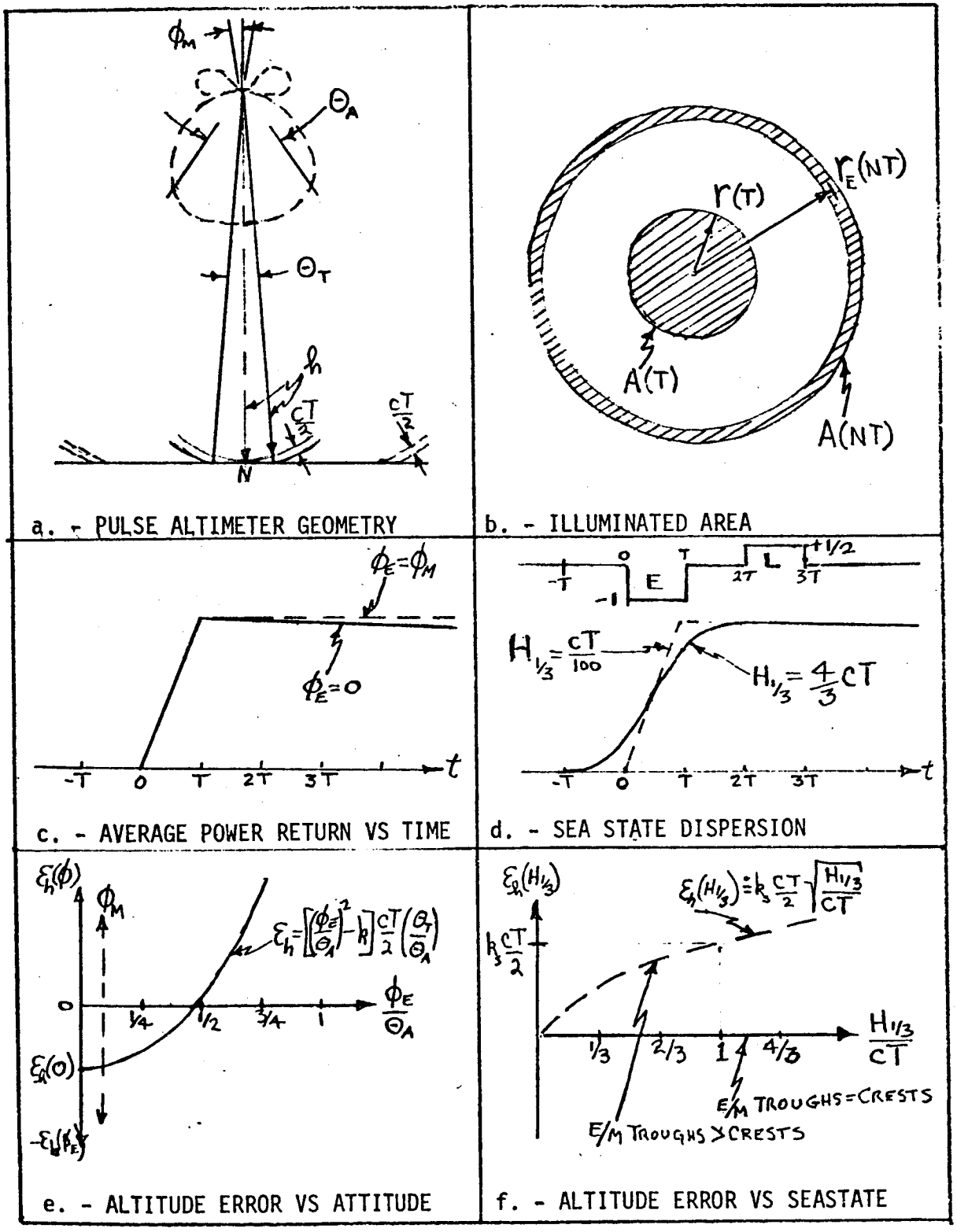

FIGURE 1. - PULSEWIDTH LIMITED SATELLITE RADAR ALTIMETRY.

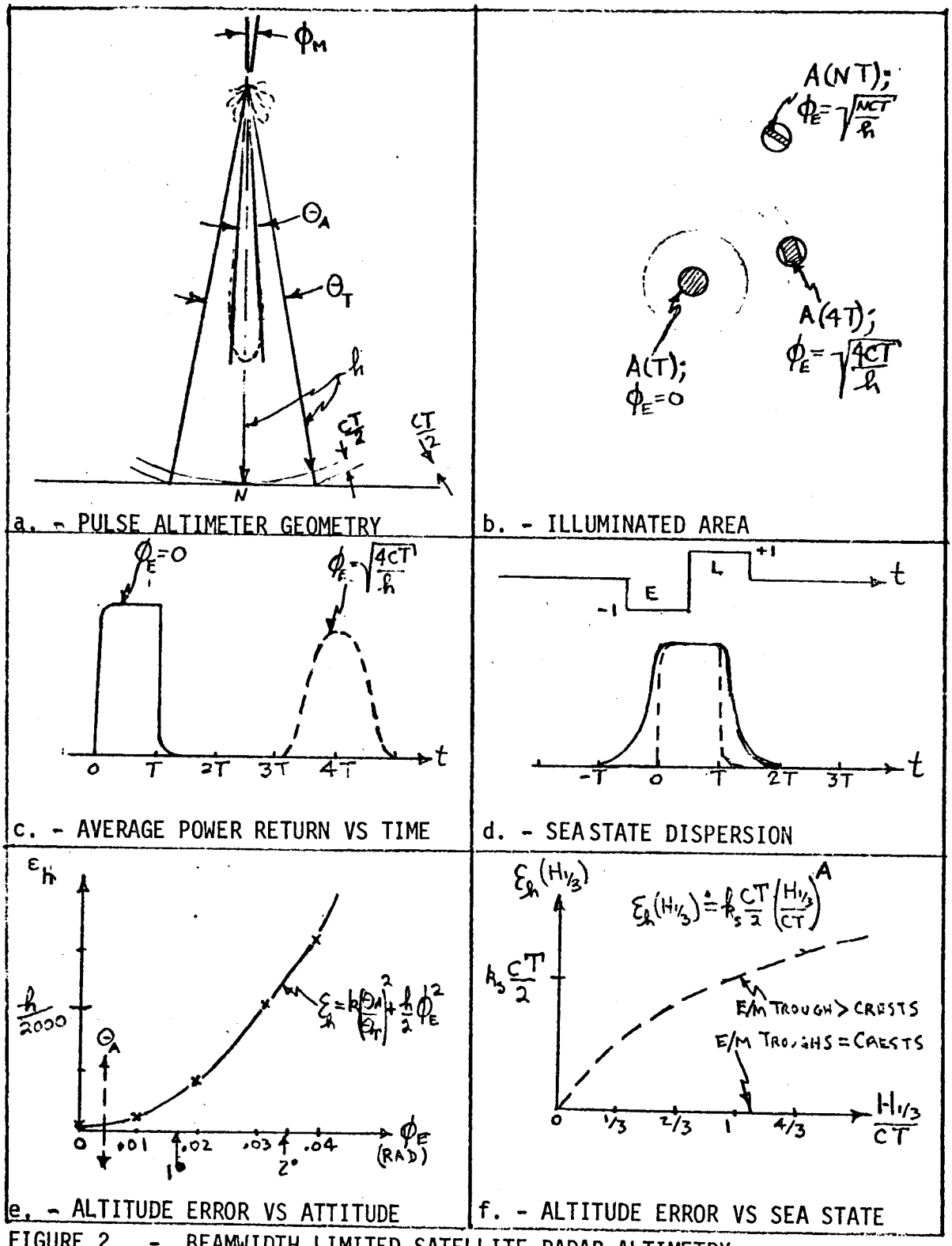

FIGURE 2. - BEAMWIDTH LIMITED SATELLITE RADAR ALTIMETRY.

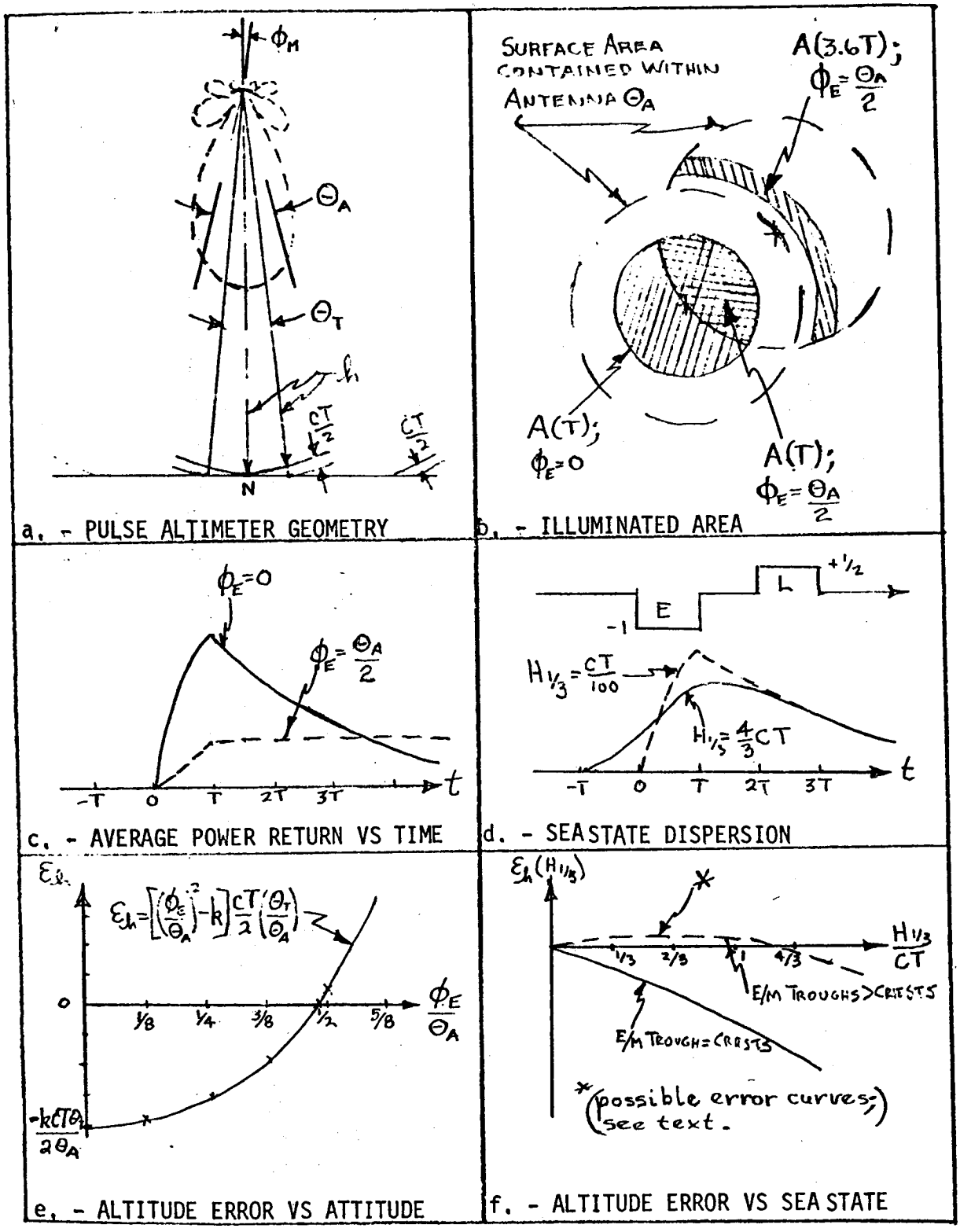

FIGURE 3. - ANTENNA EFFECTS SATELLITE RADAR ALTIMETRY.

ALTITUDE = 825 ± 50 KILOMETERS

INCLINATION - NEAR POLAR ORBIT

MAXIMUM ATTITUDE ERROR ABOUT NADIR = 1^0

a. SATELLITE PARAMETERS.

DESIGN PARAMETERS	ERROR EQUATION	ERROR PLOT
FREQUENCY - 1.4GHz $D_A = 1.25$ METERS $\Theta_A = 10°$ $\Theta_T = \sqrt{\frac{cT}{h}} \doteq 0.69°$ $T = 100$ NSec $P_T \doteq 12$ KW	$\varepsilon_h = \left[\left(\frac{\phi_E}{\Theta_A}\right)^2 - .225\right]\frac{cT}{2}\left(\frac{\Theta_T}{\Theta_A}\right)$	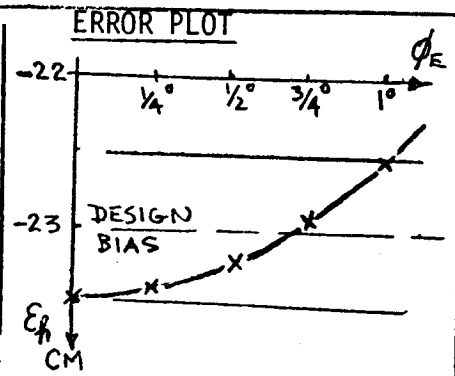

b. PULSEWIDTH LIMITED ALTIMETER.

DESIGN PARAMETERS	ERROR EQUATION	ERROR PLOT
FREQUENCY - 7GHz $D_A = 1.25$ METERS $\Theta_A = 2°$ $\Theta_T \doteq 0.69°$ $T = 100$ NSec $P_T \doteq 2$ KW	$\varepsilon_h = \left[\left(\frac{\phi_E}{\Theta_A}\right)^2 - .225\right]\frac{cT}{2}\left(\frac{\Theta_T}{\Theta_A}\right)$	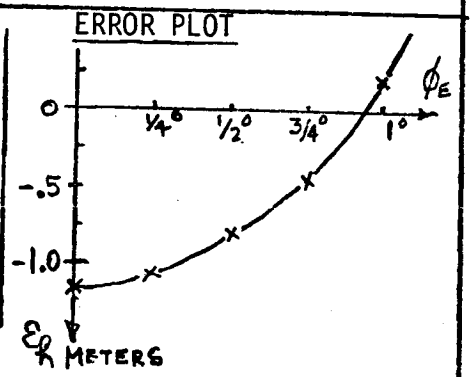

c. ANTENNA EFFECTS ALTIMETER

DESIGN PARAMETERS	ERROR EQUATION	ERROR PLOT
FREQUENCY - 14GHz $D_A = 4.15$ METERS $\Theta_A = 0.3°$ $\Theta_T \doteq 0.69°$ $T = 100$ NSec $P_T \doteq 10$ WATTS	$\varepsilon_h = .825 + \frac{h}{2}\phi_E^2$	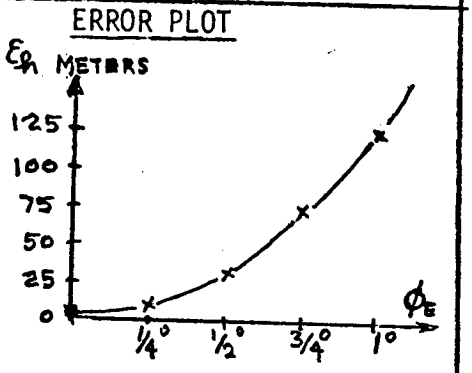

d. BEAMWIDTH LIMITED ALTIMETER

FIGURE 4. QUANTITATIVE COMPARISON OF ALTIMETER DESIGNS.

HOW - SUBTRACT-23CM DESIGN BIAS
RESULT - $e_h(\phi_E) \leq \pm 0.5$CM
JITTER ERROR, $\sigma_h \leq \pm 22$CM
ANTENNA STEERING NOT REQUIRED

a. - PULSEWIDTH LIMITED ALTIMETER - REDUCTION BY DESIGN

HOW - SAMPLE RETURN WAVEFORM AT OPTIMUM SELECTED POINTS S_1 and S_2. OBTAIN $=\bar{V}_1-\bar{V}_2$. FIND ϕ_E FROM $\phi_E=f(\Delta)$. REDUCE $\varepsilon_h(\phi_E)$ TO $e_h(\phi_E)$.

RESULT - $e_h(\phi_E) \leq \pm 20$CM
JITTER ERROR, $\sigma_h \leq \pm 22$CM
ANTENNA STEERING NOT REQUIRED

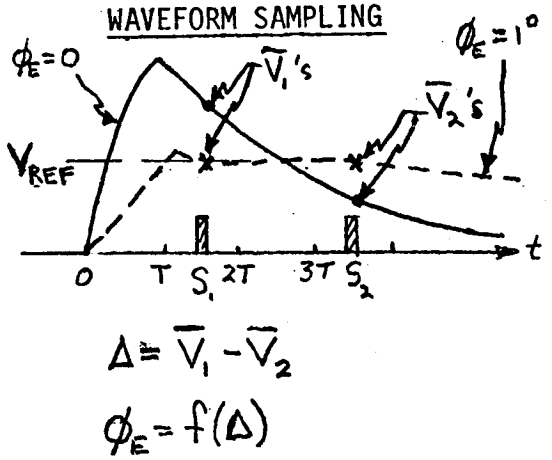

b. - ANTENNA EFFECTS ALTIMETER - REDUCTION BY WAVEFORM SAMPLING.

HOW - HILL CLIMB FOR MINIMUM TRACKED ALTITUDE OR USE "TIME DIFFERENCE MONOPULSE" AS SHOWN AT RIGHT TO MAINTAIN Σ BEAM WITHIN $\pm\theta_{A/10}=\pm.03°$ OF NADIR.

RESULT - $e_h(\phi_E) \leq \pm 11.5$CM
JITTER ERROR, $\sigma_h \leq \pm 2$CM
PRECISION ANTENNA STEERING AND KNOWLEDGE OF ϕ_E IS REQUIRED.

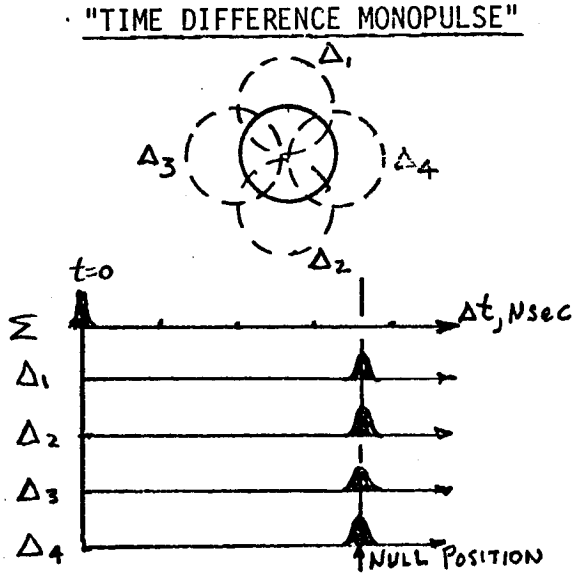

c. - BEAM WIDTH LIMITED ALTIMETER - REDUCTION BY ANTENNA STEERING.

FIGURE 5. - REDUCTION OF $\varepsilon_h(\phi_E)$ TO $e_h(\phi_E)$.

FEASIBILITY OF MICROWAVE HOLOGRAPHY FOR IMAGING THE SEA SURFACE

22

Willard Wells
Tetra Tech, Incorporated
Pasadena, California 91107

This paper considers the possibility of imaging the sea surface in three dimensions by means of microwave holography from a low-flying aircraft. This is a solution looking for a problem; perhaps it is applicable to oceanography or to the calibration of satellite-borne instruments. Others have attempted another means of imaging in three dimensions, namely stereo photography, but with only limited success. This paper is in two parts, the first of which is a brief feasibility study. The second part briefly reviews some computer experiments (published elsewhere) in which we have demonstrated the feasibility of computing three-dimensional images of objects from raw holographic data that have been recorded on magnetic tape. These experiments used synthetic data.

Let us begin by reviewing a well known two-dimensional imaging technique as a useful basis of comparison, namely side-looking radar. As shown in Figure 1, the resolution in the range direction to the side of the aircraft is achieved by range gate in the ordinary radar fashion. In the angular direction the resolution is achieved by using a long antenna aperture in the fore-and-aft direction. The scheme is necessarily side-looking because the range and angular resolution contours will fail to intersect at appropriate angles for a resolution grid in any other direction.

For high resolution the aperture length must be a great many times longer than the wavelength of the radar. The length may be either the physical length of a very long antenna, or the length may be snythesized by the forward movement of the aircraft. The latter requires that the phase of the return signal be recorded so that a data reduction procedure can add the signals in the same phase relationship as a long physical antenna. In

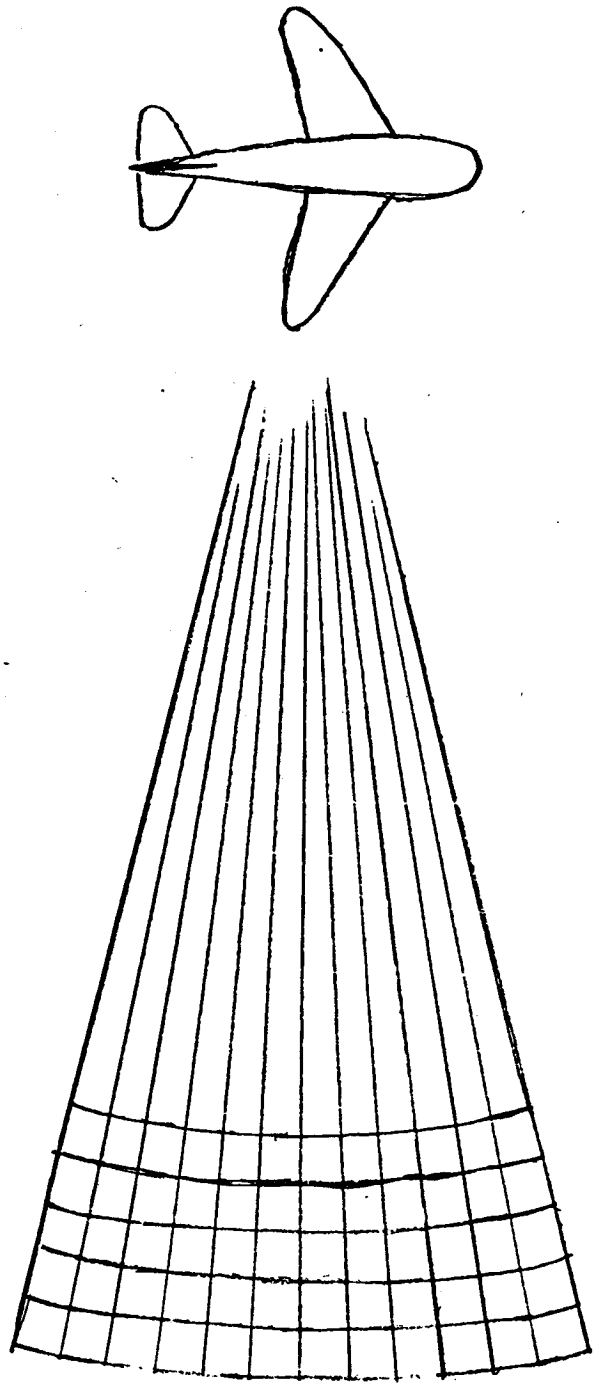

Fig. 1. Side-Looking Radar

the synthetic case, the radar beam illuminates a much wider area than the angular resolution to be achieved after data reduction. The number of resolution cells within the beam width, 12 in Figure 1, is equal to the number of signals added during aperture synthesis.

To the side-looking radar system compare the down-looking holographic system shown in Figure 2. A real lateral receiver aperture is formed by an array of simple receiving antennas beneath the aircraft. Almost certainly they would all fit in one row beneath either the fuselage or a wing, but the figure shows them staggered and situated on both the wing and fuselage to emphasize that computer data processing can introduce corrections that permit such arrangements when desired. The forward movement of the aircraft synthesizes the aperture in the fore-and-aft direction. This dimension may be only half as long as the lateral real aperture owing to the translation of the transmitter as well as the receiver. The signal from each element of the receiving array is stored on a separate track of a multi-track tape recorder. The number of elements in array determines the number of resolution cells across the swath in the final image.

Figure 3 shows typical major lobes in the antenna patterns of the receiving array, the 7 thin antenna lobes, and a single wide lobe of the transmitter illuminating the swath. If the receiving antennas were dense, e.g. dipoles spaced a half wavelength apart, or paraboloidal reflectors that are almost touching, then the receiving pattern would have only a single major lobe instead of 7 as shown. A sparce array would give the multiple grating lobes as indicated in the figure, but these lead to no spurious signals providing that the transmitting antenna pattern is narrow enough to illuminate only one of these as shown in the figure. This provision translates into a physical requirement that the transmitting aperture be at least as large as the spacing of the receiving elements.

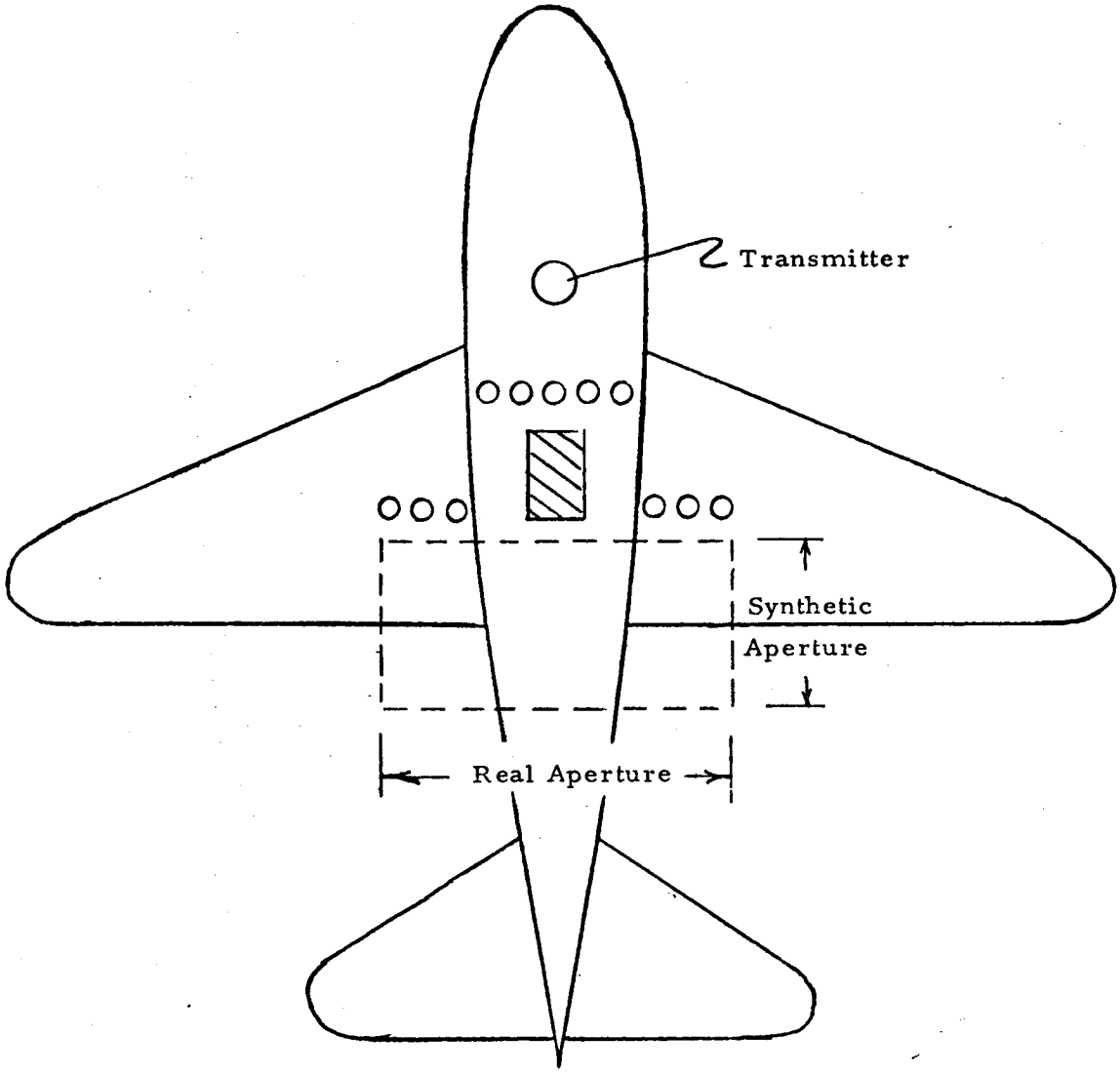

Fig. 2. Down-Looking Holographic Radar

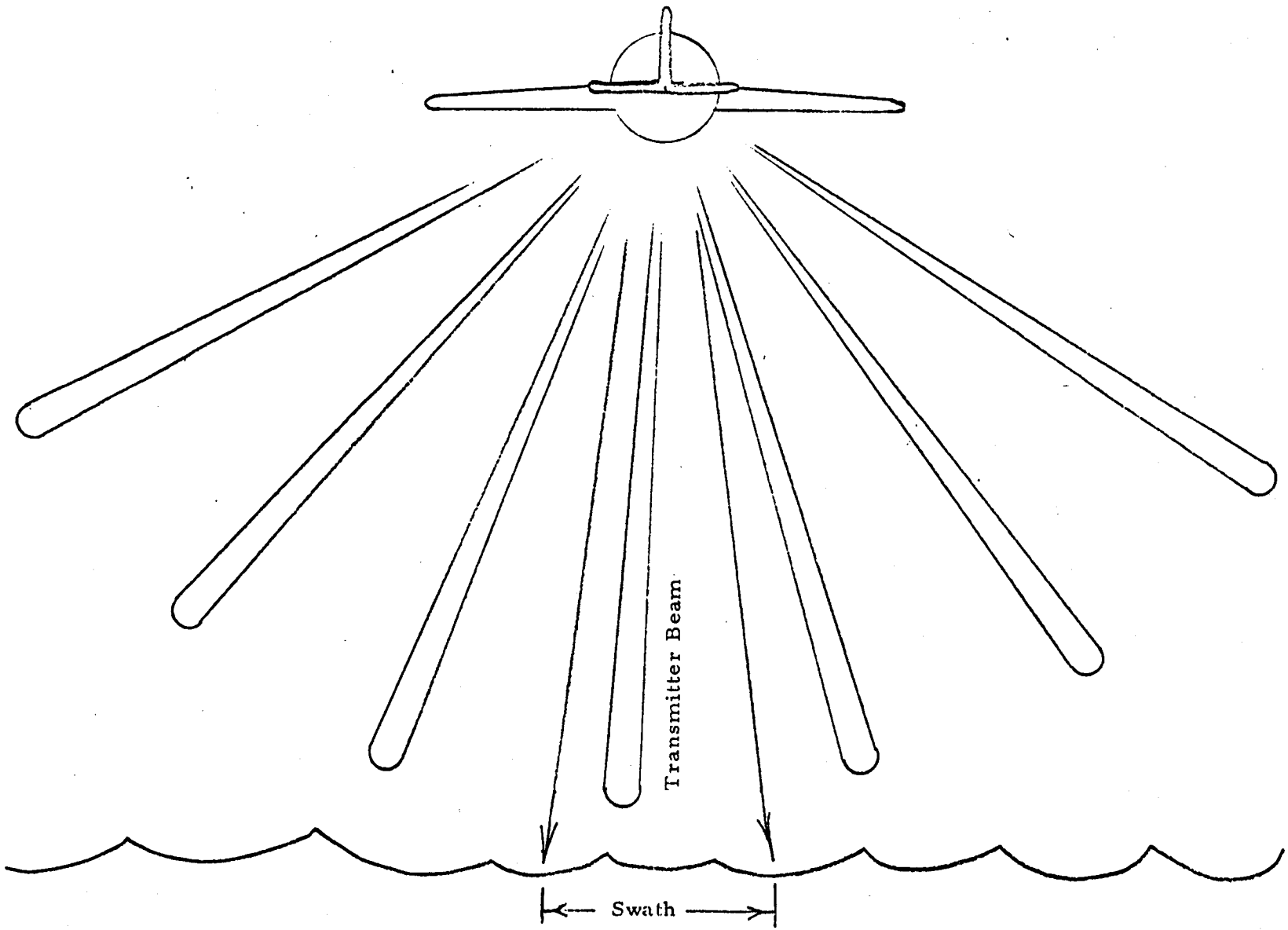

Fig. 3. Antenna Patterns

For the ocean application let us compare the systems just described on the basis of the amount of aperture that may be synthesized for high resolution. An expression derived below is valid for any synthetic aperture in either side-or down-looking systems. The linear resolutions on the water's surface is given by

$$\epsilon = \lambda r / (2L_s), \qquad (1)$$

where λ is the radar wavelength, r is range to the target (which might be called altitude h in the down-looking case), and L_s is the length of the synthetic aperture. Note that λ/L is ordinary angular resolution of an aperture, the factor of 1/2 applies to synthetic aperture since the transmitter as well as the receiver is in motion and phase shifts are thereby doubled, and r is the lever arm that gives linear resolution. The maximum length that may be synthesized is

$$L_s = Vt$$

where V is the velocity of the aircraft and t is the time during which the target holds still to sufficient accuracy. This time is

$$t = \lambda/(4\pi)/u,$$

where u is the random component of the movement of the sea surface projected along the line-of-sight. (A steady movement of a frozen sea surface is indistinguishable from a correction to the aircraft velocity. Such correction must be found by trial and error anyhow.) The above equations combine to give

$$\epsilon = 2\pi r\ (u/V) \qquad (2)$$

which curiously is independent of the microwave frequency. For high resolution (small ϵ) both r and u should be small, as they are in the down-looking case, r because the vertical distance represents minimum range, and u because the minimum projection of the random movements of the sea is along a vertical line-of-sight.

Both r and u are difficult to estimate well. Consider first a down-looking system. The range r depends on how low the pilot is willing to fly, which in turn depends on weather and the pilot's daring. Let us say r ranges from 50 to 200 feet. The surface velocity component u does not fall readily out of the theoretical models for sea states, but a value near 0.5 knots seems reasonable in moderate seas. As an example let us assume

$r = 100 \text{ ft} = h$
$u = 0.5 \text{ knots}$
$V = 200 \text{ knots}$, and find
$\epsilon = 19 \text{ inches}$.

Recall that this is horizontal resolution; vertical resolution will be that of the radar range gate. Thus sea states 1 and 2 will not be resolved, but a down-looking synthetic system will give an image of the larger structure in moderate to high seas, providing the radar is the nano-second type that generates sufficiently short pulses.

Clearly the resolution on the order of 20" is needed, so synthetic aperture side-looking radar is not applicable to the problem of imaging the sea. A side-looking system with a real aperture L_r is not unreasonable however. To estimate its size, let us assume some values compatible with the previous estimates, namely

λ = 1 inch

r = 200 feet (slant height when h=100 feet)

ϵ = 20 inches, and find

L_r = 10 feet.

These and some other comparisons between the two systems are shown in the table on the following page. In this table note the rather self-explanatory items that are not discussed here in the text, such as optical storage of bulk data, shadowing, etc.

To complete the brief feasibility study of microwave holography, let us estimate the data bandwidth that results from the previous assumptions. The bandwidth will depend on the fidelity demanded of the recording, the coding of the signals, and other electronic factors, but for a rough estimate let us allow 10 cycles for each information bit in the hologram, or 20 cycles for each resolution cell, since the information capacity of the image is less than or about equal to the information capacity of the hologram. Thus the bandwidth is determined by the speed of the aircraft and the size of the linear resolution cell. Let N_v stand for the number of vertical resolution cells or range increments. If $N_v = 5$ we find:

$$B \approx 20\, N_v V/\epsilon \text{ per channel}$$
$$\approx 20 \text{ kHz per channel,}$$

where the previous assumptions were used again. This modest bandwidth applies to each recording channel, and the number of channels equals the number of resolution cells across the width of a swath. (Of course, if desired, channels could be multiplexed in some fashion and the results recorded with megahertz bandwidths.)

	SIDE-LOOKING RADAR	DOWN-LOOKING HOLOGRAPHIC RADAR
ADVANTAGES	*Wide swath *Optical storage of bulk data *Operational technique	*Three-dimensional images *No shadowing *Strong signal from smooth surfaces
DISADVANTAGES	*Only two-dimensional *Shadowing *Real aperture required with horizontal target motion	*Narrow swath *Limited data for computer processing *Little tolerance for vertical motion
MOST OBVIOUS APPLICATION	Mapping	Detailed inspection of a statistical sample

This concludes the discussion of feasibility. The proof that pulse holographic images may be computed with reasonable speed is published elsewhere [W. Wells, Acoustical Holography, Vol. 2, p. 87, ed. Metherell & Larmore, Plenum Press, N. Y., 1970; D. M. Milder and W. Wells, IBM J. Res. & Dev., Vol. 14, p. 492 (Sept. 70)]. A sizable frame, say 50 x 50 may be computed in less than a minute on a moderate speed computer.

Several of the published images are reproduced here for convenience. In two dimensions the images of very small triangles were computed. Figures 4, 5, and 6 show a specular triangle; Figure 7 a diffuse one. These figures are analogous to a microscope view that shows the fine detail caused by edge diffraction. The contours connect points of equal image intensity. The theoretical resolution is indicated on the figures. The blooming effect at the right angle in Figure 4 is an anomoly which occurs when both legs of the triangles are parallel to the edges of the aperture and the receiver is in the direct glare of the specular reflection. The effect goes away when the triangle is rotated about the line of sight. Figure 5, or tilted very slightly, Figure 6. Figure 7 shows a diffusely reflecting triangle; often the fine structure of ocean waves will make them diffuse reflectors. The blotches of high and low intensity in this image are completely analogous to those seen when laser light illuminates a diffuse reflector. They are characteristic of coherent illumination.

Finally Figure 8 shows range slices through a three-dimensional radar image. At R=16.5 a plane greek letter Π comes into focus; its true shape is indicated by straight lines, the image by the contours. Similarly at R=17.5 a θ comes into focus.

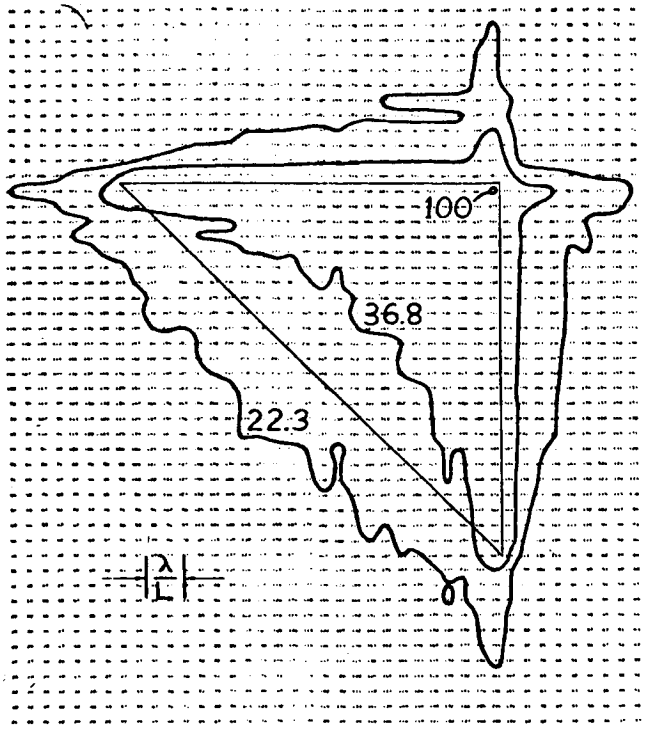

Figure 4

Specular Glare, Sides Parallel to Aperture Sides

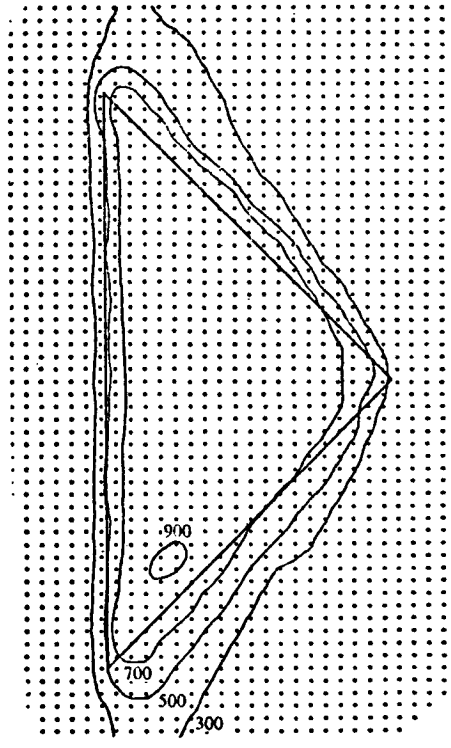

Figure 5

Specular Glare, Rotated

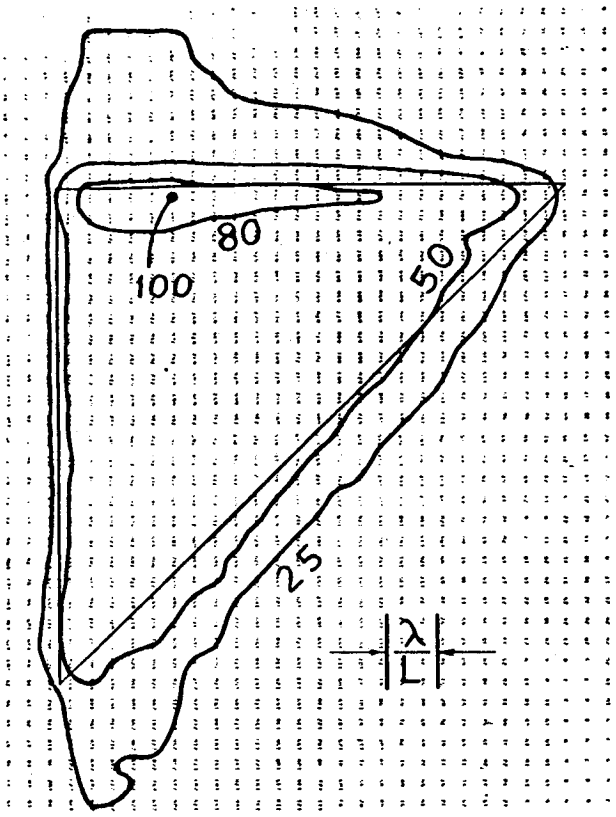

Figure 6

Tilted Off Specular

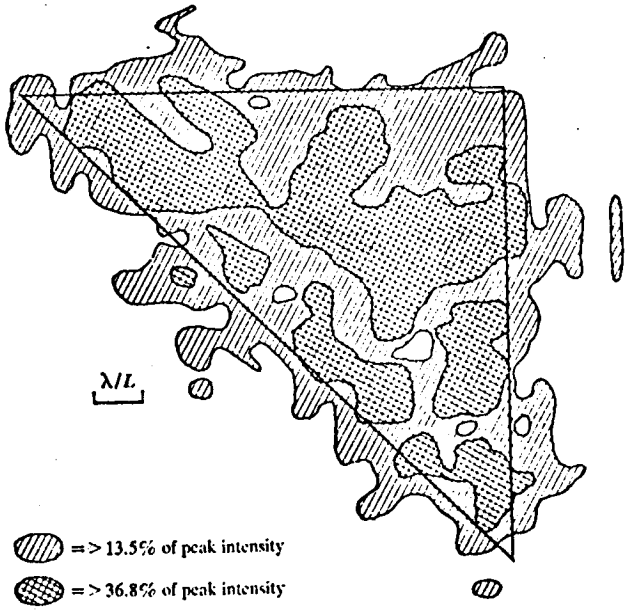

Figure 7

Diffuse Reflector

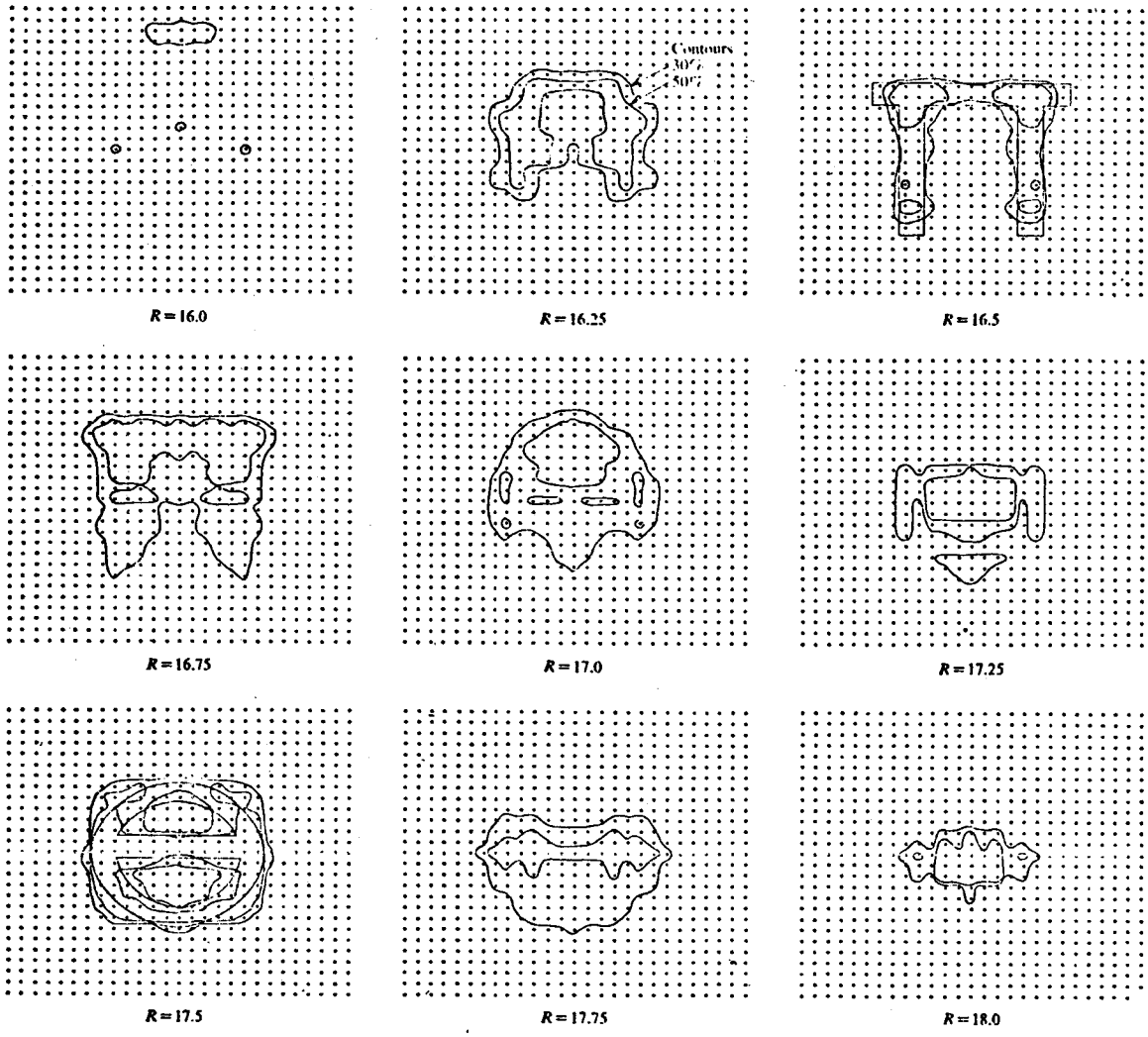

Fig. 8. Greek Letters Π and Θ Come into Focus at Ranges 16.5 and 17.5

☆ U.S. GOVERNMENT PRINTING OFFICE: 1972—780-967/187 REGION NO. 8